A novel experimental approach to elucidate the adsorption and transport kinetics of Carbon NanoTubes in microfluidic channels

Omotayo Johnson Ikwue

Submitted in accordance with the requirements for the degree of

Doctor of Philosophy

The University of Leeds

School of Mechanical Engineering

Leeds, UK

October, 2018

The candidate confirms that the work submitted is his/her own, except where work which has formed part of jointly-authored publications has been included. The contribution of the candidate and the other authors to this work has been explicitly indicated below. The candidate confirms that appropriate credit has been given within the thesis where reference has been made to the work of others.

This copy has been supplied on the understanding that it is copyright material and that no quotation from the thesis may be published without proper acknowledgement.

Acknowledgements

Abstract

A major problem in the oil and gas industry is the formation of mineral scale in production systems. One method used in industry to deal with scale is known as squeeze treatment. Squeeze treatment involves injecting scale inhibitors into reservoirs to minimize scale formation. In previous work, a way of enhancing squeeze treatment by using nanoparticles called Nanotechnology Assisted Squeeze Treatment (NAST) was proposed. The NAST methodology involves injecting nanoparticles into the oil reservoirs to modify the rock surface. This process will increase the retention of scale inhibitors on the rock surface and reduce desorption of it during the oil recovery process, hence, improving the lifetime of squeeze treatments.

One area of the NAST methodology that requires further investigation is the injection of carbon nanotubes (CNTs) into the reservoirs. To improve the methodology, the adsorption capacity of porous rock needs to be investigated under various conditions to establish what conditions affect the adsorption capacity. The transport kinetics of carbon nanotubes in microfluidic channels needs to be understood as this will provide information on factors affecting the deployment of the particles in the reservoirs. Finally, from an environmental standpoint, it is vital to monitor the quantity of particles being released from the reservoir during the NAST process. Therefore, investigating techniques capable of detecting and quantifying CNTs suspended in aqueous solution with minimal sample preparation is necessary to compliment the methodology.

This thesis has successfully demonstrated the development of an analytical integrated system capable of studying the adsorption and transport kinetics of carbon nanotubes in microfluidic channels which represents porous rock in real-time. Furthermore, this thesis investigated two potential analytical techniques with the ability to detect and quantify CNTs suspended in aqueous solution within minimal sample preparation. It was found that Raman microscopy is capable of quantifying CNTs in aqueous solution and has a limit of detection in the parts per billion level due to the resonance effect generated in the particles.

The effect of particle concentration and pH level on the adsorption kinetics are investigated using a microfluidic set up. It was discovered that there is a maximum particle concentration that provides the maximum adsorption capacity on the channel walls. A reduction in pH was found to increase the amount to CNT adsorbed in the surface of the channel. Advection was found to be the transport mechanism for CNTs flowing in microfluidic channels. Finally, it was found that salt gradients within the channel affects the transport and mixing of CNTs in microfluidic channels.

Table of Contents

List of Figures

List of Tables

Nomenclature

Term	Definition	Units
μ	Dynamic viscosity	Ns/m^2
a	Radius of the particle	m
c	Speed of Light	cm/s
C	Ionic concentration	mol/m^3
C_i	Concentration of the species	mol/m^3
D_-	Anion diffusivity	m^2/s
D_+	Cation diffusivity	m^2/s
D_{eff}	Effective diffusion coefficient	m^2/s
D_i	Diffusion coefficient of species	m^2/s
d_p	Diameter of particle	m
D_s	Diffusion coefficient of SWCNTs	m^2/s
E	Young's modulus	Pa
E	Electric field	V/m
ε	Dielectric permittivity	F/m
E_o	Amplitude	m
f	External force applied	N
IP	Induced polarization	
K	Force constant	N/m
K_B	Boltzmann constant	J/K
m_g	Mass of particle	kg
P	Pressure	Pa
Pe	Peclet Number	
r	Radius of semi - circle	m
R_i	Reaction rate	$mol/m^3 s$
T	System temperature	K
U	Velocity of fluid	m/s
u	Velocity vector	m/s
v	Frequency of radiation	Hz
$\tilde{v}$	wavenumber	cm^{-1}
V_0	Frequency of light	Hz
V_A	Attractive energy from van der Waals interactions	J
v_{ep}	Electrophoretic velocity	m/s
V_R	Repulsive force from the EDL	N
V_S	Potential energy from the solvent	J
V_T	Total potential energy function	J
β	Diffusivity difference factor	
λ	Wavelength	cm
π	Solvent permeability	
ρ	Fluid density	kg/m^3
τ_p	Particle response time	s
ζ	Zeta potential	mV

Abbreviation

Abbreviation	Definition
APTES	3- aminopropyltriethoxysilane
$BaSO_4$	Barium sulphate
$CaCO_3$	Calcium Carbonate
$CaSO_4$	Calcium Sulphate
CFD	Computational Fluid Dynamics
CNTs	Carbon NanoTubes
CO_2	Carbon dioxide
CoMoCAT	Cobalt – Molydbenum catalyst
COOH	Carboxylic
CVD	Chemical Vapor Deposition
DCC	Dicyclohexylcarbodimide
DETPMP	DiethylEneTriamine Penta Methylene Phosphonic acid
DLS	Dynamic Light Scattering
DLVO	Derjaguin, Landau, Verwey, and Overbeek
DMF	Dimethylformamide
DNA	Deoxyribonucleic acid
ε	Dielectric constant
EDL	Electric Double Layer
EDS	Energy dispersive X – ray spectroscopy
EOR	Enhance Oil Recovery
FEA	Finite Element Analysis
FTIR	Fourier transform infrared
H_2CO_3	Carbonic acid
H_2O	Water
ICP - MS	Inductively Coupled plasma – Mass Spectroscopy
IFT	Interfacial tension

k	The ionic composition of the solvent
K_{sp}	Solubility product
MIC	Minimum Inhibitor Concentration
MWCNTs	Multi Walled Carbon NanoTubes
Na_2EDTA	Ethylenediaminetetraacetic acid
NaCl	Sodium Chloride
NAST	Nanotechnology-Assisted Squeeze Treatment
ODE	Ordinary Differential Equation
PDMS	Polydimethylsiloxane
ppb	Parts Per billion
PPCA	Poly-Phosphino Carboxylic Acid
ppm	Parts Per Million
ppt	Parts Per Trillion
RM	Raman Microfluidic
SDBS	Sodium DodecylBenzeneSulfonate
SEM	Scatter Electron Microscopy
SI	Scale Inhibitors
SR	Saturation Ratio
SWCNTs	Single Walled Carbon NanoTubes
TDS	Total Dissolved Solid
TEM	Transmission Electron Microscopy
T_r	Relaxation time
Wt%	Weight percentage

Chapter 1. Introduction

The world demand for energy is predicted to grow for the next few decades as the global energy consumption continues to increase within the same time frame. It is projected that the world energy consumption will grow by 48% between 2012 and 2040 [1]. Although the use of alternative and renewable energy such as nuclear and wind power will continue to grow over the next few years, the increase will only contribute a relatively small part to the global energy production (Figure 1.1). For the near future, instead of replacing hydrocarbon, the main role of these alternative energy sources will be to complement and supplement the use of hydrocarbons [2].
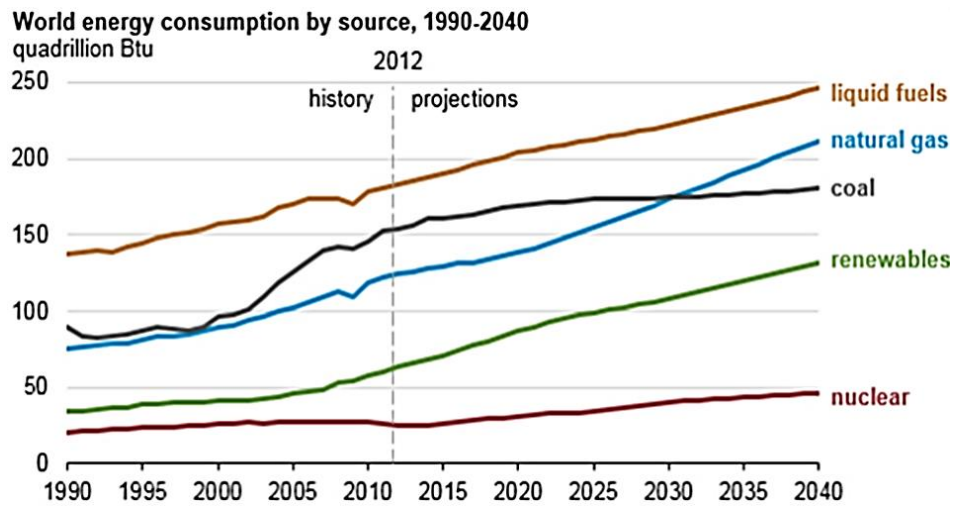
Figure 1.1: Predicted global energy consumption [3]

The demand for hydrocarbons has led oil companies to find more effective ways to recover oil from reservoirs. These methods are collectively called Enhanced Oil Recovery (EOR). Some of the challenges facing the industry, which sometimes come as a consequence of using these oil recovery methods, are formation of mineral scale, corrosion in the production systems. Mineral scale formation has been a major problem in the oil and gas industry for decades, therefore preventing the formation of scale or the removal of inorganic deposit is of great importance to the industry [4, 5].

During oil recovery processes, scale inhibitors (SI) such as Poly-Phosphino Carboxylic Acid (PPCA) and DiethylEnetriamine Penta Methylene Phosphonic acid (DETPMP) are pumped into the reservoirs with the aim of adsorbing or precipitating on the pore

surface. The production process is shut down to give the SI time to adsorb and precipitate on the rock. Once production is restarted, the SI is slowly released into the flow, resulting in the delay of scale formation. This procedure is called a squeeze treatment. After a period, the concentration of the scale inhibitor in the system will fall below a level that will make it ineffective to prevent scale formation. As a result, the squeeze treatment process is repeated. This period in between squeeze treatments is called the squeeze lifetime [6].

Research into ways to increase the squeeze lifetime is of great importance to reduce the number of disruptions to oil production and to increase the overall productivity of the oil recovery process. One of the research fields currently in development is the potential of nanotechnology to increase the productivity of the oil recovery systems.

Nanoparticles are an important class of nanostructured material that have applications in energy, biomedical and environmental industries[2, 7-10]. One area of interest is the use of nanoparticles for subsurface applications such as in porous groundwater or oil reservoirs. One emerging type of nanoparticle with a wealth of advantages for oil and gas application is carbon nanoparticles (CNPs)[11]. One advantage is that some particles, such as carbon nanotubes (CNTs), have excellent thermal and structural properties that can withstand the harsh conditions experienced in oil reservoirs[11].

During the last two decades, carbon nanotubes (CNTs) have attracted much attention due to their physicochemical properties, *i.e.,* high mechanical strength, excellent electrical and thermal conductivity which make them an ideal candidate for numerous applications in a variety of industries including construction, environmental, biomedical, including the oil and gas industry [12].

The potential application of CNTs in the oil and gas industry has been widely studies. For example, Studies have shown the potential application of CNTs as a wettability alteration agent in oil reservoirs and as an emulsion stabilizer in EOR processes [13-16]. Other studies have shown their ability to reinforce oil well cement, as a building material for composite cables located in harsh conditions, as well as their use as an additive for drilling fluids [17-21].

A patent that provides a proof of concept methodology using nanotechnology to increase the squeeze lifetime in oil reservoirs, called Nanotechnology-Assisted Squeeze Treatment (NAST), was published by researchers from the University of Leeds [11]. The NAST methodology focuses on increasing the adsorption rate of scale inhibitors on the rock surface and the slow release of the inhibitor by modifying the surface of the rock using carbon nanotubes (CNTs). The methodology is made up of three parts; the first part (NAST1) involves pre-treating the rock surface, so it is reactive to the CNTs, the CNTs are injected into the reservoir which then attach on the pre-treated rock. The second part (NAST2) involves injecting scale inhibitor into the reservoir and adsorbing onto the CNTs. When production is restarted, the scale inhibitor, which has an affinity to the CNTs, will have a slower desorption rate (NAST3). This process will increase the squeeze lifetime due to an increase in the adsorption rate and the decrease in the desorption rate of the scale inhibitor from the modified rock surface [22].

Further study of this methodology is needed to analyse its suitability for industrial use. A critical aspect of the NAST methodology is the adsorption/desorption process of the nanoparticles on the surface of the rocks (NAST1).

This thesis focuses on the first part (NAST1) of the NAST methodology. Testing this process under different conditions such as flow rate, the salinity of the aqueous solution and pH, to see the effect on the adsorption/desorption process of CNTs onto substrate is of critical importance as this will provide vital information needed to optimise the methodology. Furthermore, observing the quantity of CNTs desorbing from the rock surface is of equal importance due to the effects CNTs can have on the environment [23-30]. Therefore, researching reliable analytical techniques for quantifying CNTs suspended in aqueous solution is necessary to monitor the concentration levels of CNTs in aqueous systems such as oil reservoirs and underground water reserves.

Finally, to improve the NAST methodology, it is essential to understand factors that can affect the distribution of the injected nanoparticles in the porous system within the reservoir. The placement of injected CNTs in reservoirs is determined by the

dispersion and transport kinetics of CNTs in reservoirs systems under different conditions.

1.1   Scope of work

With this in mind, there are some critical questions of interest for this study:

- *What ways are there to monitor the injected CNTs leaving the reservoir during the NAST 1 process?*

- *What are the adsorption mechanisms of injected CNTs on functionalized rock surfaces and what factors might affect these mechanisms?*

- *What factors might affect the transport of CNTs in porous rocks?*

In light of this, the overall vision of this research project sets out to understand the adsorption and transport mechanism in porous rocks as well as to investigate analytical techniques capable of quantifying CNTs suspended in aqueous solution with minimal sample preparation.

Microscale experiments can be useful in providing mechanistic insights into macroscale flow and transport phenomena. For flow in porous media, in this case, rocks, an understanding of the conditions affecting the flow of fluids and transport of particles in porous systems are essential [31]. These conditions cannot be modelled accurately on the macroscale. Figure 1.2 shows visual and analytical limitations at different scale sizes. At the reservoir scale, physical forces caused by interfacial tension and capillary effects cannot be accurately modelled at this scale, whereas on the microscale, such forces can be modelled as well as pore structure composition, effects of wettability on flow and residual saturation [32].
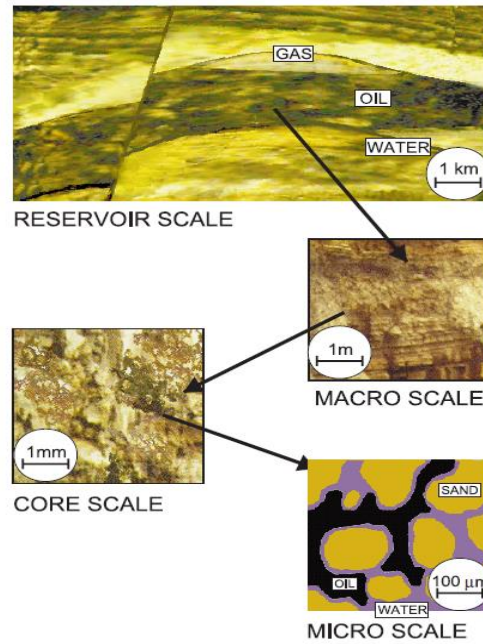
Figure 1.2 Diagram showing ranges of scale within an oil reservoir and what can be observed at these scales [32].

Microfluidic or 'lab on a chip' systems are becoming increasingly attractive in science and engineering, as they allow for the miniaturisation of systems that can then be used in laboratories. Microfluidic systems are also useful tools for handling of fluids and suspended materials, which allow experimental studies of flow in porous media to be performed under different conditions. It also allows the flexibility of performing experiments of flow in different microchannel geometries and pore structures [33-36].

One other advantage of using microfluidic chips to perform microfluidic experiments is that flow can be visually studied using optical microscopy. Nevertheless, over the years, different types of spectroscopy systems have been used with microfluidics including fluorescence, Fourier transform infrared (FTIR), ultraviolet-visible and Raman microscopy to detect and track nanoparticles in microfluidic channels [37-39]. Amongst these techniques, Raman has proven to be highly compatible with microfluidics due to its non-destructive analytical technique and its capability to offer high discrimination between sample components in the gaseous, aqueous and solid-state sample [37].

Raman microscopy provides sub-micron spatial resolution with very high sensitivity and selectivity for microfluidic systems. It can also provide information regarding target materials very rapidly, allowing for real-time monitoring processes to be practically considered in such systems. Furthermore, Raman-microfluidic systems can be employed for the study of suspended materials and particles in liquids [37, 40]. A more detailed literature on the suitability of Raman microscopy for microfluidic experiments is presented in Chapter 3.

In order to address the gaps and limitations outlined previously, this thesis provides an insight into factors effecting the adsorption and transport of CNTs suspended in aqueous solution, flowing through microfluidic channels. Crucially, the findings of this thesis will demonstrate the ability of a novel integrated Raman microfluidic analytical system to perform in-situ/real-time microfluidic experiments needed to study the adsorption and transport mechanism of carbon nanotubes in porous media. Finally, this project will present the ability of Raman microscopy to detect and quantify CNTs suspended in aqueous solution below what was previously reported with minimal sample preparation.

1.2 Aim and objectives

This project aims to study the transport of CNTs dispersed in aqueous solution through microchannels (which represent porous rocks) and the adsorption mechanism of CNTs on the walls of microchannels under various conditions as well as to determine a suitable analytical technique to monitor CNT concentrations in aqueous solution. The following objectives achieve these aims:

- Research analytical techniques capable of detecting and quantifying CNTs suspended in aqueous solution.

- Optimise the chosen technique for the specificity of the project.

- Develop a system that integrates the suitable analytical technique with microfluidic systems that will be used to study the transport and dispersion of CNTs through microchannels.

- Determine the effects of CNT concentration and pH on the adsorption behaviour of CNTs on the walls of microfluidic systems which represent pore scale channels.

- Determine the effects of brine, pH, CNT concentration and flow rate on the transport behaviour of CNTs in a microfluidic system.

- Determine the hydrodynamic conditions, salt diffusion and the trajectories of particles by modelling fluid flow conditions, transport of salt species and particle transport in microfluidic channels.

1.3 Thesis outline

In this first chapter, a brief introduction to the oil and gas industry, enhanced oil recovery methods alongside scale formation has been given. The current ways to prevent scale formation was succinctly presented. Following this, the NAST methodology was introduced as well as gaps in knowledge presented. Finally, the aims and objectives of this thesis were highlighted.

Chapter 2 gives a background on mineral scale formation issues and current squeeze treatment challenges in the oil and gas industry, the NAST methodology is mainly reviewed in this chapter. However, some aspect (NAST1) of it is mentioned in chapter 4.

Chapter 3 gives a detailed literature review relevant to this thesis. Adsorption and transport kinetics of nanoparticles in porous media are reviewed. Finally, the application of Raman spectroscopy for CNT analysis, lab on chip technology and different spectroscopy – microfluidic setups are reviewed in this chapter.

Chapter 4 presents the CNTs used in the experiments, sample preparation, experimental techniques and procedures used. It also presents the simulation software used in this thesis.

Chapter 5 introduces the analytical techniques used to characterise and quantify CNTs in aqueous solution. It will highlight the limit of detection and factors affecting the techniques used.

Chapter 6 shows the development of a Raman microfluidic integrated system used for CNTs in-situ adsorption experiments. The chapter also presents a step by step analytical and data processing procedure used in getting repeatable results from adsorption experiments. The results from these experiments provide a better understanding of the adsorption kinetics of CNTs in porous media.

Chapter 7 investigates factors affecting the transport behaviour of CNTs. It shows the application of the Raman microfluidic system in tracking CNTs in microfluidic systems. The results from this chapter highlight factors that affect transport behaviours of CNTs in porous media.

Chapter 8 CFD simulations are presented to provide a better understanding of the Transport kinetics of CNTs in porous media.

Chapter 9 contains a detailed discussion of the results of all works carried out in this research. The main contribution of this work is to develop a new integrated technique that is used to perform adsorption and transport experiments on CNTs. Chapter 7 will focus on the application of the system to the NAST methodology.

Chapter 10 presents the main conclusions of this work and the possible further work of this research to improve the Raman microfluidic system which can improve the application of the system in performing experiments relevant to improving the NAST methodology.

Chapter 2.   Background

2.1   Introduction

An overview of the oil and gas industry is discussed in this chapter, and in particular oil recovery processes. Also included is the fundamental principles of scale formation and its impact on oil recovery and squeeze treatments.

Since NAST methodology involves the application of nanoparticles, an overview of nanotechnology and its application for enhanced oil recovery is also included. Finally, a detailed description of all processes involved in the NAST methodology is presented. The chapter will conclude by presenting the focus of this thesis and why.

2.2   Challenges in the oil and gas industry

Declining conventional oil reservoirs have led oil companies to explore hard to reach offshore oil reservoirs which has increased the cost of oil recovery. The first part of the process involves finding a new reservoir; which consists of research, survey, exploration and drilling. Once the presence of oil is confirmed, and it is deemed profitable, drillin, and extraction can begin [41]

Once the oil well is drilled and completed, the oil is forced to the surface by the reservoirs natural pressure which is the primary recovery stage. Over time, the pressure in the reservoir will fall and the production decreases, which leads to oil companies using techniques to maintain the pressure required to push the oil to the surface. In order to maintain the pressure at the secondary recovery stage, water (or gas) is injected into the reservoir to push the oil to the surface. Finally, the tertiary recovery consists of techniques that require the injection of various chemicals such as detergent, solvents or bacteria. This stage is normally done in conjunction with the secondary stage [2, 42]. Figure 2.1 shows a diagram of the different stages in oil recovery.
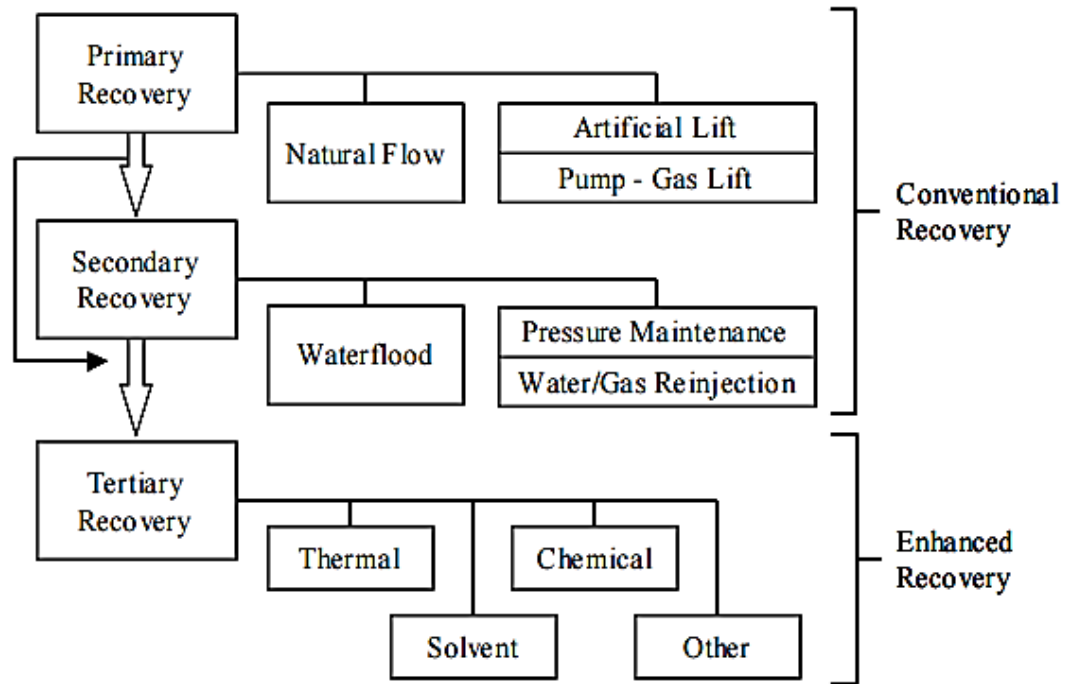
Figure 2.1: Diagram showing different stages of the oil recovery process [43]

2.3 Scale formation

Mineral scale is defined as crystalline growth of insoluble salt that either stays in the aqueous solution or adhere to the solid surface. Inorganic scales can form when two incompatible brines are mixed or where changes in environmental conditions in the system like temperature and pressure result in changes in the solubility of certain salts. Two brines are deemed incompatible if they interact chemically and produce insoluble mineral scale when mixed. An example of incompatible mixing is a situation where seawater with a high concentration of sulphates (SO_4^{-2}) mixes with formation waters with a high concentration of Calcium ions (Ca^{+2}) and Barium ions (Ba^{+2}). Mixing this water will likely cause precipitation of calcium sulphate ($CaSO_4$) and barium sulphate ($BaSO_4$) [44]. Mineral scales fall into many categories including carbonates and sulphates. Table 2.1 presents a summary of some common scale mineral types and their causes. Depending on water chemistry and environmental conditions, different types of scale crystals are formed [45].

Table 2.1: Example of common scales found in oil fields, causes and removal methods[46].

Mineral Name	Causes	Removal treatment
Calcium Carbonate (CaCO$_3$)	Partial pressure of CO$_2$, temperature, total dissolved solid (TDS), pH	Hydrochloric acid Na$_2$EDTA (Ethylenediaminetetraacetic acid)
Calcium Sulphate (CaSO$_4$)	Temperature, TDS, pressure	Na$_2$EDTA
Barium sulphate (BaSO$_4$)	Temperature, TDS, pressure	Na$_2$EDTA High – pH chelating

During offshore oil recovery, seawater is one of the fluids used to flood the oil reservoir during the secondary recovery stage to maintain upward pressure. The injected seawater may meet the formation water in the oil reservoir which tends to be incompatible due to different ions composition and as a result, scale crystals are formed. Two common types of scale crystals are barium sulphate (BaSO$_4$) and calcium carbonate (CaCO$_3$). The pressure drop in the production system is the main reason for the formation of calcium carbonate while barium sulphate is formed from the mixing of formation water and seawater in the reservoir [47]. Figure 2.2 shows a typical well bore and oil reservoir including the regions where different types of scales can occur.
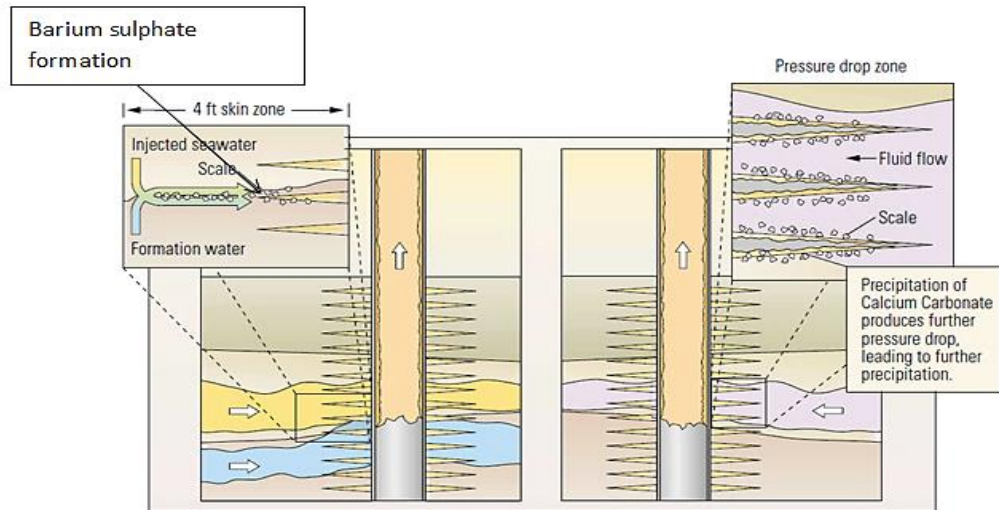
Figure 2.2: Diagram showing different regions in the production system where scale can occur [48]

As a consequence of scale formation, productivity within the recovery system reduces; costing the oil industry millions in removal and prevention of scale formation [49]. Scale deposition can occur in the reservoir, the wellbore formation and in the production well. Within the oil reservoir, scale deposition can block interconnecting pores thereby reducing the rock's permeability which could lead to formation damage in the reservoirs. Flow assurance issues in the production systems are also a consequence of scale deposition in the system. Figure 2.3 shows an example of scale deposition in a pipe.

Figure 2.3: Scale deposition in sections of pipeline [50]

As it shows, scale deposition in transport pipelines and in topside equipment such as pumps and valves can cause blockages and damage. The replacement of pumps and valves due to scale deposition can be very expensive. The economic impact of scale is estimated to be in excess of USD 1.5 billion a year [49].

2.3.1   Processes of scale formation

As stated earlier, mineral scale formation originates from chemical reactions between ions in different substances that mix during the production process. The process of scale formation happens in a number of stages; Figure 2.4 shows the overall mechanism of scale formation.
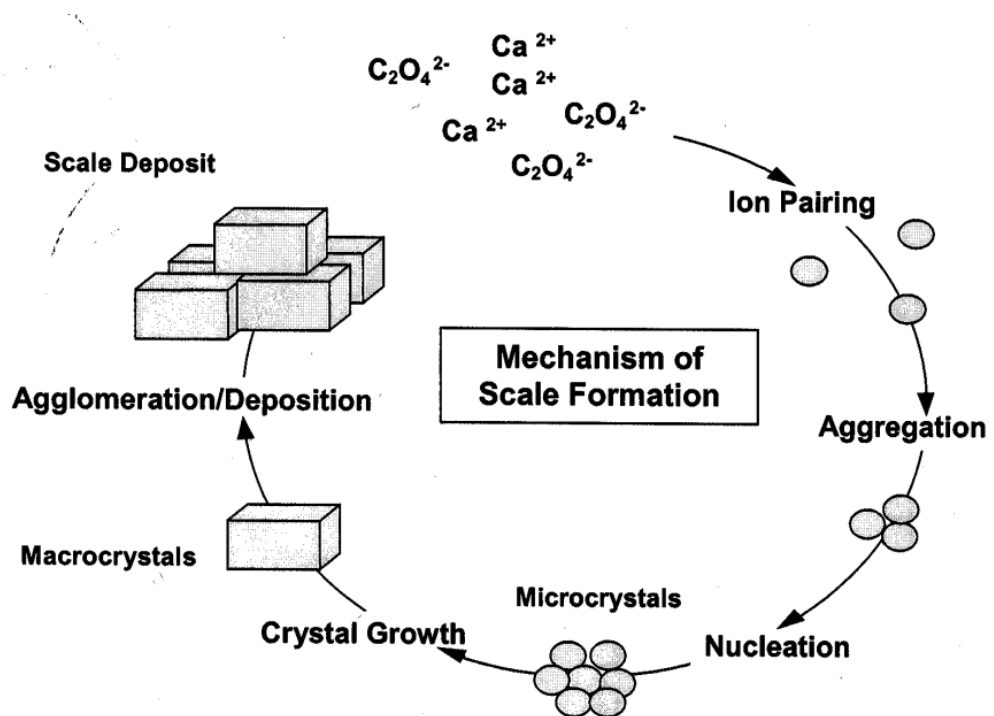
Figure 2.4: Overall mechanism of scale formation showing all the different stages [51]

A simple equilibrium approach is used to demonstrate how different parameters within the system influence the formation of scale crystals. In order to limit the extent of this review, the focus will be on the formation of calcium carbonate.

2.3.1.1 Calcium carbonate precipitation mechanism

Calcium carbonate occurs due to the presence of calcium cations and carbonate anions in the formation water. During production, this water is usually drained to the surface and as a consequence will experience significant pressure drop and temperature changes [52]. This pressure drop will instigate the evaporation of carbon dioxide from the solution due to the pressure falling below the bubble point of carbon dioxide.

Firstly, the carbon dioxide reacts with water to form carbonic acid (Equation 2.1); the carbonic acid will continue to dissociate the hydrogen ions due to loss of carbon dioxide to the atmosphere which leads to an increase in pH (Equation 2.2 to Equation 2.3).

$$CO_{2(g)} + H_2O \leftrightarrow H_2CO_3 \qquad\qquad \textbf{\textit{Equation 2.1}}$$

$$H_2CO_3 \leftrightarrow HCO_3^- + H^+ \qquad\qquad \textbf{\textit{Equation 2.2}}$$

$$HCO_3^- \leftrightarrow CO_3^{2-} + H^+ \qquad\qquad \textbf{\textit{Equation 2.3}}$$
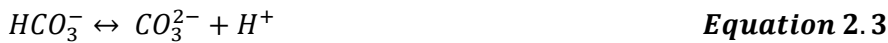
Finally, calcium ions in the production water will react with carbonate ions to form calcium carbonate (Equation 2.4)

$$Ca^{2+} + CO_3^{2-} \leftrightarrow CaCO_{3(s)} \qquad\qquad \textbf{\textit{Equation 2.4}}$$

An overall equilibrium equation is shown below illustrates the precipitation of calcium carbonate due to the reaction of calcium and carbonic acid in production water.

$$Ca^{2+} + 2HCO_3^- \leftrightarrow CaCO_{3(s)} + CO_{2(g)} + H_2O_{(l)} \qquad \textbf{\textit{Equation 2.5}}$$
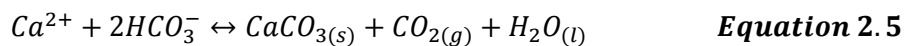
2.3.2   Saturation Ratio

The main driving force that instigates the formation of scale is the saturation level of the solution environment, which then forms as mineral scale in the solution or precipitate on the surface [46, 53-55]. For precipitation to occur, the solution must contain more ions than it can dissolve, which is known as supersaturation. The low solubility of materials in the solution leads to the development of a highly saturated solution which consequently leads to precipitation. As a result, the level of saturation in the solution can have an impact on the rate of scale formation process. The tendency for mineral scale to form can be quantified by the saturation ratio (SR). The SR is used to determine the saturation level in the solution and is defined by:

$$SR = \frac{a_1 \times a_2}{K_{sp}}$$
<div align="right">***Equation* 2.6**</div>

Where:

- a is the ion activity

- K_{sp} is solubility product

The solubility product is K_{sp} for calcium carbonate is expressed as (Ca^{2+}) (CO_3^{2-}) and is defined as an equilibrium constant for dissolution reactions. The solubility product is temperature (the value of K_{sp} at 25°C is 4.55x10^9 and at 80°C is 1.06x10^9) and pressure dependent; as such the level of saturation will change from one location of the production system to another [46]. The propensity for scale to form is determined by certain saturation ratio values:

- **SR < 1**: The solution is under saturated therefore scale formation cannot occur.

- **SR = 1**: There is equilibrium; both scale formation and dissolution rate are equal. Therefore there is no scale formation in the system

- **SR > 1**: The solution is supersaturated. Scale formation is likely to occur. The solution contains more ions than the solvent is able to maintain in a dissolved state [56].

2.3.3   Induction

The induction period is defined as the period between when the solution becomes supersaturated and when the first observable change in some physical property such as change in turbidity of the solution occurs. In order to determine the induction period visual methods could be used by observing the change in turbidity [57, 58].

Within the induction time there are three time frames; the first is the relaxation time (t_r) which is the time taken for molecular clusters to be distributed in order to reach quasi-steady state, following that is the nucleation time which is the time needed to form a stable nucleus and finally the growth time which is the time taken for the nucleus to grow to a "visible" size [46, 59].

2.3.4   Nucleation

After the induction period, crystals are formed from calcium ions and carbonate ions joining together to form stable nuclei that are the centre of crystals. This process can occur very quickly in regions of high supersaturation levels. There are two main processes for the formation of nuclei, namely primary and secondary nucleation which are shown in Figure 2.5. Primary nucleation is divided into two main part namely; homogeneous and heterogeneous nucleation[46, 60].
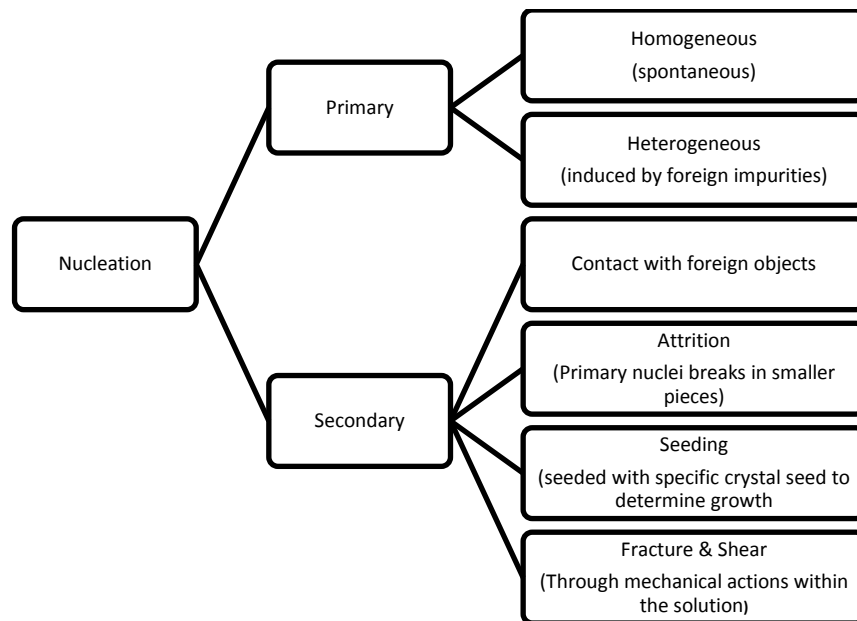
Figure 2.5: Diagram showing the different nucleation types [46, 61]

Homogeneous nucleation occurs when there is a very high level of supersaturation. Under these conditions, scale will form independently of foreign particles, whereas heterogeneous nucleation occurs as a result of foreign particles in the solution. It can also occur due to surface imperfections acting as nucleation sites. Homogeneous nucleation takes place in the bulk solution while heterogeneous nucleation happens on the solid surface since it requires an active site to grow. In order for secondary nucleation to occur, crystalline matter needs to be present in the solution as a result lower supersaturation level is required to instigate nucleation [46, 61, 62].

2.3.5 Growth

Once stable crystals are formed after nucleation, then growth will occur. During this stage the crystals will grow in size, which will reduce the supersaturation ratio of the solution in a closed system. Alongside the crystal growth there will also be agglomeration which will also increase the size of crystals [45, 63, 64]. The active site on the surface of bigger crystals or other solid surfaces will also act as a place for the scale crystals to grow as Figure 2.6 shows.
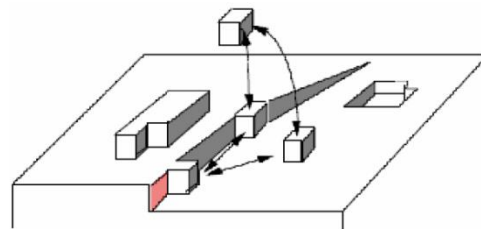
Figure 2.6: Schematic of crystal deposition and growth on a solid surface[45]

2.3.6 Types of calcium carbonate scale crystal structure

The common types of calcium carbonate crystals are shown in Table 2.2. Calcium carbonate comes in different crystal morphologies namely; vaterite, aragonite and calcite. Calcite has a higher tendency to aggregate and is more thermodynamically stable than the other crystals. It is also harder to remove than vaterite and aragonite, which are softer crystals [45, 65].

Table 2.2: Shows calcium carbonate crystal [45, 46]

	Calcite	Aragonite	Vaterite
Crystal system	Rhombohedral $\alpha, \beta, \gamma \neq 90°$	Orthorhombic $a \neq b \neq c$	Hexagonal $a \neq c$
Morphology	Calcite [66]	Aragonite [67]	Vaterite [68]
Density (g/m³)	2.71	2.93	2.66
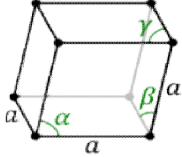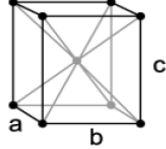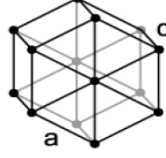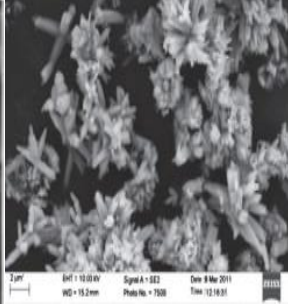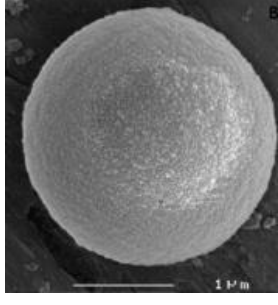
2.3.7   Factors affecting scale formation

There are physical and chemical factors that determine the tendency for scale crystals to form and what type of polymorph is created in production systems.

2.3.7.1 Temperature

During the oil recovery process, the production system experiences varying temperatures depending on the location. Experiments show that that at different temperatures, the particle size changes as well as the morphology [69]. The particle size decreased with an increase in temperature. Experiments carried out also showed that temperature plays an important role in determining the solubility of crystals, which decreases when temperature increases[46]. Feng *et al* [70] showed that as temperature increases the crystallisation process speed increases. Another part of scale formation that is affected is the morphology. Han *et al* [69] found that aragonite

formed at high temperature while calcite and vaterite form at low temperatures [69, 70].

An increase in temperature increases the supersaturation relative to $CaCO_3$ resulting in a higher tendency for scale to form. Figure 2.7 shows the relationship between supersaturation and temperature [71].
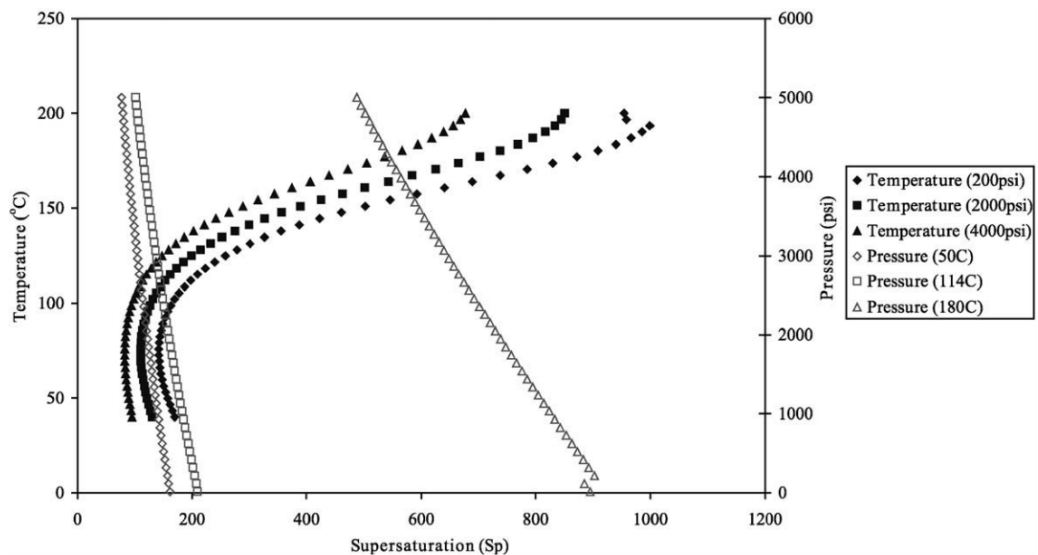
Figure 2.7: Graph showing the effect of temperature on supersaturation [71]

2.3.7.2 Pressure

As mentioned earlier, $CaCO_3$ occurs due to the presence of calcium cation and carbonate ions in the solution and also as a result of a pressure decrease in the system. Jean-Yves Gal et al [72] performed experiments with results showing the importance of monitoring the partial pressure of carbon dioxide in the system so as to manage scaling water. This pressure drop instigates the loss of CO_2 in the aqueous solution which in turn increases the pH of the solution. The supersaturation decreases as pressure increase as shown in **Error! Reference source not found.**, which will have an effect on the propensity for scale to form [45].

2.3.7.3 pH

The pH affects the morphology of the crystal. This change of morphology can be attributed to high supersaturation levels of the solution due to the high pH. The size of the crystals decreases with an increase in pH and is the result of a faster nucleation rate of the initial particles due to an increase in pH[46] .

2.3.8   Scale management

Scale can be removed chemically or mechanically after formation and deposition of scale crystals. Preventive methods are used to stop or delay the formation and deposition of scale crystals.

2.3.8.1   Scale removal

There are various solutions that are used to remove scale deposition from the production system. Mechanical method involves physically removing the scale deposition form the surface of the production systems. This is an expensive method as it requires the shutdown of the system in order to carry out the mechanical procedure. Chemical method involves using acids to dissolve the scale deposition but they are less effective due to the resistant of some inorganic scales like barium sulphate to acid treatment [45].

Scale removal methods must be non-destructive, cause minimal disruption to the system. The suitable scale removal method depends on the type of scale, the quantity of scale, its location and physical composition. A poor choice of removal method may enhance scale formation [48].

2.3.8.2   Chemical removal

Chemical removal is often the starting point to scale treatment, especially in areas where scale is difficult to reach for mechanical scale removal to be carried out. For example, scale formation in the formation matrix is not easily accessible so it would require a chemical treatment. Acid treatment is one of the ways that scale deposits, that are soluble in acid, can be removed. Calcium carbonate deposits can be dissolved by using hydrochloric acid whereas non-soluble acid scale crystals like barium sulphate can be treated using a chelating agent. This compounds break up the scale by isolating the ions within the ring – like structure [48].

2.3.8.3   Mechanical removal

Conventional mechanical removal of scale formation from the system is the most effective removal method in tubular systems that are easily accessible. Like in chemical removal methods, care must be taken in choosing the appropriate method

for removing scale mechanically. Table 2.3 shows a few removal techniques including their description and their advantages and disadvantages.

Table 2.3: Shows a number of removal methods [48]

Tool	Description	Advantages	Disadvantages
Positive displacement motor and mill	Fluid – powered motor and mill. Mill removes scale deposit by grinding.	Positive surface indication of cleaning.	Parts are expensive. Not compatible with scale dissolvers.
Impact hammer	Fluid powered percussion hammer. The shock force from the hammer is high which will shatter brittle deposits.	Simple yet robust tool.	Large cuttings size makes cleaning more difficult.
Fixed wash tool	Fixed tool with many large diameter nozzles. Used with chemical dissolvers.	Simple and robust	Inefficient jetting due to high rpm.
Sonic tools	Uses high frequency pressure pulses to remove deposits	Simple technique	Hydrostatic pressure suppresses cativation
Bridge blasting	Fluid – powered motor and jet head.	Positive surface indication of cleaning.	Parts are expensive.

2.3.9   Preventive methods

Preventive methods are the preferred way of dealing with scale, due to the fact that removal methods have significant costs. There is the direct cost of scale removal which could go into millions of dollars as well as the cost of disruption to the production of oil. Scale can be prevented by physical and chemical techniques. Anti-scale magnetic treatment, use of electric fields and sonic waves are some physical techniques currently developed or used. Chemical preventive methods range from dilution methods to chemical scale inhibitors. Dilution methods reduce the salinity in the solution by continuously flushing the system with fresh water in order to reduce the saturation in the topside system; other chemical techniques consist of adding strong acid to lower the pH, chelating agents and complex calcium ions to alter the chemistry in the solution. The most effective method of preventing scale formation is the use of chemical scale inhibitors [73, 74].

2.3.10 Scale inhibitors

Scale inhibitors are used to retard or reduce the formation of scale crystals and are added to potentially scale forming water. As Table 2.4 shows, scale inhibitors can be divided into four main categories namely: polyphosphates, polycarboxylic acids and polyelectrolytes [75]. The ideal scale inhibitor should have the following characteristics:

- It should work at low concentrations.

- It should be compatible with both sea and formation water.

- It should have balanced adsorption – desorption properties to enable slow release of the chemical into the system.

- Low cost, low toxicity and biodegradable.

Table 2.4 : Shows the different categories of scale inhibitors and their limitations [76].

Inhibitor type	Limitations
Inorganic polyphosphates [77]	Suffers hydrolysis and can precipitate as calcium phosphates due to temperature, solution quality, concentration, and phosphate type.
Organic Polyphosphates [78]	Suffers hydrolysis at certain temperature. Loses its effectiveness when there is a high concentration of calcium in the solution. Works only when high dose is applied.
Carboxylic acids [79]	Calcium tolerance is limited although some work at high concentrations of scale inhibitors, therefore high concentration needs to be applied to the system.
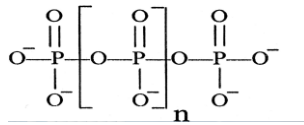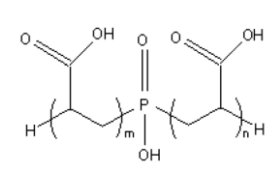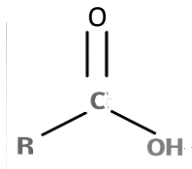
Phosphates prevent scale deposition by isolating calcium ions in the solution thereby inhibiting scale precipitation. Polyphosphates are particularly effective at inhibiting scale formation at a pH range of 8 – 10. Various forms of phosponate are used to prevent scale formation. These compounds contain bonds that are more stable than polyphosphates [45, 80].

2.3.11 Squeeze treatment

Oil companies are constantly seeking better ways of achieving effective scale control in the production system. One way of achieving this is by injecting scale inhibitor into the system during the secondary oil recovery. There are various ways of injecting the scale inhibitor in the system. It can be done continuously or by encapsulating scale inhibitors [45]. It can also be done by injecting the inhibitor in the production wells that lead into the oil reservoirs, then shutting down production for a period of time (shut-in period) to allow the scale inhibitor to either precipitate or adsorb onto the

surface of the rock. Adsorption of inhibitors on the rock surface is thought to occur through electrostatic and Van der Waals interaction between the inhibitor and the rock. The retention mechanism of precipitation of inhibitor on rock is thought to be the reaction of the inhibitor with cations like calcium in the solution to form a sparingly soluble calcium/inhibitor complex that will precipitate on the rock surface[81]. When production in the well is restarted, the inhibitor is slowly released into the system through the fluids in the system. A certain scale inhibitor concentration level is required in order to provide effective scale treatment in the system. This is called the Minimum Inhibitor Concentration (MIC). [45, 82]. Squeeze treatments consist of five stages including:

(i) **Pre-flush squeeze**: In order to pre-treat the formation rock, the system is flushed with a very dilute solution of seawater and some surfactants in order to increase the water wettability of the rock surface.

(ii) **Main treatment**: The main inhibitor is injected into the near wellbore area; the inhibitor may also contain other additives.

(iii) **Overflush**: The main inhibitor solution is pushed further down the wellbore by injecting seawater into the system in order to place the inhibitor deeper into the reservoir.

(iv) **Shut-in**: The production system is shut down a period of time to allow the inhibitor to interact with the rock surface.

(v) **Restart production**: The production system is restarted and the inhibitor is expected to return to the wellbore at a concentration above the MIC [83, 84].

As oil production continues, there will come a point when the concentration level of inhibitor in the system will fall below the (MIC) level required to effectively prevent scale formation. At this point, the squeeze treatment process will be repeated. The time in-between each squeeze treatment is called a squeeze lifetime. The graph that shows the squeeze lifetime is called the scale inhibitor concentration return profile which is illustrated in Figure 2.8.
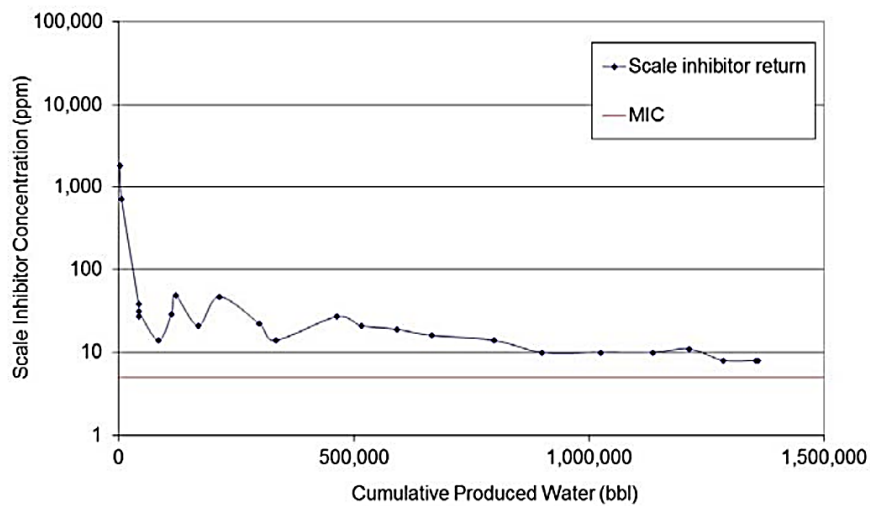
Figure 2.8: Illustrates a typical field scale inhibitor return profile [85]

As Figure 2.8 shows, there is a rapid drop in concentration of scale inhibitor as production restarts which indicates that a large portion of the inhibitor is washed out of the system when production is restarted. Factors that affect the adsorption or precipitation of scale inhibitors include formation mineralogy, solution chemistry, and rock porosity and operation parameters.

The lifetime of a squeeze treatment can last between 6 months to 2 years depending on factors such as flow rate, oil/water ratio and the factors that affect the adsorption or precipitation of scale inhibitors. In an ideal squeeze treatment, it is preferable to have a high adsorption rate of the inhibitor onto the rock and a slower desorption rate once production is restarted [45, 75, 86].

Figure 2.9 illustrates a comparison between an ideal squeeze treatment and a real treatment; from the figure it can be seen that the main difference between the two

graphs is the time taken for the scale inhibitor concentration to reach the MIC, which is longer in the ideal return profile.
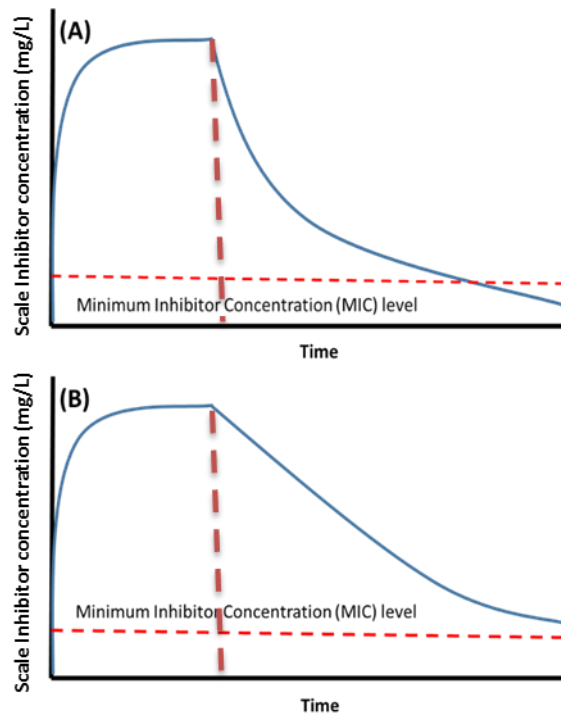
Figure 2.9: Diagram of (A) real return profile and (B) ideal return profile. Vertical line indicates where production starts. [45]

There are different types of cost associated with carrying out a squeeze treatment. Some of these costs are the scale inhibitors themselves, the cost of delivery and personnel. However, the highest cost is the cost associated to loss of income from deferred oil due to shut-in periods. If a treatment goes well, the shut-in period could last one or two days, depending on the treatment. If it goes badly, it can last up to a week. Ensuring that treatments are optimized is of great importance to enhance squeeze lifetimes and minimise shut-in periods [6].

Coreflood tests are used to characterise adsorption/desorption and precipitation/dissolution process of SI during squeeze treatments. A typical coreflood experimental set up is shown in Figure 2.10.
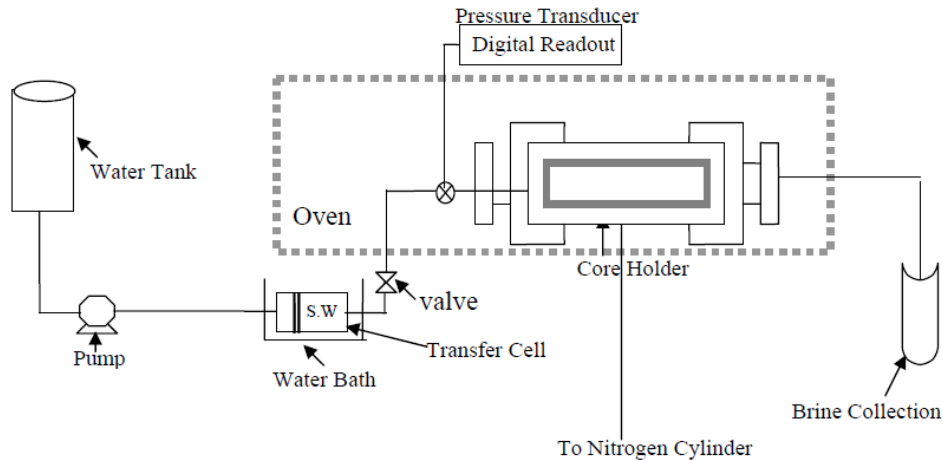
Figure 2.10: Schematic of the core flooding apparatus

The main component of the coreflood is the "core", which a piece of porous rock that represents the reservoir rock. Fluids such as brine and scale inhibitors are pumped into the core and the effluents are collected for analysis which tends to be determining the concentrations of the chemicals in the effluent at given time intervals.

The results from coreflood experiments are graphically represented as SI return curve similar to Figure 2.9. These return curves have been used to predict the adsorption processes of the reservoir. For instance, Sorbie et al [87] studied the adsorption/desorption of DETPMP in artificial seawater on sandstone core and a mathematical methodology for the adsorption process was derived from the experimental data.

Researchers are constantly looking for ways to improve the squeeze treatment process. For example, during the pre – flush process, ionic polymers such as poly amino acids and poly quaternary amines have been injected into the well and have enhanced the retention mechanism of the inhibitor [88]. Other ways of prolonging squeeze treatment include using calcium to enhance precipitation of inhibitors, using other stimulation or precipitation enhancing additives, use of inhibitor particle suspension and cross – linking the inhibitors [78]. Recently, researchers are looking at ways to implement nanotechnology to improve the squeeze treatment process and other processes in the oil and gas industry.

2.4 Nanotechnology

2.4.1 Overview of Nanotechnology

Nanotechnology can be defined as a field of science and technology that deals with control of matter on the nanoscale usually between 1 nanometre and 100 nanometres in diameter (for spherical particles) and also involves the fabrication of devices with dimensions at that scale range. One nanometre is one billionth of a meter, to put it in perspective Figure 2.11 shows a diagram of objects and their corresponding sizes [7].
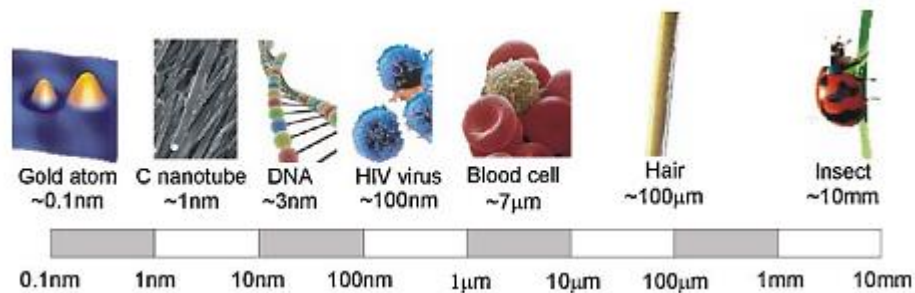
Figure 2.11: Length scale and some relating examples[9]

Nanotechnology has already contributed significantly to technological development in many industries including biomedical, aerospace, photography, pharmaceutical and recently the oil and gas industry. Nanotechnology has the potential to put the oil and gas industry beyond the current options for oil production by introducing technologies that make production more efficient and more environmentally friendly [2]. It has a multi-disciplinary background; which includes physics, chemistry, molecular biology, electronics and a host of other science subjects. There are various areas under nanotechnology as Figure 2.12 shows.
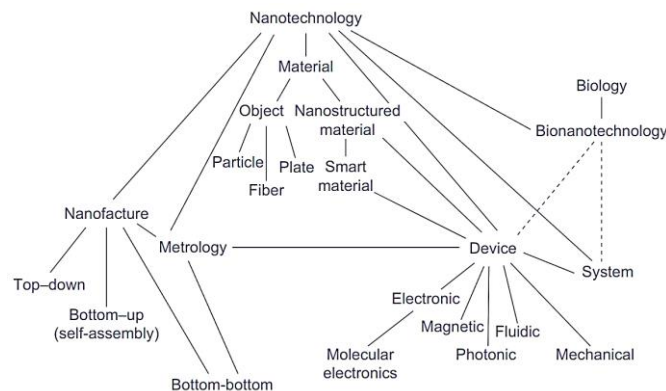
Figure 2.12: Diagram showing different areas within nanotechnology [89]

2.4.2   Nanotechnology in Enhanced oil recovery

Over the years, there have been major advances in the EOR process, but the progress still faces many challenges including high cost in techniques applied in the process, the possibility of formation damage due to EOR processes, transporting EOR chemical agents to the fields especially in the case of offshore oil reservoirs and other oil extraction challenges that hinder the advancement of EOR processes [90]. One of such advances is the role nanotechnology is beginning to play in the future of EOR processes.

2.4.3   Nano-sensors

Nanoparticles that can flow through porous rocks with minimal retention on the rock surface can be used as nano-sensors. Injecting nano-sensors into the oil reservoirs has been of interest to oil companies for the last few years. With sensors, it will be possible to increase the accuracy of mapping the reservoirs in 3-dimensions, therefore increasing the recovery amount and minimizing the environmental impact. In the case of EOR processes, nano-sensors can be used to examine individual channels, trace trapped fluids such as crude oil and EOR chemical agents. The sensors can monitor the flow of oil in the reservoirs, pressure and temperature conditions in reservoirs and be able to pass information to the surface and determine zones to focus or avoid during the production process. An example of a nano-sensor is paramagnetic nanoparticles, which when injected into the reservoir, can evaluate fluid saturations within the formation rock by the application of magnetic fields and measurement responses [90-92].

2.4.4   Nanofluids

EOR processes are divided into three main categories which are gas miscible flooding, thermal processes and chemical flooding. Miscible flooding involves injecting miscible gases into the reservoir; however one of the major problems associated with this process is poor reservoir volumetric sweep efficiency. Thermal processes provide heat to the reservoir which increases oil production by reducing the viscosity of oil; this process has limited use for deep reservoirs due to heat loss. Chemical processes involve injecting chemicals such as surfactants to increase oil production by changing properties such as wettability and interfacial tension of the rocks and fluids. Under

very harsh conditions such as high temperature and high water salinity or hardness, the chemicals could lose some of their usefulness in the oil production process. With all these challenges in mind, new technologies are needed to improve on existing technologies. Ideally, new fluids should be able to withstand harsher conditions, perform well in these conditions, improve dispersion and give an overall improved production process [93].

When nanoparticle additives are added to fluids, properties such as density, thermal conductivity, viscosity and specific heat can be modified to reach the optimum levels. For example the addition of nanoparticles such as silica nanoparticles to injected fluids has been observed to enhance oil recovery by altering the wetting property of the reservoir rock [94].

2.4.5   Carbon nanotubes

Carbon nanotubes were first discovered by Ijima in 1991 as a by-product of the synthesis of fullerene by using the arc discharge technique [95] . Carbon nanotubes (CNTs) can be described as narrow strips of graphene rolled up into tubes. These tubes are nanometres in diameter but can go up to centimetres in length. The carbon atoms, which make up the CNTs, have a well-ordered arrangement through sp^2 bonds which makes them among the stiffest and strongest fibres known. They are stronger than steel yet many times lighter. They fall into two categories namely single walled carbon nanotubes (SWCNTs) and multi walled carbon nanotubes (MWCNTs), the images in Figure 2.13 represent the SWCNTs and the MWCNTs. The mechanical, chemical, electrical properties of CNTs have led researchers to find ways of applying CNTs to various applications including electrical applications, medical application, and oil and gas applications, [96, 97].
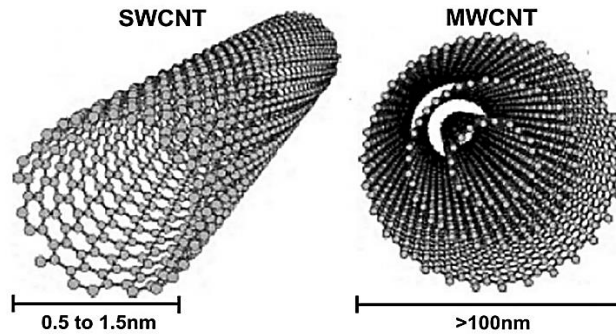
Figure 2.13: Images of single walled CNTs and multi walled CNTs [98]

2.4.5.1 Application of carbon nanotubes

2.5 Nanotechnology Assisted Squeeze Treatment (NAST)

Ghorbani's work on the NAST process has shown that nanoparticles have the potential to enhance squeeze lifetime by increasing the adsorption of scale inhibitor on the surface of reservoir rocks. The NAST process involves the use of CNTs to modify the surface of reservoir rocks. CNTs have many properties that make them suitable for well bore problems. They are stable at a high temperature and due to its high tensile strength it is able to withstand the high temperature and pressure experienced in well bores and oil reservoirs. The high specific surface area of CNTs enables the adsorption of inhibitors onto them [45]. A detailed description of the methodology and the previous experiments done to achieve proof of concept are also highlighted.

2.5.1 Stages in the NAST process

The NAST process is divided into three Stages; NAST 1-3. NAST 1 deals with treating the rock surface in order to make it reactive to the CNTs and it also deals with the delivery of the CNTs to the treated rock surface and finally, the bonding of CNTs onto the rock surface. NAST2 involves the adsorption of scale inhibitors on the CNTs and the shut-in phase. At the final stage (NAST 3), production is restarted and the slow release of scale inhibitor is expected. Once the concentration of scale inhibitor reaches the minimum inhibitor concentration (MIC), NAST 2 stage is repeated. The schematic of the NAST methodology is shown in Figure 2.14 below.
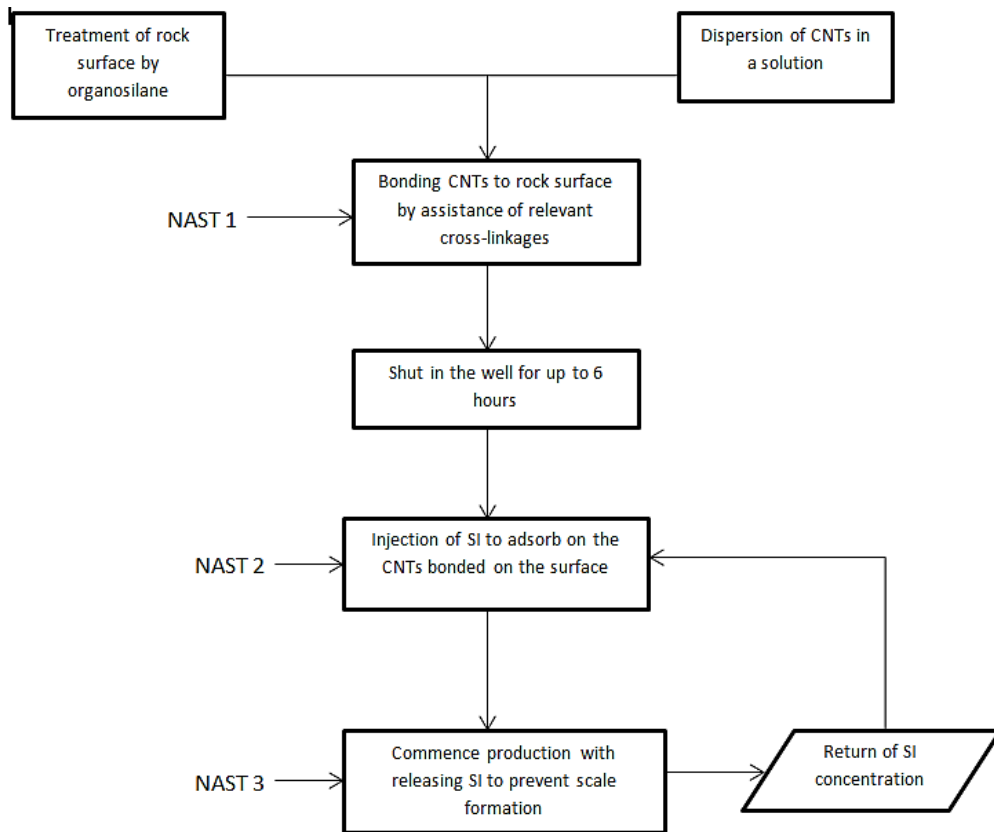
Figure 2.14: Schematic of the NAST methodology [45]

2.5.2   NAST1

The NAST1 stage is made up of three steps which are; pre-treatment of the rock surface, the dispersion of CNTs and finally the attachment of the dispersed CNTs on the pre- treated surface.

2.5.2.1   Pre-treatment of the rock surface

 The first step is to treat the rock surface in order to make the rock reactive to the CNTs. A type of organosilane is used to pre-treat the rock surface. Organosilanes are mainly used to immobilize other materials or as a link between assembled films [99]. 3- aminopropyltriethoxysilane (APTES) was the silane used to functionalise the rock surface in order to make the surface reactive to the CNTs.

APTES reaction on a single crystal of quartz (which represents rock surfaces) was investigated to see if the APTES can be implementable in the NAST methodology. The existence of an APTES film on the quartz surface was confirmed by XPS.

2.5.2.2 Dispersing of CNTs

In order to avoid blocking the pores of the reservoirs during injection, the next stage of NAST 1 is to uniformly disperse the CNTs in the system and on the rock surface. Dimethylformamide (DMF) was added to the solution to interact with the CNTs to disperse them in the solution. The solution of CNTs with DMF is sonicated (although this step is unlikely to be upscaled to an industrial level) for a period of time to ensure disaggregation of CNTs in the solution.

2.5.2.3 Attachment of CNTs on the rock

To enhance the bonding of the CNTs on the pre-treated rock, CNTs used are functionalized by carboxylic groups. The carboxylic group of CNTs reacts with the amine groups of the organosilane that is on the rock surface. In order to facilitate the reaction of carboxylic group with amine groups, cross-linkages such as Dicyclohexylcarbodimide (DCC) was used during experiments [45]. The bonding of CNTs to the APTES covered rock surfaces was shown by SEM images. As a result, the experiments conducted showed the feasibility of injection of NPs into reservoir and the practicability of bonding CNTs to rock surfaces.

A schematic diagram showing the interaction with the silane, CNTs, dispersant and cross-linkage is shown in Figure 2.15.
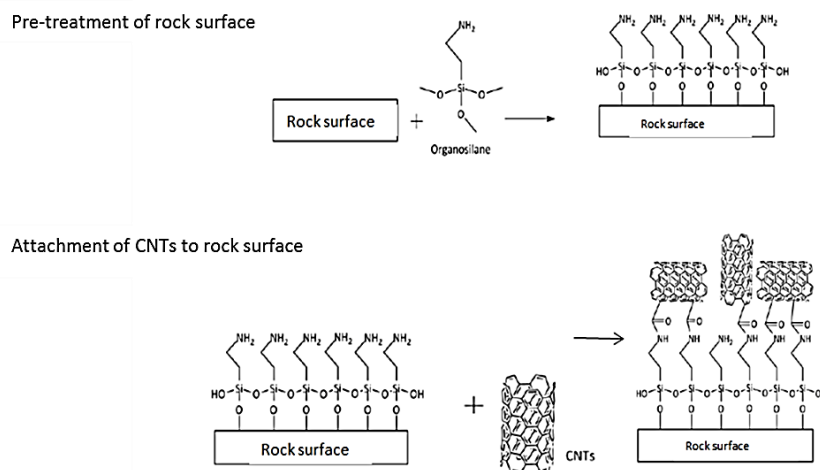
Figure 2.15: Schematic diagram showing the pre-treatment of rock with Silane and the attachment of CNTs to rock surface [45]

2.5.3 NAST 2

Increasing the adsorption rate of scale inhibitor in the reservoir will enhance squeeze lifetime thus this stage is the critical stage in the NAST methodology. PPCA was used in the experiments to test NAST 2 because it is one of the common inhibitors used in industry.

2.5.3.1 Adsorption

Static adsorption tests were performed to see whether the inhibitor will adsorb on the CNTs. In order to establish an experimental procedure for static adsorption, a number of different mass quantities of CNTs with different concentrations of scale inhibitors were used in the tests. The same static tests were conducted for sand and PPCA.

- The results shows that the adsorption of SI was significantly improved by CNTs compared to sand. The adsorption of PPCA on CNTs was observed to occur within one hour.

- The effect of high temperature on the adsorption was investigated and it was found that the adsorption of PPCA on the CNTs decreases within increasing temperature. However, the amount of adsorption was still higher than PPCA on sand.

- Agglomeration of CNTs suspended in the solution was found to have an impact on the amount of PPCA adsorption. It was shown that adsorption of PPCA on smaller concentration of CNTs suspended in solution was greater than at higher concentration.

- The effects of brine on the adsorption amount was also studied. An increase in salinity of the solution reduced the amount of PPCA adsorbed on CNTs. However, adding calcium to the solution increased the adsorption.

The overall interaction between the rock surface, APTES, the CNTs and the PPCA is illustrated in Figure 2.16 below.

Figure 2.16: Schematic of the NAST process [45]

Desorption: Two different methods for desorption experiments were carried out to see how much of the scale inhibitor is desorbed from the surface of the CNTs. Experiments were performed in distilled water and brine solutions. It was found that desorption was slow.

2.5.4 Coreflood testing of the NAST methodology

The complete NAST methodology was studied by performing coreflood experiments. They were performed in distilled water and brine solution. The aim of these coreflood experiments was to compare a conventional squeeze treatment to the NAST methodology. The results from the experiments found that adsorption of PPCA within the core with NAST occurred quicker and at a higher amount. These results showed the feasibility of implementation of the NAST methodology in squeeze treatment.

2.5.5 Further work needed for NAST methodology

From the experiments conducted by Ghorbani, it is clear that the deployment of the NAST methodology is feasible alternative to enhance the squeeze lifetime in comparison to conventional squeeze treatment. However, it was pointed out in this thesis that further experiments were needed to be carried out in more realistic conditions with the aim of improving the methodology for industrial use. For example, changes in environmental conditions such as temperature, pressure, flow rate, pH and brine composition can be observed during experiments to see the effects of these changes on the NAST process. Figure 2.17 shows a similar flowchart to Figure 2.14; however this flowchart shows the areas that need further work before field application. The flowchart is divided into three colours. The green parts identify areas which have been successfully achieved. The blue parts show areas that can be further improved and the orange sections show areas that need further investigation in order to ensure that the NAST methodology is viable for industrial use.
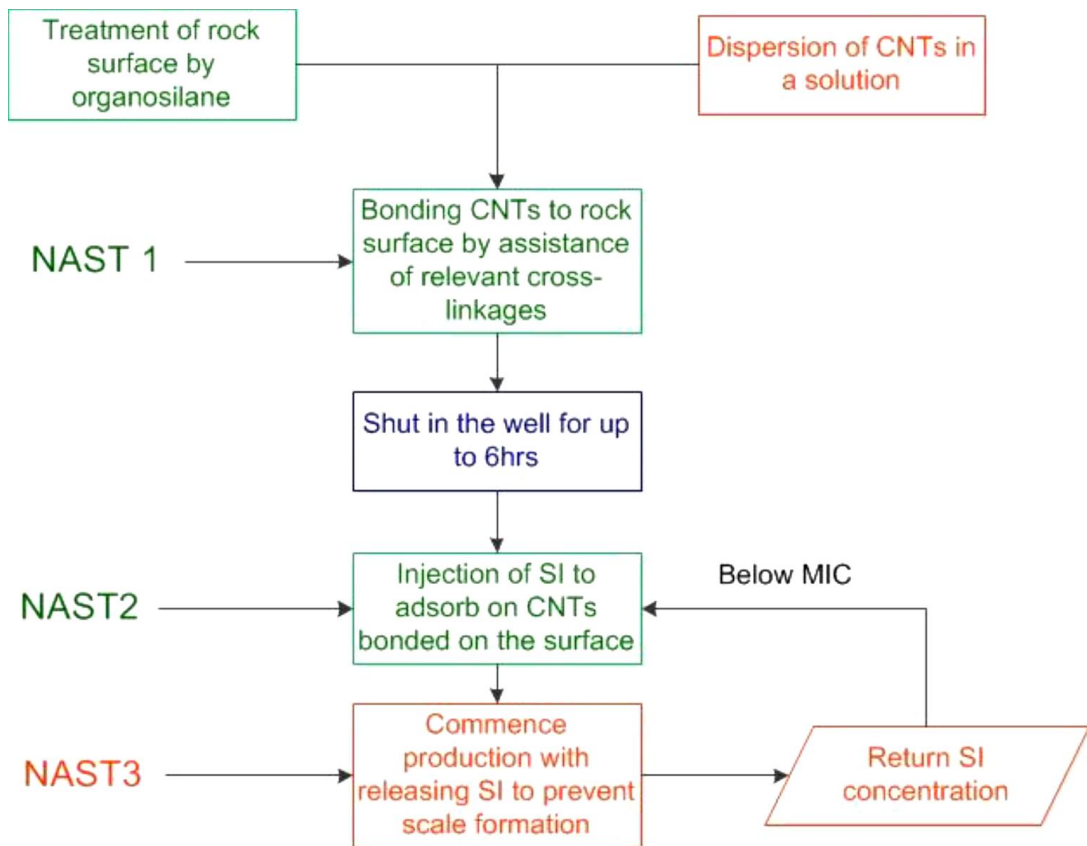
Figure 2.17: A colour coded flowchart with different levels of completeness[45].

2.6   Summary and Focus of thesis

This chapter provided a background on EOR processes, scale formation and factors affecting its formation as well as preventive and treatment methods for scale formation. Squeeze treatment process as a preventive method was presented and previous studies into ways to enhance squeeze treatment were highlighted. Previous work on the NAST methodology has shown it is viable method to enhance squeeze treatment in oil reservoirs. This chapter also presented the overall NAST process and the experiments carried out to test its practicality for use in oil field applications. Finally, further work as stated in literature, were presented.

Preliminary results, from experiments in simplified environments to establish a proof of concept for the NAST methodology, show that the methodology is feasible and promising. Furthermore, in order to proof the practicality of adsorption and desorption of SI on and from the CNTs under reservoir conditions, the complete NAST methodology was tested in coreflood experiments. The results showed that better SI retention was achieved.

2.6.1   gaps in previous research work and scope of thesis

Ghorbani work focussed on the overall NAST adsorption process and tested its practicality in its application for enhanced squeeze treatment. For NAST1, static tests were conducted and for NAST2 static and coreflood tests were conducted. One critical area that needs further investigation is factors affecting the deployment of CNTs into the reservoirs; and the adsorption and transport properties of the CNTs within the porous rocks. Coreflood experiments can provide insight to factors affecting the adsorption of CNTs in rocks. However, other areas like the effects of geological and geometrical properties of rock on the dispersion and adsorption/desorption of CNTs in the reservoirs cannot be investigated with coreflood experiments. This is due to the core casing preventing in-situ observation of core's microfluidic channels. Furthermore, the geometry of porous channel network within a rock core cannot be controlled, therefore the effect of channel geometry cannot be adequately studied in coreflood experiments.

Finally, a technique capable of detecting and quantifying CNTs suspended in solution is needed in order to keep track of the adsorption/desorption performance of CNTs during the NAST process on the field. Furthermore, monitoring the concentration of CNTs leaving the system is critical to ensure that the amount of particles being released in the environment is not at a toxic level.

Various analytical techniques are capable of detecting and quantifying CNTs suspended in aqueous solution. For NAST, the technique needs to have fast processing time and a detection limit lower than the toxic concentration levels of CNTs suspended in solution. Therefore, investigating which analytical techniques are suitable for the NAST methodology is necessary.

The use of glass microfluidic flow cells is one way to investigate the adsorption and transport of nanoparticles in microfluidic channels, which can represent porous rock. Based on microscopic visualization from the glass microfluidic flow cells, it is possible to observe nanoparticles that have deposited and adsorbed on the surface of the channel. Furthermore, it is possible to track the nanoparticles flowing in the channel and thereby study its transport behaviour. By tracking the nanoparticles flowing in microfluidic channels it is possible to study factors that might affect its placement in porous media. However, if the intention is to quantify the nanoparticles flowing through the channels then optical microscopy might have limitations in achieving this goal. Therefore, alternate techniques needs to be researched in order to minimize or eliminate this limitations.

The aim of this thesis is to understand the transport and adsorption phenomena of carbon nanotubes during the particle-injection process of the NAST methodology. Therefore the main focus of this thesis is on NAST1. Focusing on nanoparticle-injection provides the opportunity to answer question relating to CNT placements as well as adsorption behaviour in porous media.

To this end, it is important to provide the reader with adequate literature regarding adsorption behaviour and transport kinetics theories of nanoparticles in porous media as well as studies conducted in this respect. The next chapter will present the theories associated with adsorption process, fluid dynamics and particle transport.

Chapter 3.   Theory

3.1   Introduction

When injecting nanoparticles into oil reservoirs with the intention of the nanoparticles adsorbing on the rock surfaces, there are a number of theories that needs to be considered and understood. This chapter provides an insight into the theories associated with adsorption processes, particle suspension stability as well fundamentals of fluid dynamics and particle transport mechanism.

3.2   Fluid conditions at the microscopic scale

This thesis deals with flow through porous media, thus an understanding of fluid mechanics is important. There are two areas in fluid mechanics, the first is flow in the micro scale and the second is flow in the macro scale. In microscopic scale flow, the molecular structure of the fluid can be considered, whereas in macroscopic flow, fluid is treated as a continuum [100].

The field of microfluidics deals with fluid flow in channels ranging from one micron to hundreds of microns in diameter. At this scale, the flow behaves differently compared to flow in the macroscopic scale. As flow systems progressively reduce in size, they move to the environment where viscous dominated flow occurs. Scaling down from macrofluidic system to the microfluidic requires new considerations about possible changes in fluid properties, changes in boundary conditions, surface forces and other phenomena [34].

 Microfluidic flow can be described as laminar and moves in a predictable manner. These properties are useful for microfluidic experiments as they allow for the unique control of small volumes of liquid and particles suspended in such solutions. In order to have an understanding of the flow of fluids, and in particular microfluidic flow, the Navier –Stokes equation which describes the dynamics of an incompressible Newtonian fluid will be looked at in chapter 9 [101].

A fluid is said to be Newtonian if the fluid exhibits a viscosity that remains constant regardless of any external shear stress applied to it. An example is water, it viscosity remains the same whether it is stagnant or it is shaken forcefully. On the other hand,

non – Newtonian fluid changes its viscosity when external stress is applied to it. Many fluids are Newtonian, including water and certain oils [34].

3.2.1 Dimensionless numbers in microfluidics

To understand particle migration in microfluidic environments, it is important to review some of the physical phenomena that are present in microfluidic environments. Dimensionless numbers describing the ratio of these phenomena provide an understanding of particle migration in microfluidic parameter space. Depending on particle size, different mechanism will affect particle migration.

3.2.1.1 Reynolds number (Re)

The Reynolds number determines the relative influence of viscous and inertial effects in fluid flow and it also measures the tendency of flow to become turbulent [102]. This can be represented mathematically as:

$$Re = \frac{Inertial\ forces}{Viscous\ forces} = \frac{\rho U_0 L_0}{\mu} \qquad\qquad \text{Equation 3.1}$$

Where ρ denotes the fluid density (kg/m^3), U_0 the flow velocity (m/s), L_0 the characteristic length (m) and μ the dynamic viscosity (kg/m.s).

3.2.1.2 Peclet number (Pe)

The Peclet number shows the ratio of convection to that of diffusion. This ratio defines the impact of hydrodynamics forces to that of Brownian motion to particle migration. Therefore, it indicates whether hydrodynamic migration or Brownian diffusion is the dominant mechanism for particle migration. This ratio is related to the dimensions of the channel which gives the dimensionless Peclet number given below:

$$Pe = \frac{Convection}{Diffusion} = \frac{U_0 w_0}{D} \qquad\qquad \text{Equation 3.2}$$

Where U_0 denotes the flow velocity (m/s), w_0 the channel width (m) and D is the diffusion coefficient (m^2/s) of the particle.

The diffusion coefficient can be calculated using the Stoke – Einstein relationship which is described mathematically as:

$$D = \frac{kT}{6\pi\mu a}$$

Where k denotes the Boltzmann constant (1.380e-23 J/K), T the temperature (K), a the particle diameter (m) and μ is the dynamic viscosity of the fluid (kg/m.s) [103].

3.2.2 Mixing length

At high Reynolds number regime, random eddies continually disturb and churn fluids, which can induce chaotic or enhanced mixing of fluids and particles in such systems [103]. At low Reynolds number regime, mixing tends to occur due to diffusion of the particle. Therefore, mixing at low Reynolds number can be very slow.

The Peclet number can be used to determine the length needed to ensure full mixing of fluids and particles within fluids as the mixing distance is dependent on the Pe. For example, if two fluids are injected into a T – Junction channel (Figure 3.1) to flow alongside each order, it is possible to determine how far down the channel the fluids must flow before the fluids (or particles) are fully mixed [104, 105].
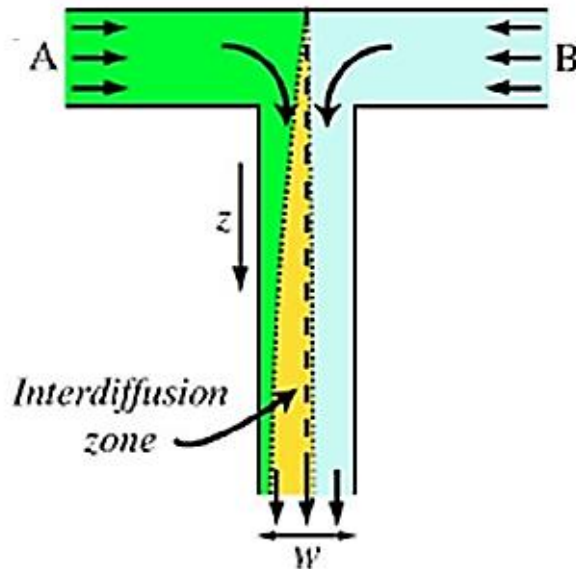
Figure 3.1 : A T- Junction channel with two different fluids flowing alongside each othe down the channel. From its channel width, flow rate of the fluids and diffusion coefficient of the species, the mixing length Z can be determined [103]

For a given flow rate and channel width, the mixing distance Z is the product of the Peclet number and the channel width w. This relationship can be mathematically expressed as:

$$Z = Pe \ X \ w = \frac{U_0 w_0{}^2}{D}$$ Equation 3.4

3.3   Electric double layer (EDL)

Colloidal particles or particles suspended in aqueous solutions are generally electrically charged. This charge on the particle is neutralized by an opposite charge in the surrounding fluid. A layer is formed around the particles which is called the electrical double layer (EDL). Figure 3.2 shows the different components of the EDL.
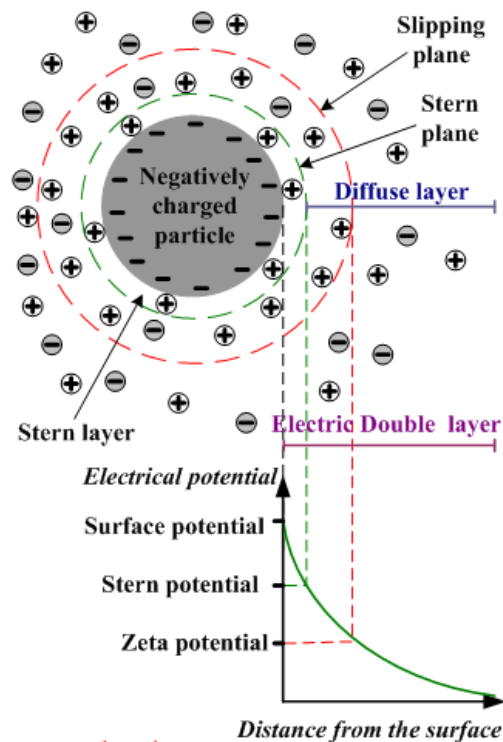
Figure 3.2: Schematic diagram showing different components of EDL including a potential curve graph which shows the relationship between electrical strength and distance from the particle (www.substech.com).

EDL is made up of two layers named the Stern layer and the diffuse layer. The Stern layer contains fixed charged ion from the solution attached on the surface of the particle and the diffuse layer contains the counter ions in the solution as a result of thermal energy and electric forces. The magnitude of the surface potential is related to the surface charge and the thickness of the double layer. The further away from

the surface, the potential drops linearly in the Stern layer and then drops exponentially through the diffuse layer, approaching zero at the boundary of the double layer. The potential curve in Figure 3.2 indicates the strength of the electrical forces between particles. The potential difference between the two layers given rise to the eletrokinetic potential or Zeta potential.

3.4 Derjaguin, Landau, Verwey, and Overbeek (DLVO) Theory

DLVO theory was established by Derjaguin, Landau, Verwey, and Overbeek in the 1940s and it describes the attractive and repulsive interaction between particles due to Van der Waals forces and zeta potential of the particles [106].

Based on DLVO theory, the stability of particles depend on the total potential energy function expressed as:

$$V_T = V_A + V_R + V_S \qquad\qquad \text{Equation 3.5}$$

Where V_T is the total potential energy function, V_A is the attractive energy from van der Waals interactions, V_R is the repulsive force from the EDL of the particles when they come close to each other and V_S is the potential energy from the solvent. Van der Waals forces and EDL repulsion play far greater roles than the potential energy for the solvent. Therefore, V_R and V_A are described further and can be expressed as

$$V_A = -\frac{A}{12\pi h^2} \qquad\qquad \text{Equation 3.6}$$

Where A is the Hamaker constant (J) and h is the distance (m) between the particles.

$$V_R = 2\pi\varepsilon a\zeta 2 \exp(-kh) \qquad\qquad \text{Equation 3.7}$$

Where ε is the dielectric constant of the solvent , a is the radius of the particle (m), k is the ionic composition, π is the solvent permeability and ζ is the zeta potential (V).

Van der Waals forces are weak electrostatic forces that attract neutral molecules together due to adjacent atoms coming close enough that their outer electron clouds slightly touch. The Hamaker constant defines the strength of the attraction and depends on the number of atoms per unit volume and the London dispersion

constant. Typical values of the Hamaker constants are between 10^{-21} and 10^{-19} J and are positive in most situations, indicating the attractive nature of van der Waals force.

The zeta potential of particle represents the surface charge and is related to interaction between particles and reflects to their stability in liquid media. The equation shows that the larger the zeta potential, the greater the repulsive force and the more disperse and stable the particle suspension system is [107, 108].

Absolute zeta potential values greater than 30 mV lead to mono-dispersity. On the other hand, low values, smaller than 5 mV, can lead to agglomeration. Zeta potential is affected the properties of nanoparticles, pH and ionic strength of the liquid media [109, 110].

The DLVO theory was originally formulated for two identical interfaces or particles which will explain homogenous aggregation. It was later extended to interaction between two different interfaces or particles (heterogeneous aggregation). Finally, in the limiting case of large size disparity, where one of the particles has an infinite dimension in relation to the other, the DLVO theory is used to describe deposition of particles on to a macroscopic surface such as microfluidic channels. Figure 3.3 illustrates these processes.
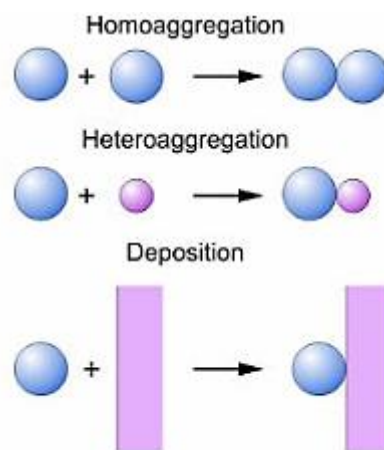
Figure 3.3: Schematic diagram showing the interaction processes based on DLVO theory [111]

3.5 Stability of particles suspended in aqueous solution

Particles suspended in solution have the tendency to aggregate due to the surface area and surface activities explained in sections 3.3 and 3.4. This agglomeration of nanoparticles can cause clogging of pore channels, which can cause formation damage in reservoirs. DLVO theory indicates that stability of the particle in liquids is determined by the EDL and the Van der Waals forces. If the Van der Waals attractive force is greater than the EDL repulsive force, the suspended particle will not be stable in aqueous solution. If EDL forces exceeds Van der Waals forces, then the particle suspension will achieve a stable state.

One common method to improve the stability of particles suspended in liquids is the application of surfactants to enhance the repulsive forces between the particles. There are two repulsion mechanisms that affect the stability of particle suspension; one is steric repulsion and the other is electrostatic repulsion.

3.5.1 Steric interaction

For steric stabilization, polymers are included in the aqueous solution to adsorb on the particle surface creating an additional steric repulsive force (Figure 3.4). The polymers consist of a hydrophobic tail portion, usually a long – chain hydrocarbon, and a hydrophilic head [112].
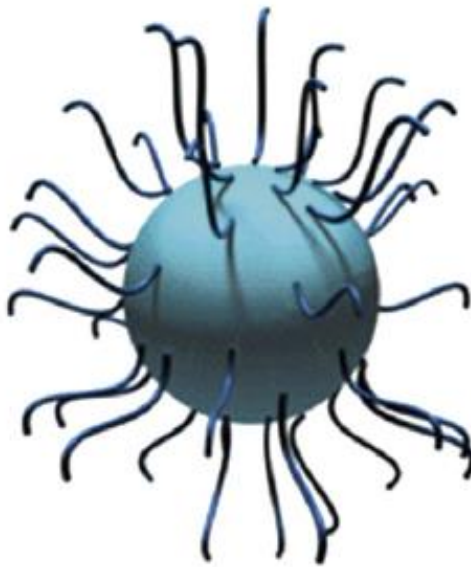
Figure 3.4: Steric repulsion on particle suspension [113]

Studies have shown the role non – ionic surfactants play in stabilising particles suspended in liquids. Studies have shown that PolyVinylPyrrolidone (PVP) can be used as the non – ionic surfactant. The results showed the important role non-ionic surfactants plays in the dispersion and stabilization of particles suspended in solution using steric repulsion as the stabilization mechanism [112].

3.5.2   Electrostatic repulsion

For electrostatic repulsion, surface charge will be created using one or more of the mechanisms; isomorphic substitutions of ions, preferential adsorption of ions and physical adsorption of charged species onto the surface [112]. Figure 3.5 illustrates electrostatic repulsion on a particle suspended in aqueous solution.
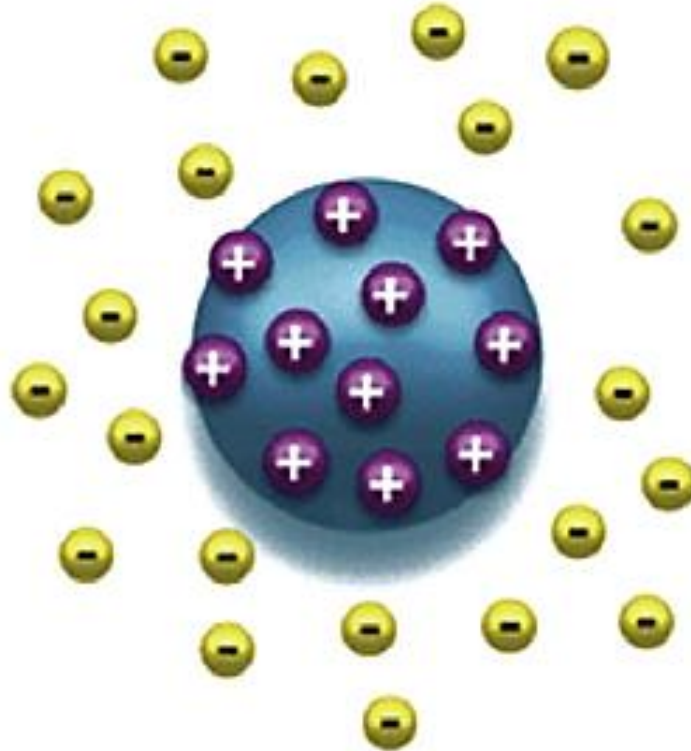
Figure 3.5: Electrostatic repulsion mechanism on a suspended particle [113]

Yang et al [114] prepared a nanofluid by adding Al_2O_3 nanoparticles with sodium dodecyl sulfonate (SDBS) in the ammonia-water solution. In this study, the results showed that SDBS is capable of dispersing particles suspended in aqueous solution.

3.6   Particle migration

Particle migration plays a major role in the placement in CNT. Therefore, a review of factors affecting particle transport is included in this thesis. Fluid flow has a significant effect on the transport of particles and hence the placement of them. The typical forces exerted on particles are shown in Figure 3.6.
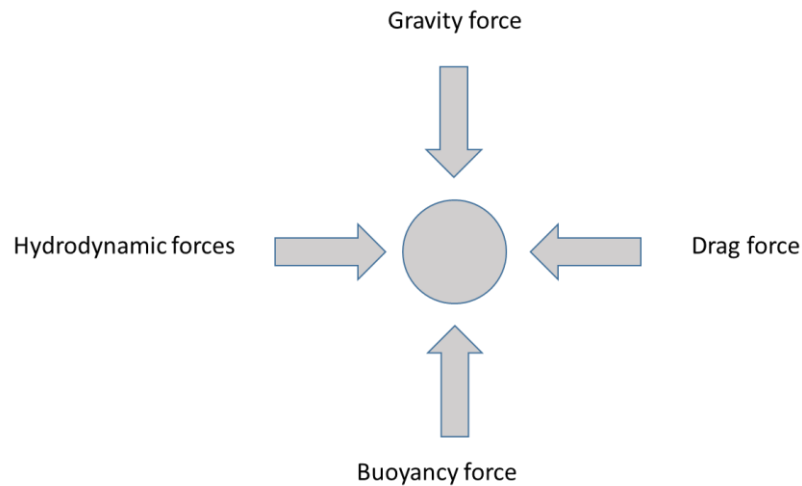
Figure 3.6: Schematic diagram of particles suspended in solution with the forces acting on it

The resultant force can be written mathematically as :

$$m\frac{du}{dt} = F_e - F_b - F_D \qquad\qquad\qquad \text{Equation 3.8}$$

Where F_D is the drag force (N), F_e is the external force (N), F_b is the buoyant force (N) and u is the velocity of the relative to the fluid.

A particle of mass m moving through fluid under the action of an external force F_e.

3.6.1   Particle transport in the presence of induced forces

The previous section showed the external forces that drive particle transport. However, there is a more subtle and indirect transport mechanism due to a chemical gradient. This transport driving mechanism is called diffusiophoresis. Diffusiophoresis is the chemically driven transport of particles induced by a solute concentration gradient without the application of an external force [115]. It does this by converting the chemical energy of the concentration gradients into mechanical energy of particle

moving through the fluid by an electric field. For charged particles suspended in a salt concentration gradient, the dominant contribution to diffusiophoresis is electrophoresis, due to the electric field generated by the diffusion of the electrolyte (Figure 3.7).
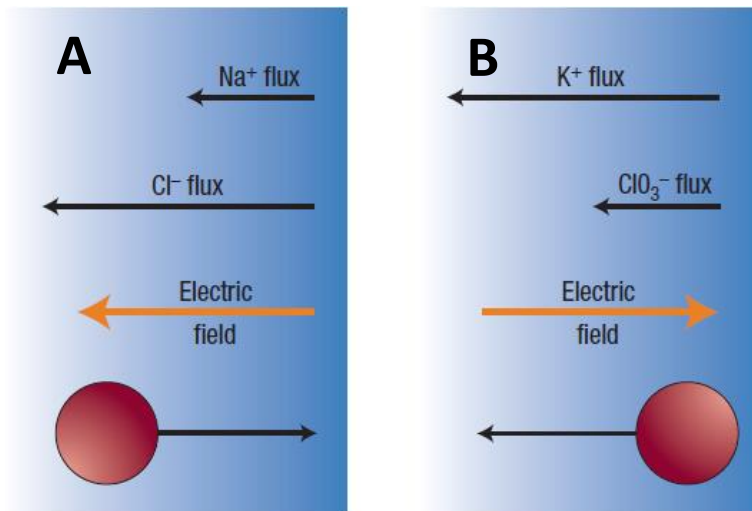
Figure 3.7: (A) A particle undergoing diffusiophoretic migration towards higher salt concentration, salt concentration is indicated by the intensity of the blue colour. The direction of electric field determined by the faster moving Cl ion (B) The direction of the electric is determine K ions [116].

For a monovalent salt like NaCl, the chloride ions, due to their smaller size, have a higher diffusion coefficient than sodium ions. Therefore, if the transport of ions is diffusion driven, chloride ions will diffuse faster than sodium ion, which lead to a net electric current and separation of charges. An electric field arises to slow down the faster ions and speed up the slower ions to ensure that their fluxes are equal [116]. The electric field generated also has an effect on the charged particles suspended in the solution which will cause electrophoresis [117]. For a salt like NaCl, the direction of electric field will be away from the region of higher concentration due to the faster moving chloride ion which will result in a negatively charged particle moving towards the region of higher concentration (Figure 3.7 a). On the other hand, for a salt like KClO$_3$, the K ions moves faster than the ClO$_3$ ion (Figure 3.7 b) which reverses the direction of the electric field. This will drive the negatively charged particles from the higher salt concentration region to the lower salt concentration region.

Diffusiophoresis also arises due to a chemiphoresis driving mechanism. Inside the EDL on the particle surface, the pressure is higher than in the bulk, due to the

attraction of ions in within it. This pressure will increase when the ionic strength of the solution increases. If there is a concentration gradient tangential to particle surface, there will be a gradient of pressure. This will cause a tangential flow near the surface of the EDL (Figure 3.8). This process can be defined as chemiphoresis [115, 118-121].
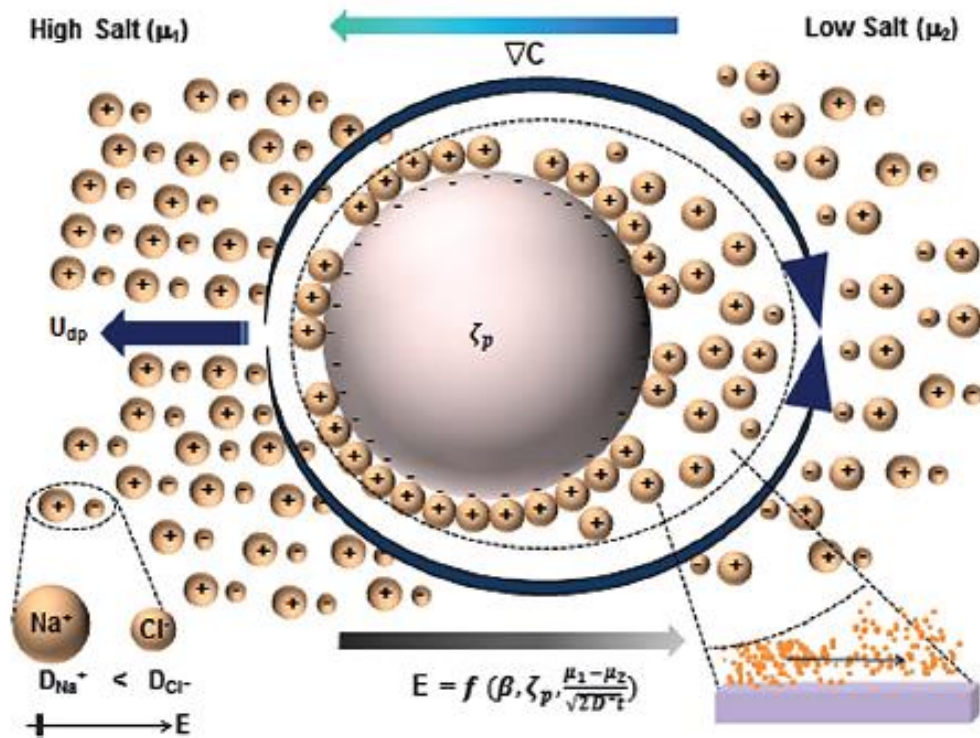
Figure 3.8: Mechanism of diffusiophoresis. Electrophoresis caused by electric field generated by the concentration gradient. Chemiphoresis caused by pressure gradient in the EDL due to the salt concentration gradient [115].

3.6.2 Relevance of diffusiophoresis studies

Although the physics of diffusiophoretic transport has been established, there are still difficulties in observing this phenomena in the laboratory. Diffusiophoresis can occurs in a variety of situations such as geological reservoirs, the human body or in a chemistry wet lab [115]. In EOR process, research has that low salinity injection water has can be used to improve the oil recovery [121-123]. As a result, if the salinity levels between the injected water and the reservoir formation are substantially different, diffusiophoresis can occur when they meet.

3.7 Adsorption processes

Adsorption is a mass transfer process which involves the attachment of particles at the interface of two phases, such as, liquid-liquid or liquid-solid interface. Adsorbates are the substance being adsorbed while the adsorbents are the adsorbing materials. If the interaction between the adsorbates and adsorbents is of a physical nature, the process is physisorption. The attraction interactions are van der Waals forces which results in a weak and reversible attachment on the surface. On the other hand, if it is a chemical bonding that occurs between the adsorbed molecules and the solid surface then the process is called chemisorption. Furthermore, unlike physisorption, chemisorption occurs only as a monolayer and the particles are hardly removed due to the stronger forces between the particles and the solid surfaces. Under favourable conditions, both processes can occur simultaneously or alternatively [124].

Aside from adsorption capacity, kinetic performance of a given adsorbent is also of great importance for the NAST methodology. From kinetic analysis, factors that determine the residence time required for adsorption may be established. Generally speaking, adsorption kinetics is used to determine the performance for adsorbents or any other flow through system. Over the years, several mathematical models have been created to describe adsorption data. These descriptions can be classified as adsorption reaction models and adsorption diffusion models. Both models are applied to describe the kinetics processes involved in adsorption [125].

3.7.1 Pseudo first-order rate equation

Ho and Mckay [126] defined Lagergren's first order rate equation as pseudo first order equation which describe the kinetic process of liquid-solid phase adsorption of oxalic acid and malonic acid onto charcoal. It can be written mathematically as

$$\frac{d_{q_t}}{dt} = k_{p1}(q_e - q_t), \qquad\qquad\qquad\qquad \text{Equation 3.9}$$

Where q_e and q_t (mg/g) are the adsorption capacities at equilibrium and time t (minutes) respectively. K_{p1} (min^{-1}) is the pseudo-first-order rate constant for the kinetic model.

3.7.2 Pseudo-second-order rate equation

The formula for pseudo-second-order kinetics is generally is expressed as

$$\frac{t}{q_t} = \frac{1}{k_2 q_e^2} + \frac{1}{q_e} t \qquad\qquad \text{Equation 3.10}$$

Where k_2 (g/mg min) is the equilibrium rate constant of pseudo second- order adsorption [127].

3.8 Summary

The theories presented in this chapter reflect the conditions and processes experienced by nanoparticles injected into oil reservoirs. Due to the micro-sized channels located in reservoirs, the fluid flow exhibits microfluidic characteristics which will affect the particle transport mechanism. Particle transport, deposition and aggregation kinetics was also presented as the particles are dispersed in aqueous solution with the intention of adsorbing on the channel surface.

Chapter 4.   Literature review

4.1   Introduction

Understanding the impact of injecting CNTs in oil reservoir (NAST1) is critical in order to study factors that might affects it placement and adsorption process; and thereby improve the methodology if necessary. Furthermore, monitoring the concentration of CNTs suspended in aqueous is important if the methodology is to be deployed in the field. Therefore, a review on analytical techniques capable of detecting and quantifying CNTs suspended in aqueous solution will be reviewed.

One of the aims of this thesis is to study the transport and retention of CNTs in porous media. The previous chapter has shown that the injected nanoparticles are transported under microfluidic flow conditions. As such, literature on microfluidics and its applications to research and engineering will be reviewed in this chapter.

In order to track the particles within the channels and to study the adsorption processes, visualization of the particles within the channel is critical. Therefore, different ways to visualize and quantify particles flowing in microfluidic channels will be reviewed.

Raman spectroscopy has been used to characterize CNTs and it has the ability to detect samples in different environments. For this thesis, Raman microscopy was used as the detection and quantification technique for the microfluidic experiments conducted. Hence, this chapter presents the theory of Raman spectroscopy and how it works for sample characterisation. From here, a review on the integration of Raman microscopy and microfluidic systems will be presented and the challenges faced when integrating both systems. Finally, the application of the integrated Raman – microfluidic systems will be reviewed.

4.2 Analytical techniques capable of monitoring Carbon Nanotubes suspended in aqueous solution

Due to the use of CNTs in the NAST methodology, there is a chance that some of the particles are released into the environment. Therefore, it is imperative that a system to monitor the release of particles is identified. The necessary cornerstone in investigating monitoring methods is to research the availability of robust analytical techniques capable of quantifying CNTs in complex environmental systems [128-130]. Figure 4.1 shows a number of techniques arranged based on their availability.
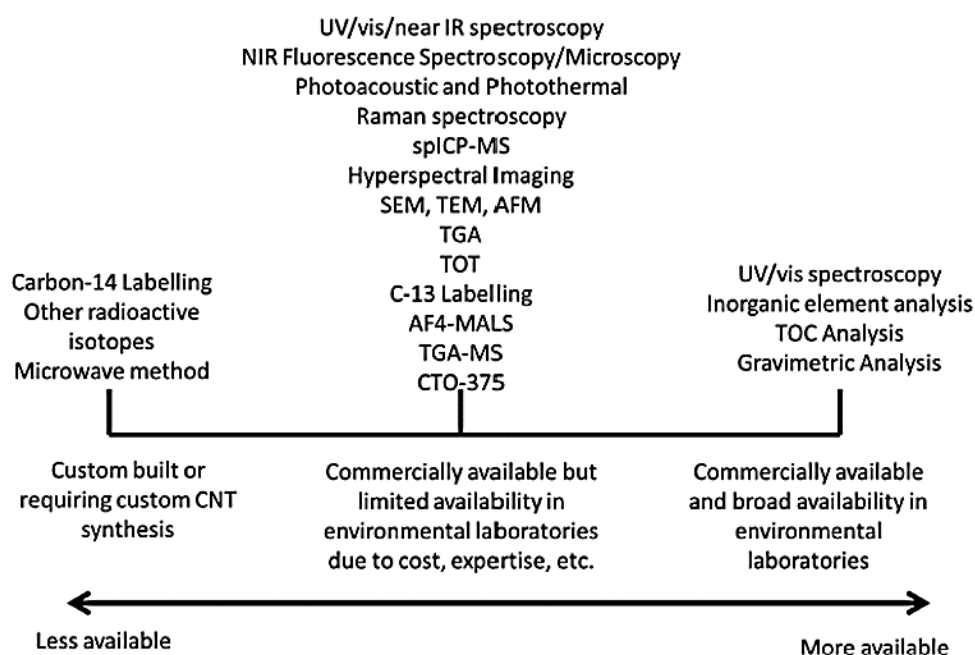
Figure 4.1: Availability of CNT quantification techniques [128]

Analytical techniques capable of detecting and quantifying CNTs usually rely on unique physicochemical properties of CNTs to identify them in relevant media. In general, these techniques can be divided into four main groups: the first one distinguishes the CNTs from matrices through the unique spectroscopic and thermal characteristics of CNTs *e.g.,* instruments such as Thermal Gravimetric Analysis (TGA) uses the CNTs thermal stability to differentiate them from the matrix [131].

Similarly, several studies have reported the use of Raman spectroscopy to characterize and quantify the composition of elements in CNT by making use of properties that are specific to each chiral index and phonon energy in the nanoparticles [132-135]. The resonance from Raman scattering derived from CNTs

generates intensities at particular wavelengths and laser power. The main strengths of Raman spectroscopy are its relative simplicity of use, its ability to generate rapid results as well as its non – destructive and non – invasive nature. The information provided from the intensities can be correlated to the concentration of CNTs in aqueous solution[135, 136]. The primary challenge remains the propensity of CNTs to agglomerate when dispersed in an aqueous solution which influences the intensities generated by the instrument [137-139].

The second group of analytical techniques relies on the metal catalyst used during the manufacturing process and present as impurities in the final product ; inductively coupled plasma mass spectroscopy (ICP-MS) is a popular technique to quantify such impurities. Studies have used ICP-MS to characterize SWCNTs by detecting and determining the level of metal catalyst constituents. Furthermore, other studies have shown that ICP-MS can be used to quantify SWCNTs in simple matrices by digesting them and analysing the amount of metallic impurities in the digested solution [140, 141]. Its main strength is its ability to detect particles at extremely low concentration levels which, under a carefully controlled procedure, can be in the parts per trillion (ppt) level. However, these levels are rarely reached due to elemental interference within the sample [141, 142].

The third group of analytical techniques uses isotopic labelling by tracking CNTs with carbon 13 or carbon 14, and lastly, the fourth group uses a range of microscopic techniques to directly observe the nanoparticles [128, 137, 143]. Examples of such techniques include Scanning Electron Microscope (SEM) and Transmission Electron Microscope (TEM).

These techniques play an essential role in characterizing SWCNTs due to their high efficiency and high spatial resolution; they provide detailed morphological properties of individual SWCNTs [144].

4.2.1 Detection limits of quantification techniques

The Limit of Detection (LOD) for CNT quantification is vital for comparing the performance of different analytical techniques. It is even more important for the NAST methodology as the monitoring technique needs to be able to detect CNT concentration levels below the levels that maybe considered harmful to the environment. In Figure 4.2, detection limits of various analytical techniques for CNT quantification is shown and compared to a species sensitivity distribution for CNT acute toxicity to aquatic organisms.
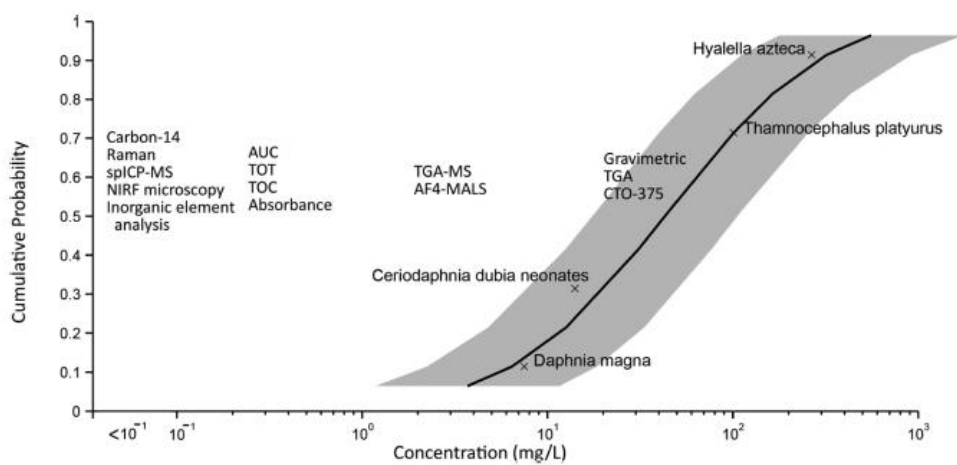
Figure 4.2: Comparison between LOD for analytical techniques in pure water solution with place alongside a species sensitivity distribution for acute toxicity testing of pelagic organism [128].

It can be seen from Figure 4.1 and Figure 4.2 that the availability of Raman spectroscopy and Inductively Coupled Plasma (ICP) are both commercially available and have limits of detections well below CNT concentrations tested on the aquatic organisms for acute toxicity. Therefore, this thesis will focus on Raman microscopy and will be benchmark against ICP.

4.3 Overview of microfluidics

Microfluidics involves the characterizing and manipulation of fluids and particles within microchannels. It can also be defined as the science of the flow of fluid at the micro scale. Microfluidics is still a developing field and as such has not reached its full potential. Microfluidic systems allow precise handling and control of microliter, nanolitre and even picolitre volumes of liquid, thus the field of microfluidics is

applicable to a number of other fields [145]. The main advantage for doing microfluidic experiments is that the experimental set up can be scaled down by a factor of 1000 or more [146]. The advantage of scaling down is that there is a drastic reduction in the amount of required sample. Such small sizes and volumes allow for fast analysis. Another benefit of scaling down is the miniaturization of flow systems such as pumps, flow device reagent holders and sensors. It is envisaged that these types of devices will be used as point of care devices in hospitals and hostile or remote environments where, at this point in time, conventional equipment fail to reach [34] .

4.3.1   Application of microfluidics

Advances in microfluidic technologies have allowed micro-scale experimentation to produce more realistic and better results. Development in microfluidics has also given rise to micro devices such as micropumps, sensors and a host of other devices that can be used in the medical industry for things like drug delivery and DNA sequencing, cell counting and sorting, drug screening, and many others. In chemical applications, there have been improvements in reaction and processing conditions on the microscale by devices having the ability to control the surface chemistry, heat and mass transfer. The greater level of control may help increase knowledge about different chemical processes. The pharmaceutical industry is also benefiting from it by applying microfluidic devices in the discovery and development of drugs [34, 147]. The flow of fluids and transport of particles (as well as any reaction processes that may occur in porous media) needs to be understood in order to find solutions to problems that may arise due to various mechanisms in microfluidic systems such as groundwater supply and oil recovery [148].

4.3.1.1   Micromodels

Micromodels are ideal for microfluidic experiments of flow in porous rocks at the pore scale. Micromodels contain pore networks that can have various geometrical shapes and dimensions, and it also permits the visualization of fluid flow and particle transport through the pore structures. Visual analysis enables certain features, like adsorption and dispersion of particles, to be identified and analysed when certain parameters such as temperature and flow rate are altered. Micromodels give

researchers the opportunity to carry out a range of experiments by changing some features of the porous media. Changes to the pore system can produce a range of values concerning porosity, permeability, grain size and shape. Other areas that can be altered are the wettability, surface roughness amongst other things [32].

 Micromodels are made by etching a pore network pattern on a Polydimethylsiloxane (PDMS), glass or silicon plate which is then fused with another etched or smooth glass plate. The pore network can be taken from a 2D section of thin section of a real rock or it can be designed manually. Figure 4.3 shows a range of micromodels pore network pattern ranging from a simple system to a more realistic porous system.
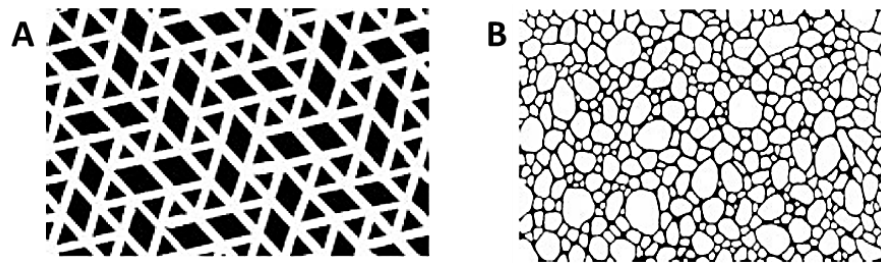
Figure 4.3: Images showing designs of (A) a simple pore system (B) a realistic section of a porous rock[32]

Micromodels have been used to perform microfluidic experiments for the study of nanoparticles in EOR applications. For example, Wang *et al* [36] performed experiments using micromodels in order to investigate the mobilization and deposition of iron nanoparticles in porous media. They found that nanoparticles formed aggregates and caused a reduction in flow paths.

Hendraningrat *et al* [149] also performed experiments using micromodels. The experiments were done to study the retention of hydrophilic nanoparticles in porous media for EOR. It was found that due to the retention of nanoparticles in the porous media (glass micromodel) the permeability of the porous media reduced. This occurred due to the deposition of nanoparticles on the pore surfaces and blockages of pore throats in the glass micromodel.

These previous studies show the contribution of glass micromodels to experiments involving the transport and retention of particles in porous media. Moreover, they show that micromodel experiments provide essential information about the

behaviour of particles in porous media on a microscopic scale through visualization of the particles during experiments combined with other post analytical methods after experiments are performed.

4.4   Integrating microfluidic systems with analytical instrumentation

While optical techniques, such as light microscopes and high speed cameras are commonly used with microfluidic systems to conduct microfluidic experiments, development of microfluidic system that integrate spectroscopic analytical techniques have been extensively reported [150].

Different types of spectroscopy systems have been integrated with microfluidic systems such as fluorescence spectroscopy, Fourier transform infrared (FTIR) spectroscopy and Raman spectroscopy/microscopy. Due to improvements in hardware, Raman spectroscopy has proven to be highly compatible with microfluidic systems. Raman microscopy integrated with microfluidic systems (also known as Raman – Microfluidic systems) have already been applied in the analysis of low volume liquid and in areas requiring constant monitoring such as water quality check and biosensing [150].

These examples show that the integration of Raman microscopy with the unique properties of microfluidics systems, has the potential new grounds in other important applications.

4.5   Theory of Raman spectroscopy

As a majority of this thesis is based on Raman spectroscopic results and analysis, an understanding of the underlying theory of Raman spectroscopy is essential.

Raman spectroscopy is an analytical technique commonly used to characterize material which utilizes a phenomenon of the change in frequency of light when it scatters by molecules. It provides characteristic fundamental vibrations that used for the understanding of molecular structure in a sample. Therefore, this section is divided into two parts, electromagnetic radiation, which is a property of light, and molecular vibration, which provides the analytical information for Raman spectroscopy.

4.5.1 Electromagnetic radiation

Light is classified as electromagnetic radiation which consists of alternating electric and magnetic field which is describe as a sinusoidal wave like motion of the fields. For Raman spectroscopy, only the electric field component is considered. Oscillation of the electric field is given by Equation 4.1 [151, 152]:

$$E = E_o \cos 2\pi v t \qquad \qquad \text{Equation 4.1}$$

Where E_o is the amplitude (m) and v is the frequency of radiation (number of cycle s per unit time)

The distance between two points within the same phase in successive waves is called the wavelength (λ) and is related to the frequency by the following mathematical expression:

$$v = \frac{c}{\lambda} \qquad \qquad \text{Equation 4.2}$$

Where c is the speed of light at 3×10^{10} cm/s

If the wavelength is in cm, then the dimension of v is 1/s, which is reciprocal second, another term of frequency which has the unit of "hertz" (Hz).

In vibration spectroscopy, the wavenumber, $\tilde{v}$, is defined by

$$\tilde{v} = \frac{v}{c} \qquad \qquad \text{Equation 4.3}$$

Hence combining equations 4.2 and 4.3

$$\tilde{v} = \frac{v}{c} = \frac{1}{\lambda} \qquad \qquad \text{Equation 4.4}$$

which is the inverse of the wavelength (cm^{-1}), which is the unit of the wavenumber.

The wavenumber term is conventionally used by Raman methods for frequency shift [152-154].

4.5.2 Molecular vibrations

In diatomic molecules, the vibrations occurs within the chemical bonds connecting the nuclei. Therefore, to better understand the molecular vibrations that are observed in Raman spectra, a simple model derived from classical mechanics theory will be considered by assuming that a diatomic molecule with two masses m_1 and m_2 is connected together by a massless spring (Figure 4.4). The massless spring, which represents the chemical bond, obeys Hook's law [152, 153]. Figure 4.4 shows the displacement of each mass from the equilibrium along the spring as X_1 and X_2. It can also be seen that the displacement of the masses as a function of time for a simple harmonic oscillator varies periodically as a sine or cosine function. Although each mass oscillates with different amplitudes along the axis, they both share the same frequency and therefore go through their equilibrium positions at the same time. As a result, the amplitudes are therefore inversely proportional to the mass of the atoms which keeps the centre of mass fixed.

$$\frac{X_1}{X_2} = \frac{m_2}{m_1}$$
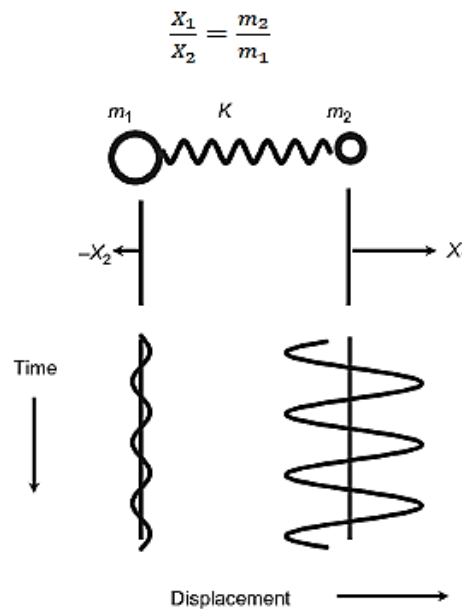
Figure 4.4: Motion of a simple diatomic molecule. K is the spring constant, m1 and m2 are the masses and the displacement vectors of each mass from equilibrium are X1 and X2 where the oscillator is assumed to be harmonic[152, 153]

 The classical vibrational frequency for a diatomic molecule is given by

$$v = \frac{1}{2\pi}\sqrt{K\left(\frac{1}{m_1} + \frac{1}{m_2}\right)}$$
<div align="right">Equation 4.5</div>

Where K is the force constant in N/m and m_1 and m_2 are the masses in grams and v is the cycles per second.

Since the wavenumber is typically used in vibrational spectroscopy, Equation 4.5 is replaced by Equation 4.6 which is shown below:

$$\tilde{v} = \frac{1}{2\pi c}\sqrt{K\left(\frac{1}{m_1} + \frac{1}{m_2}\right)}$$
<div align="right">Equation 4.6</div>

This equation shows that the wavenumber is or frequency of a diatomic molecule is directly proportional to the force constant K, which relates to the bond energy between two atoms and inversely proportional to the atomic masses within the vibration system. Therefore, for a given frequency and masses, the diatomic force constant can be calculated [152, 153, 155].

4.5.3 Raman Spectroscopy

Raman spectroscopy is based on the occurrence of the interaction between dipoles and the incident radiation which is known as Raman scattering. The light, usually from a laser source, interacts with the molecular vibrations or photons in the sample which results in the Raman effect. The Raman effect is a result of the energy of the laser photons shifting up or down when compared with original monochromatic frequency. These shifts in energy provide information needed for molecular analysis.

4.5.3.1 Raman scattering

When electromagnetic radiation radiates on a molecule, the electromagnetic fields exerts a force on atoms of the molecules which causes an induced dipole. Raman scattering is the polarization (the movement of electrons relative to the nuclear framework) induced in a molecule by the electric field of the light, which causes the induced dipole to radiate scattered light [156]. This can occur with or without the exchange of energy with vibrations in the molecules. The strength of the induced polarization, P, is given by

$$P = \alpha E \hspace{6cm} \text{Equation 4.7}$$

Where α is the polarizability which is the ease at which electrons can move due to electromagnetic radiation and E is incident electric field due to electromagnetic wave and is expressed as:

$$E = E_o \cos 2\pi v_o t \hspace{5cm} \text{Equation 4.8}$$

Where E_o is the amplitude and v_o is the frequency of laser light

The molecular vibrations are considered to consist of normal modes, Q_j, for N atoms, there is either 3N − 6 in a molecule or 3N − 5 for a linear molecule. Hence the electric field equation can be rewritten as:

$$Q_j = Q_j^o \cos 2\pi v_j t \hspace{5cm} \text{Equation 4.9}$$

Where v_j is the characteristic harmonic frequency of the jth normal mode and hence the polarizability α of the electrons can be modulated at the vibrational frequency of the molecule. For the jth term, α can be expanded in a Taylor series as shown in Equation 3.20

$$\alpha = \alpha_o + \left(\frac{d\alpha}{dQ_j}\right) Q_j + \cdots \hspace{4cm} \text{Equation 4.10}$$

Therefore, the polarization P, which is the product of Equation 4.9 and 4.10, gives:

$$P = \alpha_o E_o \cos 2\pi v_o t + \left(\frac{d\alpha}{dQ_j}\right) E_o \cos 2\pi v_o t \, Q_j^o \cos 2\pi v_j t \hspace{1.5cm} \text{Equation 4.11}$$

Using the trigonometric identity cos(A)cos(B) = {cos(A+B)+cos(A-B)}/2, polarization P can be rewritten as:

$$P = \alpha_o E_o \cos 2\pi v_o t + E_o Q_j^o \left(\frac{d\alpha}{dQ_j}\right) \frac{\cos 2\pi (v_o + v_j)t + \cos 2\pi (v_o - v_j)t}{2} \hspace{0.5cm} \text{Equation 4.12}$$

Equation 3.22 shows that light can be scattered at three frequencies: v_o , $v_o + v_j$ and $v_o − v_j$. The first term is the Rayleigh scattering, which is at the same frequency as the light source and is proportional, in magnitude, to the inherent polarizability of the electrons in the molecules. The second term which contains the $v_o + v_j$ is the anti-

stokes Raman scattering and $v_o - v_j$ is the stokes Raman scattering and they represent the values at which the induced dipole oscillates at. Stokes Raman scattering occurs when the molecule was initially at an unexcited state before interaction with the laser light occurred. While anti-stoke Raman scattering occurs when the molecules are at an excited state, usually when it is heated. In most cases, molecules are in unexcited states and as a result, most recorded scatter is stoke Raman scattering. Figure 4.5 shows a schematic diagram that illustrates the different types of scattering [153, 156-158].
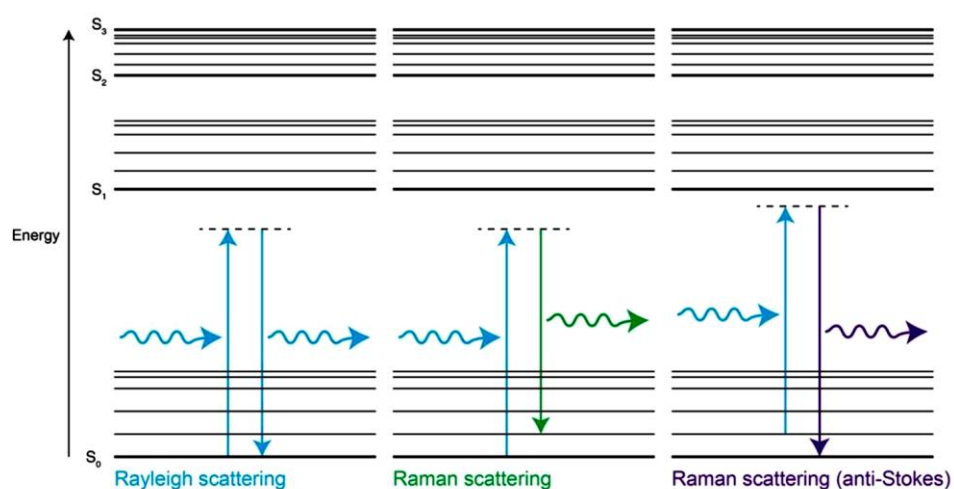
Figure 4.5: Schematic diagram showing Raman scatter phenomenon [156]

From Equation 4.9, $\frac{d\alpha}{dQ_j}$ is generally smaller than α_o and as a result Raman scattering is much weaker than Rayleigh scattering. The wavenumber (cm^{-1}) is the unit for Raman spectra on the x axis, which is the reciprocal of the shift in wavelength relative to the wavelength of the laser. The Raman intensity is represented on the y –axis.

Figure 4.6 shows the typical bonds identified by Raman spectroscopy and their corresponding the Raman shift on the spectra.
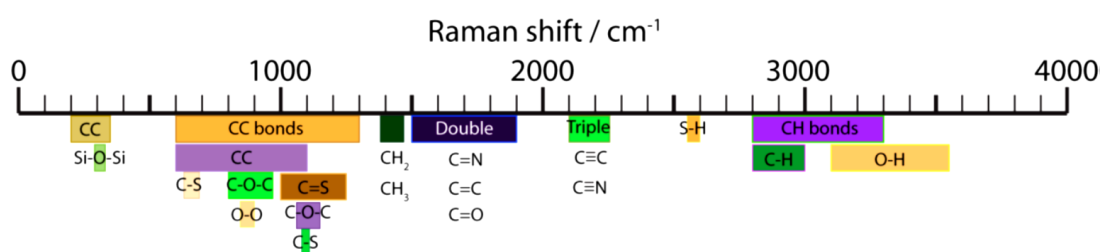
Figure 4.6: Raman shift peak ranges for organic bonds [150]

4.6   Raman microscopy integration with microfluidic systems

Raman microscopy integrated with microfluidic systems have already being used in the monitoring of environmental samples for example water quality and biosensing, for analysing rare and expensive samples; and in microreactors for which constant monitoring is required.

In Raman-microfluidic systems, the laser is focused into the microfluidic system through an objective lens of a microscope. The objective lens collects the backscattered light from the sample and it goes to the spectrometer through a dichroic filter. The strong Rayleigh scatter is removed by the filter, leaving the Raman scatter to go through to the spectrometer. A schematic diagram showing the typical Raman microfluidic system is shown in Figure 4.7.
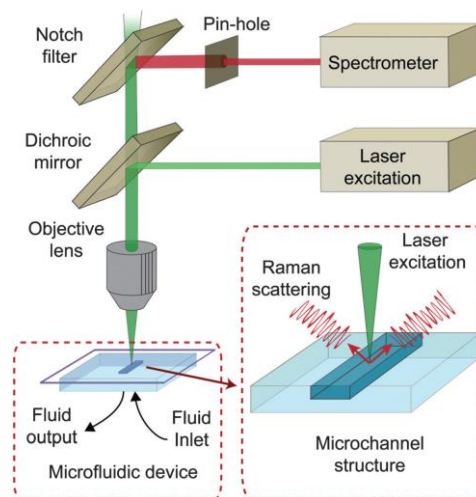
Figure 4.7: Schematic diagram illustrating the inner working of a Raman microscopy system integrated with a microfludic flow cell [150]

Due to the application of Raman spectroscopy to perform microscopic analysis through the use of a microscope, it has the capability of collecting Raman spectra data from very small volumes, which can be less than 1 µl, making it suitable for microfluidic type analysis. For instance, using a 633 nm laser source with a 60 x magnification lens and a pinhole of 50 µm in radius can achieve a lateral resolution of 0.25 µm and depth resolution of 1.7 µm. The dimensions of these resolutions are comparable to the dimensions found in microfluidic systems [150].

4.7 Challenges and considerations for Raman microscopy integration with microfluidics.

Although various benefits of integrating Raman microscopy and microfluidic systems have been highlighted, there are some challenges that must be considered. These challenges stems from the limitations of Raman microscopy and microfluidic as well as their integration.

4.7.1 Shape of channel

If the microfluidic channel has an open top, the convex/concave shape of a droplet surface can adversely affect Raman microscopy system's ability to accurately measure materials suspended in aqueous solution. The curvature of the fluid will create a difference in the refractive index between the fluid and the air. Furthermore, the shape of the droplet creates an effect that distorts the focus and hence, a reduction in spatial resolution. Therefore, it is important to ensure the laser enters the droplet through a flat top Raman transparent surface such as glass or quartz [159].

4.7.2 Focal length

Due to the microfluidic channel walls having thicknesses in the millimetre range, the focal length must be long enough to penetrate the walls and focus on the liquid media in the channel. Therefore an appropriate focal length is required to ensure the successful integrated system. The focal length is determined by the objective lens of the microscope. Lower magnification objective lenses have longer focal length which make them suitable for microfluidic system. However, energy density is directly proportional to magnification of the lens, hence, using a lower magnification lens comes at the expense of energy density [150, 156]. On the other hand, it is possible to use high magnification, long working distance objective lenses to achieve the requirement for depth penetration. However, this comes at the expense of optical intensity and as a result, reduced signal to noise ratio [160].

4.7.3 Detection volume

Raman microscope systems focus the laser into the sample using an objective lens. The size of the detection area is dominated by the diameter of the laser at the focal point (Figure 4.8). The laser diameter (d) is proportional to the focal length (f) of the

lens and the wavelength (λ) of the laser source, and is inversely proportional to the diameter of the lens (D). Therefore the diameter, or spot size can be expressed as

$$d \propto \frac{f\lambda}{D}$$ Equation 4.13

The parameter that is of equal importance to the detection volume is the depth of focus. The depth of focus, or confocal parameter, is estimated to be twice the Rayleigh range ($\sqrt{2}d$) and approximately as

$$Depth\ of\ focus = \frac{\pi d^2}{2\lambda}$$ Equation 4.14

To achieve a small depth of focus, the microscope must be set to confocal mode, where the size of the entrance slit of the spectrometer is reduced to smallest value compatible with the signal throughput [37, 150, 153, 156].
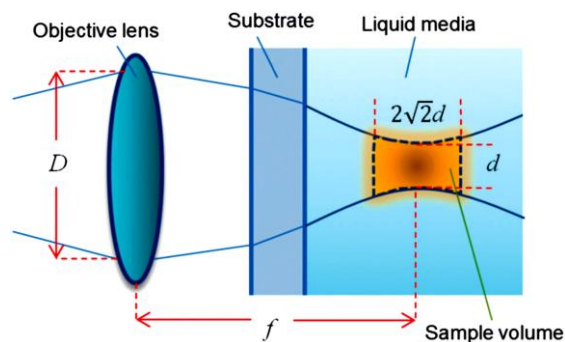
Figure 4.8: Schematic diagram illustrating the optical system the definition of spot size, depth of focus, focal length and overall detection volume [37].

In order to produce good results from a Raman – microfluidic setup, the optimum spot size must be selected, as the full detection volume is normally required to be place within the liquid medium to ensure Raman signal comes from the samples located within the medium.

4.7.4   Laser wavelength

The choice of wavelength is important for Raman microfluidic systems. The intensity of Raman scattering is inversely proportional to the fourth power of the wavelength, so it is commonly preferable to use lasers with shorter wavelength. However, for samples that require Raman microscopy, there is the tendency for the system to produce large interfering fluorescence signals as photon energy increases. These

signals can mask the Raman signals from the samples. One way of solving this issue is to use lasers with longer wavelength such as in the red or near infrared, so that the photon energy is below the fluorescence excitation band. This comes at the expense of Raman scattering efficiency which would then require power laser or longer integration time. Additionally, the choice of laser wavelength is important for resonance and surface – enhance resonance Raman scattering which may be advantageous for trace level detection [161-163].

4.7.5   Power setting

Increasing the laser power will normally increase the intensity of Raman scattering. However, high power can cause damage to samples located at the focal point. Therefore, care must be taken when setting the laser power to ensure samples are not damaged during Raman measurements [164, 165]. One way of reducing potential damage is by reducing the exposure time of the laser. However, this comes at the expense of a reduction of the signal to noise ratio.

 This is where microfluidic systems benefits from Raman microscopy, as fluids flowing through the channels tend to dissipate heat energy and hence allowing the use of higher laser power. However, the overall effect of laser power still depends on the fluid properties and flow parameters in the microfluidic system [166].

4.7.6   Memory effect

One other issue is the possible occurrence of "memory effect". This is due to some particles sticking to surface of the microfluidic channel causing permanent Raman signal from the channel. This problem can be eliminated by using disposable flow cells. If this not possible, then changing the wettability of the wall in order to prevent particles and analyte from interacting with the wall surfaces [167-171]. For a part of this thesis (Chapter 7), the memory effect is useful in order to conduct adsorption experiments.

4.7.7 Materials used for Raman microfluidic set up

The type of materials is also of importance and should be considered when integrating Raman microscopy and microfluidic systems.

4.7.7.1 Metals

Pure metals do not produce any Raman signals in bulk which is due to the presence of free electrons in the metallic structures. However, thin films or particulate of pure metals have shown to produce signals. Metallic nanoparticles and other nanostructures are particularly capable of producing surface – enhanced Raman scatter as discussed earlier. These properties are useful in enhancing scattering in microfluidic devices during experiments [172, 173].

4.7.7.2 Non-metals

Inorganic, non-metallic materials are capable of producing Raman scattering which gives Raman microscopy the ability to provide information regarding their chemical bonds, lattice and crystal arrangements. Furthermore, Raman scattering can provide information about the structures of materials like graphene and carbon nanotubes [174, 175].

4.7.7.3 Aqueous solution and material of microfluidic channels

The commonly used materials for microfluidic or lab on a chip system are glass, quartz, PDMS and other similar materials. As such, it is important to ensure that the choice of flow cell material does not interfere with Raman signal produced by the samples (Figure 4.9). Furthermore, aqueous media are the basis of microfluidics. Pure water produces weak Raman peaks at 1640 cm^{-1} and at 3300 cm^{-1} and is suitable for use in suspending various organic materials and particles without the fear of interference from the aqueous solution [176, 177].
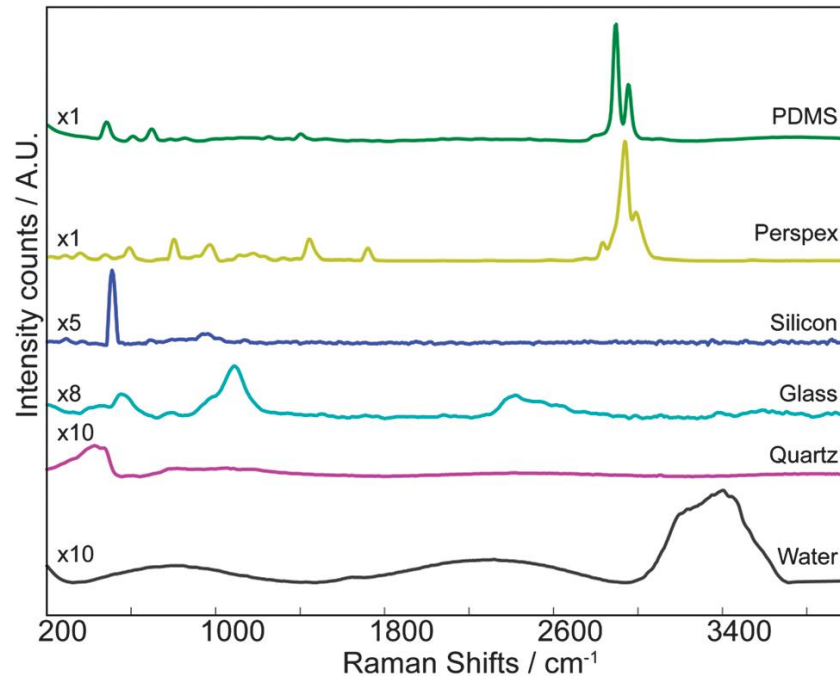
Figure 4.9: Raman spectra of possible microfluidic substrates [150]

4.8   Applications of Raman – microfluidic systems

As stated earlier, Raman spectroscopy and microfluidics have useful applications in their own right. The integration of the two allows for the utilization of the benefits available to microfluidics and the benefits of Raman spectroscopy to provide detail analysis of the targeted samples in microfluidics, including information from suspended samples and their environment.

4.8.1   Investigation of analytes

One of the most important features of Raman spectroscopy is its ability to provide information relevant the types of chemical bonds and quantity in the sample. The size of the laser beam makes it possible to focus on samples within a microfluidic systems. As a result, Raman – microfluidic system have shown great potential for the detection of analytes in complex mixtures.

Organic liquids can be efficiently detected with Raman microscopy as they can produce strong Raman scatter. For instance, Fletcher et al used a T – shaped microfluidic device to study the mixing of ethanol and acetic acid (Figure 4.10).
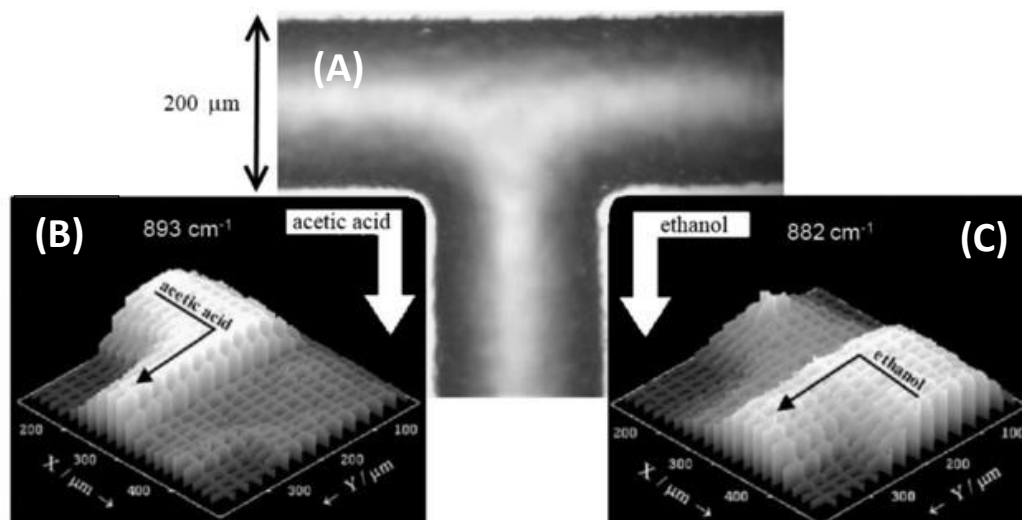
Figure 4.10: (A) A T – Junction microfluidic channel used for the purpose of mixing ethanol and acetic acid. (B) rasterised Raman image of acetic acid using its Raman peak (C) rasterised Raman image of ethanol using its Raman peak.

Raman microscopic mapping was used to detect the two fluids at various mixing stages. The figure above depicts the Raman beam rasterised image of the T – channel which demonstrates the accuracy of analyte detection in a microfluidic system. This method uses the two distinct Raman peaks for the detection of ethanol and acetic acid.

4.8.2   Nanoparticle detections

The ability of the system to identify and measure suspended materials is useful with applications in assessing water contaminants and micro-reactor outputs to determine mixtures and unknown suspended materials.

Nanoparticles can be synthesised and suspended in aqueous solution, which is suitable for microfluidic processing. Raman microscopy can provide non-invasive information such as the type of nanoparticles in the solution, the concentration of the nanoparticles in the solution and the even the size of nanoparticles.

4.9   Summary

The first part of the review presented different analytical techniques capable of detection and quantifying CNTs suspended in aqueous solution. It showed that Raman microscopy and inductively coupled plasma mass spectroscopy (ICP-MS) are ideal techniques for the NAST methodology's monitoring system. This is due to availability of the both techniques in industry and their relative ease of use when compared to other techniques. Another reason for the choice of techniques is that they are both able to detect CNTs at concentration levels that are lower than concentrations that research has shown to be toxic to aquatic ecosystem.

An overview of microfluidics and fluid flow conditions experienced in oil reservoirs was presented in the second part. A review of applications of microfluidic experiments for reservoirs and porous media study have shown that these kind of experiments can be used to achieve the aim of this thesis.

The third part of this chapter presented some analytical techniques that can be integrated with microfluidic system as an alternative to optical instrumentation for visualization purposes. From here, Raman spectroscopy and its application were also presented and more importantly, the integration of Raman microscopy and microfluidic systems were reviewed. Finally, the application of Raman – microfluidic system was review which shows the applicability of the system to perform experiments needed to elucidate the adsorption and transport kinetics of carbon nanotubes in microfluidic channels.

Chapter 5. Experimental and Computational Methodology

This chapter is divided into two sections. The first section is the experimental methodology part of the project which presents information on material, experimental procedures and analytical techniques used in this study. The focus of this study is on NAST 1 which involves injecting CNTs into APTES coated rock surfaces. For this thesis, glass microfluidic flow cells were used to represent porous sandstone rock. The second section presents the computational methodology used for the simulation part of the project to evaluate the role of salt gradient in the mixing of CNTs.

5.1   Modified NAST1 methodology

The main components of NAST1 are the CNTs, organosilane (APTES), the cross-linkages such as Dicyclohexylcarbodimide (DCC) and the rock surface. The first stage in NAST1 is to inject the APTES solution to react on the rock surface, the next stage is to inject the CNTs dispersed with a surfactant and DDC to ensure the CNTs attach to the APTES covered rock. However, in order to minimize the steps and chemicals used for NAST1, DDC was removed from the methodology.

5.2   Materials

5.2.1   MWCNTs

Carboxylic functionalized MWCNTs (COOH –MWCNT) with diameter of 7 – 15 nm and length of 0.5 – 2 μm were purchased from CheapTubes.com. The MWCNTs were produced by the manufacturer using a combustion chemical vapour deposition (CVD) process with a reported carbon purity of 95%.

5.2.2   SWCNTs

The SWCNTs used for experiments (purity 95%; product number: 773735; purchased from SouthWest Nanotechnology) was produced using a chemical vapour deposition (CVD) process in the presence of Cobalt-Molybdenum catalyst.

5.2.3   Tween 80

Tween 80 is a hydrophilic non-ionic viscous surfactant purchased from sigma Aldrich LTD. It is often used for dispersing hydrophobic particles in aqueous solution. The surfactant was deemed appropriate due to its dispersing power at certain CNT concentration levels and its low toxicity levels [178]. The chemical structure is shown in Figure 5.1**.**
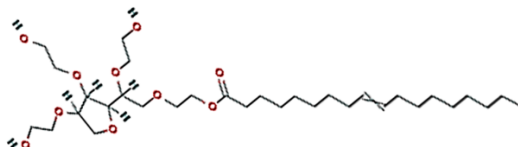
Figure 5.1: chemical structure of Tween 80 [179]

5.2.4   Silane coupling agent

To functionalize the microchannel walls, 3-aminopropyltriethoxysilane (APTES) (98%) with molecular formula of $H_2N(CH_2)Si(OC_2H_5)_3$ was purchase from Scientific Laboratory Supplies and kept in the fridge. The chemical structure is shown in Figure 5.2.
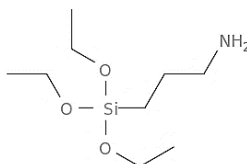
 Figure 5.2: Chemical structure of 3-aminopropyltriethoxysilane (APTES) [180]

5.3   Sample preparation

For all experiments and quantification analysis, aqueous dispersions of CNTs were obtained by adding the appropriate mass of SWCTS into an aqueous solution containing 1.5% v/v of Tween 80 in water. This was followed by a 2-hour sonication step at room temperature.

For adsorption experiments, the silane solution comprises of 2% solution of the 3-aminopropyltriethoxysilane and ethanol/water (95/5, v/v).

5.4　Microwave acid digestion procedure

Digestion of CNT samples was performed in pressurised vessels HF100-multi-wave 3000 (Anton Paar). 10 mg samples of CNT were transferred to the microwave reaction vessels. The reagent, about 7.0 mL of concentrated nitric acid, 1.0 mL of concentrated hydrochloric acid and 2.0 mL of hydrogen peroxide, was carefully added into the microwave reaction vessel and allowed to react for a couple of minutes. A seal forming tool to expand the seal vessels was used, and the venting screws on each vessel were closed with a key. The microwave reaction vessels were inserted into the rotor according to their reference positions. The rotor lid then covered the rotor and placed into the microwave oven cavity.

After the sample digestions finished, 45 mL of high purity deionised water (HPDW) was used to rinse each vessel. The resulting solution was then transferred to a pre-weighed 50 mL centrifuge tube.

5.5　Quartz cell

To obtain reliable and repeatable quantitative values from a contained solution, 300 μl of a solution containing dispersed CNTs are pipetted into a Raman cell (Figure 5.3) made of quartz. Each concentration level was analysed in triplicates, and sample measurements were taken at five random points in the quartz cell.
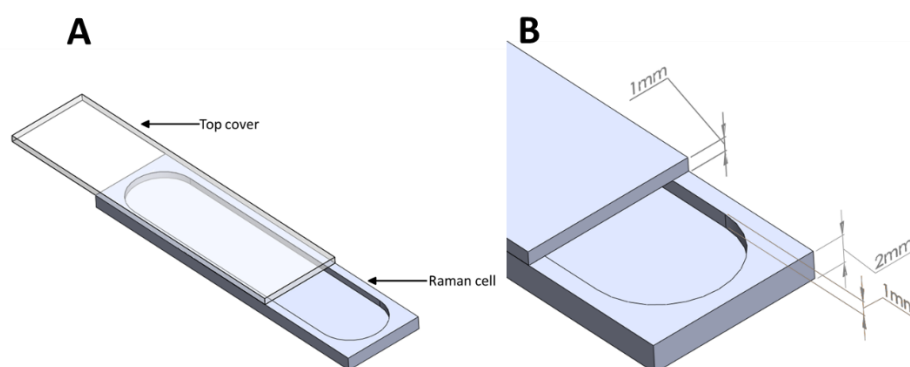
Figure 5.3: Schematic of the Raman cell (A) illustrates the full image of the cell including the top cover (B) shows the dimensions of the Raman cell

5.6 Microfluidic flow cell

The microfluidic flow cell is made of glass (Figure 5.4), for its optical properties; it is transparent at visible wavelength and is Raman active in the low wavenumber region with a broad peak at 1000cm^{-1}. This ensures that the dominant G peak of SWCNT (1580 cm^{-1}) is not masked. The flow cell has three microchannels as shown in Figure 5.4a below. Figure 5.4b shows the cross sectional dimensions of the micromodels. The top end is flat to improve the optical transmission and enables the lens to focus on surface.
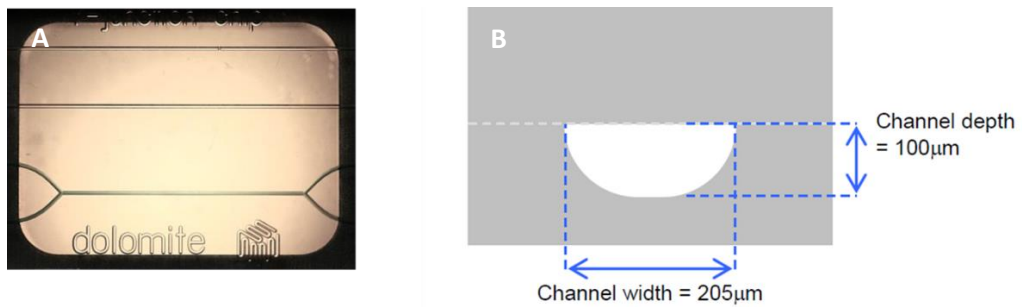
Figure 5.4: (A) Microfluidic flow cell showing channel geometries and (B) Schematic diagram showing cross sectional dimensions.

5.7 Experimental procedures

The experimental methods are categorized in relation to the adsorption and transport experiments. Relevant literature to each experimental method is given. Figure 5.5 shows a schematic of the experimental set up. The syringe pump provides steady flow rates on a microliters per hour level flow rate. The straight line microfluidic channel was used for adsorption study experiment while the Y – junction channel was used for transport study experiments.
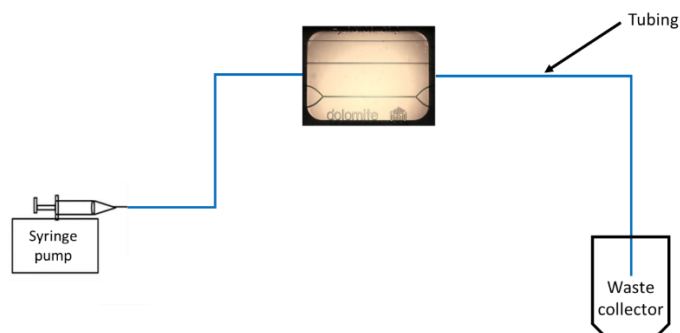
Figure 5.5: Schematic of experimental setup

5.7.1 Adsorption test experimental procedures

1. Surface functionalization is achieved by pumping the prepared silane coupling agent solution into the microfluidic cells for 1 hour, following this, the flow is stopped for 1 hour.

2. Ethanol is then pumped in the channels to remove the unreacted silane.

3. The aqueous solution containing suspended CNTs is then injected at a given flow rate into the APTES coated microfluidic flow cell.

5.7.2 Transport test experimental procedures

1. The aqueous solution containing suspended CNTs is injected at a given flow rate into the microfluidic flow cell without the application of APTES on the microchannel walls.

5.8 Analytical techniques

The literature review chapter has shown the suitability of Raman spectroscopy and Inductively Coupled Plasma – mass spectrometry (ICP – MS) for quantifying CNTs suspended in aqueous solution. Furthermore, the chapter showed the application of Raman microscopy integrated with microfluidic system for fluid experiments. In order to understand the results from experiments conducted, characterisation and quantification of the CNTs suspended in aqueous solution is required. Therefore, aside from presenting Raman spectroscopy and ICP–MS, Dynamics Light Scattering (DLS), Transmission emitting Microscopy (TEM) and Energy dispersive spectroscopy (EDS) will be presented in this section. These other analytical techniques presented in this chapter are

5.8.1 Raman spectroscopy

Raman analysis in this study was carried out using a Renishaw InVia spectroscopy (Figure 5.6). This equipment has two lasers; 488 nm and 785 nm wavelength laser operating with a maximum power of 10 mW and 220 mW respectively at the source. Integrated with the equipment is a Leica microscope with a 5x, 20x and a 50x short distance objective lens and also a 50x long distance objective lens.
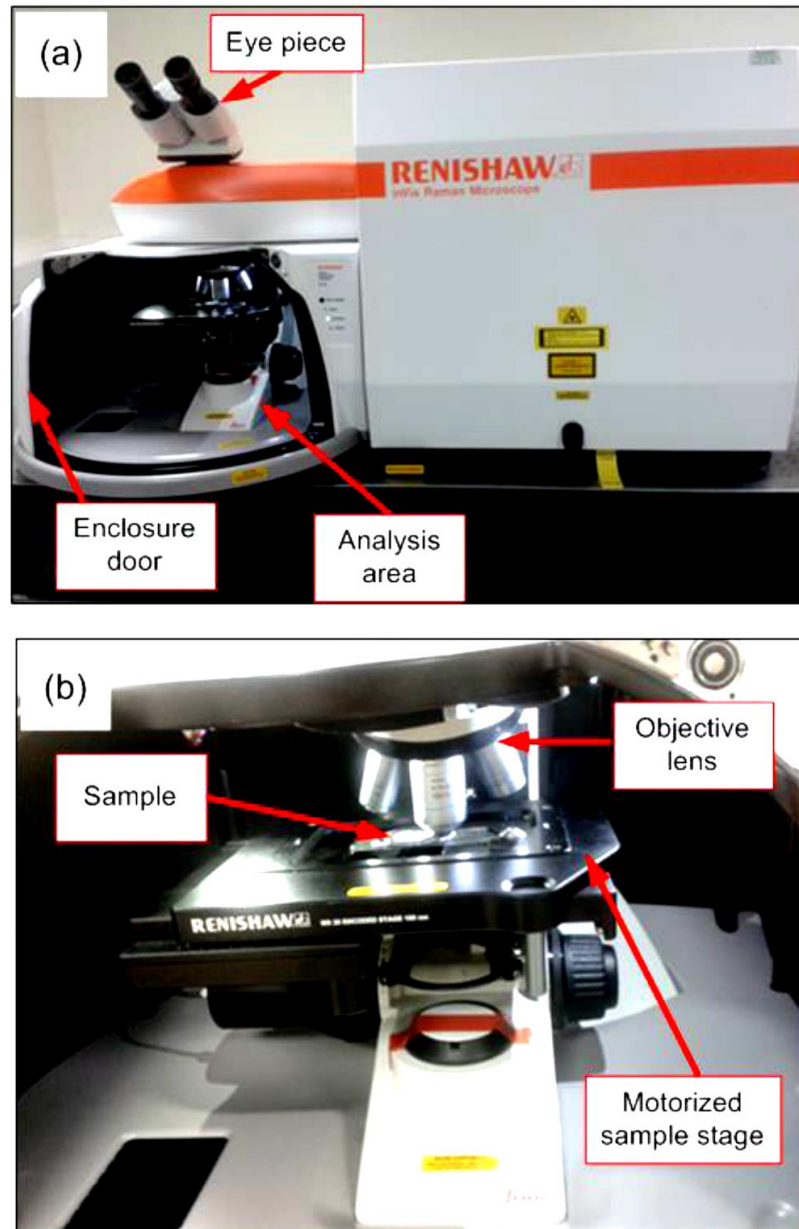
Figure 5.6: Image of (a) The Raman equipment used for analysis (b) Inside the chamber of the Raman equipment.

Samples are placed on a motorized stage and the Raman laser is focused through the objective lenses for analysis. The Raman equipment can collect spectra from the sample in two ways:

- Single spot analysis: This option allows for a single spectrum to be collected from a single spot on the sample

- Spot-to-spot mapping: With the motorized stage, several spectra can be collected from different spots on the sample in a single analysis. This done by using the in-built software to instruct the motorized stage to move to

different positions during analysis. The mapping option makes it possible to scan larger areas of the sample.

In this study, spectra were collected by both type of analysis option. For the quantification of CNTs in aqueous solution (Chapter 5), single spot analysis was used. For adsorption and transport studies of CNTs in microfluidic channels (Chapter 6 and 7), spot-to-spot mapping was used.

Figure 5.7 shows a schematic diagram of the internal instrumentation of the Raman equipment. The Raman signal is collected from the sample at 180° backscattering geometry and the scattered light passes through filters that removes Rayleigh scattering. Then the signal is focused and directed onto a diffraction grating by a lens through a slit. The signal is split into a spectrum that is detectable on a charge couple device (CCD) detector.
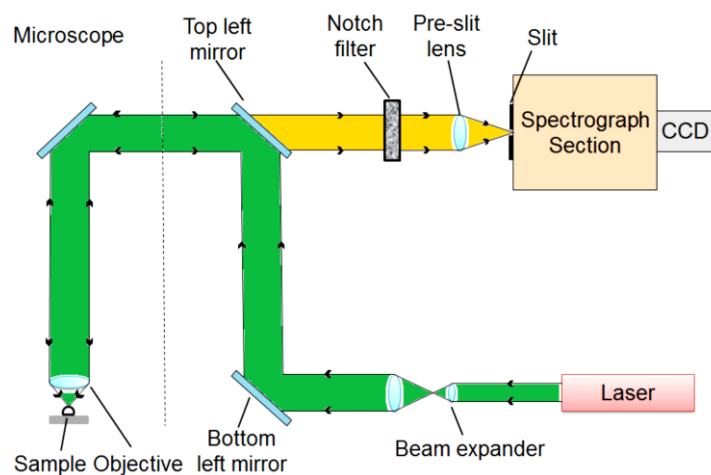
Figure 5.7: Schematic diagram of Raman spectroscopy [153]

A computer is connected to the equipment to collect spectral data during analysis. Samples can be viewed through the microscope's eye piece or by using the computer. A software package provided by Renishaw was used to control the Raman system. The software allows the adjustments of various parameters such as laser power and exposure time before analysis is undertaken. A procedure to optimize the laser power and exposure time was undertaken to obtain good signals with various Raman parameters while ensuring no sample damage. A detail analytical study on this procedure will be provided in chapter 5.

5.8.2 Dynamic Light Scattering (DLS) and Zeta potential measurements

For this study, Particle size distribution and zeta potential were measured using Malvern Zetasizer Nano ZEN1600.

The Zetasizer uses DLS to measure the sizes of particles suspended in aqueous solution. DLS measures the size of small particles by scattering light from them. Particles suspended in a solution undergo Brownian motion. The larger the particle, the Brownian motion of the particle will be slower. DLS uses light scattering to monitor the Brownian motion of particles in order to determine its size [181]. The process involves shining a monochromatic light beam onto a solution containing particles, when the light hits the particles in Brownian motion, the wavelength of the light will change. This change is related to the size of the suspended particle. DLS periodically refers to measurements and interpretation of light scattering data on a microsecond timeframe [182].

The Zetasizer measures zeta potential by applying an electrical field into the solution containing particles and measuring the electrophoretic mobility of the charged particles due to the applied electric field. The velocity of the particle under electrophoresis is dependent on the Zeta potential, electric field strength, Dielectric constant and viscosity of the medium. Zeta potential is related to the electrophoretic mobility by the Henry Equation:

$$U_E = \frac{2\varepsilon z F\,(ka)}{3\,\eta} \qquad\qquad\qquad \text{Equation 5.1}$$

Where U_E is the electrophoretic mobility (m/s), z is the zeta potential (V), ε is dielectric constant, η is viscosity and F(k a) is the Henry's function.

5.8.3 Inductively Coupled Plasma – Mass Spectrometry (ICP–MS)

ICP – MS enables the detection of elemental composition of samples by measuring the ions concentrations. Liquid samples are injected into a radiofrequency – induced argon plasma, which at its core the ICP maintains a temperature of approximately 10000 k. The ions from the plasma are collected into a mass spectrometer using a quadrupole. The elemental concentration in the sample is proportional to the ion concentrations measured in the ICP-MS detectors. ICP-MS analysis was performed

using a Perkin Elan DRCII equipped with an auto sampler. This analytical technique is used to characterise the CNTs used and quantify the concentration of CNTs suspended in aqueous solution.

5.8.4   TEM EDS

Transmission electron microscopy (TEM) is an elastic scattering spectroscopy imaging technique in which a beam of electrons to transmit through a sample to form an image. The technique can provide images in the sub-nanoscale. This is due to the wavelength of ~0.2 nm for electron compared to wavelengths of ~200 nm in light microscopes. TEM images were obtained on an FEI Titan Themis Cubed 300 operated at 300 kV. The CNTs sample was prepared by suspending a small amount of powder sample in methanol, followed by ultra-sonication for 5 min. One drop of this suspension was put on a carbon-coated copper grid for TEM analysis.

The TEM system is also equipped with an Energy dispersive X – ray Spectroscopy (EDS) which analyses the elemental components of the CNTs which will therefore allow for the characterization of the distribution of the individual elemental impurities located in the CNTs.

5.8.5   Turbiscan

The dispersed CNTs were analysed using Turbiscan Lab Expert stability analyser to assess the dispersion stability of the CNTs. The backscattering (BS) of a pulsed near-infrared light of wavelength 880 nm scanned the samples from the bottom to the top at specific time intervals. During the scan process, it measures the percentage of transmitted light through the samples as a function of height of the tube to quantify the rate of destabilisation. The instrument accounts for particle agglomeration and sedimentation. The larger the shift in measurement over time, the more unstable the particle are in the solution.

5.9   Computational methodology

The simulation done in this thesis is conducted by using Computation Fluid Dynamics (CFD). CFD is part of fluid mechanics that predicts flow behaviour by solving partial differential equations (Navier – Stokes equations) which govern the fluid flow

properties using computational resources. An understanding of the underlying physics of fluid mechanics is required to solve a fluid flow problem. For simple fluid flow problems, these equations can be solved analytically. However, for more complex problems, the partial differential equation need to be translated to a discretized form, which divides the domain of the complex problem into small parts (grids), hence, converting a continuous equation into a form that be solved using numerical analysis. The CFD process is illustrated in Figure 5.8.
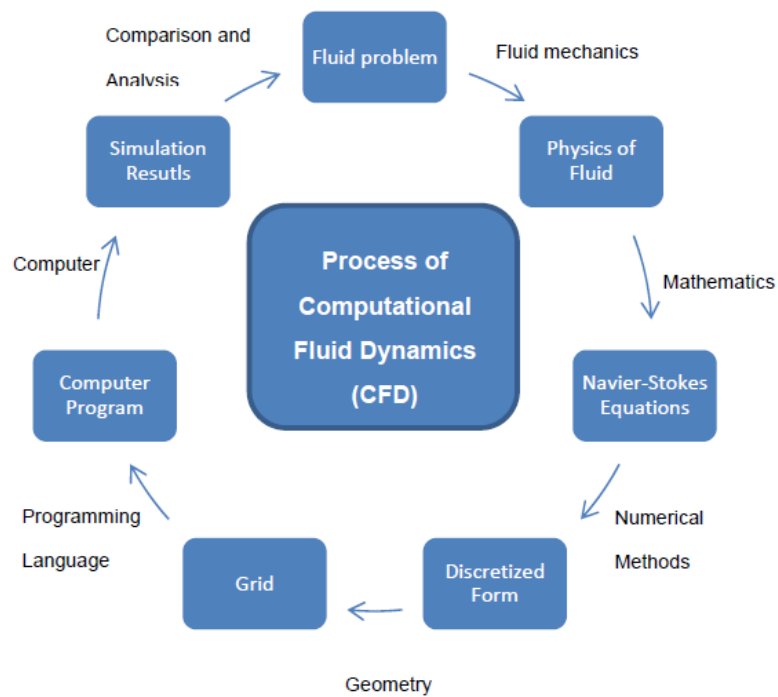
Figure 5.8: Process of Computational Fluid Dynamics (CFD)

There are tools that aid in the translation process, including Finite Volume Method, Finite Difference Method and Finite Element Method.

In this thesis, COMSOL version 5.3a was used to conduct the simulation using Finite Element Analysis (FEA). FEA is based on a direct physical approach and is a suitable numerical analytical method for solving computational problems over complex domains. The solution of the problem involves solving the governing equations iteratively until the error falls below the required tolerance. The fundamentals of FEA include the discretisation, interpolation and minimising the error. Discretisation means that the domain of the model is divided into smaller finite sizes called elements. Hence, the term Finite Element Analysis. The elements come in various

shapes such as triangular, tetrahedral, cubes e.t.c. These elements must cover the entire domain without overlapping each other. Each element contains the governing equations which is then converted into algebraic equations by approximation. Thus, the value location within the elements can be computed, which is known as interpolation. The approximation has to be validated using an error function [41].The iterations minimises the errors to obtain highly accurate results.

A major benefit of using Comsol Multiphysics is the ability of the software to "couple" different physical processes together. For this thesis, three physical processes were considered; fluid flow, particle transport and transport of dilute species (Figure 5.9). The fluid flow was used as the driving mechanism for both particle transport and transport of dilute species.
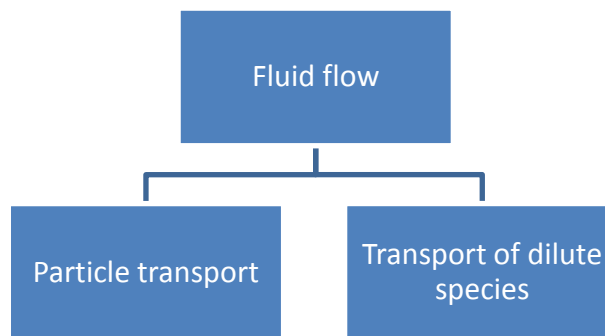
Figure 5.9: Schematic diagram illustrusting the coupling between different physics. Fluid flow physics is the common controlling physics for both dependent physics.

Chapter 8 presents a detailed description of the procedures used for the simulations. The results obtained from the simulations will be used to understand the flow regime in the microfluidic channel as well as the transport kinetics of particles in the channel. Furthermore, it provides an understanding of salt diffusion which occurs as result of fluid flow.

5.10 Summary

This chapter outlines the experimental and computational methodology for this thesis. It explains the setup, test procedures and the materials used for this thesis. This chapter presented all the analytical techniques used for the experiments which are Raman microscopy, ICP – MS, DLS , TEM, EDS and Turbiscan. For quantifying CNTs suspended in aqueous solution, Raman microscopy and ICP – MS were used. For characterizing the particles and its suspension properties, DLS, TEM, EDS, Turbiscan and zetasizer were used.

The computational methodology section presents the software (COMSOL) used for fluid dynamic, transport of dilute species and particle transport simulation. It showed the different physical processes and that the fluid dynamics process was the used as the driving mechanism for the particle transport and transport of dilute species processes.

Chapter 6. Characterisation of CNTs dispersed in aqueous solution and study of analytical techniques for quantification of CNTs suspended in aqueous solution.

6.1   Introduction

One of the objectives of this thesis is to investigate analytical techniques capable of detecting and quantifying CNTs suspended in aqueous solution which will also partly accomplish one of the other objectives; which is to develop an integrated analytical system capable of performing real time microfluidic experiments. To achieve this, the in-situ/ex-situ detection and quantification of carbon nanotubes in microfluidic systems is a requirement. Furthermore, the analytical technique chosen, need to have short processing times and procedural simplicity, while maintaining an acceptable level of accuracy and precision. This will ensure quick analysis needed for monitoring CNTs concentration levels in reservoir systems.

Techniques used to effectively monitor CNTs in different environment should overcome certain inherent challenges; the first one being able to detect CNTs at relevant levels relative to the environmental requirements, which can be as low as part per trillion (ppt) range. Another challenge is the avoidance of potential interference from substances found in different environmental conditions [183]. As stated in the literature review, studies have shown that Raman microscopy and ICP – MS can be used to detect and quantify CNTs in aqueous solutions. However, there are limited studies which give a comprehensive report on relevant experimental and analytical parameters, characterisation of CNTs used in the analysis and complete calibration graphs.

This chapter focuses on investigating the applicability of Raman and ICP - MS to detect and quantify carbon nanotubes in aqueous solution, while also meeting the requirements of the integrated microfluidic system. Furthermore, it looks at the effects of sample preparation and analytical procedures on the accuracy of these techniques.

The chapter is divided into four sections. Firstly, the CNTs dispersions used in the study will be characterised using TEM, SEM and Raman. Secondly, CNTs are

suspended in an aqueous solution using a percentage of Tween 80, a non-ionic surfactant, as a dispersant, needed to prevent the particles agglomeration. Dynamic Light scattering (DLS) will characterise the dispersion and particle size distribution of the CNTs while Turbiscan shows the dispersive effectiveness of the surfactant on CNTs. The Third part of this chapter presents a standardized calibration procedure for quantifying SWCNTs and MWCNTs using Raman microscopy and also investigates the influence of Raman parameters on the particle structure/property and the measurement accuracy. The Fourth section presents ICP- MS measurements with and without digesting the CNTs. Finally, it will evaluate and compare the sensitivity and limitation of both Raman spectroscopy and ICP-MS in quantifying a number of different types of CNTs in aqueous solutions.

6.2   Characterization of the carbon nanotubes

6.2.1   Transmission electron microscopy

TEM analysis was carried out to determine to what extent the metallic catalysts were associated with the SWCNTs and MWCNTs. Figure 6.1a shows TEM images of SWCNTs, which appear as long, grey rods with a diameter of approximately 1 nm. The dark areas within the CNTs are metallic impurities (Cobalt), as confirmed with EDS (Figure 6.1b and Figure 6.2). The supplier of the SWCNTs also stated that the cobalt-molybdenum-catalyst (CoMoCat) process was used for synthesising these CNTs, thus providing further confirmation of its presence.
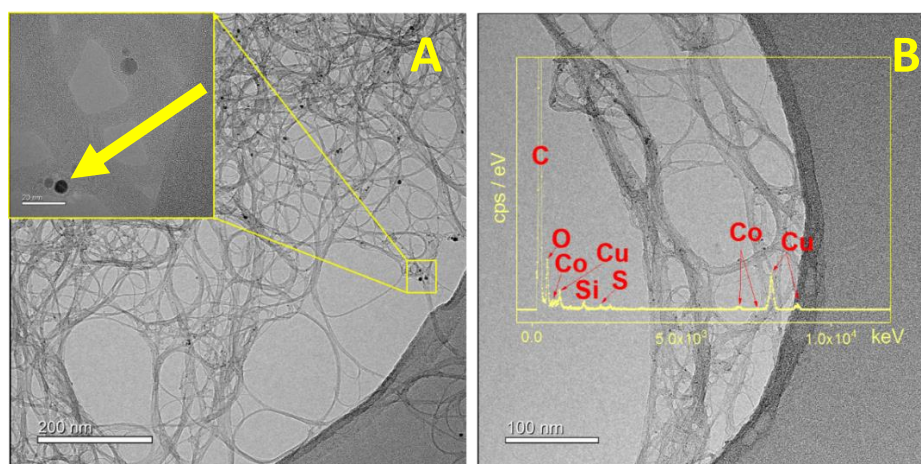
Figure 6.1: TEM images of SWCNTs (a) Arrow denotes dense metallic impurities within the NPs (b) EDS peaks representing elements within the NPs, except Cu and C from TEM grids
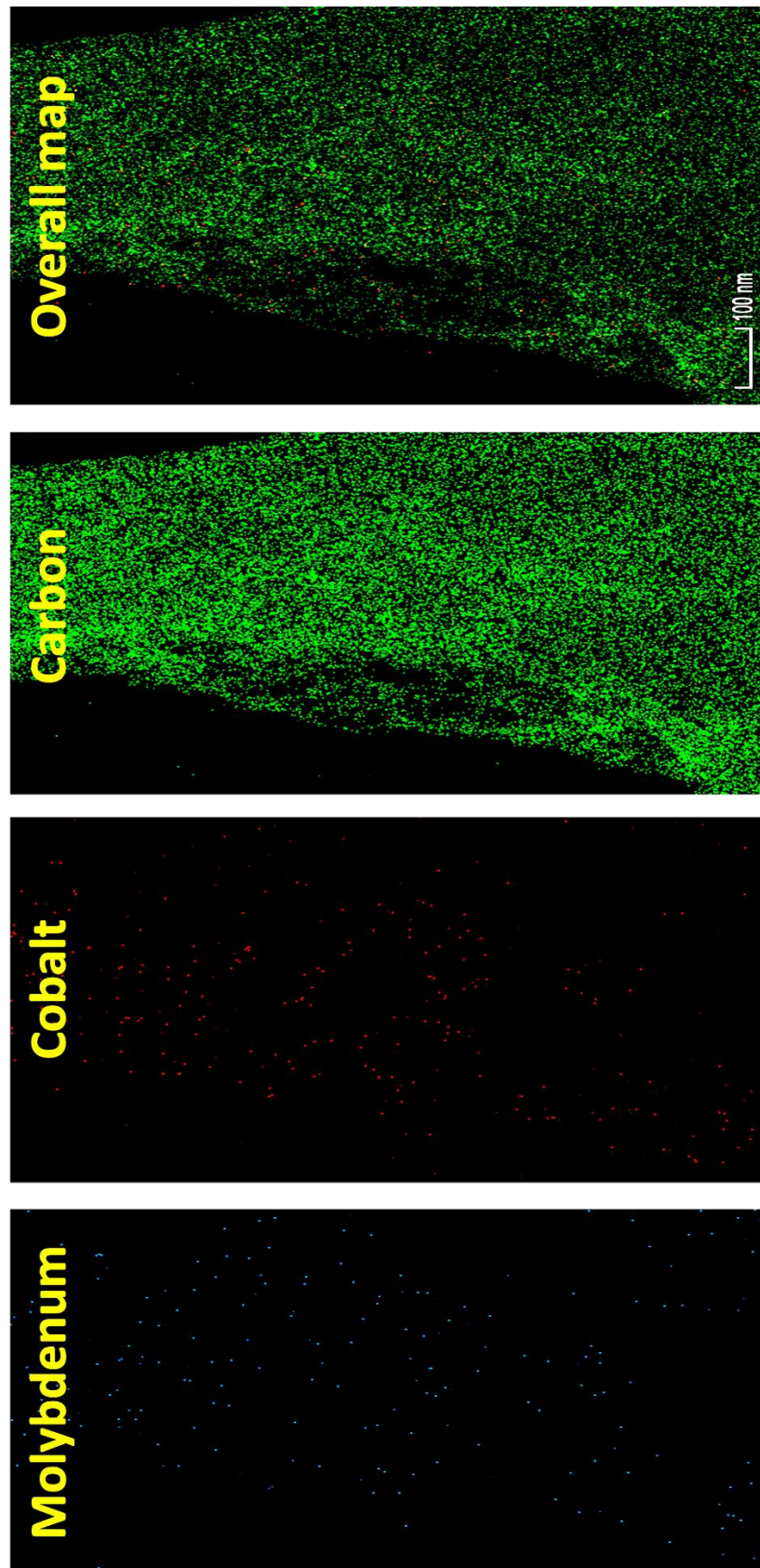
Figure 6.2: TEM EDS-mapping of SWCNTs showing colour coded elemental content (A) Overall mapping of CNTs (B) Green dots represent carbon content (C) Red dots represent Cobalt content (D) Blue dots represent Molybdenum

To quantify the metallic impurities, the elemental mass was calculated by EDS (Table 6.1).

Table 6.1: EDS elemental analysis for SWCNT sample

Element	Atomic Fraction (%)	Mass Fraction (%)
Carbon (C)	96.13	89.40
Oxygen (O)	1.89	2.39
Silicon (Si)	0.17	0.34
Cobalt (Co)	0.11	0.42
Molybdenum (Mo)	0.10	0.68

Figure 6.3a and Figure 6.3b show the TEM images of functionalized COOH-MWCNTs. In Figure 5.3a, the layers of walls can be seen as well as the arrow that indicates the metallic impurities. Figure 5.3b shows the dominant elements in the MWCNTs to be Cobalt, Iron and Carbon.
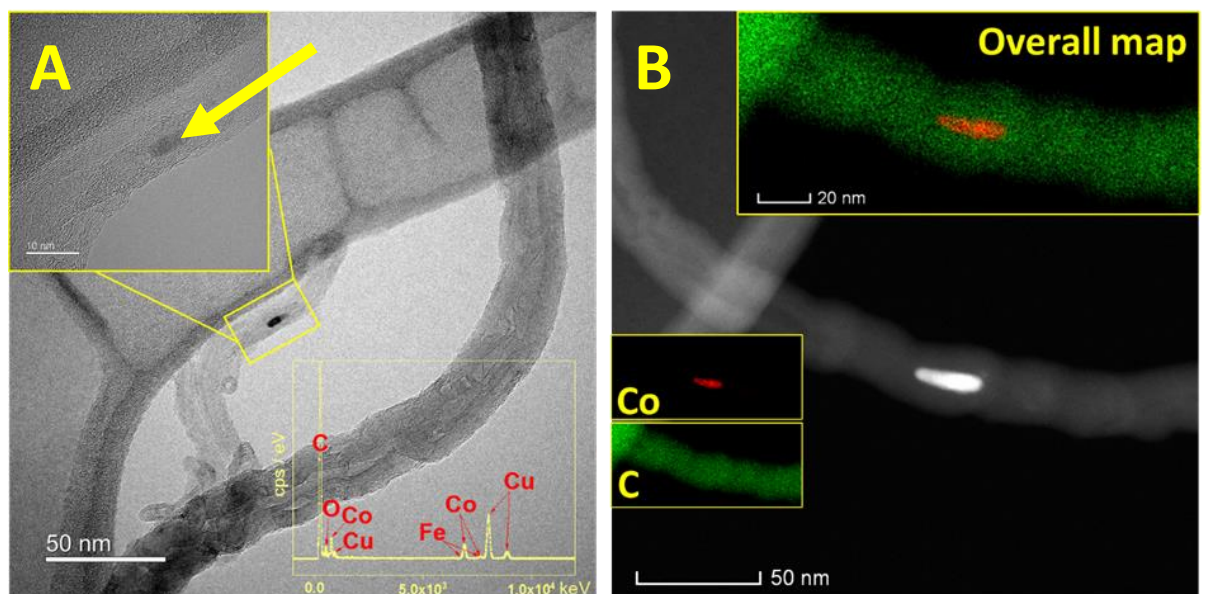
Figure 6.3: TEM images of MWCNTs (a) arrow denotes dense metallic impurities within the NPs (b) EDS peaks representing elements within the NPs, except Cu and C from TEM grids.

Once again, EDS analysis was performed to quantify the elemental make-up of the MWCNTs (Table 6.2).

Table 6.2: shows the elements found in the MWCNTs and their corresponding masses.

Element	Atomic Fraction (%)	Mass Fraction (%)
Carbon (C)	97.67	93.72
Oxygen (O)	1.14	1.48
Iron (Fe)	0.01	0.06
Cobalt (Co)	1.18	4.74

6.2.2   Raman Microscopy

Two regions of interest in the Raman spectroscopy of CNTs are the radial breathing mode (RBM) and the tangential mode (TM). The RBM corresponds to radial vibrations, (expansion and contraction) of the nanotube. It is used to determine the diameter of the CNTs and is a unique property of the particles. All carbon forms appear on the Raman spectra in the range of 1000 to 1700 cm^{-1} [139]. Figure 6.4 and Figure 6.5 show the two distinct peaks namely the D and G peaks. The D-peak occurring around the 1350 cm^{-1} is attributed to the presence of disordered amorphous carbon and the double resonance effects in sp^2 carbon. The G-peak occurring around the 1590 cm^{-1} corresponds to the tangential vibrations, the TM, of the C=C stretching transition of the graphitic carbon atoms [184].

 The G-/D- band intensity ratios have been used in several studies to characterize CNTs under various conditions and environments [134, 184, 185] which has shown that the most prominent feature in SWCNTs is the G-band at 1590 cm^{-1} (Figure 6.4). The G peak was adopted as the analytical signal for the SWCNTs calibration graphs [133, 186, 187].
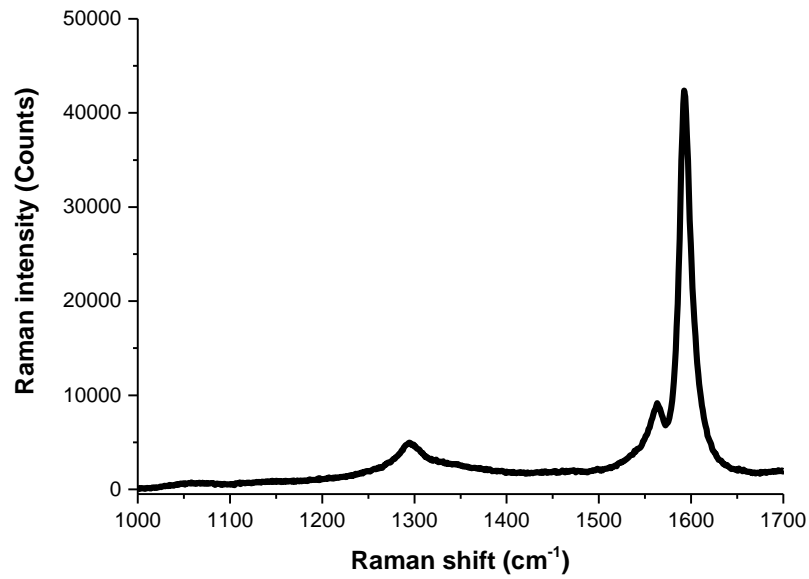
Figure 6.4: Raman spectrum of SWCNTs

For the COOH-MWCNTs, the G band is located at 1580 cm^{-1} with a shoulder at 1600 cm^{-1} which is typical of defective graphite-like material and the D peak shows the presence of disorder in carbon systems, the D peak is more prominent than the G peak (Figure 6.4) [187] due to destruction of the graphitic structure when COOH group attaches on the surface of MWCNTs [188]. As a result, the D peak was adopted as the analytical signal.
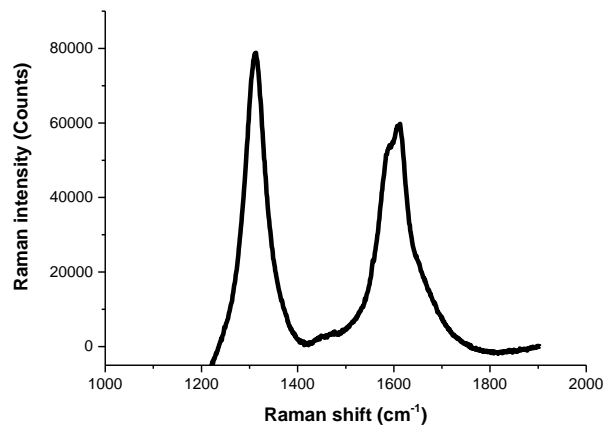
Figure 6.5: Raman spectrum of MWCNTs

6.3   Characterization of dispersed CNTs in aqueous solutions

Dynamic light scattering (DLS) analysis was conducted to observe the particle size distribution and the zeta potential of 20 mg/L CNTs suspended in aqueous solution. Figure 6.6 shows the particle size distribution of CoMoCat SWCNTs. The graph shows the poly-dispersed nature of suspended CNTs. The orientation of the particles has an effect on the DLS analysis as indicated by the intensities located within the 10 nm range, however, majority of the particle sizes are within the size range specified by the supplier (1 µm). The figure also shows that there is some agglomeration as indicated by the intensities located above 5 µm.   The zeta potential of the CNTs suspended in the tween 80- water mixture is approximately -14mV.
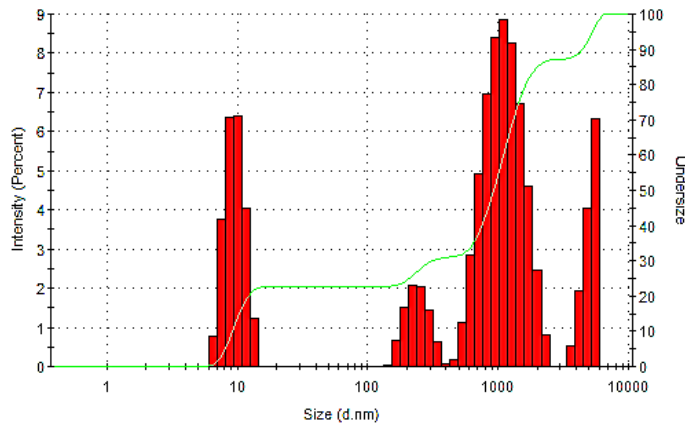
Figure 6.6: DLS analysis showing particle size distribution which shows the effect of the tubular shape of SWCNTs on the analysis.

The same analysis was carried out on MWCNTs. It yielded similar results when compared to the SWCNTs. Figure 6.7 shows the particle size distribution of the MWCNTs suspended in the tween 80 – water mixture. The distribution of particle size is more spread when compared with the SWCNTs and is further confirmed with the manufacturers datasheet which stated the diameter of the MWCNTs to be between 0.5 µm and 2 µm.
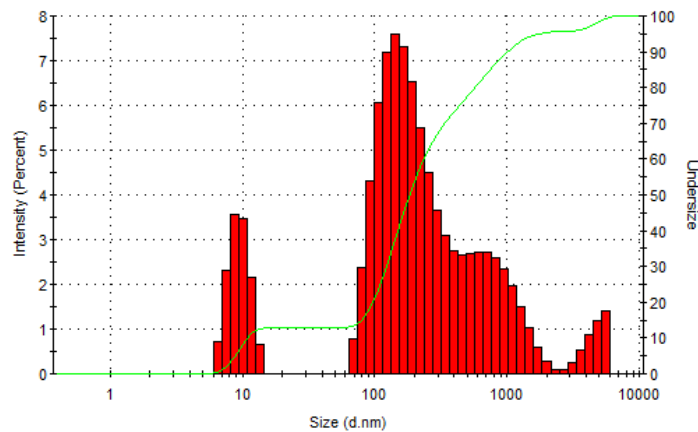
Figure 6.7: DLS analysis showing particle size distribution which shows the effect of the tubular shape of MWCNTs and the variation of particle size on the analysis.

6.4   Stability of SWCNTs dispersed with the aid of Tween 80 in aqueous solution

Turbidity scan measurements were done to analysis the suspension stability of the CNTs dispersed in aqueous solution with the aid of Tween 80 as a surfactant. Figure 6.8 and Figure 6.9 show that there is little change in backscatter received from the measurements which shows that over a period of 24 hours, sedimentation is kept to a minimum. This indicates that the suspension of both types of particles is stable for that period of time.
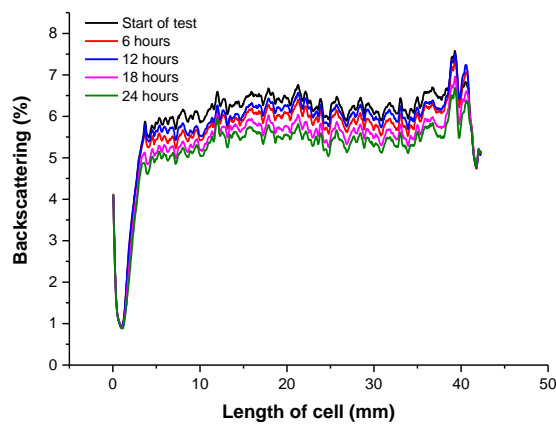
Figure 6.8: Turbidity measurements of MWCNTs suspended in aqueous solution for a period of 24 hours.
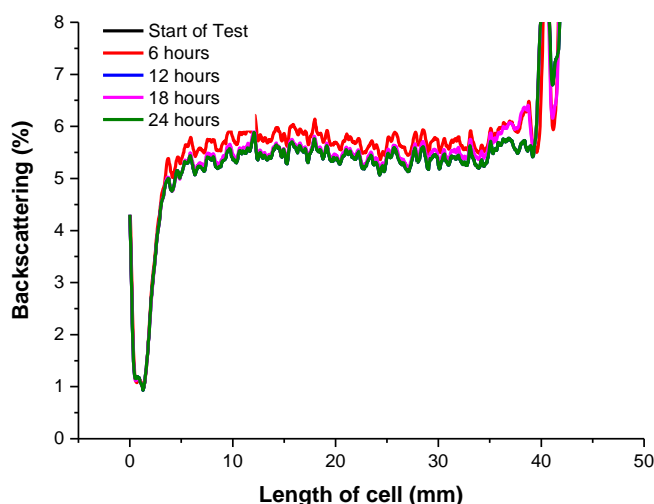
Figure 6.9: Turbidity measurements of SWCNTs suspended in aqueous solution for a period of 24 hours.

6.5 Quantification procedure for Raman microscopy

6.5.1 Optimizing the setup parameters

To obtain reliable and repeatable quantitative values from a contained solution, 300 µl of a solution containing dispersed CNTs was pipetted into the Raman cell. The instrument stage was then calibrated by performing a spectral depth analysis on the sample. This calibration was done to evaluate the best stage position required to obtain consistent results. In order to increase the effective field of view, Raman spectra were recorded using the long distance 50x magnification lens with a spot diameter size of 800 nm to focus the laser with a wavelength of 785nm. For quantitative analytical experiments, the Raman spectrum depends on the instruments parameters, such as the laser power and exposure time. Therefore, these parameters were optimized to ensure that the best Raman spectra were obtained.

6.5.2 Optimizing the stage

Calibration of the Raman stage was performed to reach the optimum recording position. Using the top of the cell cover as the point of origin, depth analysis was carried out by an increment of 200μm until the laser focus was at the base of the cell (Figure 6.10)
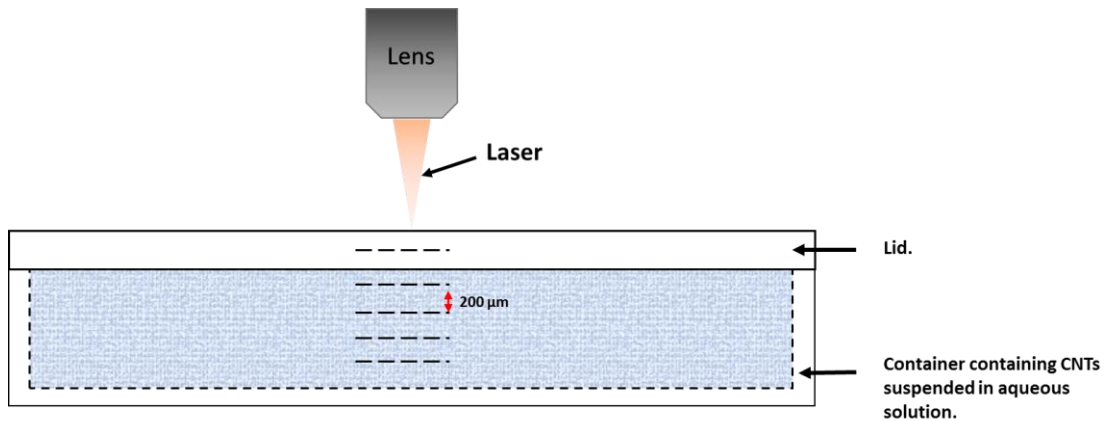
Figure 6.10: Schematic diagram highlighting the position changes of the laser. The dashed lines represent the new postion of the laser as it goes down the cell with a change of 200 μm between positions.

The results in Figure 6.12 show that the walls of the cell block the signals (the region between 0 – 1000 μm and 2000 – 3000 μm) where the signal is zero.
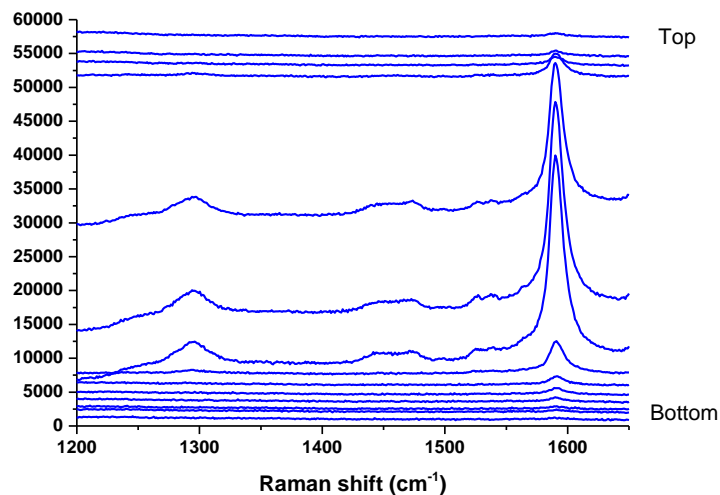
Figure 6.11: Depth acquisition analysis of the Raman cell with SWCNTs suspended in solution.
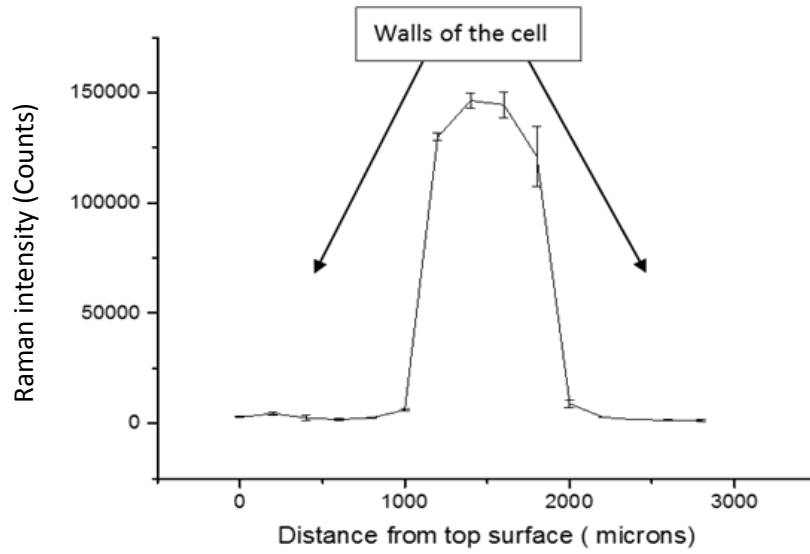
Figure 6.12: Depth acquisition analysis of solution containing suspended CNTs

Furthermore, Figure 6.13 shows the limited variation in Raman intensities within the cell (the region between 1000 μm – 2000 μm) which indicates that the CNTs are stable in solution, and Raman analysis could be conducted at any depth level within the cell with a low probability of sedimentation during analysis. However, the best position to get the highest signal is at the middle of the cell.
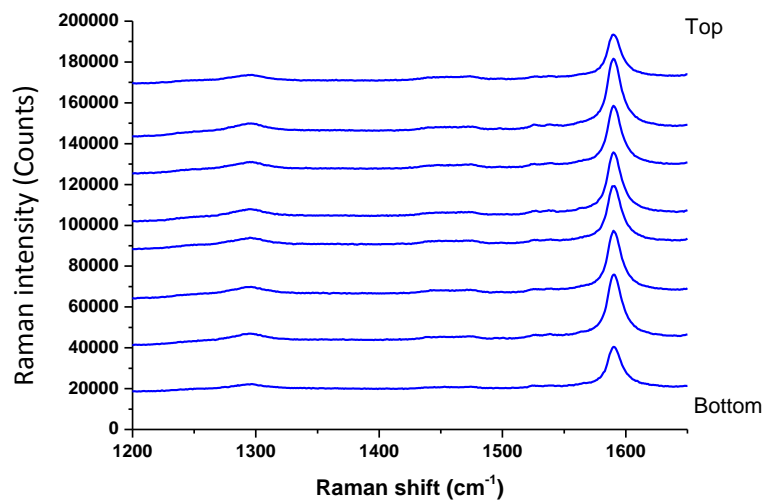
Figure 6.13: Depth acquisition analysis of SWCNTs suspended in solution within the Raman cell

6.5.3 Optimizing the laser power and exposure time

The influence of laser power and exposure time on CNTs was studied on MWCNT and SWCNT dispersions at a concentration of 10 mg/L. Figure 6.14 and Figure 6.15 present the effects of these Raman parameters on MWCNTs and CoMoCAT manufactured SWCNTs respectively. The purpose of doing these experiments is to establish the limits of the instrument settings which can be affected by the CNT properties and will give the reader the knowledge needed to determine what settings are appropriate for the type of particles. Furthermore, it will bring to light any effects of the settings on the particle properties, and also the effect of these settings on the accuracy and detection limit of the calibration graphs. The blank areas at a laser power of 5% and an exposure time of less than 20 seconds in Figure 6.14 represent the parameters that generates Raman signals too weak to detect the CNTs at the given concentration level. However, the blanks areas at a laser power of 50% and an exposure time of more than 10 seconds in Figure 6.15 represent the parameters setting that generates Raman signals that saturates the sensors of the instrument.
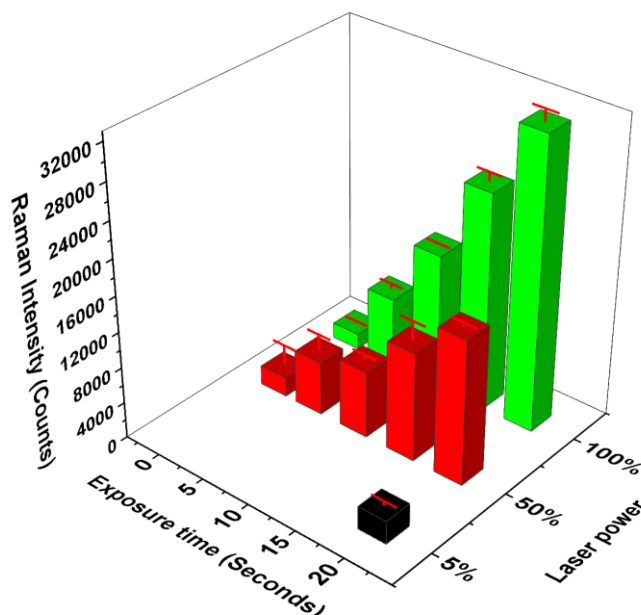
Figure 6.14: Effects of laser power and exposure time on Raman intensity emitted from MWCNTs
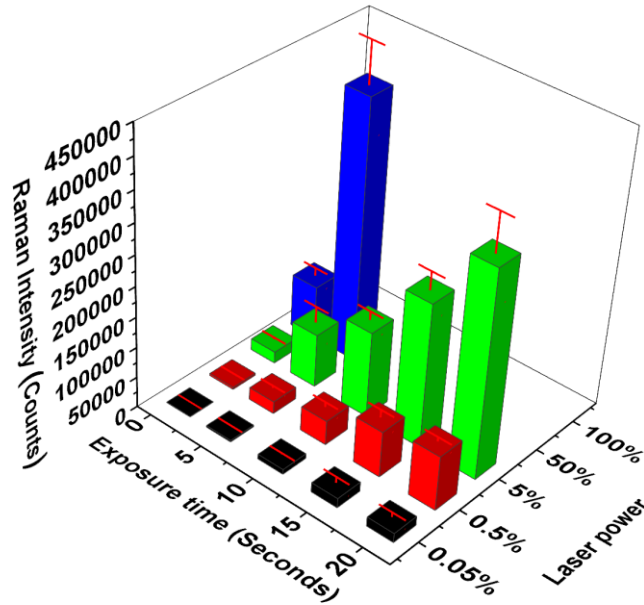
Figure 6.15: Effects of laser power and exposure time on Raman intensity emitted from CoMoCAT Manufactured SWCNTs

Figure 6.14 shows that for 10 mg/L of MWCNTs, the minimum exposure time required at a laser power set at 5% is 20 seconds. On the other hand, Figure 6.15 shows that for 10 mg/L of SWCNTs, less laser power and less exposure time is required to generate Raman intensities from the particles. However, for high exposure times and laser power, the Raman sensors become saturated for SWCNTs.

6.5.4 Effects of Raman laser power and exposure time on MWCNTs and SWCNTs properties.

For MWCNTs, increasing laser power, for a fixed exposure time of 20 seconds, proportionally increased the intensities of the peaks (Figure 6.16) and more importantly, there were no shifts in intensities and no significant changes in the ratio of the peaks (Figure 6.17), which indicates that an increase in laser power has no detrimental effect on CNTs. Influence of laser power has been described in literature as having little effect on CNTs dispersed in aqueous solution due to solutions acting as a 'heat sink' [189].

Y = 184x + 671

$R^2 = 0.9999$
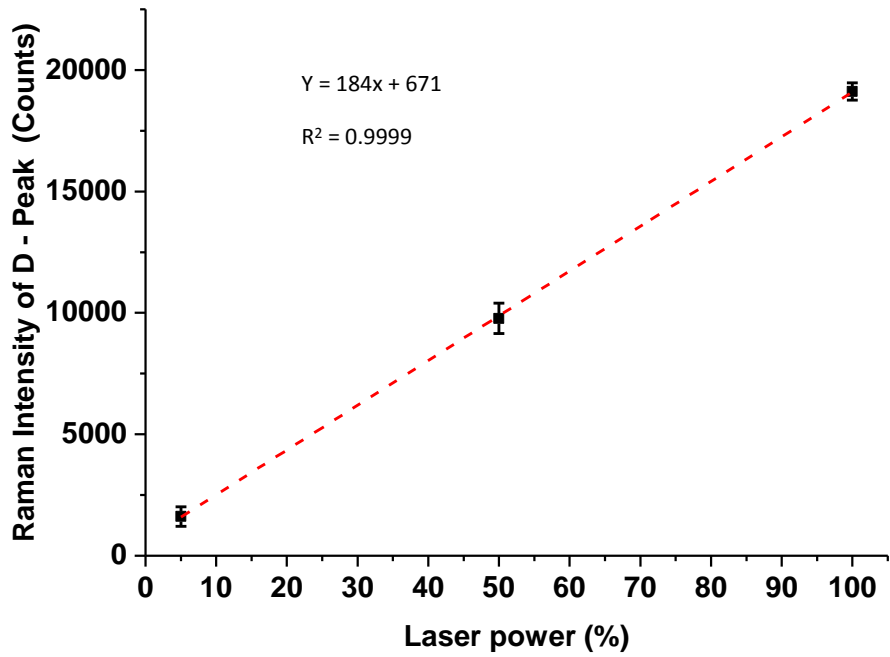
Figure 6.16: Effects of laser power on Raman intensity from MWCNTs at an exposure time of 20 seconds
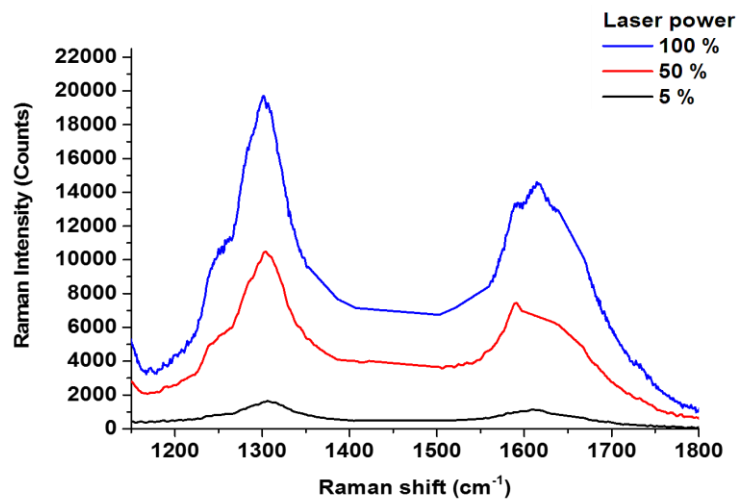
Figure 6.17: Effects of laser power on MWCNTs properties at an exposure time of 20 seconds.

For the MWCNTs, in order to get the optimum signal intensity, the maximum laser power was used with an exposure time of 40 seconds. An exposure time of over 40 seconds resulted in the G – peak becoming the dominant peak which is shown in Figure 6.18.
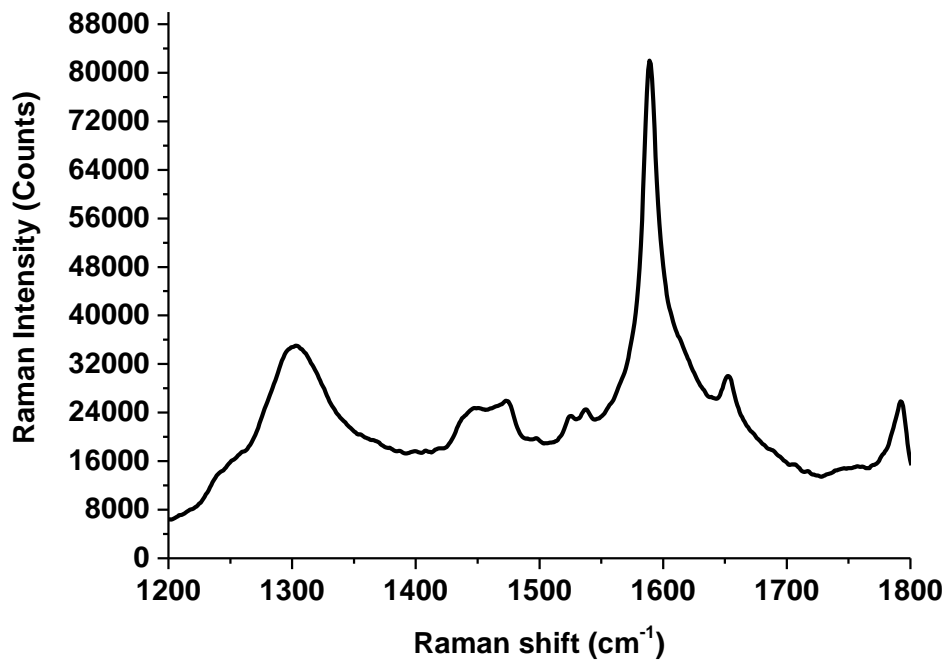
Figure 6.18: Raman spectrum of MWCNTs at 100% laser power and 50 seconds exposure time

For the SWCNTs, Figure 6.19 and Figure 6.20 show the effects of laser power on its properties and the Raman intensity emitted from the particles. As expected, increasing the laser power produces a stronger G peak (Figure 6.19). However, the linear proportionality between laser power and Raman intensity is not the same when compared to MWCNTs. Figure 6.20 shows laser power has little to no effect on SWCNT properties as the G peak does not shift with increased intensity. However, increasing the laser power to 50 % at an exposure time of 10 seconds and above resulted in the Raman sensors getting saturated with excessive intensity. As a result, 0.5% laser power was used to create the calibration curve for CoMoCAT manufactured SWCNTs.

$Y = 31015x + 7169$

$R^2 = 0.89429$
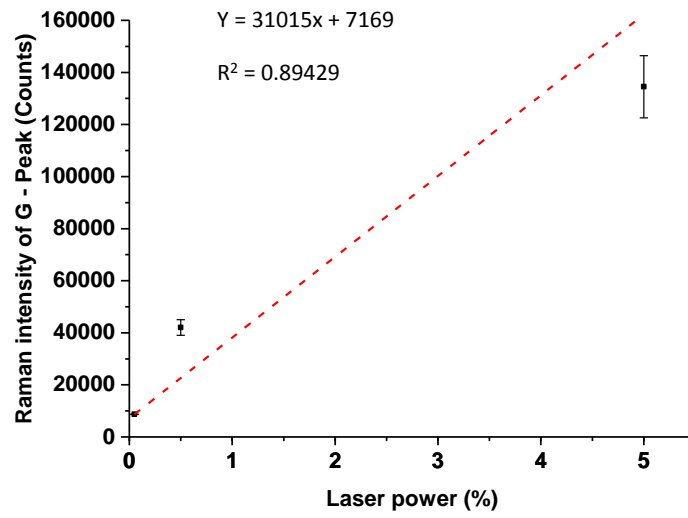
Figure 6.19: Effects of laser power on Raman intensity from SWCNTs at an exposure time of 10 seconds
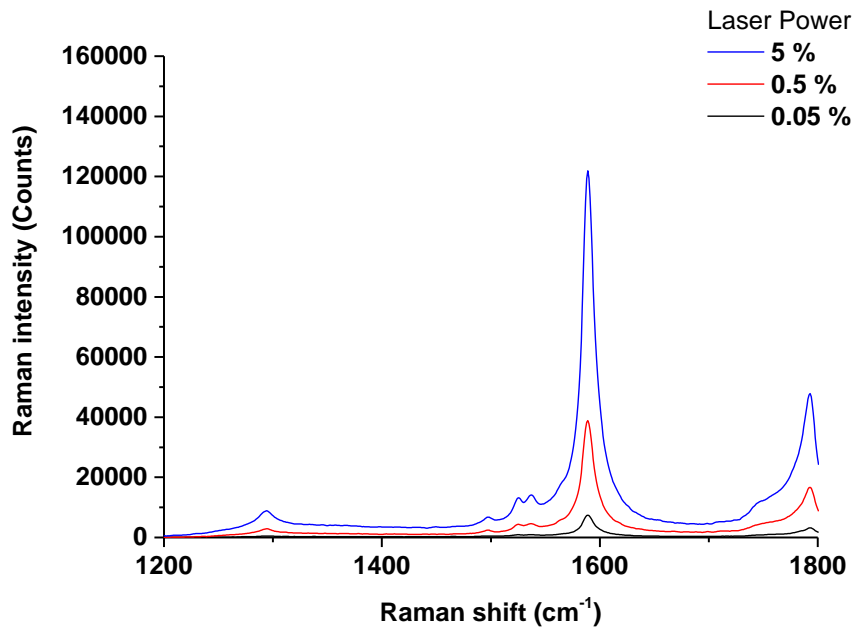
Figure 6.20: Effects of laser power on SWCNTs properties at an exposure time of 10 seconds.

6.5.5 Effect of expose time on the accuracy of Raman measurements for MWCNTs and SWCNTs.

With the laser power set to the appropriate output for the single and multi-wall of CNTs, the exposure time was incrementally adjusted from 1 seconds to 20 seconds. Increasing the exposure time had a similar effect on the D and G peaks of the CNTs as increasing laser power had. Furthermore, the lower the exposure time, the lower the error (Figure 6.21 and Figure 6.22).
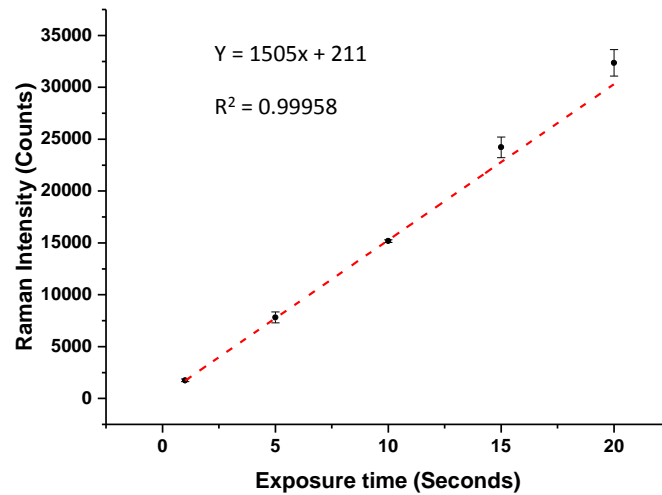
Figure 6.21: Effects of exposure time on the accuracy of Raman measurements of MWCNTs at 100% laser power.
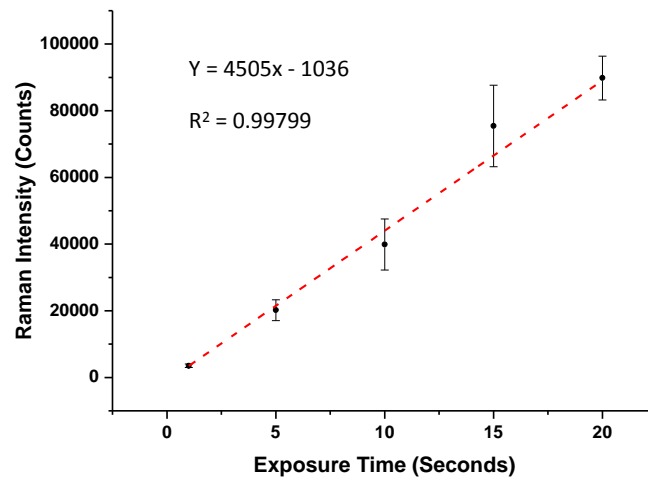
Figure 6.22: Effects of exposure time on the accuracy of Raman measurements of SWCNTs at 0.5 % laser power.

6.6   Calibration curves

The main calibration curves were determined for concentrations ranging from 0.5 to 10 mg/L. Each concentration level was analysed in triplicates, and sample measurements were taken at five random points in the quartz cell. Following this step, a detection limit was established for each type of CNTs.

6.6.1   Multi – wall carbon nanotubes

The maximum laser power with an exposure time of 40 seconds was used in order to get the most signal for the range of concentration. The response was linear (R^2 = 0.994) however, the precision varied along the range of concentrations tested (Figure 6.23). Furthermore, although the limit of detection of MWCNTs appears to be 0.5 mg/L, the error margin is higher when compared to SWCNTs as shown in Figure 5. This is due to the lower number of particles present in the solution coupled with the fact that the number of walls vary from one MWCNT to another. Studies have shown that the size of CNTs has an effect on the sensitivity of the intensities of D and G peaks [134, 136]. As a result, a wider variation of intensities was registered for the same concentration at different points in the cell. This results in the error margins overlapping at concentrations below 1 mg/L.

$Y = 26367x - 13941$

$R^2 = 0.99443$
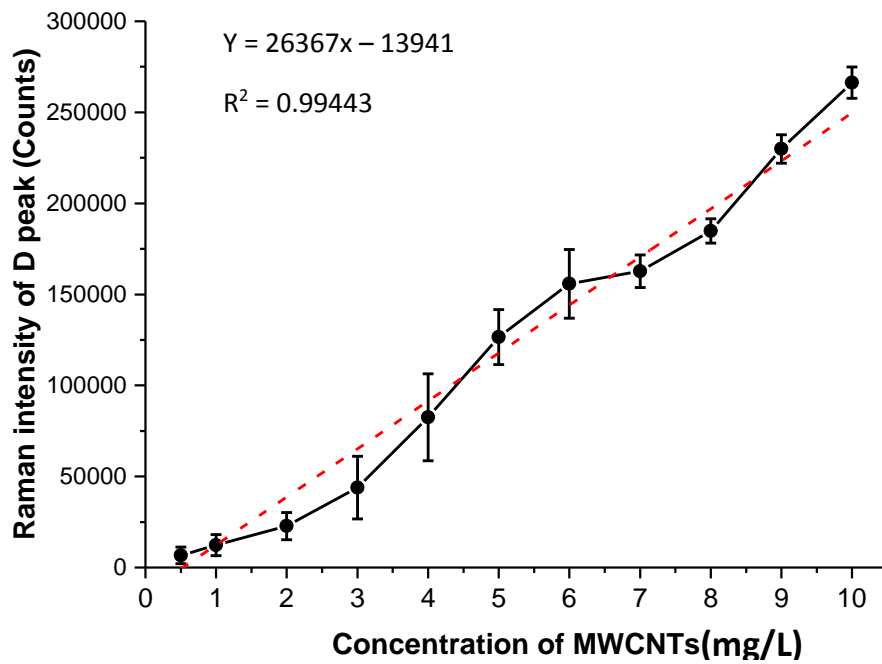
Figure 6.23: Calibration graph of MWCNTs

6.6.2 Single Wall Nanotubes and limit of detections

A calibration curve for CoMoCAT manufactured SWCNTs was determined using a range of 1 to 10 mg/L (Figure 6.24). The calibration graph created for SWCNTs had better quality when compared to MWCNTs. Figure 6.25 highlights an improved limit of detection achieved by adjusting the laser power and exposure time. The calibration graph does not go through the origin which might be due to instrumental noise and possible effects of CNT concentration on the Raman signal intensity. The higher the CNT concentration, the higher the likelihood for aggregates to occur which might affect the Raman signal intensity.
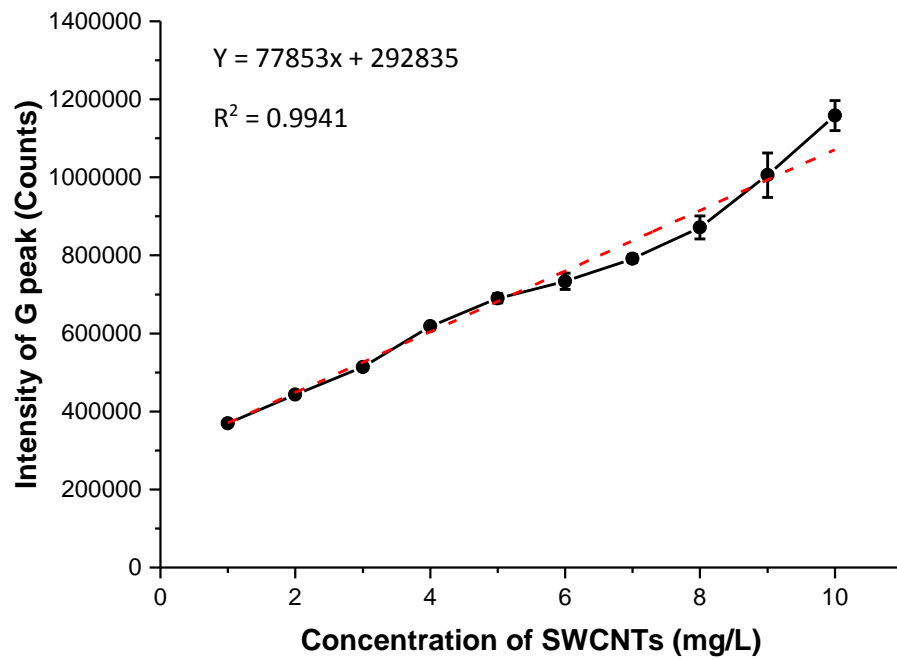
Figure 6.24: Calibration graph of CoMoCAT manufactured SWCNTs
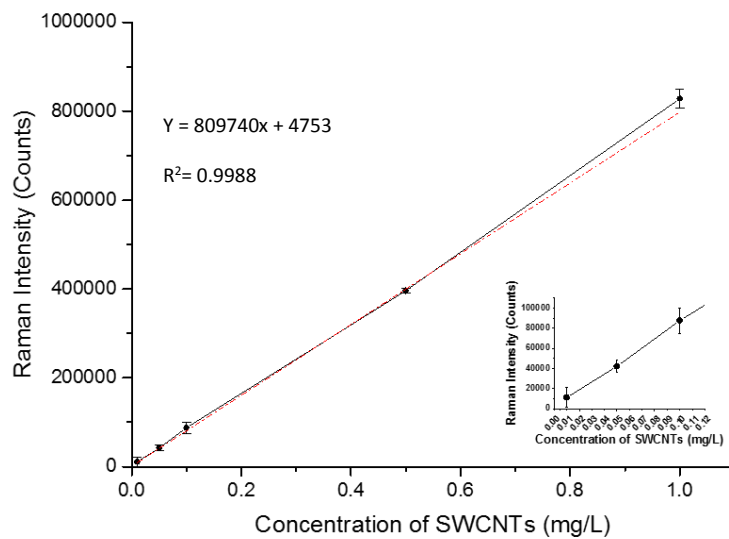
Figure 6.25: Calibration graph of low concentration SWCNTs

SWCNTs are known to produce exceptionally high G peak intensities due to laser energy being resonant with the electronic transition of metallic SWCNTs [190]. Therefore, the limit of detection (LoD) is significantly better when compared to

MWCNTs. The lower density of SWCNTs means that for a given mass, more SWCNTs than MWCNTS will be present in dispersion which will also contributes to the LoD.

For concentrations below 1 mg/L, the Raman parameters were adjusted in order to increase the intensities collected from the SWCNTs. As previously stated, the exposure time and laser power has no effect on CNTs suspended in aqueous solution. As a result, the exposure time and laser power were raised to 40 seconds and 100% respectively. Figure 6.25 shows that with appropriate Raman parameters SWCNTs can be quantitatively determined for concentration as low as 0.01 mg/L for CoMoCAT produced SWCNTs.

6.7   Quantification by inductively coupled plasma- mass spectroscopy

6.7.1   Single Walled Nanotubes

Concentrations ranging from 0.01 mg/L to 1 mg/L were analysed to establish the linear correlation of the metallic impurities found in the SWCNTs obtained from the EDS results, to the concentration of SWCNTs suspended in aqueous solution. Figure 6.26 shows a linear trend for the metallic impurities (Co and Mo) with increased SWCNT concentration.
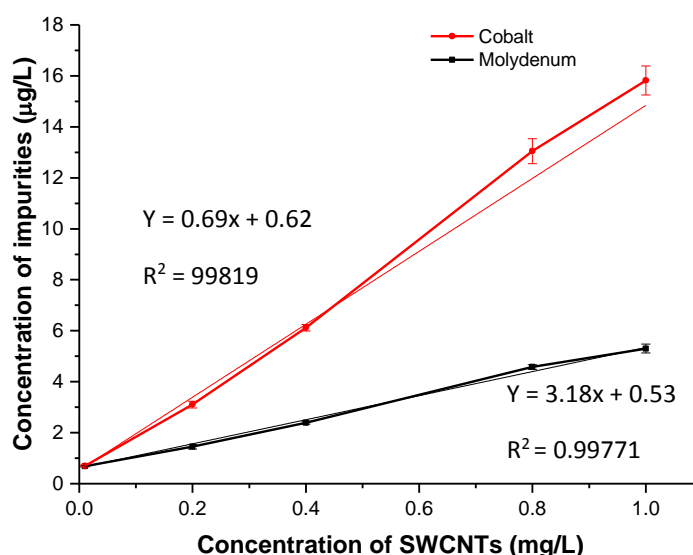
Figure 6.26: ICP analysis of SWCNTs showing molybdenum and cobalt concentration as function of SWCNT concentration.

6.7.2 Multi-Wall Carbon NanoTubes

For MWCNTs suspended in aqueous solution, low concentrations ranging from 0.1 mg/L to 2 mg/L were prepared for ICP analysis. Without digestion, Cobalt or Molybdenum were not detectable by ICP at these concentration levels, however Iron (Fe) was detectable. One reason for this could be that most of the Cobalt catalyst is located within the inner walls of the MWCNTs as reported in the TEM images (Figure 6.3), hence becoming undetectable by ICP-MS. Figure 6.27 shows a trend of iron impurities with respect to concentration of CNTs dispersed in solution. This shows that the Fe impurities might be located on the surface of the outer walls.
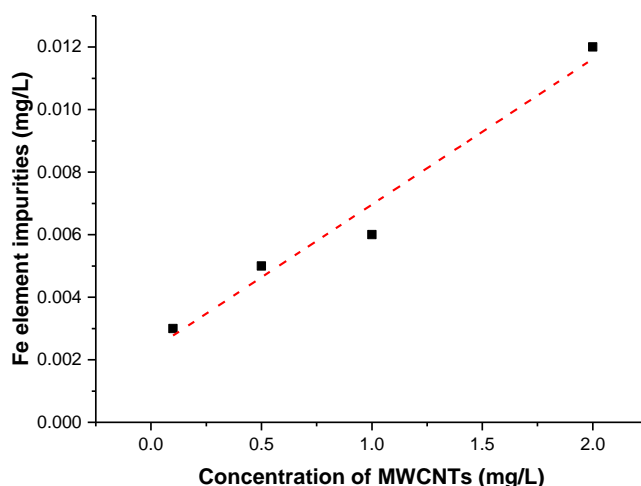
Figure 6.27: ICP analysis of MWCNTs

6.7.3 Digestion step

One way of unlocking the encapsulated metallic impurities is by performing an acid digestion pre-treatment. This procedure is needed due to the CNTs extremely stable structure [140]. This can then be back calculated to determine the concentration of CNTs suspended in the original aqueous solution. By performing this digestion step, it is possible to improve the detection limits of ICP analysis if the CNTs are fully digested and their metallic impurities analysed.

The first step is to digest a known amount of CNTs and to analyse the impurities found in order to determine the viability of the digestion step. Acid digestion processes (Methodology chapter section 4.3) were performed on three samples of 3

mg of dry MWCNTs, to see the percentage level of impurities in the particles. A full elemental scan was carried on these samples (Figure 6.28). The results show a variation of error margins based on amount of elemental impurities present in the acid digested solution and can be attributed to the varied incomplete digestion of MWCNTs in the digested solution. Undigested CNTs have trace elements "locked in", which account for the variation in the results shown. However, Co and Mo appear to have the lowest error and can be used to further quantification analysis. The same process was conducted with SWCNTs which are presented in Figure 6.29. Furthermore, the results from the digested SWCNTs provide further confirmation that Cobalt makes up a higher percentage when compared to Molybdenum. However, the error margin are relatively high which indicates that the SWCNTs were not fully digested.
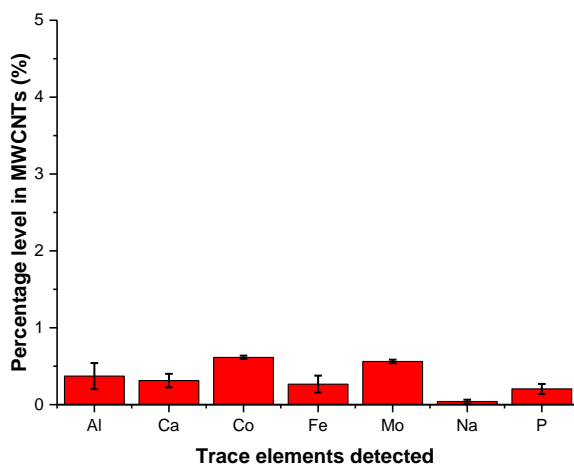
Figure 6.28: Digested MWCNTs results from ICP-MS analysis
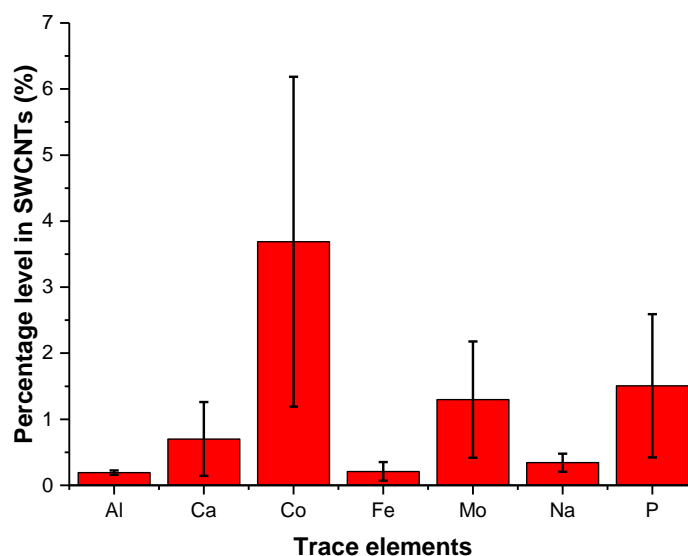
Figure 6.29: Digested SWCNTs results from ICP-MS analysis

6.8 The applicability of ICP and Raman spectroscopy for MWCNTs and SWCNTs suspension in aqueous solution

Figure 6.26, and Figure 6.27 show that ICP can be used to quantify CNTs in aqueous solution using the metallic catalyst as a tracer. However, analysing CNTs without digestion makes ICP measurements highly dependent on the dispersion of CNTs in aqueous solution. The main benefit of using Raman spectroscopy is its relative simplicity and one step procedure. This benefit allows for shorter processing time, and for SWCNTs, adjustments can easily be made to improve the limits of detection.

The chapter also demonstrated that various characteristic factors of CNTs can affect the Raman and ICP -MS quantification of different types of CNTs suspended in aqueous solution. The detection limit achieved for CoMoCAT manufactured SWCNTs using Raman, without performing a pre-concentration step, is 0.01 mg/L, which is better than previously reported to date. This is as a result of the size and surface charge of the particles, which will be further discussed in the discussion section. The calibration graph for the MWCNTs highlights the effects of its properties on the accuracy of Raman microscopy. Studies have shown that ICP-MS can be used to detect SWCNTs suspended in solution by pre-treating the SWCNTs, using acid digestion, before analysis. However, this work has shown that ICP-MS has the

potential to quantitatively determine concentration of both CNTs suspended in solution, with and without a digestion step. Due to its exceptional accuracy and sensitivity, ICP-MS can be used to detect concentrations, with appropriate sample preparation (complete digestion of CNTs), below what Raman is capable of.

6.9   Summary

This chapter presents the characterization of the CNTs used in this work which highlights the differences in MWCNTs and SWCNTs.

It presents a standardize procedure for quantification, by varying the Raman parameters needed for quantifying the CNTs in aqueous solution and checks to determine the effects of parameter changes to the CNTs properties.

The calibration graphs were created for the CNTs used in this project. These graphs highlight the detection limits and repeatability of Raman in quantifying CNTs in aqueous solutions for each type of CNTs and factors that will affect the technique.

In conclusion, this chapter shows that SWCNTs and MWCNTs can both be detected and quantified in aqueous solution using Raman microscopy and ICP which is necessary for monitoring CNTs concentration levels. Raman microscopy can be used for in situ monitoring of CNTs flowing in porous media due to its relative simplicity and one step procedure while ICP can be used for ex situ monitoring, where further sample preparation can be done to quantify the concentration level of CNTs in aqueous solution. From the calibration graphs, it is clear that SWCNTs produce a better analytical response for Raman analysis than MWCNTs. Hence, SWCNTs will be used for the remainder of this thesis in order to produce quality results.

Chapter 7.   Development of an integrated Raman microfluidic system for carbon nanotubes transport and adsorption experiments

7.1   Introduction

The main aim of the thesis is to study the transport and retention of carbon nanotubes in reservoirs, which is the main component of NAST1. As such, an integrated analytical system was developed to perform microfluidic experiments that simulate porous media (oil reservoirs).

The previous chapter has shown the suitability of Raman microscopy for detecting and quantifying CNTs suspended in aqueous solution. Literature has shown that combining Raman microscopy with microfluidics allows for the in-situ monitoring and analysis of a wide variety of particles in microfluidic systems.

This chapter focuses on the integration of Raman microscopy and a microfluidic flow cell system. A syringe pump is used as a fluid controlling feature, and also the methodologies used to process and interpret data obtained from the system are also presented. The microfluidic flow cell was chosen from a supplier with specifications that were compatible with Raman microscopy. Raman parameters (laser power and exposure time) were set to monitor CNT adsorption on APTES coated microchannel walls. Furthermore, a technique that can produce repeatable and semi – quantitative results was designed by using calibration graphs of CNTs mass flux within the microfluidic channel. A MATLAB program was written for data processing and OriginPro was used to plot the processed data in 3D graphs. Figure 7.1 highlights the work flow of the chapter.

Integration of Raman and flow cell set up	Setting appropiate Raman parameters	Data processing	Application of integrated technique
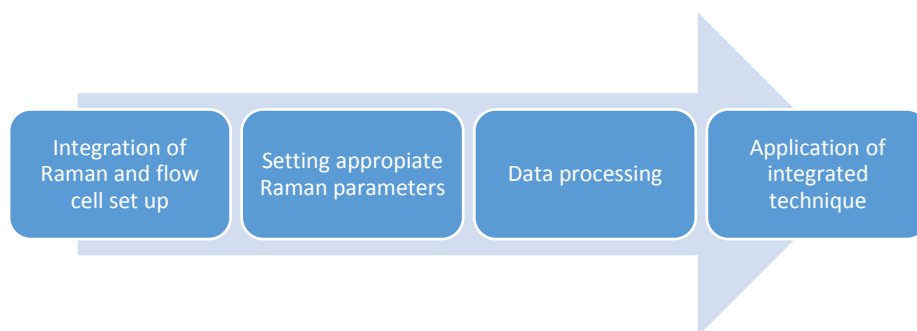
Figure 7.1: Steps of integrated Raman – Microfluidic integrated system

7.2   Set-up

The set up consists of an off-the-shelf microfluidic flow cell placed in a Raman microscopy instrument (insert of Figure 7.2). A 50 x magnification long distance lens was used to focus the 785 nm laser in the microchannel.
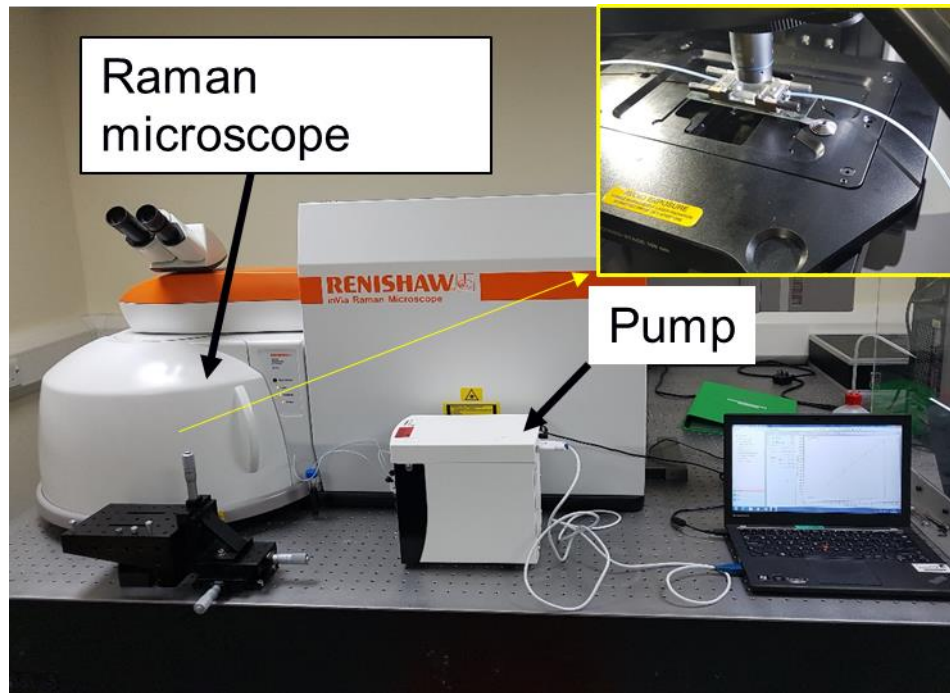
Figure 7.2: Raman microfluidic setup with inserted image showing the microfluidic flow cell under the microscope

7.2.1   Raman Parameters for system

As stated in the methodology section, Raman microscopy can collect spectra in two ways; single spot analysis and spot-to-spot mapping. Spot-to-spot mapping is used for analysis because it provides information about CNTs adsorption and transport in a given square area and volume of the microchannel. The previous chapter highlighted the effect of the electrical properties of SWCNTs on the Raman intensity peaks. These properties allow for a reduction in exposure time needed to obtain peak signals from SWCNTs. The spot map scan was set to scan an area of 200 by 200 µm in steps of 20 µm (shown in Figure 7.3). The radius of the each spot scan is roughly 2 µm. In order to reduce the scan time, the exposure time of the laser was set to 0.25 seconds and the laser power set at 100% which gives a scan time of 1minute 30 seconds.
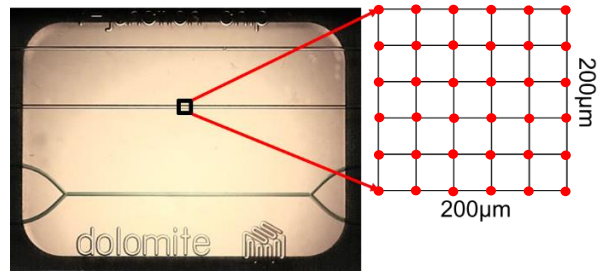
Figure 7.3: Schematic diagram of spot map scan showing grid system (the red spot represent the laser spot).

7.2.2 Laser adjustments

The 50x long distance magnification lens was chosen for the same reason as in Chapter 5. The laser was focused, using the objective lens, on the top flat side of the channel (Figure 7.4) to ensure the SWCNTs on the walls were detected.
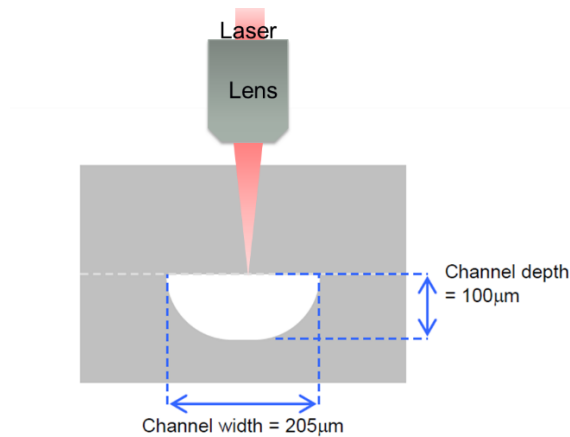
Figure 7.4: Schematic diagram of 785 nm laser focused by the 50x long distance lens

7.2.3 Data processing

Samples sometimes produce Raman spectra with varying degrees of fluorescence or thermal background. This results in the spectra having a sloping background (Figure 7.5), which may vary for different tests. These variations can have an effect on the repeatability of the results obtained. Baseline correction in Raman spectroscopy is an important step for data processing, used to remove fluorescence or thermal effects which will improve the accuracy and precision of intensity peaks obtained.
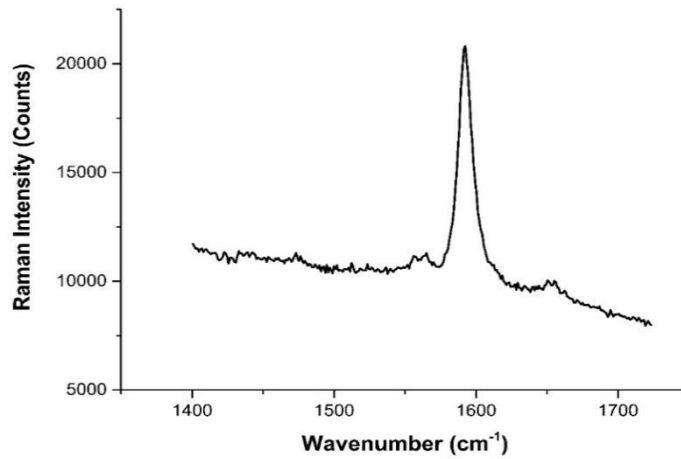
Figure 7.5: Raman spectrum showing G peak and sloping baseline due to background noise

The map scan produces a 4 dimensional dataset which consists of coordinates in the X and Y direction and a Raman scan, including wavenumber and intensity, at each coordinate point (Figure 7.6). The number of coordinate points for the map scan 165, which required selecting the dominant peak for each Raman scan for analysis. This can be time consuming, and as a result, a MATLAB program was written to speed up the process and ensure consistency.
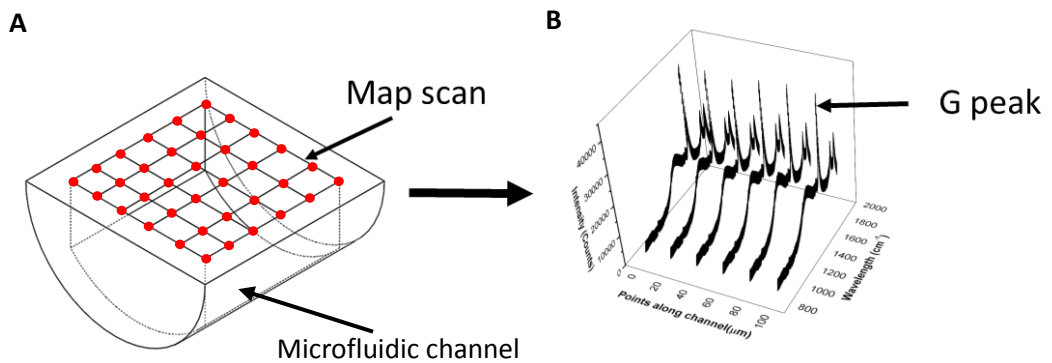
Figure 7.6: (A) The schematic diagram of the microfluidic channel illustrating the rasterised map scan on top (B) Illustrates the compilation of Raman spectrum graphs done using a MATLAB program which then uses the selected peak as the tracer for SWCNTs during the experiments.

7.2.4 MATLAB Program

The Raman spectra from the map scans were converted into text files and loaded on a MATLAB program (Figure 7.7). In order to ensure consistency and quality results, the program automated the baseline correction for each Raman spectrum. An iterative polynomial algorithm, created by Zhao [191], was used within the program. This algorithm takes into account the effects of noise level and peak contribution, thereby suppressing the undesirable artificial peaks that may occur in polynomial fittings. Appendix B contains the MATLAB code used for the data processing.
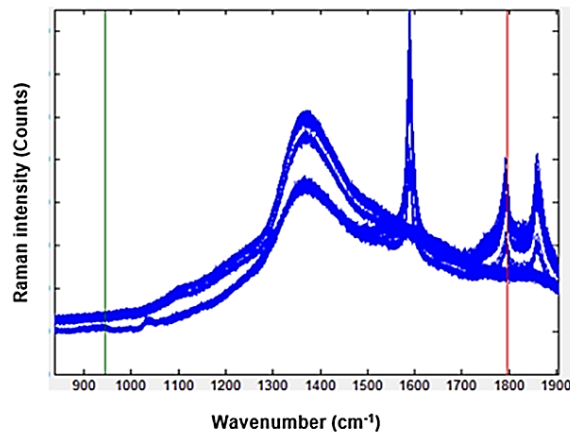
Figure 7.7: Raman spectrum before baseline correction

This algorithm performs the correction on every spectrum in the map scan, finding the optimum baseline for each one, an example is shown in Figure 7.8.
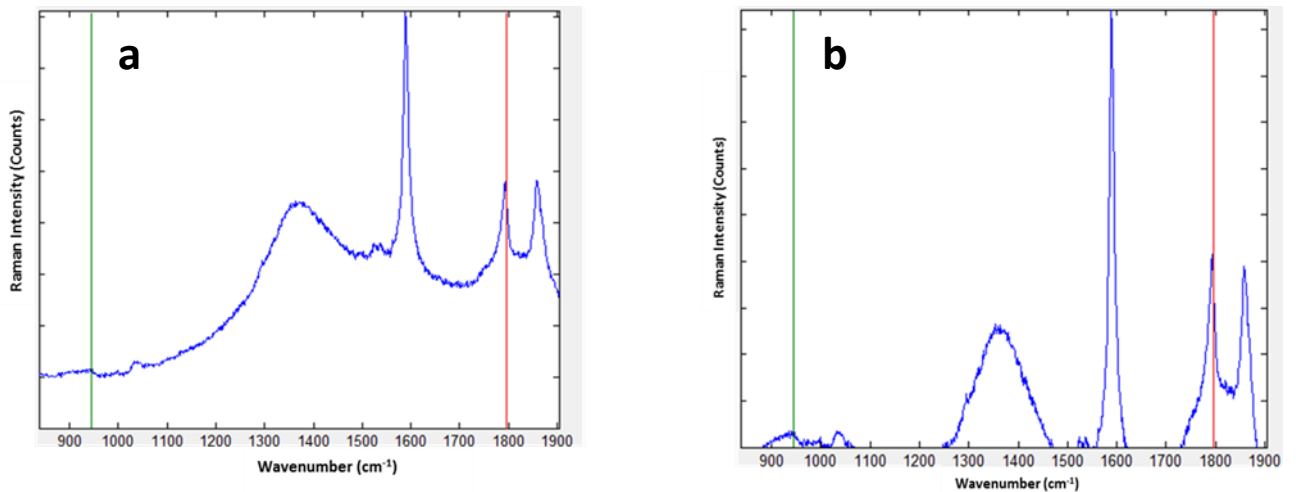
Figure 7.8: Raman spectrum (a) Before baseline correction (b) After baseline correction

In order to use the G peak as a tracker for SWCNTs, the program allows for a region on the spectra to be selected (Figure 7.9), and the highest peak within the chosen region is recorded as the selected Raman intensity. This point selection process is done automatically for all the spectra in the map scan area. These steps convert the 4 D dataset into a 3D dataset. These datasets are then plotted in OriginPro to produce Raman intensity graphs which represents the presence and location of SWCNTs in the microchannel.
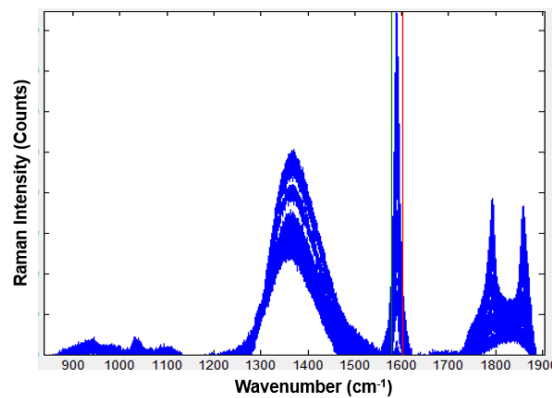
Figure 7.9: Raman spectra loaded on MATLAB program; the green and red lines indicate region selection. The program selects the maximum value in region for all Raman spectra in the matrix.

7.3   Graphical representation of map scan and data processing

Figure 7.10 shows the Raman intensities from a map scan on a 20 mg/L concentration of CNTs flowing at 0.05 ml/hr. It shows the increase in Raman intensity as the laser moves to the centre of the channel.
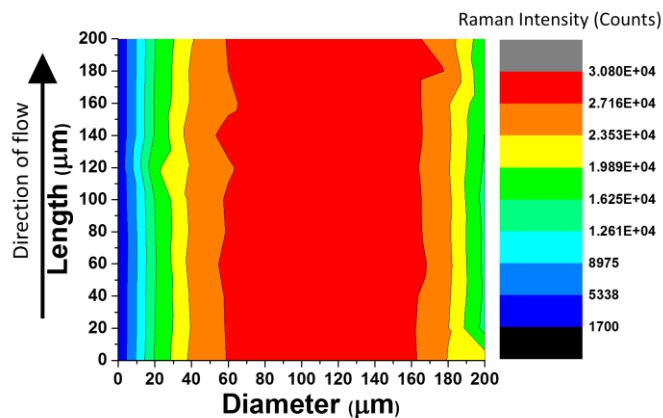
Figure 7.10: Variation in Raman intensities across the cross section of the channel

This feature is highlighted in Figure 7.11 which shows the similarity between the Raman intensity distribution and cross sectional shape of the microchannel.
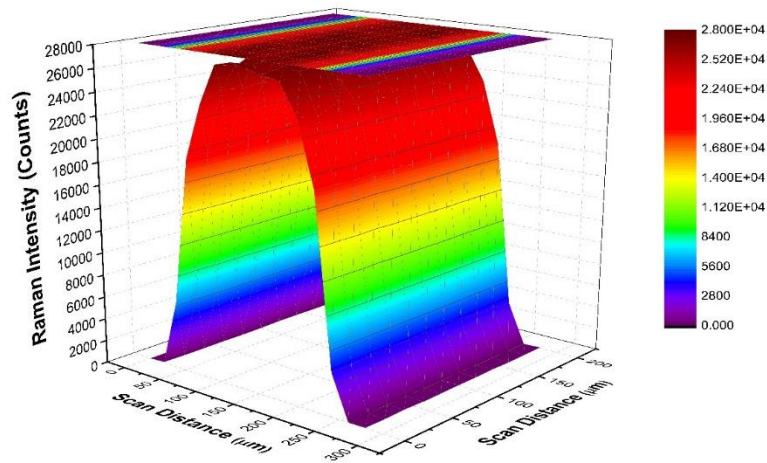
Figure 7.11: Variation of Raman intensity showing the shape of the cross sectional area of the channel.

7.3.1 Effect of Detection volume

The penetration depth and detection volume has been discussed in the literature review. The effects of these Raman properties are shown in Figure 7.10 and Figure 7.11. Figure 7.12 shows that even though the laser was focused on the top wall of the channel, the laser does detect particles suspended in the solution. Moving the laser across the channel affects the intensities generated due to the different channel depths along microfluidic channel (Figure 7.13). These graphs show that the laser detects the CNTs on the surrounding walls around the channel as well as the CNTs flowing in the solution.
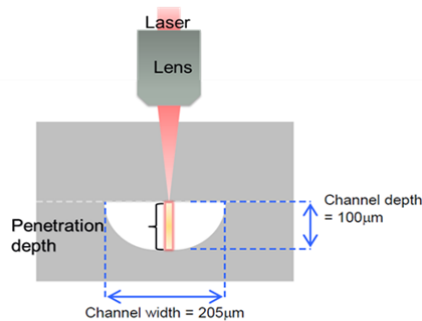
Figure 7.12: Cross-sectional schematic diagram showing penetration depth and detection volume of the laser within the channel .
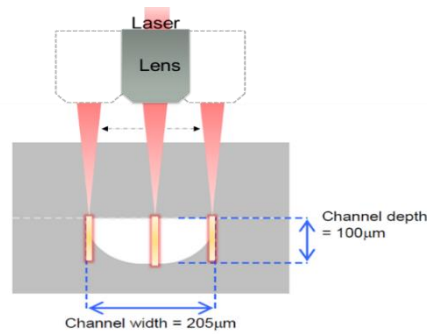
Figure 7.13: Variation of Raman intensity showing the shape of the cross sectional area of the channel.

This variation in Raman intensity across the map scan determined how the experimental results were interpreted.

7.4 Calibration curve

A calibration graph used to quantify the mass flux in the map scan area of the microchannel has been created and applied to the adsorption experiments. This calibration graph shows the viability of the technique by giving quantifiable data of the mass of CNTs adsorb on the channel walls.

Although there is already a calibration graph for CNTs suspended in aqueous solution (Chapter 6), a new graph is needed due to the size and shape of the channel which affects the Raman intensities received.

The experiments conducted show an increase in overall intensity at different time intervals, which indicates that the mass flux, or the amount of CNTs, has increased in the scan area as illustrated in Figure 7.14 .
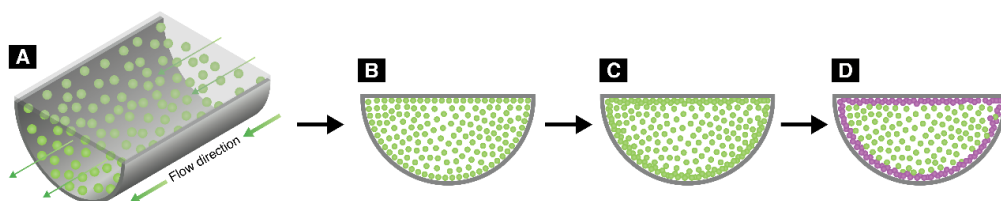
Figure 7.14(A) Schematic diagram illustrating mass flux of CNTs through the microchannel (B) Schematic diagram illustrating Concentration of CNTs at the start of the experiment (C) Schematic diagram illustrating Concentration of CNTs at a later time of the experiment. (D) Schematic diagram illustrating the adsorbed particles (red).

7.4.1 Creating the calibration graph

Concentrations ranging from 1 mg/L to 20 mg/L were injected through the straight line microchannel, and the corresponding intensities recorded. The flow rate used in the experiment was 20 ml/hr, and the walls were not functionalized to minimize particle adsorption. For each concentration, intensity map scans were taken twice and taken twice again after 20 minutes. Figure 7.15 shows the two calibration curves at time 0 minute and 20 minutes respectively which confirms that there was minimum adsorption (the intensity remained constant). One of the calibration graphs will be applied to the results obtained from the adsorption experiments.
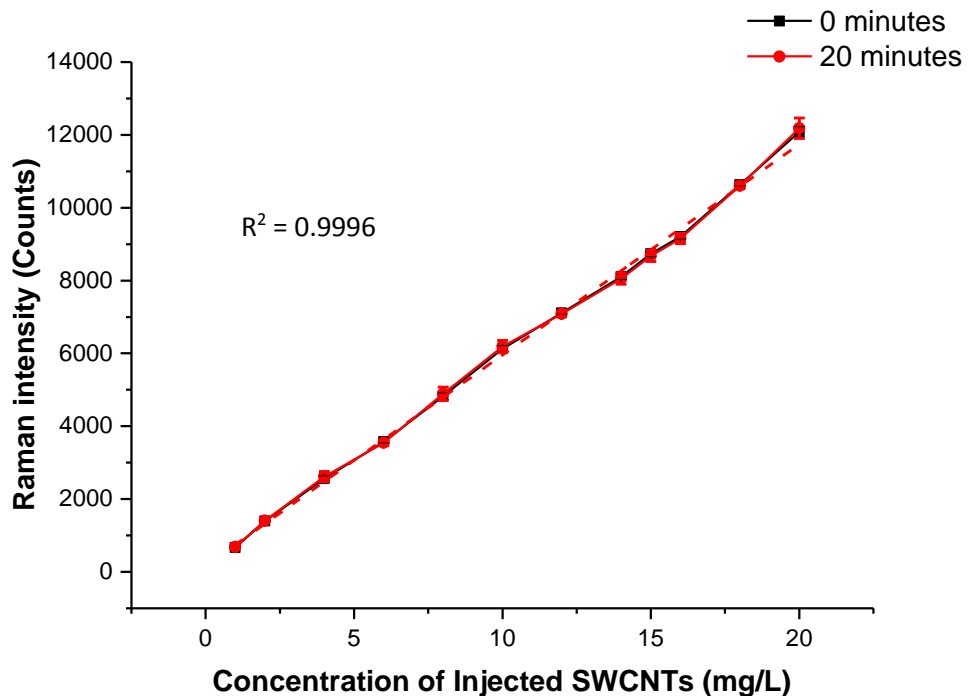
Figure 7.15: Calibration graph for Raman microfluidic system

7.4.2 Estimating the mass of CNTs adsorbed on the surface

Hand calculations used to estimate the mass flux of CNTs are based on the volume of liquid in the channel (in Litres) within the map scan area and the concentration of CNTs flowing through the channel (mg/L). All hand calculations are included in Appendix A. The graph below is the result of the calculations for each concentration used. As expected, there is a linear relationship between Raman intensity obtained from the calibration graph and the mass of CNTs (Figure 7.16).
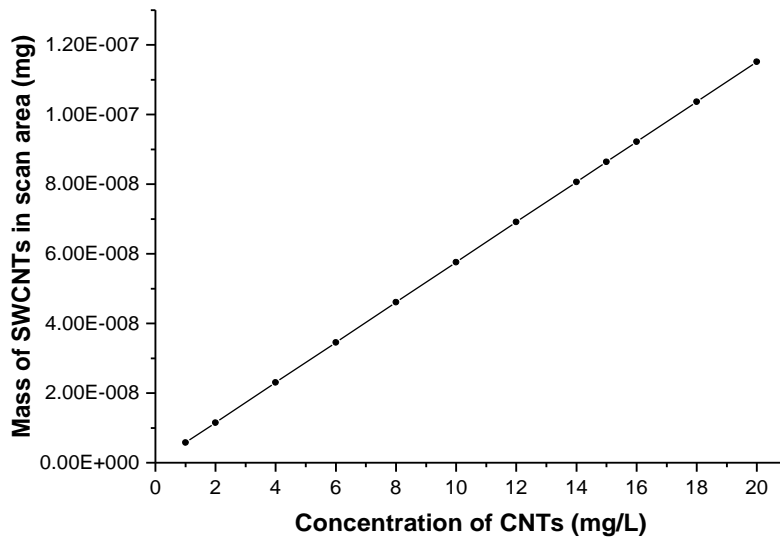
Figure 7.16: Graph showing calculated mass of CNTs in scan area from different concentrations of CNTs injected into microchannel.

It is now possible to link the Raman intensities used in the calibration graph (Figure 7.15) with the mass of CNTs flowing through the channels at a given concentration (Figure 7.16). Figure 7.17 shows the linear relationship between the Raman intensity generated and mass of CNTs within the map scan area.
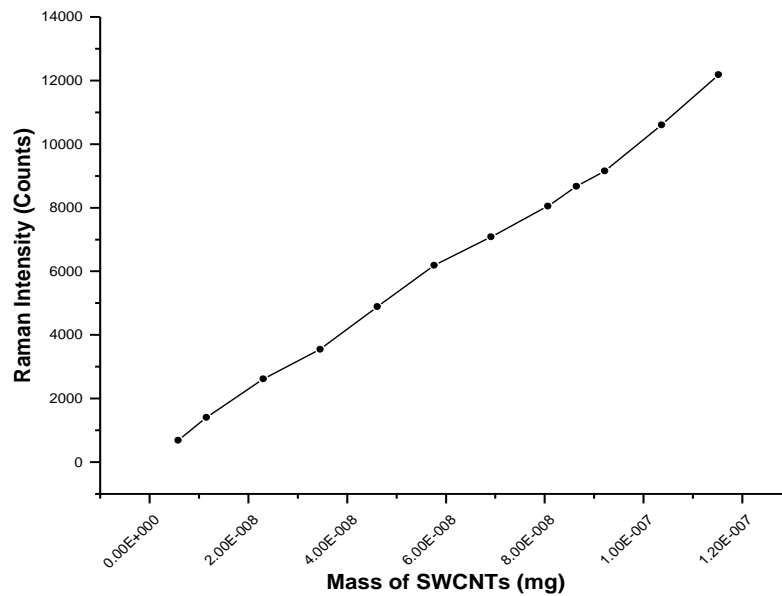
Figure 7.17: Graph showing the linear relationship between Raman intensity and mass of CNTs flowing through the channel.

7.4.3 Application of the graphs

This section will show the application of the procedure developed. Using the data from the experiments done for 10 mg/L of CNTs flowing through a microchannel functionalized with 3-aminopropyltriethoxysilane at a flowrate of 50 μL/h, Figure 7.18 shows the detected changes in Raman intensity over time.
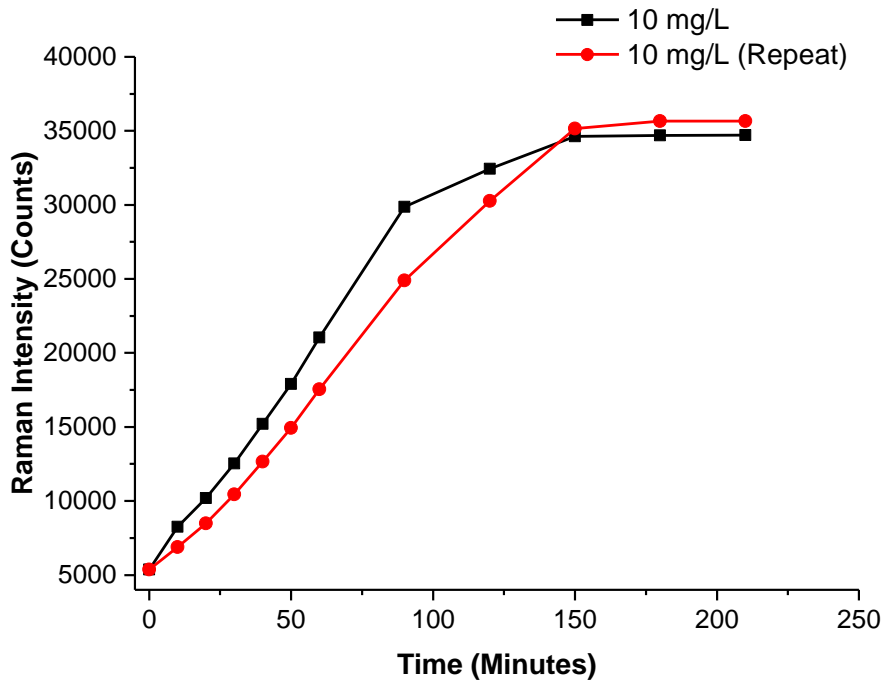
Figure 7.18: Changes in intensity over time during injection of 10 mg/L concentration of CNTs

Although the initial adsorption rate of SWCNTs show a different trend, the maximum points are similar. This shows that the overall rate of adsorption is approximately the same. The Raman intensities in Figure 7.19 are converted to concentrations of CNTs using the calibration graph, which increases over time (Figure 7.20).
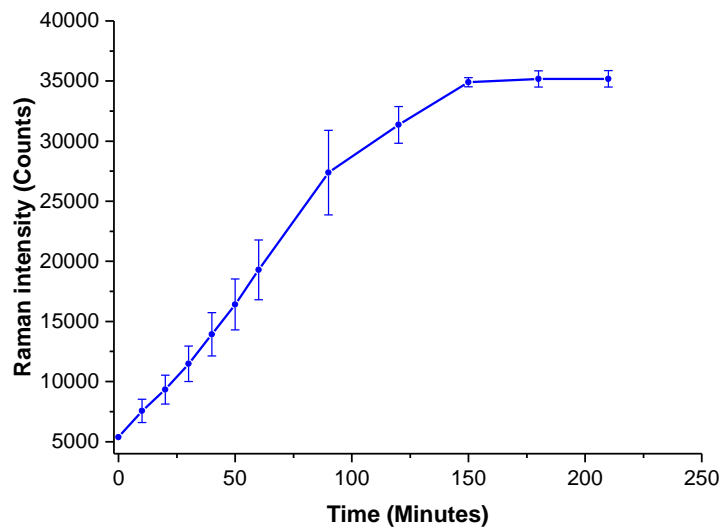
Figure 7.19: Changes in concentrations over time during injection of 10 mg/L concentration of CNTs
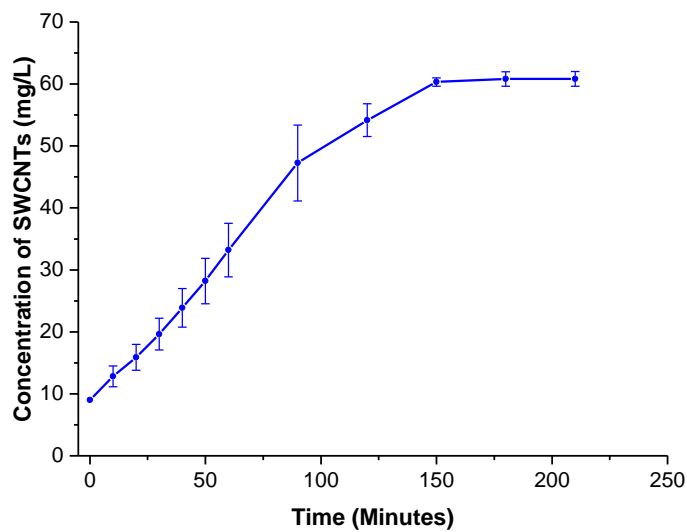
Figure 7.20: Graph showing concentration of CNTs detected in scan area over time

Finally, the data from Figure 7.20 is converted to mass of CNTs detected in scan area over time (Figure 7.21). The intensity at the start of the experiment represents the CNTs moving in the bulk, with minimal amount on the surface. Hence, in order to get the mass adsorbed at each time interval, this intensity is subtracted from intensities obtained at later periods. The results are shown in Figure 7.22. From the graph, it can

be seen that the maximum mass of CNTs adsorbed on the surface occurred at 150 minutes.
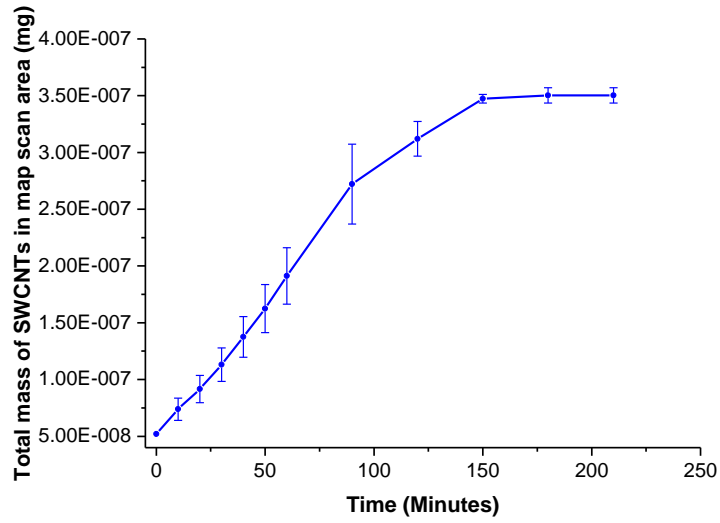
Figure 7.21: Graph showing mass adsorbed over time of experiment
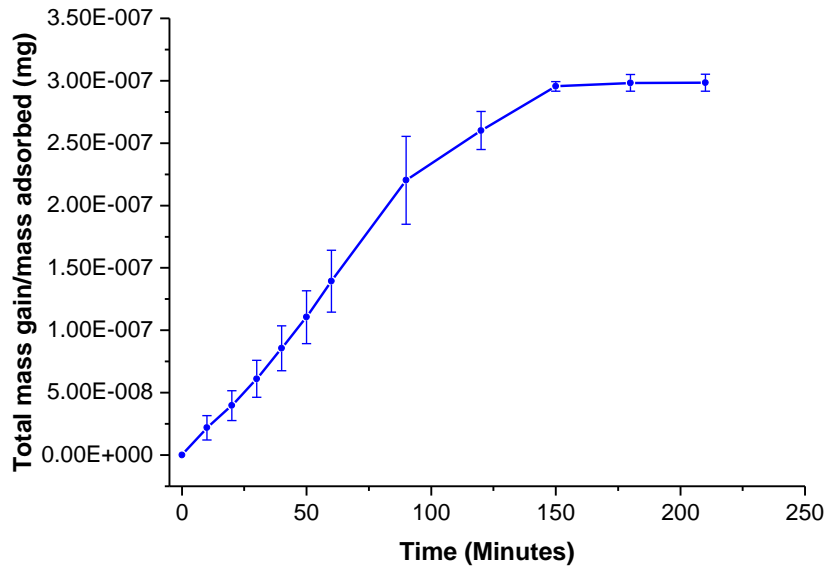
Figure 7.22: Mass gain over time in microchannel

7.5 Effect of map scan area

To ensure the repeatability of the procedure as well as assessing the suitability of the procedure, the effect of map scan area is assessed. As previously stated, the Raman intensities collected from the system includes the SWCNTs suspended in the bulk as well as on the microchannel walls. The intensity results obtained from the microchannel depends on the size and position of the map scan area (Figure 7.23). This is due to the shape of the microchannel which is explained in section 6.4 (Figure 7.13) and the corresponding volume of liquid within the map scan area.
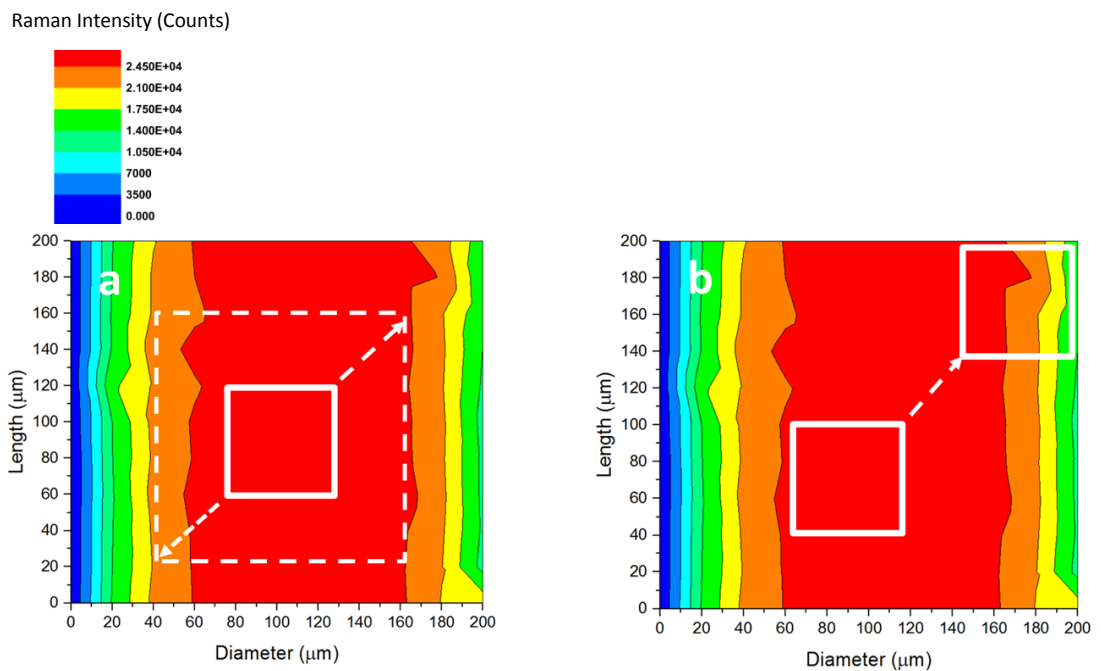
Figure 7.23: Effects of map scan (a) illustrates the enlarged scan (dash lines) (b) illustrates change in position

Results from experiments show that SWCNTs adsorption is not uniform (Figure 7.24). This has an effect on the accuracy of the results from the map scan. As a result, an understanding of how the size and position of map scan affects the accuracy of results is vital.
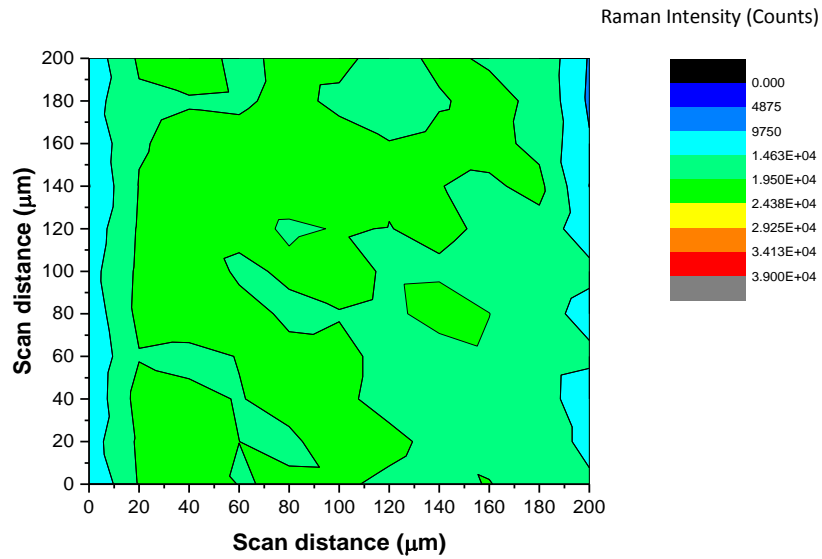
Figure 7.24: Map scan from an adsorption experiment at a specific time interval.

Due to these changes in map scans, the volume of the scan area changes. Hence, to accurately measure the mass of CNTs adsorbed on the walls, new calibration graphs were created that correspond to the new map scans.

7.5.1   Calculating the volume within the map scan area

The shape of the microchannel requires some calculations in order to obtain the volumes for each map scan size and position (Figure 7.25). The volume of the channel can be measured using the map scan coordinate direction, X direction represents the distance across the diameter of the channel.
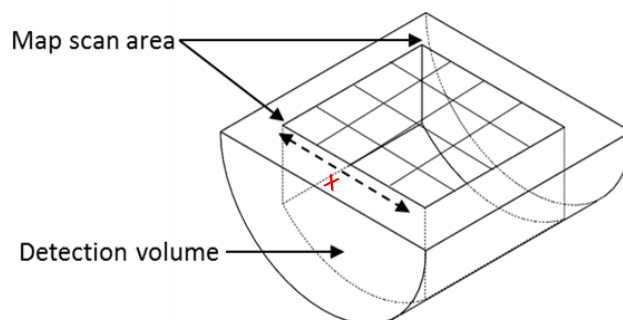
Figure 7.25: Schematic diagram showing map scan area with corresponding volume, the dashed arrow represents the cross sectional scan direction (x) used in the integral function.

The cross sectional shape of the microchannel is a semi – circle (Figure 7.25), is described in algebraic form as:

$$y = \sqrt{r^2 - x^2}$$ **Equation 6.1**

Where r is the radius of the semi-circle and x and y represents the Cartesian coordinates with the centre of semi-circle at the origin (0, 0). The integral of this equation is the area of the semi-circle (Equation 6.2), where x represents the boundary of scan area in the x direction.

$$\frac{\pi r^2}{2} = \int_{-x}^{x} \sqrt{r^2 - x^2}$$ **Equation 6.2**

From the results obtained, the volumes of different scan areas are calculated. From these values, new calibration graphs for each map scans were created, and the corresponding mass of SWCNTs were calculated.

7.5.2 Effects of Map scan size

The initial map scan covered an area the span of the channel diameter (200 μm) and a length of 200 μm along the channel with results shown in Figure 7.22. Different map scan sizes were assessed to see its effect on the repeatability of the procedure. Two map scan sizes were selected for comparison. The map scans have the same length along the channel (200 μm) but have shorter lengths across the diameter of the channel. Figure 7.26 shows a map scan area, with the shorter length located between scan distance 60 and 160 μm and the results are shown in Figure 7.27.
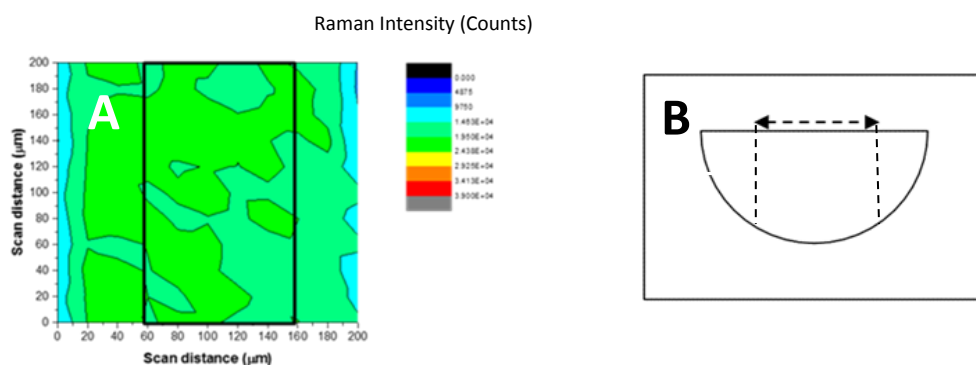
Figure 7.26: (A) Entire map scan with highlighted area used in plotting graphs (B) Schematic diagram shows the detection volume (dashed lines) as a result of the map scan.
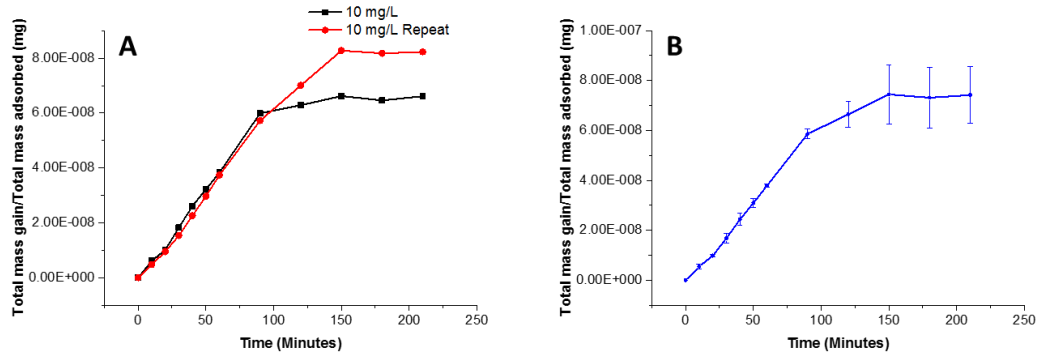
Figure 7.27: (A) Adsorption rates of two 10 mg/L experiments (B) Average adsorption rate highlighting variation of error margins.

Figure 7.27 shows the adsorption rate is roughly the same, however, the differences in the amounts of SWCNTs adsorption at equilibrium between repeat experiments are relatively greater than the results shown from the full scan. Similar results are seen for a narrower scan shown in Figure 7.28 and Figure 7.29.

Raman Intensity (Counts)
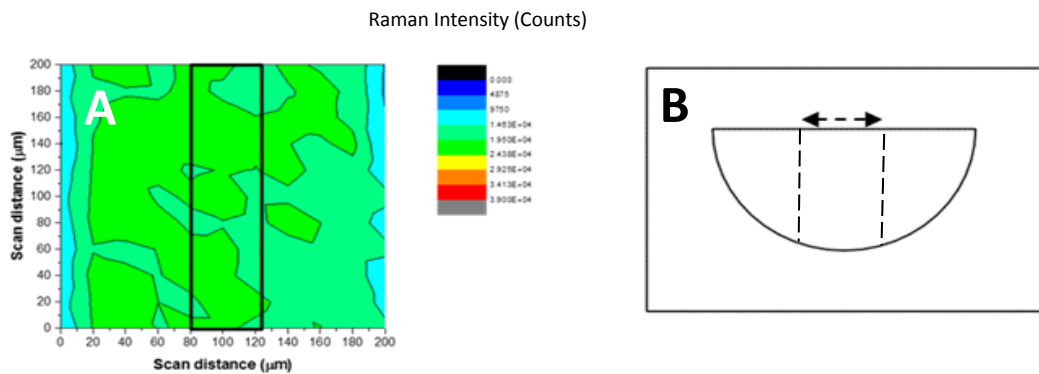
Figure 7.28: (A) Entire map scan with highlighted area used in plotting graphs (B) Schematic diagram shows the detection volume (dashed lines) as a result of the map scan.
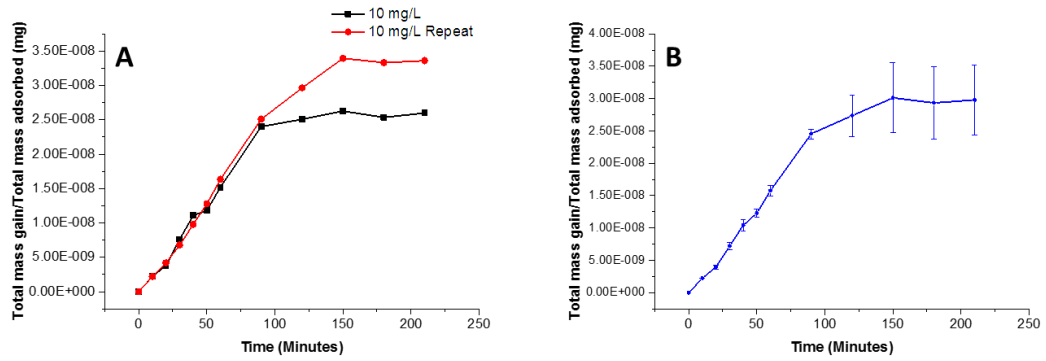
Figure 7.29: (A) Adsorption rates of two 10 mg/L experiments (B) Average adsorption rate highlighting variation of error margins.

Figure 7.30 shows the combination of all scan area plotted as a ratio of the mass of adsorbed CNT to the surface area coverage (q_t) and time, which highlights the effects of scan area on error margins. The graph shows that the narrower the scan area, with respect to the cross sectional diameter of the channel, the smaller the errors at the section where adsorption is taking place (between 0 minutes and 120 minutes). However, the error margins after 120 minutes is the reverse for the smaller map sizes. The graph shows that the ratio of adsorbed CNTs to surface area is more for the full scan than the smaller map scans.
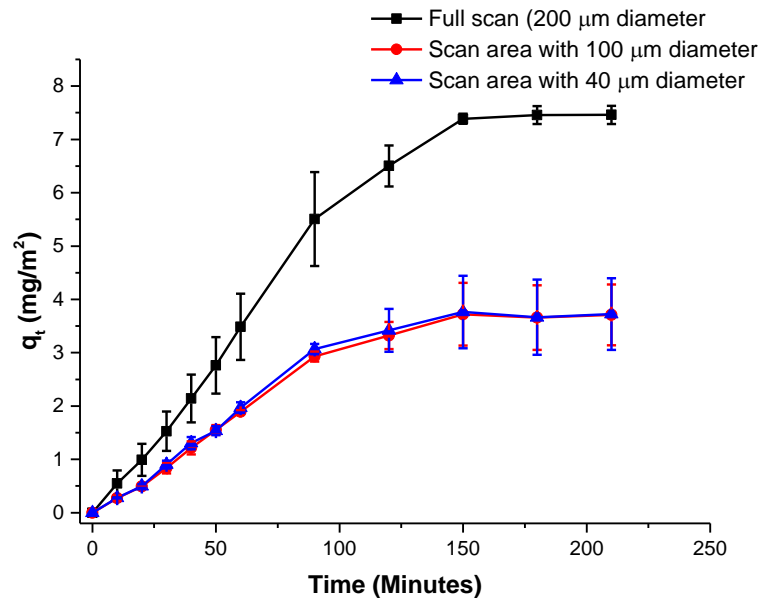
Figure 7.30: Effects of scan area on error margins

This could be as a result of the edges of the channel trapping CNTs. The next section will investigate the effects the corners have on the repeatability of the technique.

7.5.3 Effects of map scan position

The position of the map scan will cause a variation in results due to the shape of the channel under the scan area (Figure 7.31B). The graphs in Figure 7.32 highlight these differences. Furthermore, when compared to the other map scans, it show the opposite trends (Figure 7.32). The repeat experiment has lower values than the original which is the reverse in other scans. The error margins in Figure 7.32B show the effect of map scan position on the repeatability of the procedure.

Raman Intensity (Counts)
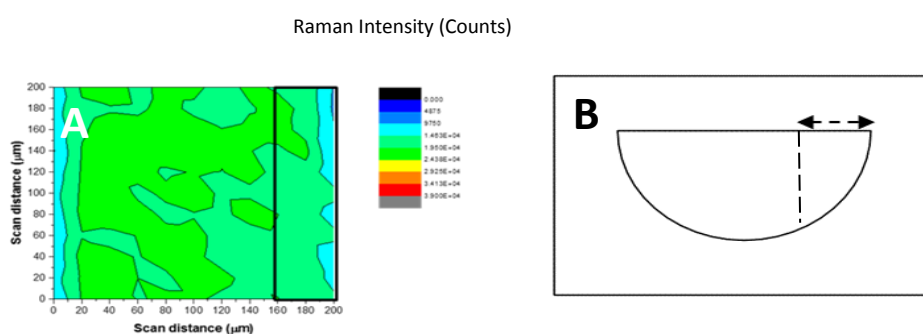
Figure 7.31: (A) Entire map scan with highlighted area used in plotting graphs (B) Schematic diagram shows the detection volume (dashed lines) as a result of the map scan.
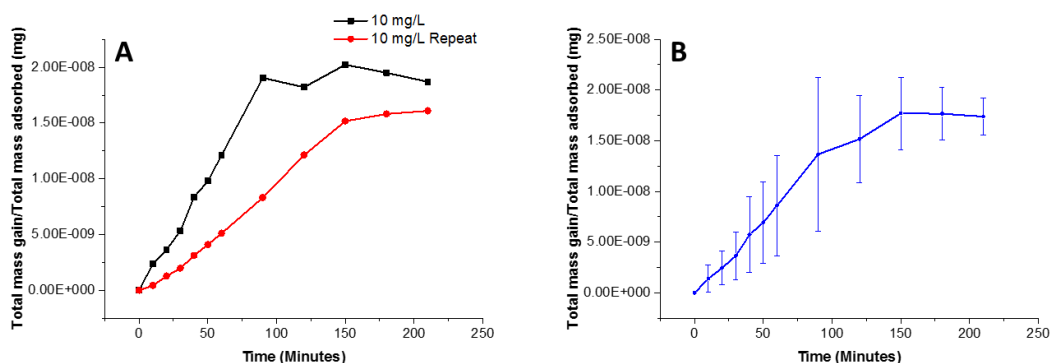
Figure 7.32: (A) Adsorption rates of two 10 mg/L experiments (B) Average adsorption rate highlighting variation of error margins.

The results from the map scans of difference sizes and positions shows the main effect on the repeatability of the procedure comes from the position of the map scan. This is as a result of the corners (Figure 7.31 and Figure 7.32) of the microchannels affecting the transport and adsorption of CNTs. The size of the channels does not

appear to have an effect on the repeatability of the procedure, as long as the position of the map scan is located at the centre of the channel and does not include the edges of the channel. However, it appears that for the full scan, the error is minimised when the adsorption is at equilibrium. For the rest of this study, the full scan results were used.

7.6   Application of the integrated system

As previously stated, this technique was developed to study the adsorption kinetics of SWCNTs in porous media needed to provide further insight into NAST 1. Hence, this section will showcase an application of the system to determine the optimum concentration of SWCNTs suspended in aqueous solution needed for NAST1.

7.6.1   Effects of CNT concentration on adsorption kinetics of CNTs on APTES coated glass

One important aspect of the NAST1 process worth investigating is the concentration of CNTs being injected into the reservoir and its effect of the adsorption kinetics of the CNTs. Therefore, a range of suspended SWCNTs concentrations in aqueous solution were tested.

The flow rate used for all the experiments was 50 µL/hr, at room temperature, at a pH of 7 and the walls of the microchannel was silanised using APTES. Different masses of CNTs were dispersed in a given volume of aqueous solutions of water and Tween 80 and injected into the microchannel. Figure 7.33 shows the adsorption rate of different concentrations of SWCNTs flowing through the microchannel. It can be seen that the rate of adsorption is roughly the same for concentrations ranging from 5 – 15 mg/L and the maximum amount adsorbed increased with an increase in concentration of SWCNTs. However, for concentration over 10 mg/L, the maximum amount adsorbed begins to drop. Furthermore, for 20 mg/L of SWCNTs, the adsorption rate also drops. This could be due to higher aggregation of CNTs at higher concentrations of CNTs affecting the adsorption process. This will be investigated further in the discussion chapter.
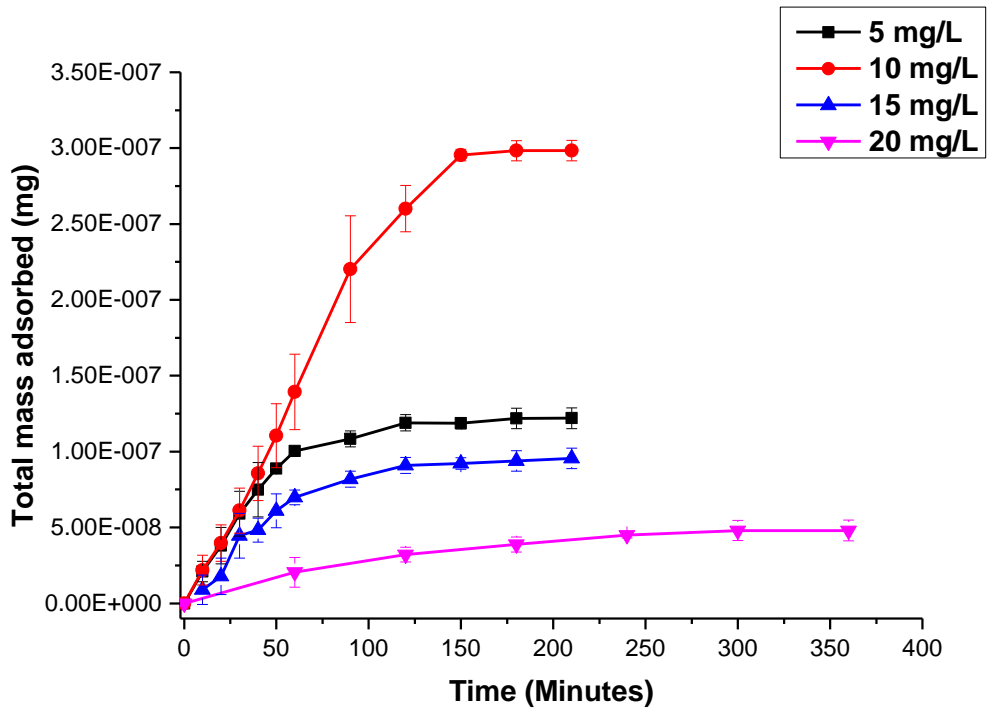
Figure 7.33: Adsorption rate and maximum mass adsorbed on the microchannel walls over time for different concentration of SWCNTs suspended in aqueous solution

7.6.1.1 Mass gained after post flush

Following the 20 mg/L adsorption experiment, the microfluidic channel is flushed with water at a high flow rate of 10 mL/h. A map scan was performed and the results is shown in Figure 7.34.
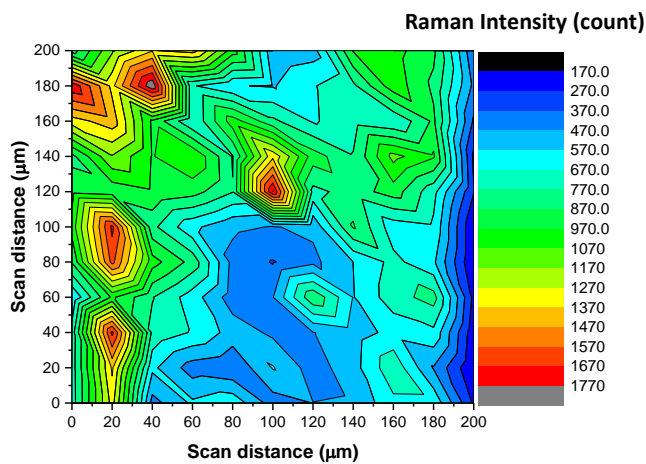
Figure 7.34: Map scan showing distribution of CNTs on the surface after post flush at high flow rate.

It can be seen that there is some CNT adsorbed on the surface even with though the channel was flushed at a high flow rate. Using the calibration graphs, the mass of CNTs left in the channel is calculated to be 6.14e-9 mg. This shows the effectiveness of the APTES covered surface in retaining CNTs even at high flow rates.

7.6.2   Effects of pH on adsorption kinetics of CNTs on APTES coated glass

Equally important is the effect of pH on the adsorption kinetics of SWCNTs in microfluidic systems due to the varying pH levels within the reservoirs which will have an effect on adsorption kinetics of CNTs.

The experimental conditions for these experiments were the same as the previous section. The concentration of the CNTs injected was 20 mg/L. The CNTs were dispersed in a tween 80 and water solution at a pH level of 4 and 10. Figure 7.35 shows the effect of pH level on the adsorption of SWCNTs in microfluidic channels. It appears that for a low pH level, the adsorption capacity of the APTES coated wall surfaces increased. However, at high pH level, the adsorption capacity is nearly non-existent, albeit an initial adsorption rate. This could be as a result of the effect pH has on the zeta potential of CNTs shown in Figure 7.36.
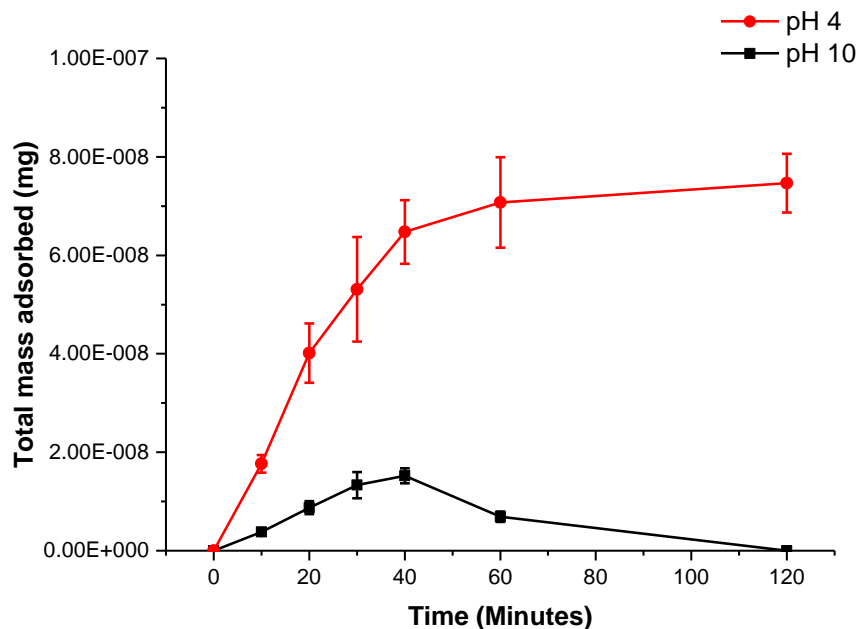
Figure 7.35: Adsorption rate and maximum mass adsorbed on the microchannel walls over time of SWCNTs suspended in aqueous solution with different pH levels
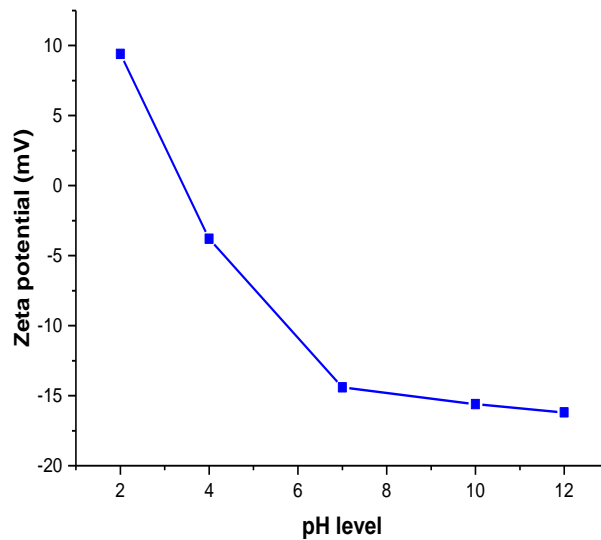
Figure 7.36: Effect of pH on the zeta potential of SWCNTs

7.7 Summary

This chapter has shown the development of a Raman microfluidic integrated system, which can be used to study the adsorption kinetics of SWCNTs in the microfluidic channel. The development encountered a few challenges; such as the effect of Raman detection volume on data analysis. These challenges were mitigated by creating a calibration graph for the mass flux through the channel. Hence, the mass flux of SWCNTs flowing through the channel can be quantified for a given concentration of SWCNTs. Finally, the system has been used to show the effect of SWCNTs concentration and pH on the adsorption kinetics of SWCNTs. The key findings from the experiments are mentioned below:

- CNT concentration has an effect on its adsorption on to APTES covered surfaces under dynamic fluid flow conditions.
- It also showed that at lower pH CNT adsorption rate and amount on the surface increases. On the other hand there is a reduction in adsorption at higher pH levels.
- One critical finding is that even when the channel is flush with water at relatively high flow rates, CNT retention is still present on the surface.

These experimental results will then be fitted to adsorption kinetics models in the discussion chapter. These results will provide a further understanding of the CNT adsorption mechanism needed for NAST1. The next chapter will show the application of the Raman microfluidic integrated system for tracking carbon nanotubes in the microfluidic system.

Chapter 8.   Tracking Carbon nanotubes in microfluidic system

8.1   Introduction

An understanding of CNT transport in microfluidic channels is of great importance to NAST1 as their transport mechanism differs from polymers or molecules, which are mostly diffusion driven. The knowledge gained from this study can be used to predict CNT placements in a reservoir under various conditions.

Transport studies of SWCNTs have been done in recent years and they have shown that SWCNTs transport follows advection – dispersion transport [192]. One factor that affects particle transport kinetics, where flow is laminar, is diffusiophoresis. Hence, the effects of diffusiophoresis on the transport of SWCNTs are shown in this chapter. The applicability of this diffusiophoretic study to industry is it will provide a better understanding of how the salinity of the aqueous solution, in which the SWCNTs are suspended in, will affect their placement in the reservoirs.

EOR and squeeze treatments regularly inject chemicals and particles using water as a transport medium into reservoirs. As stated in chapter 2 section 2.3, injected waters tend to meet formation waters in the reservoirs. These waters have different salinity levels and different ionic strengths [123, 193, 194]. These differences will have an effect on the transport of SWCNTs in reservoirs when these waters meet. Furthermore, this chapter shows the applicability of the integrated system in studying the transport kinetics of carbon nanotubes. The first part of this chapter will highlight the Raman parameters used for the experiments as well as details of the microfluidic channel used. The next part shows results from transport experiments to establish the transport behaviour of SWCNTs in microfluidic environments. Finally, the effects of diffusiophoresis will be explored.

8.2   Raman parameters for the system

The spot map scan was set to scan across the width of the channel (200 µm) and along the length of the channel (shown in Figure 8.1a). The Y – Junction is angled at 45° (Figure 8.1b) to ensure passive diffusion mixing of the fluids injected in both inlets [195]. On the Y axis of the spot scan, the step interval between was set to 5 µm while on the X axis the step interval was set to 200 µm. The exposure time of the laser was set to 0.25 seconds, this was done in order to reduce the scan time for the map area which is considerably larger than the scan area done for the adsorption experiments. The laser power set at 100% which gives a scan time of approximately 20 minutes. All experiments were in a steady state, which means time was not a factor.
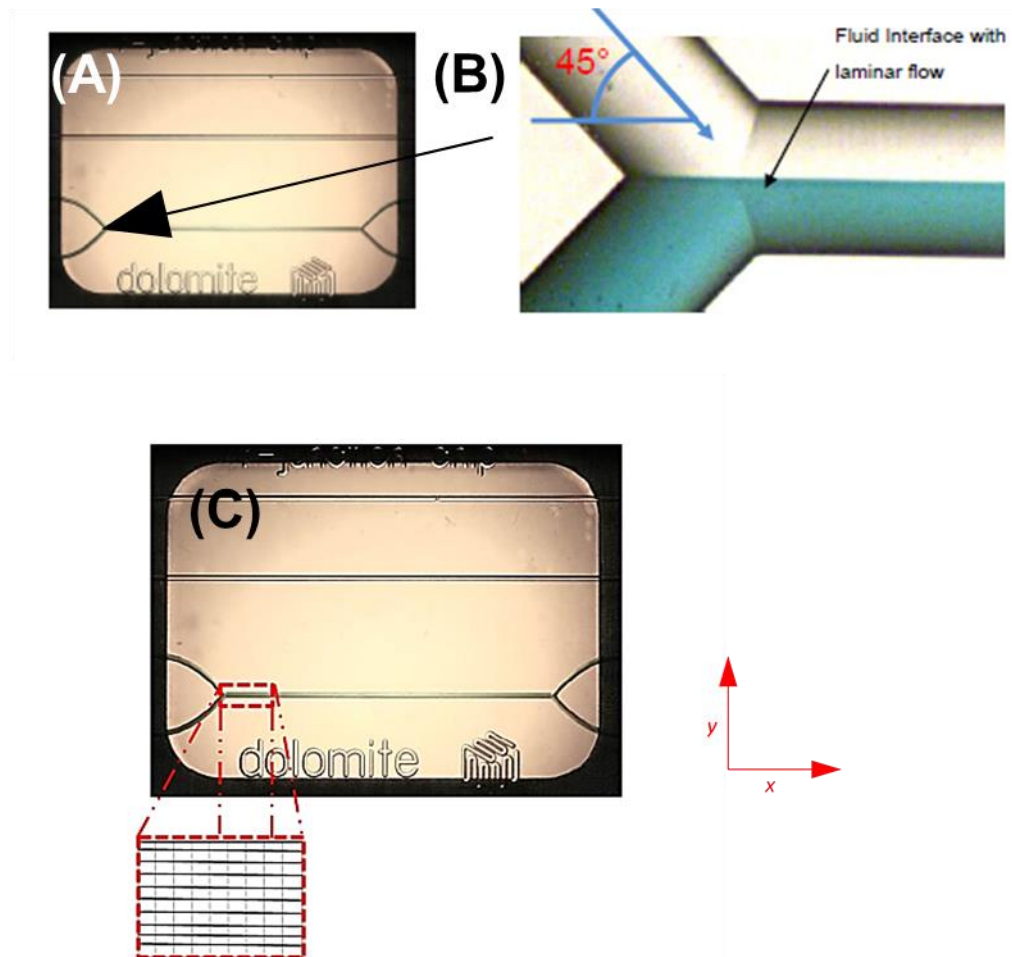
Figure 8.1: Schematic diagram of spot map scan showing grid system

The grid system used in this map scan is specifically designed to achieve a systematic and quantitative analysis of Raman data generated from the RM integrated system. The vertical lines are used to divide the scan area into sections while the horizontal lines are used to determine the area covered by CNTs within these sections. Advection transport of SWCNTs is confirmed when the area covered by SWCNTs within the channel remains constant along the length of the channel and the direction of flow (Figure 8.2a). Diffusiophoretic transport of SWCNTs is confirmed when the area covered increases (Figure 8.2b).
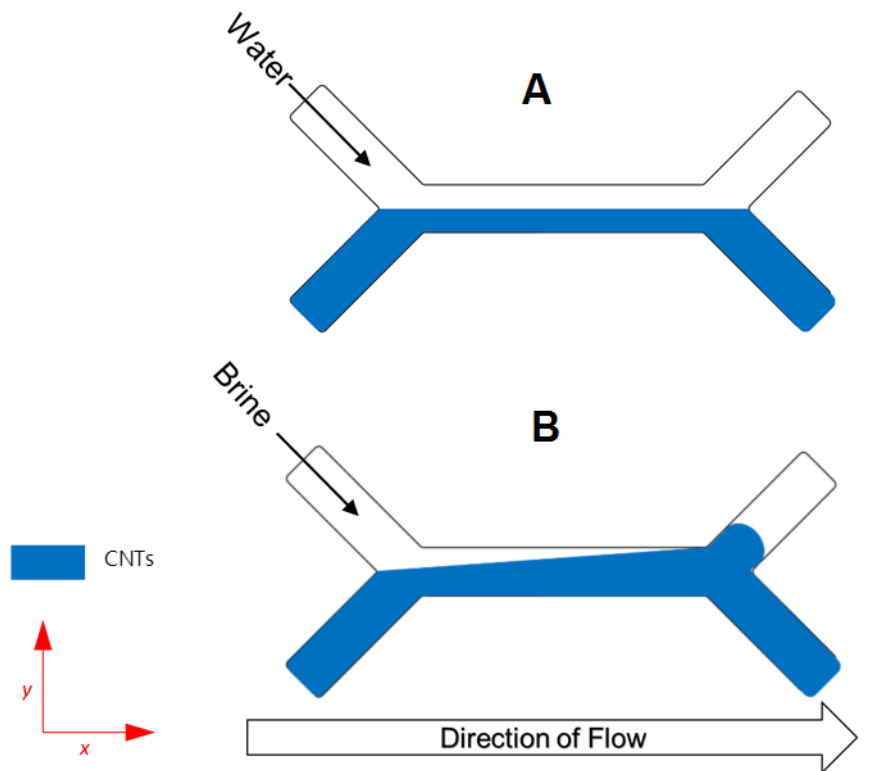
Figure 8.2: Schematic diagram of flow cell illustrating (A) Advection transport of SWCNTs (B) Diffusiophoretic transport of SWCNTs due to salt concentration gradient across the channel.

8.3   Interpreting data from map scan

The map scan uses the spot-to-spot mapping, which represents the locations of the particles flowing through the channel. The area of a given section is divided by the number of spot scans in that section. The value obtained represents the area allocated to each map scan spot (Figure 8.3).
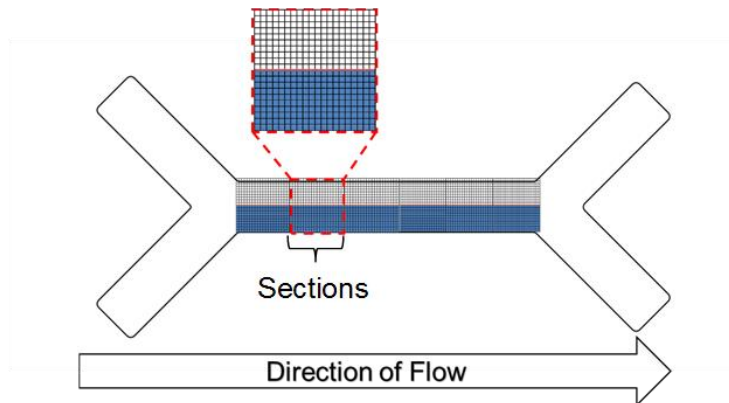
Figure 8.3: Schematic diagram highlighting the spot scan, the positioning of the spot forms a grid system (exploded section).

Figure 8.4A and Figure 8.4B show three sections of the microchannel which apply the map scan grid system to detect diffusiophoretic transport of particles in the channel. Each section has height of 205 µm (diameter of the channel) and a length of 1 mm. The red line going through the centre of the channel represents the baseline position of the CNTs as they transport through the channel from section 1 to section 3. The number of blue squares represents the spot scans that detected CNTs in that location. Increase in squares along the channel indicates diffusiophoresis. This data is used to calculate the effective diffusion coefficient in m^2/s.
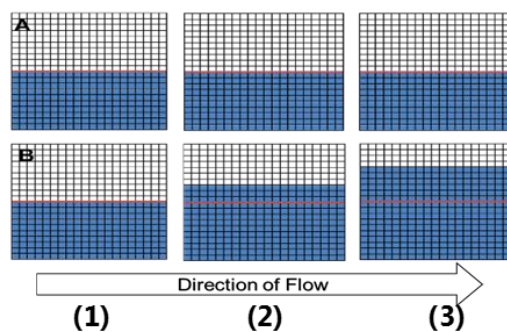
Figure 8.4: Schematic diagram of (A) Sections showing advection transport of SWCNTs (B) Sections showing diffusiophoretic transport of SWCNTs.

8.4 Experimental results without a salt concentration gradient in the system

The set of experimental results presented in this section aims to demonstrate the advection transport of CNTs in microfluidic channels. It will also show the effect of pH, CNT concentration, flow rates and on the transport kinetics of CNTs. These parameters were selected as these are the environmental factors that the particles might experience during the injection process of NAST 1. Figure 8.5 shows a three dimensional graphical representation of SWCNT particle transport in the microchannel at a flow rate of 50 µL/h, a pH of 7 and a CNT concentration of 20 mg/L. It can be seen that the detection area tracking the SWCNTs transport in microfluidic channels keeps a constant area over the length of the channel. It confirms advection transport.
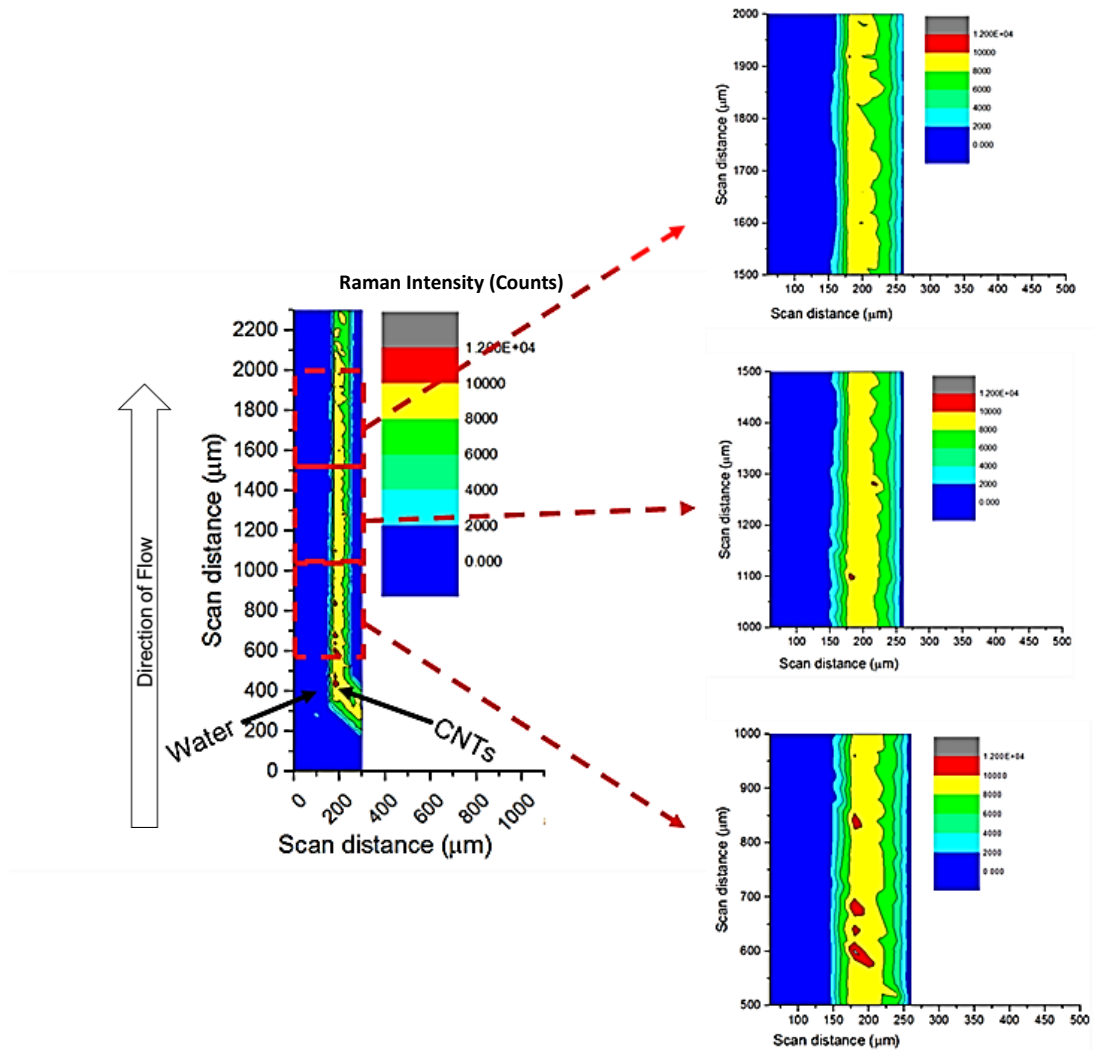
Figure 8.5: The transport of SWCNTs through the Y-Junction microfluidic channel. The sections (exploded views) show a constant area covered by SWCNTs which indicates advection transport of SWCNTs.

Figure 8.7 illustrates how data from the microfluidic channel can be turned into information, by dividing the channel into sections to determine the effects of flow rates on the transport kinetics of CNTs. The first section starts at the junction of microfluidic channel (Figure 8.6), and the other sections follow in the direction of flow. Since the length of each section is 1mm, the particles in each section will travel by that same distance to go the next section along the channel.
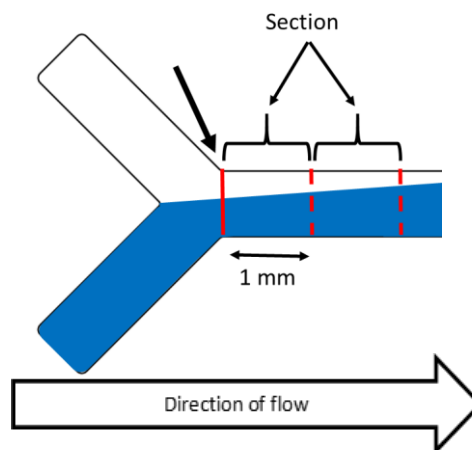
Figure 8.6: Schamatic diagram illustrates the start of the first section (indicated by arrow). The diamensions of the sections are also highlighted.
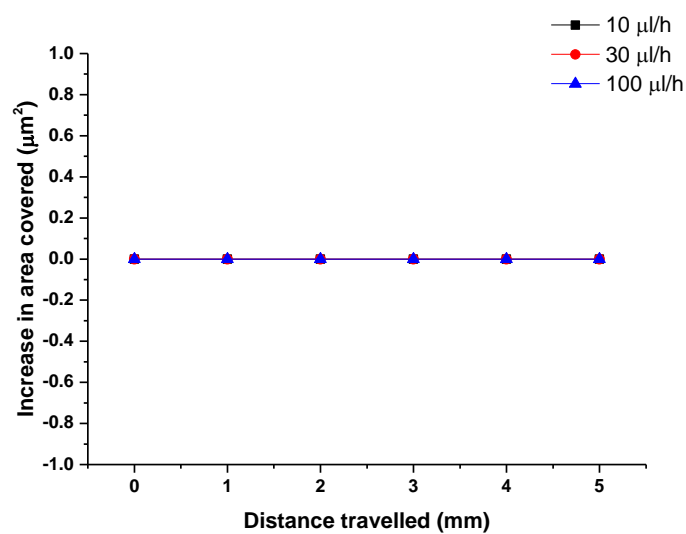
Figure 8.7: Effect of flow rate on the transport kinetics of SWCNTs in microfluidic transport showing no effect on transport kinetics.

Figure 8.7 shows that the effect of flow rates has minimal effect on the transport kinetics of SWCNTs in microfluidic channels. Following these results, the effects of pH and CNT concentration were tested. Figure 8.8 and Figure 8.8 shows the effect of pH and CNT concentration on transport kinetic is also minimal.
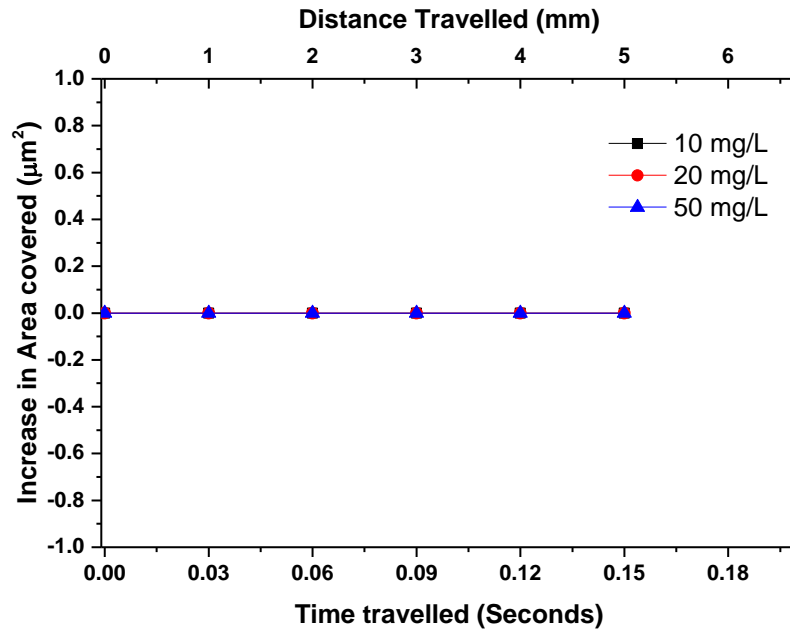
Figure 8.8: Effect of CNT concentration on the transport kinetics of SWCNTs in microfluidic channels showing no effect on transport kinetics.
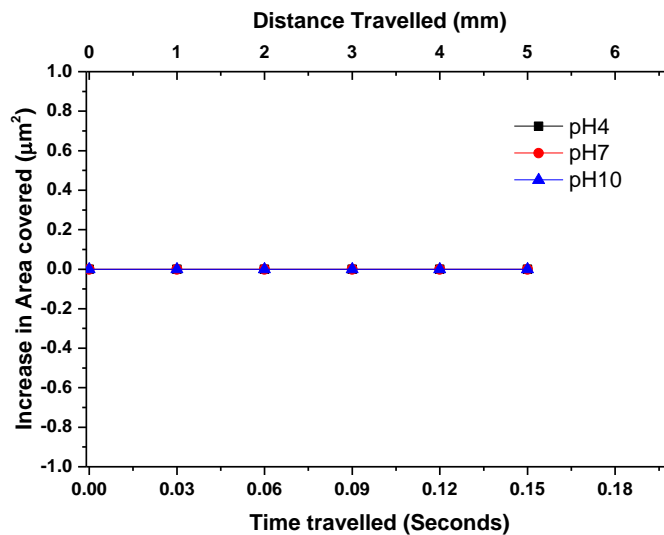
Figure 8.9: Effect of pH on the transport kinetics of SWCNTs in microfluidic channels showing no effect on transport kinetics.

Figure 8.7, Figure 8.8 and Figure 8.9 indicate that these different factors have minimal effect on the advection transport of SWCNTs. One reason for this transport property is due to the flow conditions in which the particles are subjected to. Under microfluidic flow conditions, flows tend to be dominated by laminar/creeping flow. This is due to the low Reynolds numbers experienced at the micro level. Under laminar/creeping flow condition, particles tend to flow the streamlines of the fluid. Furthermore, at the microfluidic level, viscous forces dominates inertia forces which affects the shape of the streamlines and transport of SWCNTs. The next chapter will provide a more fundamental understanding of the flow condition and how this phenomena affects particle transport.

8.5   Experimental results with salt concentration gradient in the system

As stated earlier, one condition that can affect the transport kinetics of particles is diffusiophoresis. For these set of experiments, a monovalent salt (NaCl) was added to water and injected into one inlet of the Y – Junction microfluidic channel while the CNTs (dispersed in water) are injected into the other inlet (Figure 8.10). The flow rate was 30 µL/h for both inlets. The experimentally measured zeta potential of the SWCNTs is -14 mV.

Figure 8.10 shows the occurrence of particle migration due to salt diffusion across the width of the channel. Furthermore, it highlights the effect of ionic strength on migration of SWCNTs which shows that the stronger the ionic strength of the salt solution being injected, the greater the mobility of particles across the system. This is as a result of the increase in magnitude of the electric field across the system which originates from the increase in the solute concentration gradient in the system.
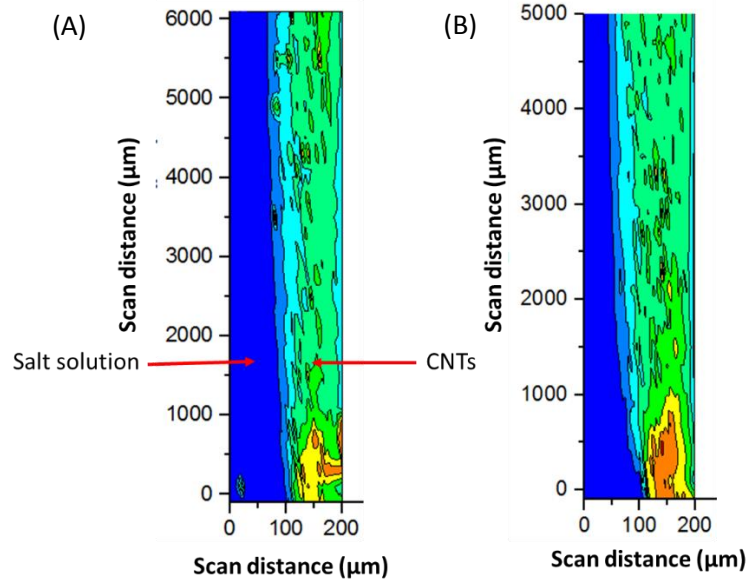
Figure 8.10: 3D graphical representation of SWCNTs mobility when (A) 10% NaCl solution is injected in the system. (B) 20% NaCl solution is injected in the system.

8.6 Effect of ionic strength on diffusiophoretic velocity of carbon nanotubes

Figure 8.11 presents the effect of solute concentration on diffusiophoretic migration along the channel. It can be seen that the higher the salt concentration in the system the faster the diffusiophoretic velocity. This is due to increases in amplitude of the electric field generated from salt diffusion.
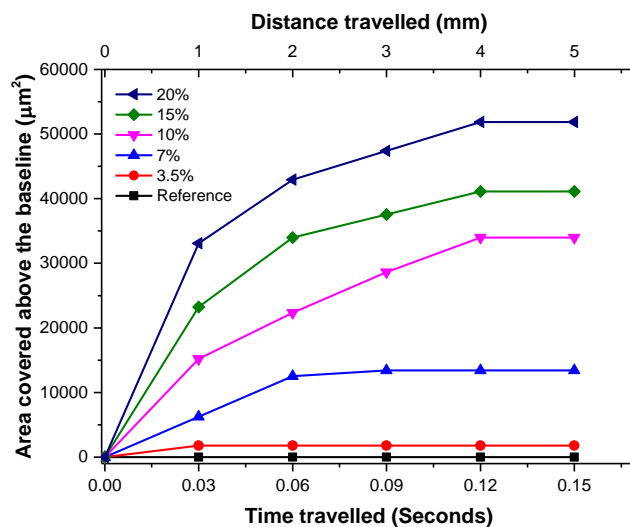
Figure 8.11: The effect of NaCl ionic concentration on the displacement of SWCNTs in microfluidic channels

Although the gradient of the slope in Figure 8.11 has the same dimension as a diffusion coefficient (μm^2/s), the diffusive transport of SWCNTs under these conditions differs from classical diffusion in several aspects. For instance, it can be seen that after a certain point, the diffusiophoretic mobility and velocity becomes zero. This shows that within that region, the solute has fully diffused; hence, the salt concentration gradient is zero. Therefore there is a clear link between the diffusive – like dynamics of the SWCNTs and the time dependent salt diffusion process. This transport dynamics differs from classical diffusion process which is associated with Brownian motion.

8.7   Effect of salt diffusion on diffussiophoretic velocity of SWCNTs

The effect of solute concentration gradient on diffusiophoretic velocity is related to the increase in area coverage between each section. Figure 8.12 illustrates this relationship.
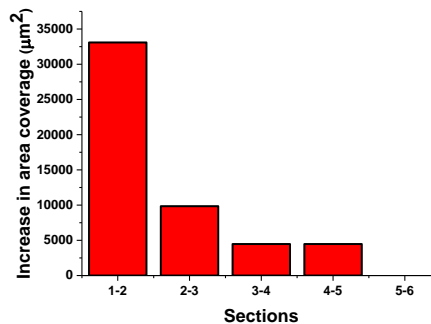
Figure 8.12: Diffusion – like motion of SWCNTs across the sections from the diffusion of a 20% salt concentration solution

Figure 8.13 shows the all the different salt concentrations used for this set of experiments. As expected the higher the salt concentration, the higher the magnitude of the increase at different sections. However, it can be seen that for all salt concentrations, the increase in area covered is zero between sections 5 and 6. This could be as a result of the salt gradient going to zero at this point.
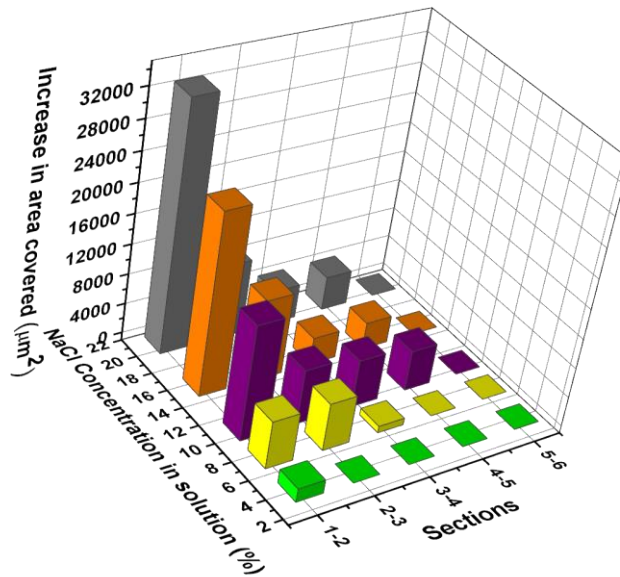
Figure 8.13: Increase in area between sections as a result of the salt gradient from all salt concentrations used.

For charged particles, the diffusiophoretic migration is proportional to the solution concentration gradient. These results can be compared to the salt concentration gradient at each section to have an understanding of how the magnitude of the salt gradients affect the diffusiophoretic velocity of the particles. The next chapter will provide relevent data from the salt diffusion needed for analysis.

8.8   Effect of Surfactants on particle migration of carbon nanotubes

SWCNTs used in this project are dispersed in water using a non-ionic surfactant tween 80. It has been well established by previous research that surfactants have an effect on the zeta potential of the particle. Ionic surfactants, such as Sodium dodecylbenzenesulfonate (SDBS), have a larger effect on the magnitude of particle zeta potential. In this case, SWCNTs suspended in water containing 1% SDBS has a zeta potential of -44 mV. Figure 8.14 shows the effect of SDBS on particle migration of SWCNTs. It can be seen that there is an instant migration of SWCNTs from the inlet. However, it appears that further down the channel, diffusiophoretic migration of SWCNTs ends. This fast diffusiophoretic velocity could be as a result of the magnitude of the zeta potential value of the SWCNTs which will have an effect on the

transport. Furthermore, studies have shown that salt solution has an effect on SDBS, which might have an effect on the transport of SWCNTs .
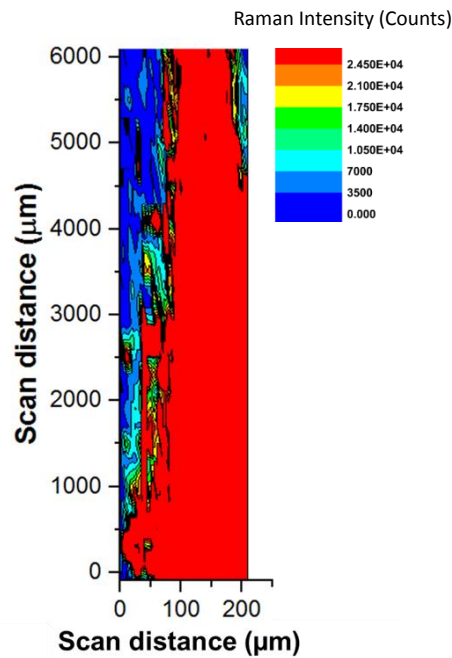
Figure 8.14: 3D graphical representation of the mobility if SWCNTs dispersed in 1% SDBS and water in the presence of 10 %NaCl diffusion.

8.9 Summary

This chapter has highlighted the need to study the transport kinetics of SWCNTs in microfluidic channel for particle injection during squeeze treatment and specifically NAST1. The key findings are mentioned below:

- The integrated system confirmed the advection transport of SWCNTs in microfluidic channel under various environmental conditions.
- More importantly, it has shown the effect diffusiophoresis has on the migration of SWCNTs.
- Furthermore, parametric studies have shown the effects of surfactants and salt concentrations on the diffusiophoretic velocity of SWCNTs.

The next chapter will provide a fundamental understanding of how the diffusion of salt solution causes migration of particles across the channel by modelling the kinetics of salt diffusion in the channel.

Chapter 9.   Modelling the transport kinetics of SWCNTs and the electric field produced by salt diffusion in microfluidic channels.

9.1   Introduction

The previous chapter showed the effects of diffusiophoresis on the migration of SWCNTs as well as established the advection transport of the particles in microfluidic channels. This chapter presents a developed particle transport COMSOL model to give the reader a better understanding of the transport kinetics of SWCNTs in microfluidic channels. Also presented in this chapter is a COMSOL model of salt solution diffusion across the microfluidic channel. This will aid in providing a theoretical understanding of the time – dependent salt diffusion process. From the this model, the electrical potential generated across the microfluidic channel from the salt solution diffusion is calculated.

9.2   COMSOL Model Development

The COMSOL model is developed through five stages:

- **Geometry:** This is where the 2-dimensional shape of the microchannel is drawn and are the boundary domain. The geometry is drawn to represent the microfluidic channel size for future experimental correlation.

- **Material:** The material flowing through the system is defined as water with all its relevant properties such as viscosity and density at room temperature.

- **Physics:** In this stage, three different physics area defined. Creeping flow is defined for the fluid flow physical phenomena due to microfluidic principles. This is coupled with particle tracing for fluid flow as well as Transport of dilute species which facilities the definition of the diffusion coefficients of the ions present in the salts used in the experiments as well as ionic concentrations.

- **Mesh:** The most appropriate mesh is defined for accurate, efficient Multiphysics solutions. A mesh sensitivity study is performed to determine the best mesh density needed to provide acceptable results for analysis.

- **Study:** A time – dependent solver was used in the model for the particle tracking simulation and a stationary solver was used for the salt diffusion model and creeping flow condition which are in a steady state.

9.3 Simulation set up

9.3.1 General assumptions of the simulations

Some assumptions are made in order to simplify the mechanism of the transport of particles and the salt diffusion processes in the microchannel.

- The carrier fluid is water and is assumed to be incompressible. There is also no slip between the fluid and the microchannel wall, hence, the velocity at the wall is zero. The wall is fixed and receives no deformation.

- At this stage, the particles are considered spherical as the particle shape. This is due to the low Reynolds numbers of the fluid [196]. The size of the particle is considered to be 1 µm which is the dominant dimension for the SWCNTs from the DLS data in Figure 6.6 and the manufacturer's datasheet. The particles were assumed to be evenly distributed at the inlet and throughout the channel. It is assumed that the particles do not influence the fluid flow due to the low concentration of particles (20mg/L) flowing though the channel. Particle – particle interactions were neglected to limit computational time.

- Particles were assumed to have a starting velocity equivalent to the fluid flow rate of 8.33×10^{-12} m^3/s. This value matches the flow rate used in the experiments.

The density and viscosity values for all injected brine are presented in Table 9.1:

Table 9.1: Density and Viscosity values for each brine simulated [194]

Salinity (%)	Density (kg/m^3)	Viscosity (Pa.s)
0	998	1.00E-03
3.5	1024	1.07E-03
7	1051	1.17E-03
10	1075	1.27E-03
15	1116	1.44E-03
20	1158	1.50E-03

9.3.2   Geometry configuration

To reduce complexity and computational time, a 2-dimentational model was simulated to show the particle transport and the salt diffusion. 2D geometry has the same dimension as the Y – Junction microchannel from the flow cell used for the experiments. This is used as the basis for further modelling which considers Junctions and restricted boundaries in the channel (Figure 9.1).
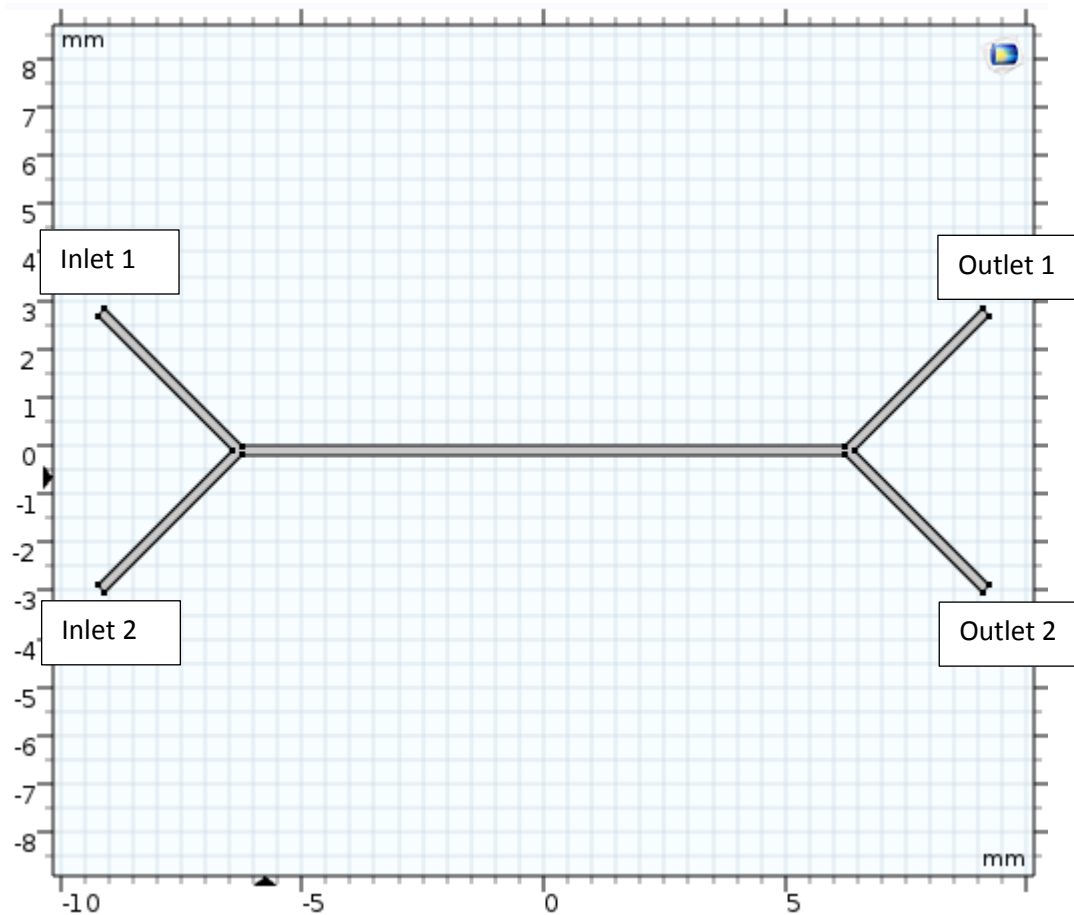
Figure 9.1: Geometry for 2D model

9.3.3   Governing equations

In order to build a model, it is important to understand the theory behind the physics employed in building the model. There are three primary physics considered; namely fluid flow, particle transport and transport of dilute species.

9.3.3.1   Flow conditions

For fluid flow condition, the dynamics of an incompressible Newtonian fluid is described mathematically by the Navier – Stokes equation which is shown in Equation 9.1 [33].

$$\rho\left[\frac{\partial u}{\partial t} + u.\nabla\mathbf{u}\right] = -\nabla p + \mu\nabla^2\mathbf{u} + \mathrm{F} \qquad\qquad Equation\ 9.1$$
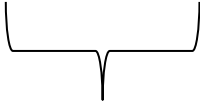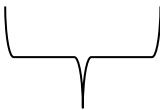
Acceleration   Viscosity term

Where ρ is the fluid density (kg/m^3), u is the fluid velocity (m/s), μ is the dynamic viscosity (Ns/m^2), F is the external force applied (N) and p is the pressure (Pa).

The left hand side of the equation represents the acceleration in the fluid. $\frac{\partial u}{\partial t}$ is the local acceleration while $(u.\nabla)u$ is the advection term. On the right hand side, $-\nabla P$ is the pressure difference across the system while $\mu\nabla^2\underline{v}$ represents diffusion [197].

For flow restricted by microfluidic channels and with no external force, the Navier – Stokes equations can be simplified; by taking into account the fact that the inertial forces on the left hand side of the equation is negligible (viscous forces dominates over inertial forces) at the microscopic level. This leaves the Stokes equation shown in Equation 9.2 [198, 199].

$$-\nabla P = \mu\nabla^2\underline{v} \qquad\qquad Equation\ 9.2$$

This is the laminar/creeping flow version of the Navier-Stokes equation.

This laminar flow regime can also be expressed mathematically by the Reynolds number (Equation 9.3).

$$Re = \frac{Inertial\ forces}{viscous\ forces} = \frac{\rho UD}{\mu} \qquad\qquad Equation\ 9.3$$

Where Re is the Reynolds number, U is the mean velocity of the fluid (m/s), D is the hydraulic diameter of the flow container (m), μ is the dynamic viscosity of the fluid (Pa.s) and ρ is the density of the fluid (kg/m^3).

It can be seen that when the channel diameter is on the microscale, the top half of the equation becomes very small (hence inertial forces become small) and the Reynolds number will be extremely low, normally, below 1. So for example, at the flow

rate given in section 9.3.1, the Reynolds number is 0.119. Hence, further confirming that the flow regime is in the creeping flow regime.

9.3.3.2 Particle tracking

The particle tracing module on COMSOL is a flexible tool that computes the trajectories of particles based on external forces placed on the particles and the properties of the particles. There is also a dedicated physics interface for computing particle movements in a fluid environment. Within this interface, there are a wide variety of predefined forces such as drag and Brownian force. The main force acting on the particle is drag force, which is due to flow velocity of the fluid acting on the particle. Brownian motion is negligible due to the extremely low diffusion coefficient of CNTs coupled with the dominate viscous forces in creeping flow .

Transport of particles larger than 0.1 µm is typically dominated by the drag force acting on particles immersed in a fluid. The drag defined is known as stokes drag which is applicable for creeping flow where the Reynolds number is far less than one. Equation 9.4 represents the drag force:

$$F = \frac{1}{\tau_p} m_p (u - v) \hspace{3cm} Equation\ 9.4$$

Where m_p is the particle mass, τ_p is particle response time u and v are the fluid and particle velocity respectively.

The particle velocity response time for spherical particles in a laminar flow is defined mathematically as:

$$\tau_p = \frac{\rho_p d_p^2}{18\mu} \hspace{3cm} Equation\ 9.5$$

Where µ is the fluid viscosity (Pa s), ρ_p is the particle density (kg/m^3), and d_p is the particle diameter (m),

9.3.3.3 Transport of dilute species

The diffusion of salt was modelled using the transport of dilute species physics module. This module supports the simulations of chemical species transport by convection, migration and diffusion. In order to model the chemical species transport through diffusion and convection, COMSOL solves the mass conservation equation for the relevant chemical species i, using:

$$\frac{\partial c_i}{\partial t} + \nabla \cdot (-D_i \nabla c_i) + \mathbf{u} \cdot \nabla c_i = R_i \qquad\qquad Equation\ 9.6$$

Where c_i is the concentration of the species (mol/m^3), D_i is the diffusion coefficient of the species (m^2/s), R_i is a reaction rate expression for the species (mol/m^{3}s) and u is the velocity vector (m/s).

The first term on the left hand side of Equation 9.6 ($\frac{\partial c_i}{\partial t}$) corresponds to the change in concentration of the dilute species over time. It is considered zero due to the steady state nature of the domain which is then computationally solved using the stationary solver. On the right hand side of Equation 9.6, R_i represents a source or sink term, normally due to a chemical reaction. In this model, R_i is not specified as there is no chemical reaction. This leaves the following equation:

$$\nabla \cdot (-D \nabla c_i) + \mathbf{u} \cdot \nabla c_i = N_i \qquad\qquad Equation\ 9.7$$

 Where N_i is the flux vector (mol/m^{2}s) and is expressed as:

$$N_i = -D_i \nabla c_i + c_i u \qquad\qquad Equation\ 9.8$$

N_i in Equation 9.8 accounts for the convection and diffusive mechanism in the system. The first term on the right hand side of Equation 9.8 accounts for the diffusive transport as a result of the diffusion coefficient of the dilute species (Fick's law). The diffusion coefficient of sodium chloride (NaCl) is obtained from literature. The second term describes the advection transport due to a velocity field u. The velocity field is obtained from the computed fluid flow physics module.

Finally, the model is developed from the above discussed parameters, and by coupling the difference physics to produce an output of particle transport due to creeping flow condition and salt gradients due to the diffusivity of NaCl and the fluid flow conditions.

9.4   Mesh sensitivity analysis

The accuracy of the modelling output is directly dependent on the mesh density, element type and shape. The higher the mesh density the more accurate the output will be. However, this is at the expense of an increase in computational time. Therefore, it is important to carry out a mesh sensitivity study to find the right balance between accuracy and computational intensity. To do this, a simple study was carried out by conducting simulation in a variety of mesh density settings and using free triangular mesh shape. The study uses the velocity profile at the mid-section of the channel for comparing against different mesh density. The results of the investigation are shown in Figure 9.2**.**
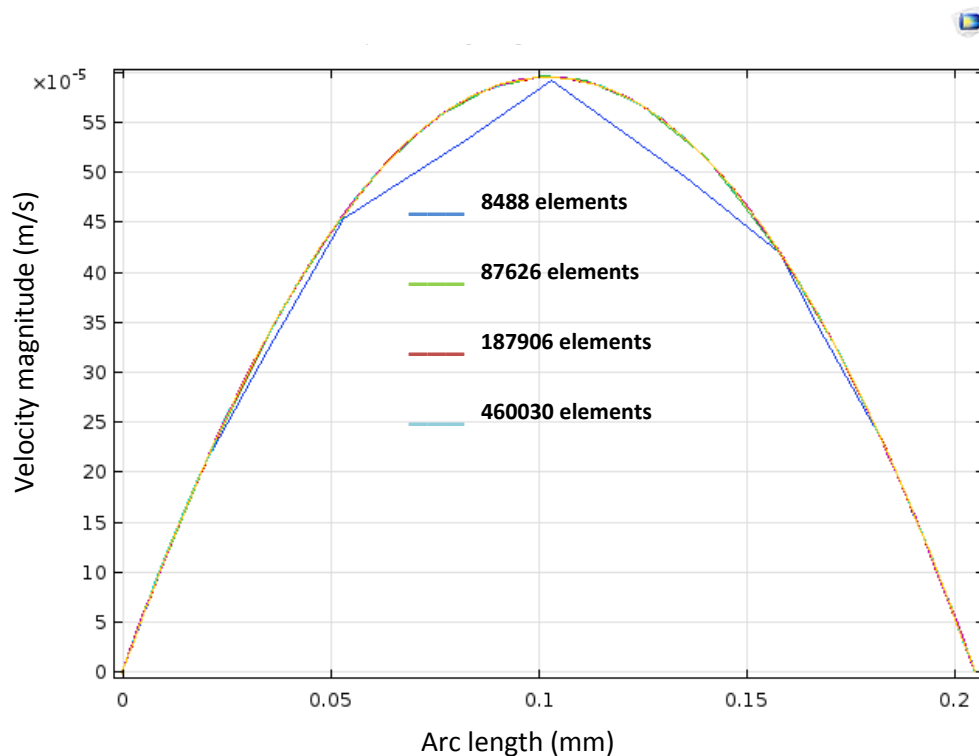
Figure 9.2: Result of mesh sensitivity study for fluid flow

The simulation result is insensitive when the number of elements is larger than 187906. Hence, the number of mesh elements 187906 is used for all subsequence simulations in the study.

The particle tracing model on COMSOL requires a lot more computational time and memory as this is a time-dependent study. Furthermore, for each particle, a second-order ordinary differential equation (ODE) is solved for each component of the particle position vector. As a result, two ODEs are solved for each particle for the 2

dimensional model. Hence, the number of particles will have an effect on the computational time and memory needed for the simulation. Using the velocity fields from the fluid flow module to generate particle transport, a particle number sensitivity study (varying the number of particles) is performed. The particles were injected in inlet 2 and the percentage of particles exiting outlet 2 was used for the study. Figure 9.3 shows the result of the study. It shows that injecting a value larger than 200 does not significantly change the percentage of particles coming out from outlet 2.
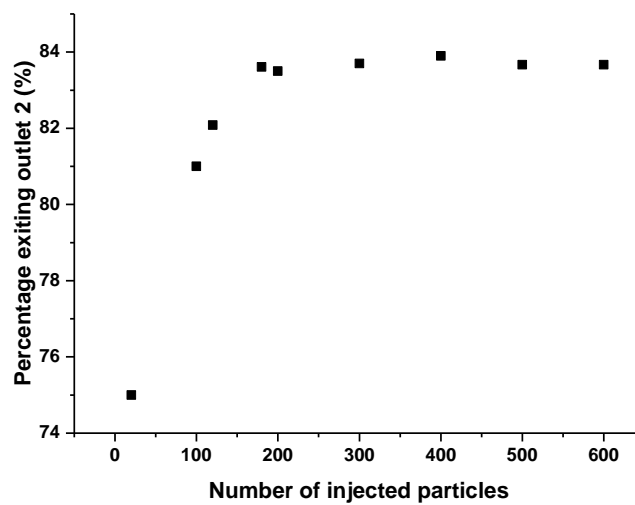
Figure 9.3: Results of particle number sensitivity study

The first study was conducted by injecting water through the left boundary (inlet1 & 2) of the Y – Junction channel under a steady state creeping velocity and constant pressure. The velocity profile of the fluid flow across the channel follows a parabolic trend. This is the flow regime expected to occur in the microfluidic set up. The typical trend of the velocity magnitude at the inlet and outlet is shown in Figure 9.4 and Figure 9.5 which shows the highest velocity at the middle of the channel and the lowest at the wall.
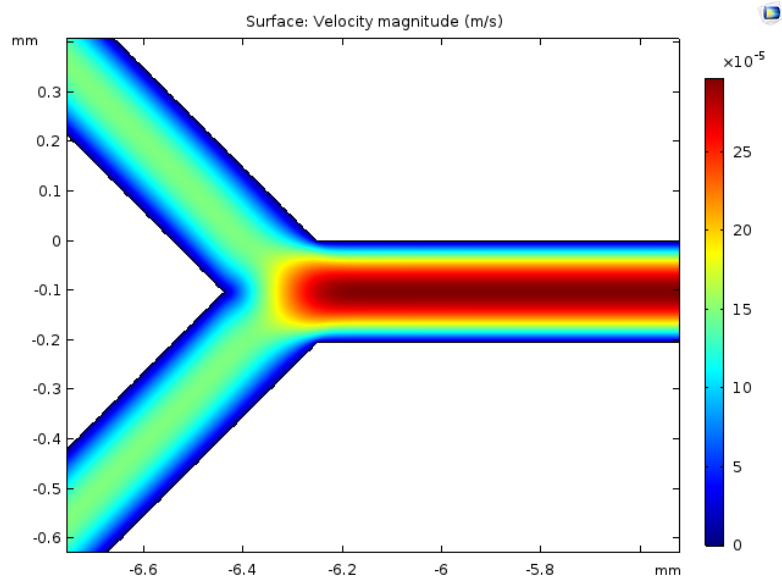
Figure 9.4: The velocity magnitude profile at the inlet of the channel
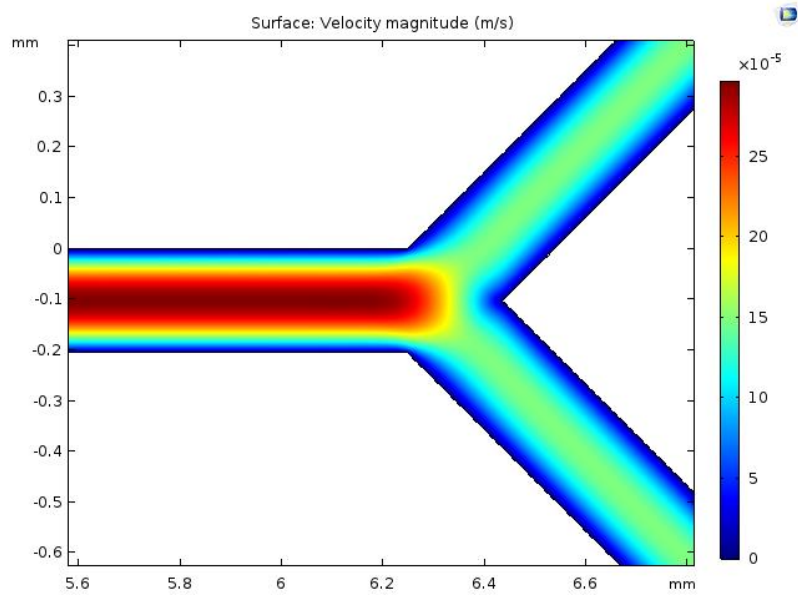
Figure 9.5: The velocity magnitude profile at the outlet of the channel

9.5 Comparison of model with experimental results

The next stage is to compare the experimental particle transport results (Chapter 8 section 8.4) with the simulated one. The two parameters used are the change in flow rate. Figure 9.6 to Figure 9.8 show the particle trajectory flowing through the microfluidic channel at different flow rates.
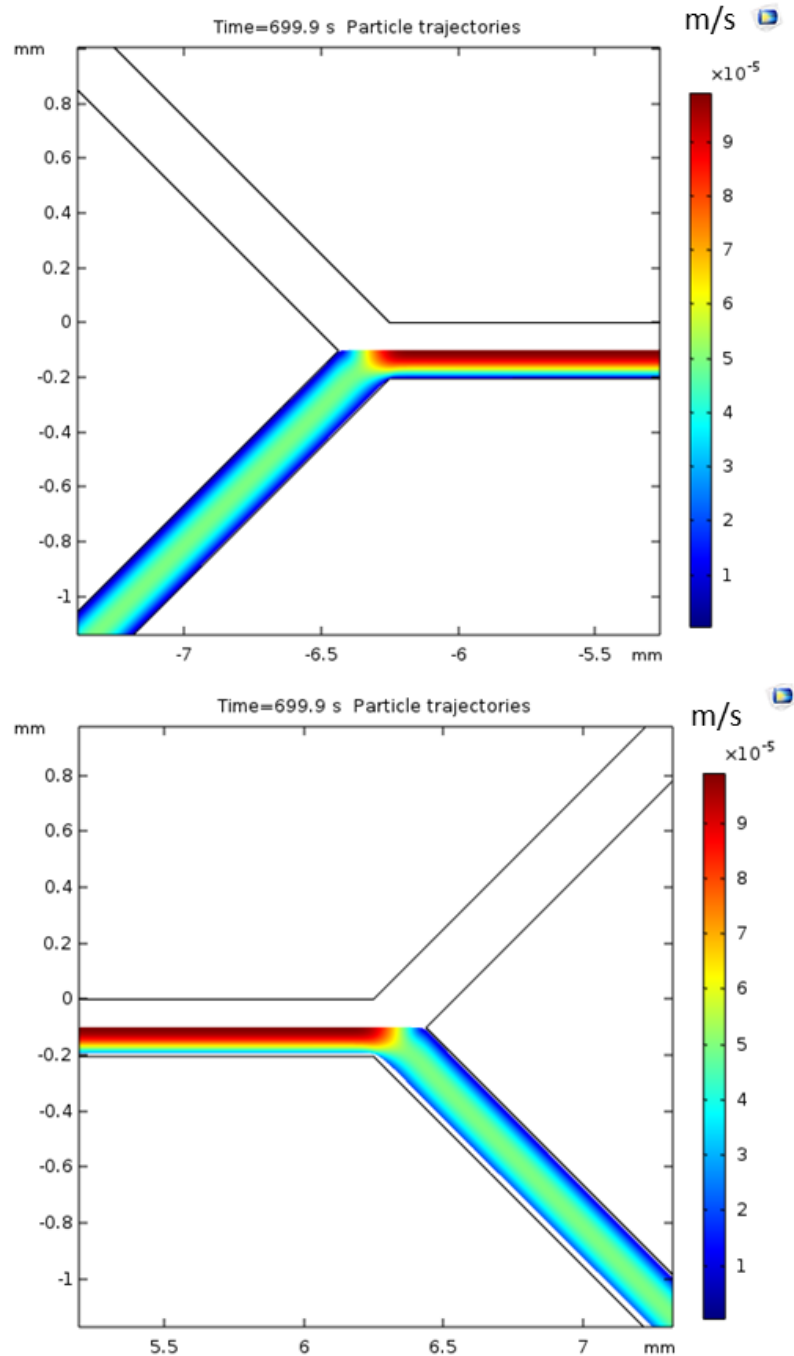
Figure 9.6: Particle trajectory at a flow rate of 0.01 mL/h (A) the inlet (B) the outlet
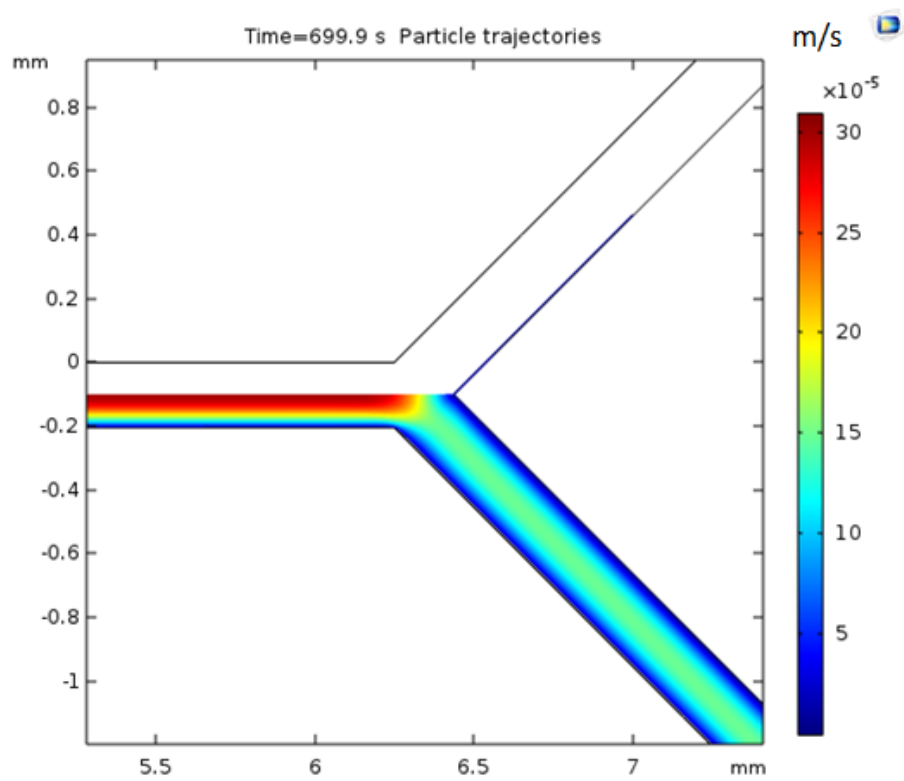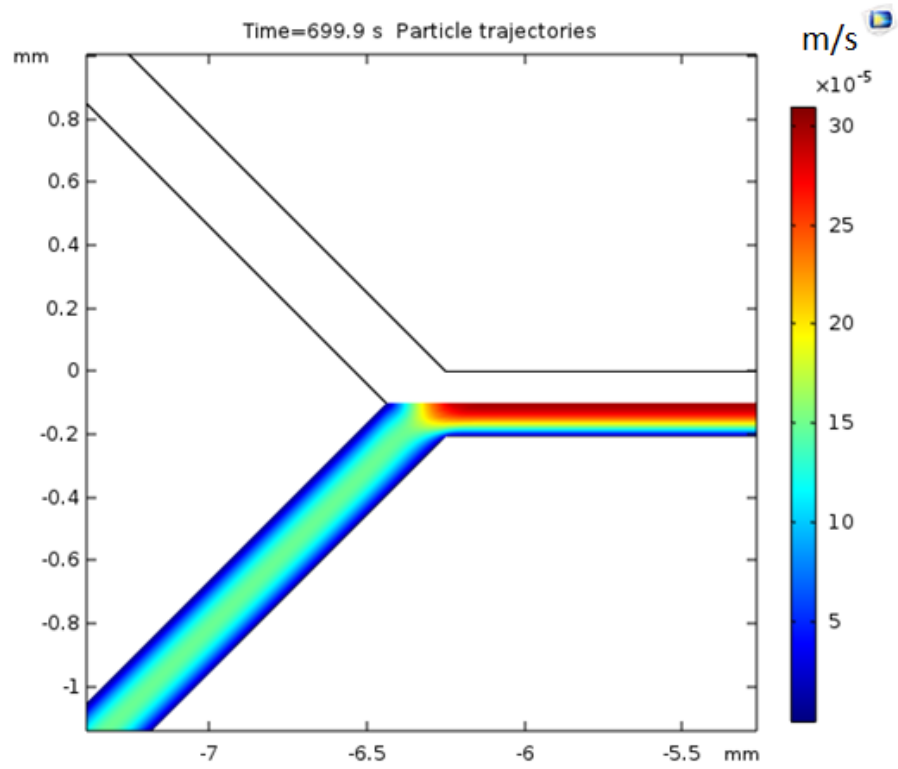
Figure 9.7: Particle trajectory at a flow rate of 0.03 mL/h (A) the inlet (B) the outlet
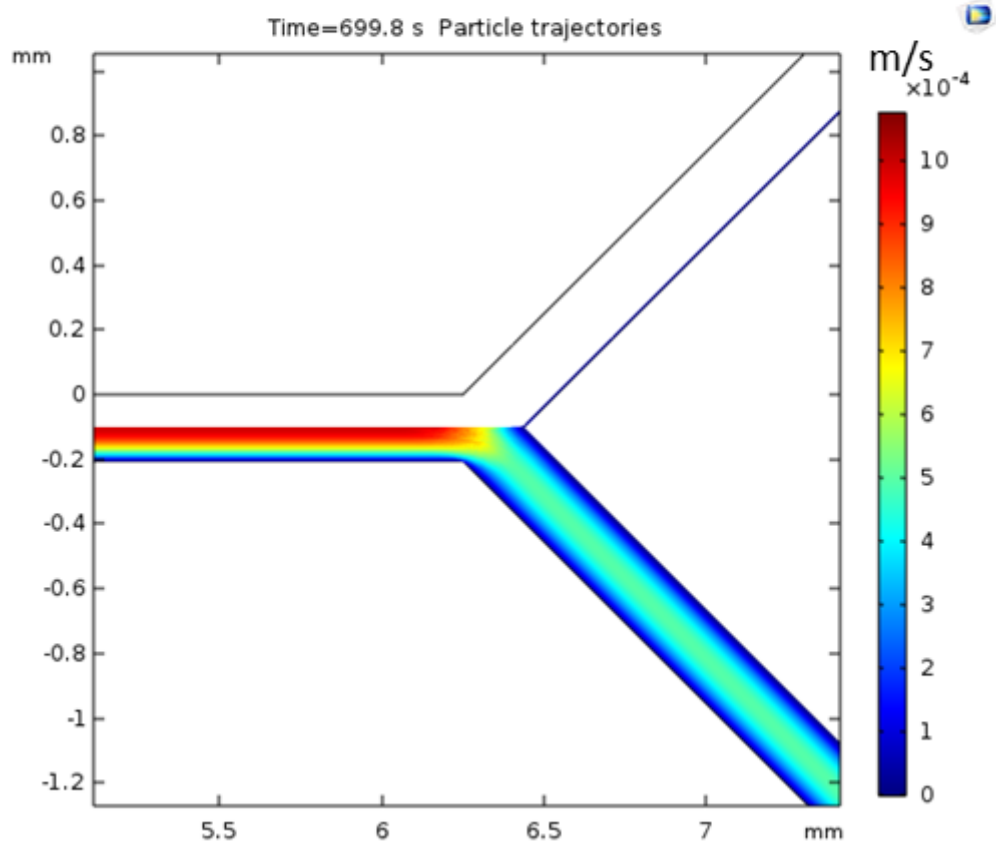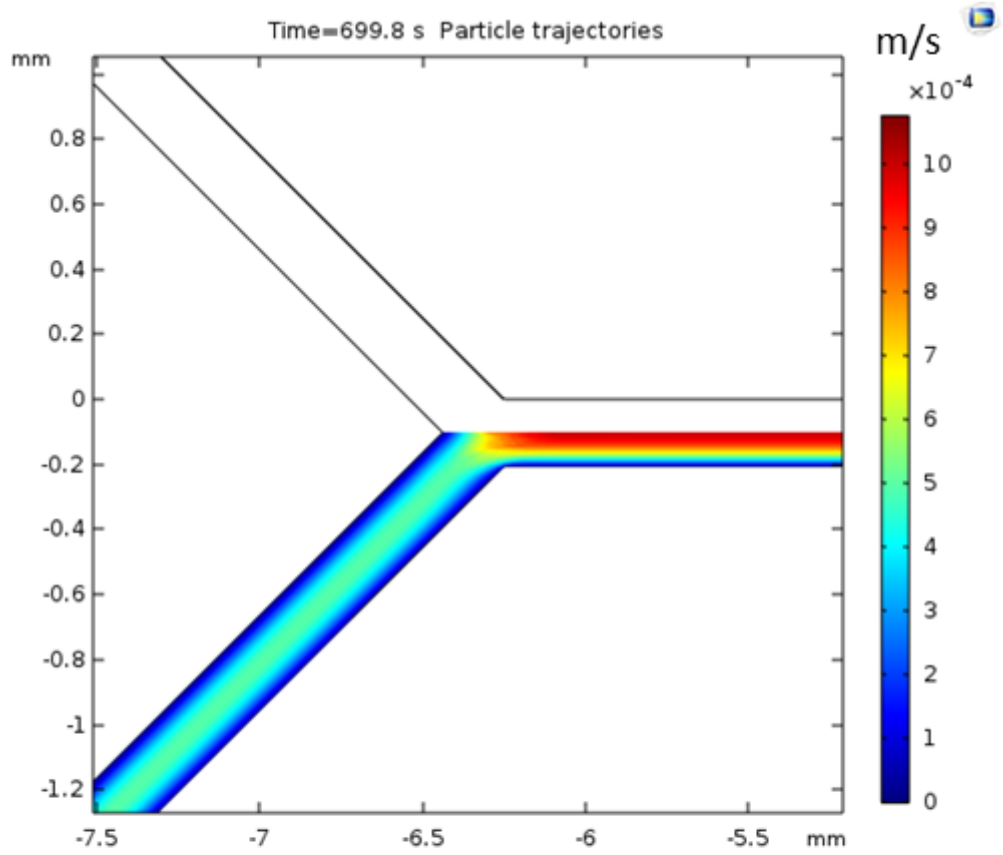
Figure 9.8: Particle trajectory at a flow rate of 0.1 mL/h (A) the inlet (B) the outlet

The results show that change of flow rate has no effect on the transport of particles, further confirming the advection transport of SWCNTs. These results are comparable to the experimental results in chapter 8. Figure 9.9 shows a graph from one of the experimental results to highlight the similarities of its CNT transport profiles with the profiles obtained from the computational results.
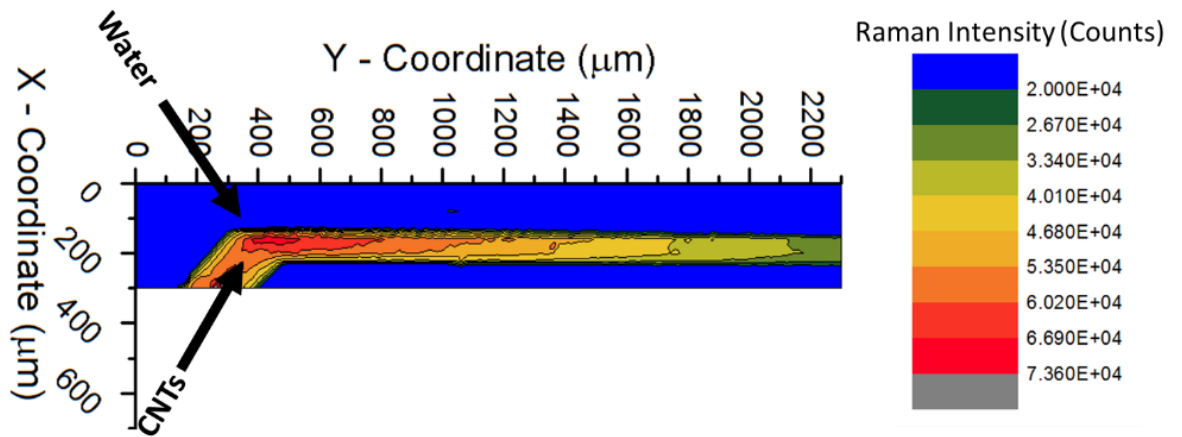
Figure 9.9: Graphical representation of an experiment of CNT transport in the Y – Junction microfluidic channel showing no diffusion across the channel.

9.6   Salt diffusion

Diffusiophoresis occurs due to the diffusion of salt across a system which produces an electric field which then causes the migration of charged particles. Hence, a study is needed to generated a flow of diluted salt species through the microfluidic channel in inlet 1 and a flow of water inlet 2, which produces a salt concentration gradient across the channel. A range of NaCl salt concentration (mol/m^3) with the known ionic diffusivity of the Na$^+$ and Cl$^-$ was injected at a flowrate of 0.03 ml/h. Figure 9.10 shows the diffusion of NaCl across the channel.
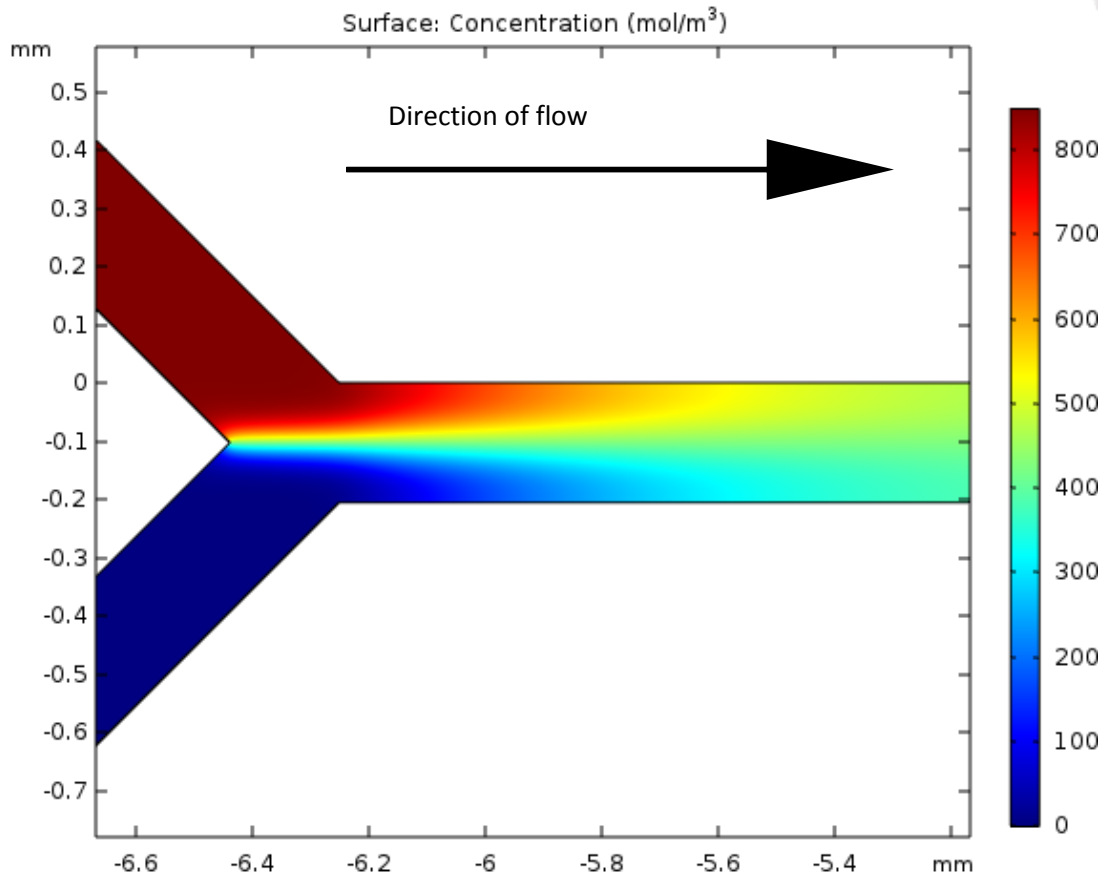
Figure 9.10: Salt gradient generated by injecting salt solution in inlet 1 and water in inlet 2

It can be seen that as the salt diffuses from the top half of the channel to the bottom half, a concentration gradient is formed across the channel. This gradient gradually decreases along the channel as salt diffusion reaches equilibrium further down the channel. The overall mapping of the concentration gradient is shown in Figure 9.11. It shows that the magnitude of the concentration gradient is highest at the centre of the channel.
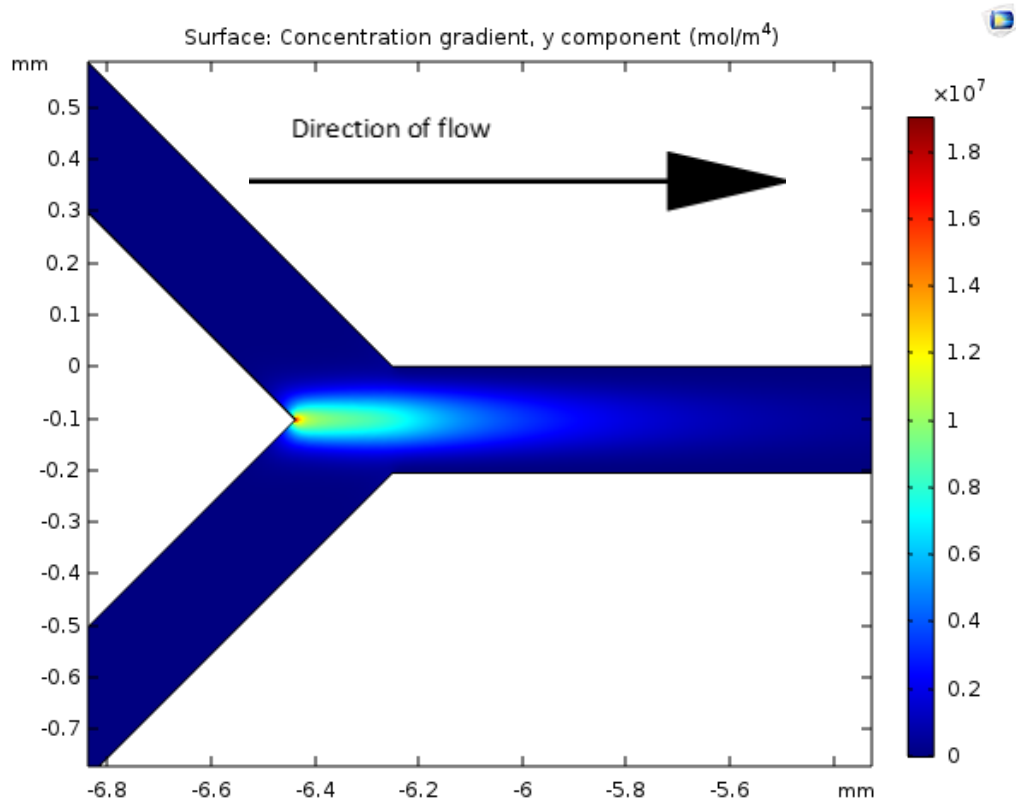
Figure 9.11: Salt gradient profile along the microfluidic channel by injecting salt solution in inlet 1 and water in inlet 2.

9.7 Link between computational results and experimental results

The areas used for comparison between the experimental results and the computation results are the particle transport kinetics and the salt gradient mapping of the in the Y – Junction channel.

9.7.1 Particle transport kinetics

The Raman microfluidic (RM) experimental results show that the injected particles do not deviate from the streamlines at the flow rates tested in the absence of a salt gradient. The simulated results show the same outcome and can be explained by the microfluidic flow regime (creeping flow) and the size of the particles flowing through the Y – Junction channel.

9.7.2 Salt gradient mapping

The RM results for particles injected into the Y – Junction channel in the presence of a salt gradients shows that at the junction, the diffusiophoretic velocity of the particle

is at its peak and then it gradually reduces to zero further down the channel. This is comparable to the salt gradient mapping shown in Figure 8.10. This shows that the salt gradient can be coupled to the migration of particles flowing in the microfluidic channel.

9.8   Summary

This modelling work carried out within this chapter has been developed to complement the experimental work to provide an understanding of the transport kinetics of particles in microfluidic channels and factors that might affect this transport.

The importance of the model is that it extends the mechanistic understanding of diffusiophoresis by providing the profile of the salt diffusion which was generated for the experimental work in chapter 8. This information provides a link between the electric field and the diffusiophoretic velocity of SWCNTs which will be fully discussed in the next chapter.

Chapter 10. Discussion

10.1 Introduction

The focus of this project is on NAST1, which involves injecting carbon nanotubes into oil reservoirs in order to increase scale inhibitor retention. There are various questions that need to be answered. For instance, how can the CNTs injected be measured in order to monitor the amount of particles desorbing from the reservoirs? What are the adsorption kinetics of CNTs under different pH levels and how does different CNT concentrations affect these kinetics? What factors affect the transport kinetics of CNTs? The results chapters contain some answers to those questions. Hence, this chapter brings together all the results from this thesis in order to provide the reader an overarching narrative of the aims and objectives of this thesis and a detailed analysis of the results obtained. Discussing these results will provide answers that will help improve the NAST methodology

Lastly, these results show the capabilities of the Raman microfluidic integrated system developed in this thesis in performing particle adsorption and transport kinetics experiments.

This chapter is divided into three main sections

- The first part explains what criteria makes an excellent analytical technique for the detection and quantification of CNTs in aqueous solutions needed for the NAST methodology. As Raman and ICP were demonstrated in chapter 6 as suitable techniques, this section discusses the factors that affect the quality of the results from the techniques. It then concludes with the role of Raman and ICP in monitoring the CNTs concentration for the NAST methodology.

- The second part presents the development of the Raman – microfluidic setup and the need for the setup. This section compares this microfluidic approach to that of coreflood as corefloods experiments were performed in the previous work by Ghorbani. From here, the adsorption results are discussed and fitted to two adsorption kinetic models which will provide information on the kinetics of the CNT adsorption. This section gives an insight into how pH

and CNT concentration affect the adsorption kinetics, and it discusses the underlying reasons for these effects on the kinetics.

- The final part discusses CNT transport kinetics under various conditions and how salt diffusion in microfluidic channels affects the CNT transport. Finally, it presents the relevancy of the results from this thesis to the NAST methodology.

10.2 Characterisation and quantification of carbon nanotubes suspended in aqueous solution

Chapter 6 showed the use of Raman spectroscopy, ICP and TEM for characterising and quantifying CNTs in aqueous solution. It had shown that the properties of the particles affect the accuracy, detection and quantification limits of the analytical techniques chosen.

Each procedure were tested for the quality of their repeatability to ensure the robustness of the techniques. For each technique, known concentrations were statistically analysed using regression analysis. This analysis provided the precision and accuracy of the techniques investigated. Accuracy is the measure of agreement between the measure value and the true value. The absolute true value of the sample concentration is seldom known. Precision is the repeatability of the results (magnitude of the error margins), hence, precision of the techniques will be used to determine the suitability of the techniques for quantifying CNTs suspended in aqueous solutions.

10.2.1 Raman microscopy

Figure 6.23, Figure 6.24 and Figure 6.25 show that calibration graphs can be created using a range of exposure time and laser power setting without damaging the samples or reducing the quality of the precision to an unacceptable level. However, CNT properties determines how wide the range can be. MWCNTs require high power (maximum power in this case) and exposure time setting. For SWCNTs, the settings require much less output in order to produce sufficient intensities needed for detection and quantification procedure. This is mainly due to the exceptional Raman

intensity of the G peak generated due to the resonance effect of SWCNTs which will be discussed in detail later in this section.

Results from Chapter 6 showed that SWCNTs suspended in aqueous solution produce better regression analytic results in terms of repeatability within a concentration range of between 0.01 ppm and 10 ppm.

Raman scattering is one of the common ways of studying the fundamental properties of carbon nanotubes. As such, the Raman signals generated from the particle will vary with corresponding properties of CNTs. Metallic and semiconducting SWCNTs can be distinguished from the rest of the particles by the double resonance effect that produces an exceptional strong G peak signal at a Raman shift in the range of 1590 to 1600 cm^{-1} [200]. The origin of the double or even triple resonance is from what happens during the exchange in energy between the light and the medium. Although the exchange in energy is transferred to the atomic vibrations, the light – particle interaction is mediated by electrons. Therefore, under normal conditions, Raman scatter is generated when the electron that absorbs the light is excited to a virtual state. However, when the laser energy matches the energy gap between the valence and conduction bands in a semiconducting particle, there is a chance that the Raman scatter increases by orders of magnitude. This is the called the resonance effect [190].

This property has allowed the limit of detection and quantification of semiconducting SWCNTs suspended in aqueous solution to be in the part per billion (ppb) level. Furthermore, due to the lower error margin in the calibration graphs, it is possible to detect concentration changes below 0.1mg/L. Lastly, the laser power and exposure time of the Raman instrument can be adjusted to improve the limit of detection without these parameter affecting the SWCNTs properties due to the solution dissipating the heat generated by the laser.

The SWCNT calibration graph also shows that as the concentration increases, there is an increase error margin (Figure 10.1). This could be as a result of the dispersion of the particles suspended in aqueous solution. The higher the concentration the less efficient the surfactant is in dispersing the particles [201]. Therefore, care must been taken to ensure the particles are well dispersed before analysis.
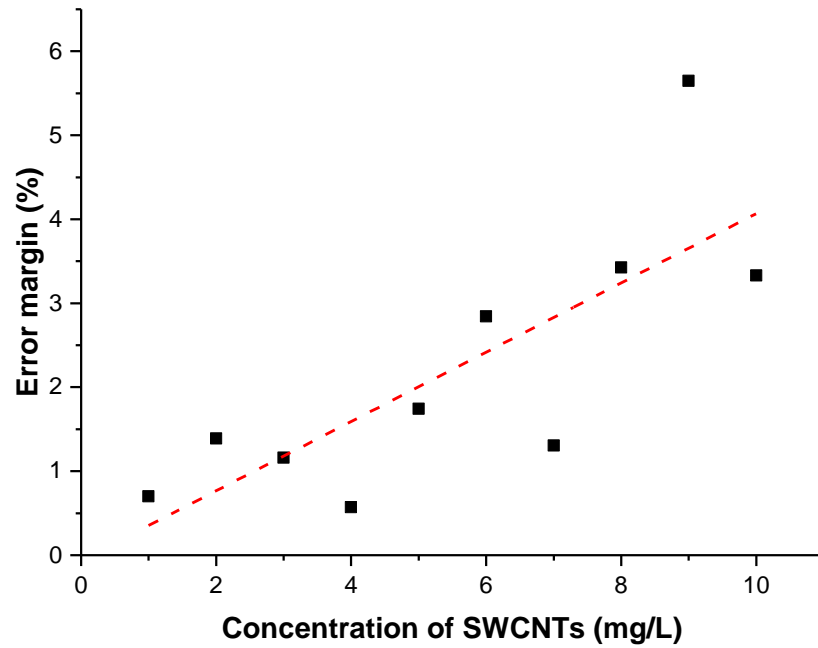
Figure 10.1: Relationship between SWCNT concentration and error margins

MWCNTs produce a dominant D peak signal and the diameter of the walls vary which has an effect on the signal produced by the particles. This will in turn have an effect on the precision of the technique.
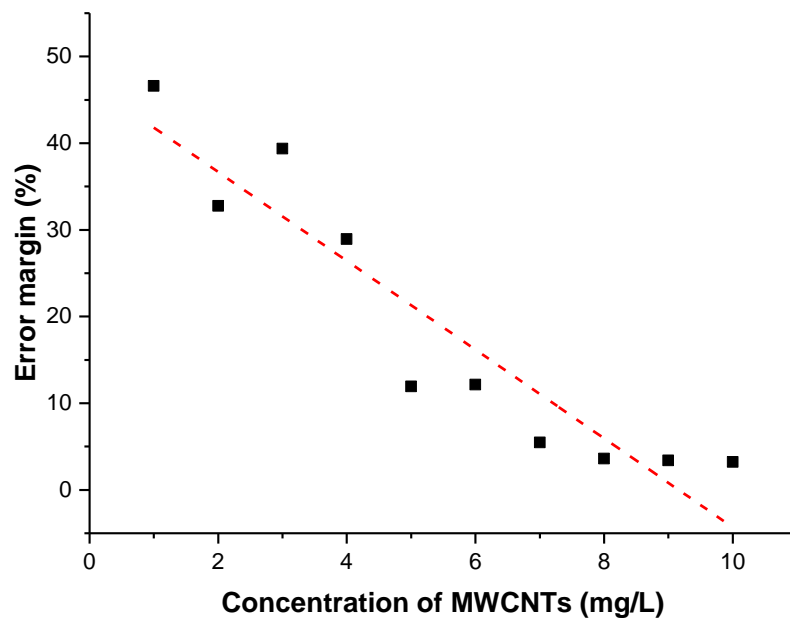
Figure 10.2: Relationship between MWCNT concentration and error margins

Furthermore, this variation in diameter seems to have a greater effect on lower concentrations of MWCNTs. As stated in the methodology chapter, the Raman spectra was collected from random points within the cell (Figure 10.3). This method can produce different Raman intensities due to the variation of particle diameter at different locations.
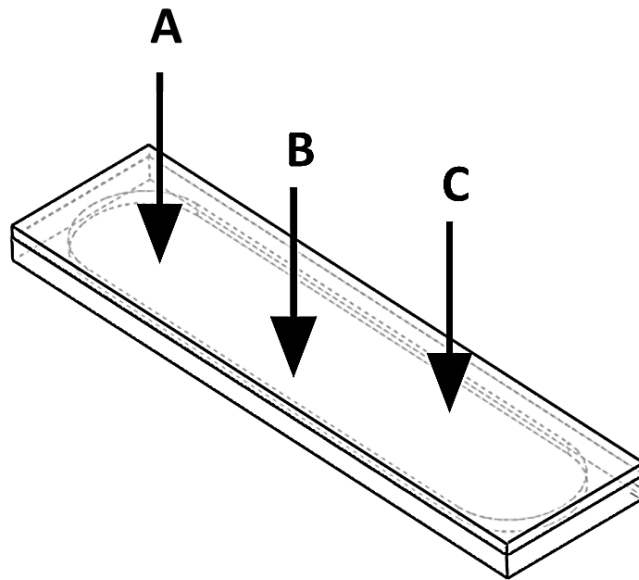
Figure 10.3: Schematic diagram showing random points in the Raman cell where Raman spectra was collected.

At lower concentration of MWCNTs, the variation in diameter size can be more pronounced. This variation will affect the Raman signal collected from the instrument. As a result, the error margin of Raman signals at lower concentration are higher.

10.2.2 ICP – MS

This thesis has shown that ICP – MS can detect both SWCNTs and MWCNTs suspended with aqueous solution to a concentration level down to 0.01 mg/L with minimum sample preparation (no acid digestion). However, previous studies have shown that it is possible to detect CNTs at concentration in the region of μg/L to ng/L with a digestion step. The ICP results from acid digested CNTs show that if the CNTs are not fully digested, the quality of the results will be affected as indicated with the large error margins. Therefore, in order to improve the accuracy of the results and to obtain detection limits in the μg/L and ng/L levels, the CNTs need to be fully digested.

10.2.3 Benefits and limitations of investigated techniques

10.2.3.1 Raman spectroscopy

The Raman results show that for both MWCNTs and SWCNTs, the limits of detection is well below the concentrations used for acute toxicity testing on aquatic species [202]. From an environmental standpoint, this is much more critical than the precision of the technique. However, the precision of the technique is more important when there is requirement to monitor the adsorption rate of injected CNT in the reservoirs and the desorption rates of the particles during production as this information might be useful to improve the NAST 1 methodology.

Raman spectroscopy can therefore be used to detect both types of CNTs suspended aqueous solution at concentrations below 1 mg/L which will ensure that if an unacceptable level of CNT concentration is leaving the reservoir it will be detected.

One limitation of Raman spectroscopy is the precision of the technique in quantifying CNTs suspended in aqueous solution. The results show that the precision of the technique is affect by the property of the particles, in this case MWCNTs. The calibration graph shows that , for CNT concentrations below 4 mg/L, Raman unable to distinguish between concentrations that differ by less than 2 mg/L.

10.2.3.2 ICP - MS

The main benefit of using ICP as a quantification technique is its ability to detect CNTs in concentrations below 0.01 mg/L. However, as it uses the elemental impurities in the particles as a proxy in the detection method, care must be taken during sample preparation to ensure that there is no elements in the solution that can mask the elements from the CNTs. For example, using an ionic surfactant like SDBS might content a high amount of sodium which will be detrimental to the analysis. For this reason, surfactants used to disperse the CNTs should be non-ionic like Tween 80. This limitation is not present in Raman as it uses the C=C bonding as the detection method. Table 10.1 shows a summarized comparison of the two techniques highlighting their strengths and limitations.

Table 10.1: Raman and ICP – MS strengths and limitations as CNT quantification techniques

Technique	Strengths	limitations
Raman spectroscopy	• Minimal sample preparation needed to produce calibration graphs for quantification technique. • Low detection limits achievable in the sub µg/L with the help of resonance Raman conditions. • Ability to use D and G vibrational bands as tracer for detection technique, hence overcomes the issue of elemental contamination.	• Dependent on calibration graphs, therefore, prone to experimental errors • Affected by suspension stability of CNT in aqueous solution. • Sensitive to Raman setting (laser power and exposure time)
ICP - MS	• Multi-elemental capabilities and highly accurate due to the extreme sensitivity of ICP – MS • Low detection limit of CNT if they are fully digested	• Elemental contamination is a risk as the techniques uses the metallic impurities as a proxy which could lead to analytical bias in the solution.

10.2.4 Role of chosen techniques to NAST methodology and Recommendation

One of the aims of this thesis is to investigate techniques capable of detecting and quantifying carbon nanotubes during the NAST process. In light of this, the techniques require a one-step preparation before analysis. This has been achieved with Raman microscopy. Therefore, Raman can be used as an on-site monitoring technique.

If concentrations at the ng/L levels are required, then ICP – MS can be employed. In order to ensure a high level of precision and accuracy of the ICP – MS analysis, there needs to be a digestion step that can fully digest the particles and unlock all elemental impurities needed for analysis. Furthermore, ICP can be used to complement Raman, with periodic sampling taken for ICP analysis to confirm the accuracy of the onsite monitoring technique.

10.3 Development of a Raman – Microfluidic integrated system for adsorption kinetic studies.

Ghorbani et al [45] showed the adhesion of CNTs onto APTES coated surfaces which is a part of the NAST methodology (NAST1). However, the purpose of conducting those experiments was to provide the proof of concept needed for the study. As such, most of the adsorption experiments conducted were under static conditions with no parametric studies to see factors that might affect the retention of CNT onto APTES coated surfaces. The coreflood experiments performed in Ghorbani's work focussed on the scale inhibitor adsorption process and not the CNT adsorption. As such, this thesis focuses on CNT adsorption process in fluid flow conditions. Although coreflood experiments can be used to study particle adsorption processes, there are some limitations to these kind of experiments which are mentioned below:

- There is limited control on the shape and size of the channels within the "cores" used in coreflood experiments. Hence, it is not possible to control the effects of channel geometry on CNT adsorption and transport kinetics.
- Visualization of adsorption and transport kinetics is not possible in coreflood experiments due to opaque properties of the core holders. As a results, in situ experiments are hard to conduct.

It is important to perform real time experiments as the data collected provides information about the sample in its experimental environment without exposure to an external environment. Furthermore, it is possible to track the particles in real time in order to study its transport kinetics.

This thesis has shown the applicability of integrating Raman microscopy and a microfluidic flow system to study the adsorption kinetic of SWCNTs in microfluidic channels under various conditions. Chapter 7 presented a detailed description of the procedures carried out in order to obtain repeatable, quantifiable results. Therefore, this section will focus on the results obtained from the Raman microfluidic (RM) system. The experimental parameters tested were the effects of particle concentration and pH on the adsorption of SWCNTs on APTES coated glass. From these results, the next section will provide an insight as to how these parameters affect the adsorption capacity and the adsorption kinetics of the SWCNTs on glass surfaces.

10.3.1 Deposition of SWCNTs on APTES coated glass

Injecting 10 mg/L SWCNT concentration into the APTES coated microfluidic channel showed adsorption or deposition of CNTs on the surface. The APTES used, which has a slight positive charge at neutral pH, provides the system with an attractive double layer interaction between the particles and the surface [203]. It can be seen from the results in Chapter 7 that the adsorption rate is relatively fast but slows down after a certain point (60 minutes), then reaches equilibrium by 150 minutes.

Chapter 7 presented the effects of detection volume. It showed that depth of focus permits the laser to detect the SWCNTs on the surface as well as in the bulk solution. What should be clarified here is that the size of the detection diameter is larger than the laser diameter. This means that in addition to the laser detecting a multilayer adsorption of CNTs on the surface, the laser will detect an increase in surface coverage of SWCNTs on the surface (Figure 10.4). This effect could be the reason for the change in adsorption rate over time as shown in the graphs in Chapter 7 which could be as a result of the number of active site decreasing with time as well as the decrease of SWCNT build-up over time.
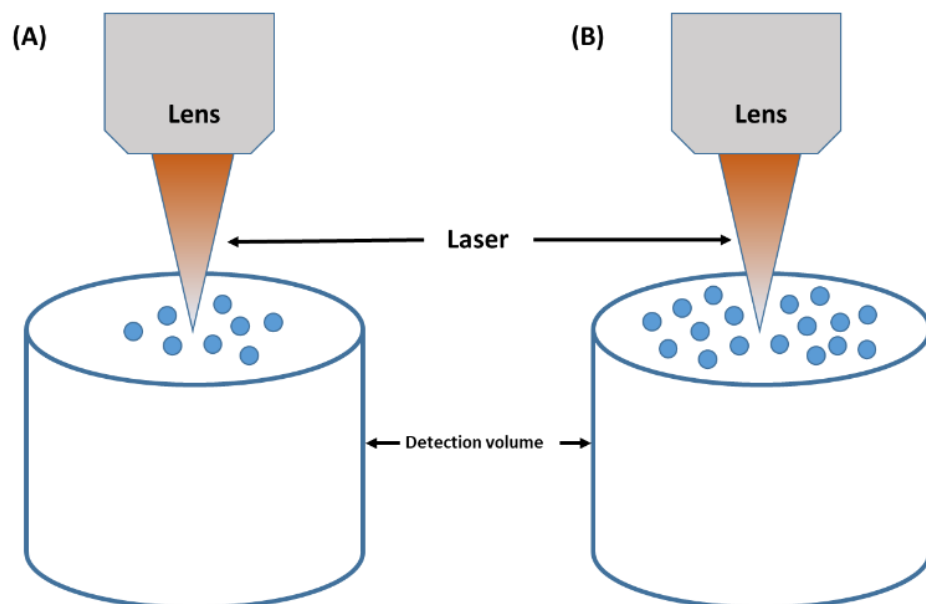
Figure 10.4: Schematic diagram illustrating effect of detection volume with lateral detection

For monolayer adsorption, the adsorption rate is generally quick and equilibrium is more or less instant, however, in the case of multilayer adsorption, adsorption rate is gradual and equilibrium is achieved later [106]. For well dispersed or monodispersed particles, monolayer adsorption is in theory guaranteed due to dispersion and stabilization by virtue of mutual repulsion. Hence, when a particle is adsorbed on the solid surface, any incoming particles are repelled by the adsorbed particle [204] . The particle size distribution obtained for the SWCNTs show that they are poly-dispersed, hence a monolayer adsorbed film of SWCNTs is less probable. One reason for this kinetics is the stability of the suspended particles flowing in the microfluidic channel. The particles are dispersed with the aid of Tween 80 and has a zeta potential of -14 mV, which is a relativity low value needed to fully stabilize the particles. In general, in the absence of steric hindrance, full stabilization is achieved when the absolute value of the zeta potential is around 30 mV [110]. While Tween 80 is able to stabilize the particles for an extended period of time, the zeta potential shows that some agglomeration is bound to occur over time as the particles are not completely stable due to the presence of Van Der Waal forces.

Tween 80, a non – ionic surfactant, aids in stabilizing the particles by creating steric interactions between the particles. It does this by adsorbing on the surface of particles in such a way that a portion of the polymer extends in the aqueous solution (Figure 10.5). In the case of Tween 80, the hydrophobic section has an affinity to the particle while the hydrophilic section extends out, creating a hydrophilic layer around the SWCNTs [106]. As particles come close to each other, the adsorbed layers come in contact. Any overlapping of the layers will cause some dehydration and hence a repulsion force between the particles [106].
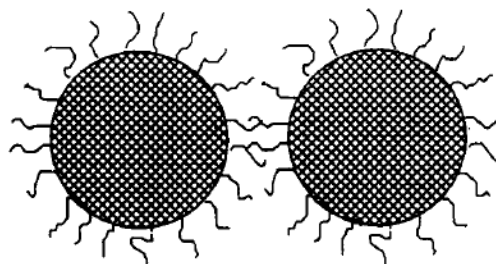
Figure 10.5: Schematic diagram describing steric interaction by polymer attachment on particles[106].

The most important factor that determines the degree of steric stabilization is the thickness of the adsorbed layer relative to the particle size. Therefore, larger particles will need more stabilizing layers to achieve the same level of stability due to the fact that van der Waals attraction is proportional to particle size [106]. Finally, although the particles have a repulsive interaction, there is still little van der Waals attraction between the layers, hence it is reasonable to limit the attraction between the particles by keeping them a finite distance apart where van der Waals attraction is minimised [106]. Therefore, in microfluidic channels, there is a high possibility of particles coming together and aggregating on the solid surface, thereby creating a multilayer film of adsorbed SWCNTs.

10.3.2 Adsorption kinetics of SWCNTs on APTES coated glass surfaces

If the adsorption rate of particles on surfaces plateaus (reaches equilibrium) in three hours, then there is some kinetics (Transport kinetics or chemical reaction). If equilibrium is reached in a day, then diffusion is the driving factor [205, 206]. In the case of the experiments carried out in this thesis, all adsorption reached equilibrium in under three hours. Therefore, there is some kinetics controlling the adsorption. Hence, adsorption kinetics will be done on each of the experiments carried out.

For the NAST methodology, the adsorption mechanism is of extreme importance as it determines factors that affects the kinetic performance of the adsorbent, in this case, Silane-functionalized rock. Pseudo first order and Pseudo second order adsorption kinetics models are the commonly used models. First order and second order adsorption kinetics models were used to determine the driving mechanism in the adsorption process, which could be physisorption or chemisorption. Identifying whether the driving mechanism is physisorption or chemisorption is important for the NAST methodology as it determines the likelihood of desorption of particles happening when oil production is resumed. Physisorption shows an electrostatic attachment which tends to be weak while chemisorption shows a chemical reaction is the attachment mechanism which is has a stronger bond. To further investigate the adsorption mechanism, the kinetic process was studied by fitting the experimental data to the kinetic models, presented in Table 10.2.

Table 10.2: Mathematical equations applied in the kinetic adsorption study of SWCNTs on APTES coated microfludic wall surfaces.

Kinetic models	Linear equations	Plot	Calculated coefficient
Pseudo first order	$ln(q_e - q_t)$ $= \dfrac{lnq_e - K_1 t}{2.303}$	$ln(q_e - q_t)\ vs.\ t$	$K_1 = -\text{slope} \times 2.303$ $q_e = e^{\text{intercept}}$
Pseudo second order	$\dfrac{1}{q_t} = \dfrac{1}{K_2 \times q_e^2} + \dfrac{t}{q_e}$	$\dfrac{t}{q_t}\ vs.\ t$	$K_2 = \dfrac{\text{slope}^2}{\text{intercept}}$ $q_e = \text{slope}^{-1}$

Where q_e and q_t (mg/m^2) are the adsorption capacities at equilibrium and time t (minutes) respectively. K_1 and K_2 (min^{-1}) is the pseudo first and second order rate constants respectively for the kinetic model.

An example of the fitted kinetic graph is shown in Figure 10.6 and Figure 10.7 which show the modelled first and second adsorption kinetic models for 10 mg/L concentration of CNTs. The 10 mg/L concentration of CNTs fits the first order adsorption kinetics models. This shows that it is a physisorption process. The rest of the adsorption kinetic graphs are located in appendix A.
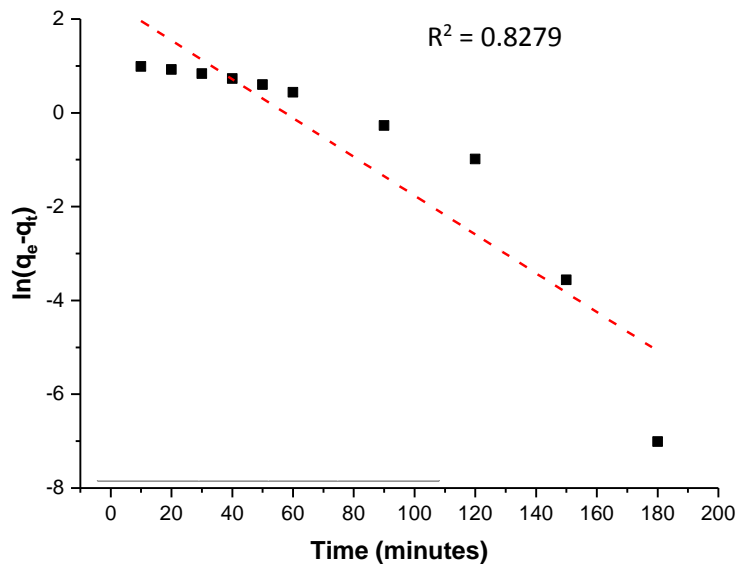
Figure 10.6: First order kinetic fitting for 10 mg/L of injected CNT concentration.
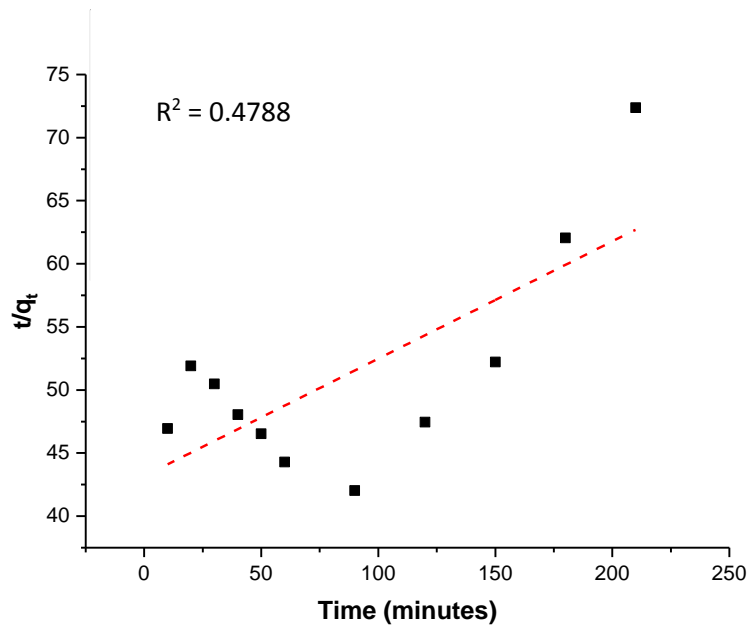
Figure 10.7: Second order kinetic fitting for 10 mg/L of injected CNT concentration.

10.4 Factors effecting adsorption capacity and adsorption kinetics of SWCNTs on APTES coated microfluidic channels

The previous sections have shown and analysis the overall adsorption processes occurring within the microfluidic channel and has therefore shown the capability of the Raman – microfluidic system in performing adsorption experiments. The next sections will analyse the effect on CNT concentration and pH on the adsorption capacity and kinetics of CNTs flowing in microfluidic channels.

10.4.1 Effects of particle concentration on adsorption capacity of salinized glass surfaces

The results presented in Chapter 6 showed that there is an optimum amount of injected SWCNT concentration in aqueous solution which is shown in Figure 7.33. Figure 10.8 shows that not only does a SWCNTs concentration of 10 mg/L have the maximum adsorption capacity within the range of concentrations, but that the adsorption capacity begins to diminish at higher concentrations. One of the major factors that plays a part in the adsorption kinetics and adsorption is the particle size of the SWCNTs.
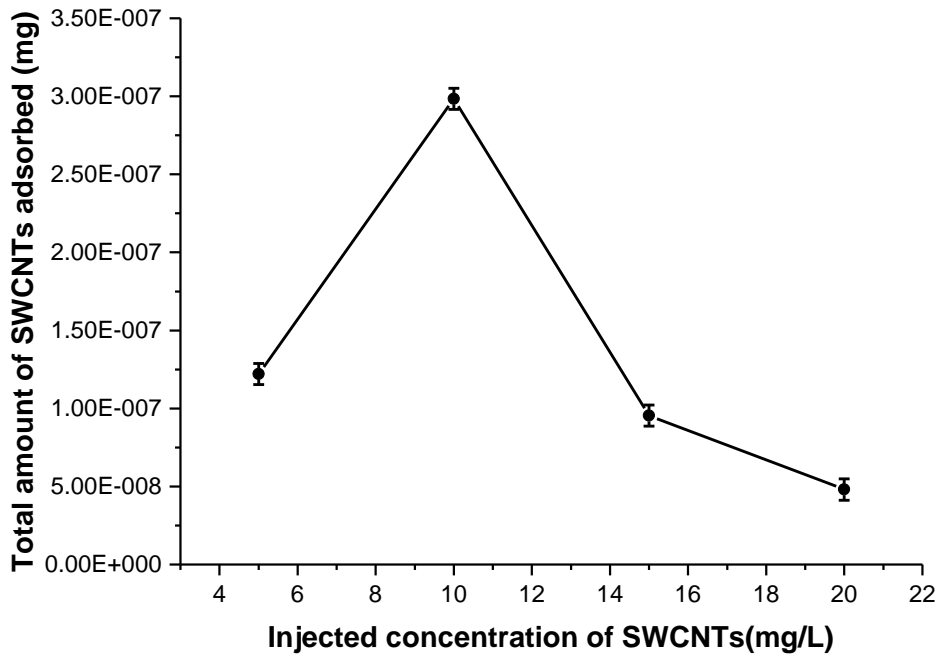
Figure 10.8: Maximum amount of CNTs adsorbed for each injected SWCNT concentration.

A number of factors are affected by particle concentration suspended in aqueous solution and hence, aggregation and deposition of particles. The effectiveness of the surfactant in stabilizing the particles reduces as the concentration of SWCNTs suspended in the aqueous solution increases after a certain concentration [106, 201, 207]. As the amount of SWCNTs suspended in aqueous solution increases, the required amount of surfactant needed to stabilized them increases as well in order to meet the required amount of long chained polymers needed to adsorbed on the surface of the particles.

From the results, it is clear that there comes a point at which the concentration of SWCNTs suspended in aqueous solution becomes detrimental to the quantity adsorbed to the APTES covered surface. This is due to a reduction in the dispersion effectiveness of the surfactant used for dispersing the particles.

10.4.1.1 Polymer bridging

As stated in the previous section, surfactants like Tween 80 attach on particles causing steric stabilization. However, when there are less long chain polymers attached to a particle due to bigger particles sizes, an individual chain can become attached to

another particles thus "bridging" them together (Figure 10.9). Furthermore, as the amount of SWCNTs increases in the solution, the closer the particles will be in confined place such as microfluidic channels.
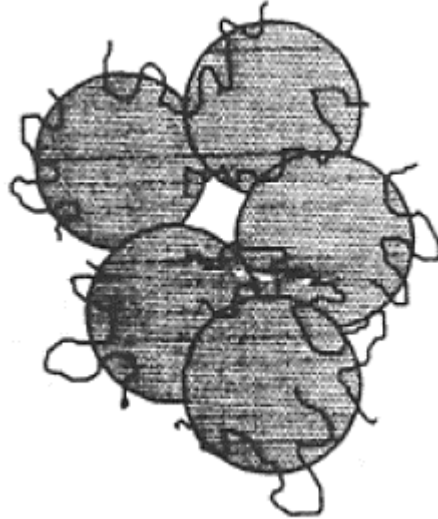
Figure 10.9: Schematic diagram illustrating bridging effects

This means that particle agglomeration will occur quicker and more bundling will be in the solution at higher SWCNT concentrations. Hence, there will be larger particle sizes in the solution. This bridging effect will be enhanced in very confined spaces such as in microfluidic channels. This has an effect on the adsorption capacity under dynamic conditions as drag will hinder adsorption of large particle when compared to smaller particles. Furthermore, the force of attraction between the particles at higher particle concentration will have an impact on the electrostatic attraction of SWCNTs on silane.

Elimelech [208] studied the role of particle size on the particle deposition and his experiments showed that the data point passes through a maximum, which indicates that there is optimum point at which a further increase in particle size is detrimental to rate of deposition and the adsorption capacity.

10.4.2 Effect of pH on adsorption capacity of salinized glass surfaces

Figure 7.35 in Chapter 7 section 7.6.2 shows an enhanced adsorption capacity at low pH. This could be as a result of hydrogen bonding occurring on the surface of the

particle which can enhance the adsorption of SWCNTs on the APTES coated surface. The effects of pH on amine functionalized surfaces have been well established. Koen van der Maaden, Jasmine Tomar, Wim Jiskoot, and Joke Bouwstra [209] showed the relationship between pH and 3-aminopropyltriethoxysilane (APTES) which is shown in Figure 10.10. At around pH 7, the APTES has only a very slight charge, which could be slightly positive or negative. Above pH7, the surface charge becomes more negative. At lower pH, the surface charge becomes positive. pH also affects the zeta potential of particles and in the case of SWCNTs, Figure 7.36 shows the effect of pH on the zeta potential of SWCNTs. These results show that electrostatic interaction is the driving mechanism as at low pH the adsorption capacity of the APTES functionalized glass is more than at higher pH which correlates with the increase positive surface charge at lower pH levels. Furthermore, Burgin et al [210], showed the increase in surface coverage of CNTs on amine functionalized glass upon a reduction of pH to below 5.
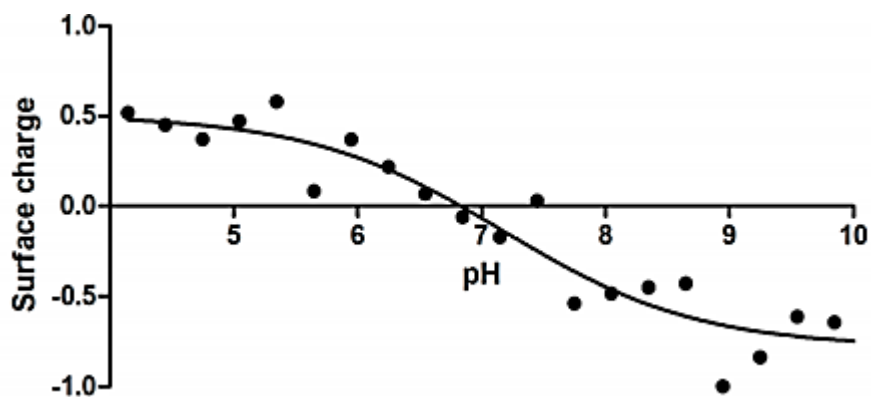
Figure 10.10: Effect of pH on the surface charge of APTES[209]

10.4.3 Adsorption kinetics modelling

Using pseudo first and second order kinetic modelling, it is possible to see the effect of SWCNT concentration and pH level on the adsorption mechanism. The important parameters are given in the following sections and the graphs are located in the appendix A.

10.4.3.1 Effects of particle concentration

Using first and second order kinetic modelling, Table 10.3 shows the major parameters needed to understand the adsorption kinetics for the different concentration of SWCNTs injected into the microfluidic channel.

Table 10.3: Data obtained from first and second order kinetic models fitted on experimental data.

Concentration (mg/L)	Experimental Q_e (mg/m^2)	First order kinetics			Second order kinetics		
		Q_e	K_1	R^2	Q_e	K_2	R^2
5	1.19	2.04	0.08	0.89	1.6	0.19	0.97
10	2.92	10.70	0.09	0.83	10	0.02	0.48
15	0.98	0.43	0.04	0.84	1.03	0.04	0.99
20	0.67	8.30	0.08	0.70	0.65	0.011	0.99

It can be seen that for the entire length of the experiments, with the exception of 10mg/L CNT concentration, the other concentrations of CNTs follow the second order kinetic. This will imply that the adsorption mechanism is driven by chemisorption. This is contradictory to other studies on particle adsorption and to what was mentioned in the previous section. Y.S. Ho and G. McKay [127] have shown that first and second order kinetic models can be mathematical fits for experimental data points depending on the length of time of the experiments. When considering just the first 60 minutes of the experiments, Table 10.4 shows the data obtained from the kinetic studies.

Table 10.4: First and second order kinetic parameters for different concentration of CNTs injected in the microfluidic channel for the first 60 minutes

Concentration (mg/L)	Experimental Q_e (mg/m^2)	First order kinetics			Second order kinetics		
		Q_e	K_1	R^2	Q_e	K_2	R^2
5	1.19	1.46	0.07	0.98	4.6	0.009	0.84
10	2.92	4.7	0.09	0.97	10	0.02	0.37
15	0.98	0.43	0.11	0.96	1.03	0.01	0.83

It can be seen that most of the experimental data (with the exception of 20 mg/L) fits the first order kinetics which shows that the initial adsorption period has physisorption mechanism.

The second period, after 60 minutes, Table 10.5 shows that the injected CNTs are better fitted to the second order kinetics than the first order kinetics.

Table 10.5: First and second order kinetic parameters for different concentration of CNTs injected in the microfluidic channel for the second 60 minutes

Concentration (mg/L)	First order kinetics			Second order kinetics		
	Q_e	K_1	R^2	Q_e	K_2	R^2
5	5.55	0.10	0.90	1.33	0.034	0.99
10	147.25	0.13	0.86	6.67	0.0007	0.91
15	0.15	0.02	0.89	0.94	0.1596	0.99

For later times, polymer bridging might be occurring between the particles adsorbed on the surface and the particles still suspended in the solution. The process occurs at

slower rate of adsorption than at the start of the experiments. This might explain the second order kinetic fitting for the later period and the entire experimental time.

10.4.3.2 Effect of pH

Table 10.6 shows the kinetic study done on the SWCNT adsorption at pH 4 for the entire time period. According to the R-squared values of the regression analysis present in Table 10.4, the pseudo-first-order model offers the best mathematical fit to describe the adsorption kinetics of SWCNTs at pH 4 level condition. Once again, this fitting implies a physisorption driven mechanism in the kinetics. This further confirms the processes discussed in section 9.7 which shows that there is more of a physical adsorption process happening which could be as a result of the effect zeta potential of the SWCNTs and the surface charge of silane at pH4. Furthermore, Burgin et al [210] showed similar results due to changes in pH level and concluded that electrostatic interaction plays a major role in the adsorption process.

Table 10.6: First and second order kinetics parameters at pH 4

pH Level	Experimental Q_e (mg/m^2)	First order kinetics			Second order kinetics		
		Q_e	K_1	R^2	Q_e	K_2	R^2
4	0.84	1.00	0.09	0.99	1.09	0.026	0.96

10.5 Transport kinetics of SWCNTs in microfluidic channels

The Raman Microfluidic (RM) system allows for steady state diffusion of salts due to the pumping system and microfluidic channel's geometry which provide passive mixing needed to necessitate the natural diffusion of salt in an undisturbed creeping flow regime. Data collection and analytical processes for transport kinetics are similar in terms of grid system and baseline correction used for adsorption experiments. The grid system is used as a way to track the location of the particles flowing through the system by using the signature G peak.

Particle transport phenomena will happen during the NAST 1 processes. As a result, it is important to understand the transport kinetics of particles and what conditions might affect them in reservoirs. Common environmental parameters that are experienced in the reservoirs are pH level, temperature, flow rate, salinity level amongst other things. One other environmental condition that can occur in reservoirs is a salt gradient in the fluids due to contact between low and high salinity waters in EOR processes.

Figure 8.9 in chapter 8 showed that under creeping flow in microfluidic channels, SWCNT transport will be advection driven under different pH levels, particle concentration levels and flow rates. Particle transport under laminar or creeping flow tend to follow stoke drag law which was presented in chapter 9 using COMSOL simulation software. This shows that the response time for particles of this size (1µm) will be very small in relation to changes in fluid flow direction and speed in the channels.

10.5.1 Effect of salt gradient on transport kinetics of SWCNTs

Since CNTs have a surface charge, an applied electric field in the system will cause particle mobility due the zeta potential. A salt gradient in the reservoir might induce an electric field which causes particle migration called diffusiophoresis. Studies have shown this phenomena under different condition [117, 119, 211-213]. Therefore it is useful to establish the effect of salt gradients on the transport of SWCNTs.

These salt gradients can be used the determine the magnitude of the electric field generated from the salt diffusion across the channel. The electric field generated from the salt diffusion is proportional to the concentration gradient and is expressed mathematically [115] as:

$$E = \frac{kT}{Ze} \beta \frac{\nabla C}{C} \qquad\qquad Equation\ 10.1$$

Where k is the Boltzmann constant (J/K), T is the system temperature (K), Z is the valence of the constituent ions of the solute, e is the proton charge and C is the ionic concentration.

β is the diffusivity difference factor which is dependent on the nature of the salt.

$$\beta = \frac{D_+ - D_-}{D_+ + D_-} \qquad\qquad Equation\ 10.2$$

Where D_+ is the cation diffusivity (m^2/s) and D_- is the anion diffusivity (m^2/s).

In the case of a monovalent salt like NaCl, the diffusivity of Na$^+$ is less than Cl$^-$, which gives a negative value (-0.207). This determines the direction of the electric field and hence the direction of the particle migration. For a β negative salt like NaCl, the negatively – charge particles transport towards a higher ionic concentration. The results from the transport experiments confirms these particle movements [115].

The diffusion coefficient (D_s) of SWCNT as predicted by Stokes-Einstein relationship (Appendix A) is calculated as 0.399 μm^2/s. This is the value under static conditions. In order to compare the diffusiophoretic migration of particles with the migration of particles under a controlled environment (no salt gradient), it is important to take the common parameters used in both sets of dynamic flow experiments. These parameters are the width of the channel and the speed of the fluid flow. Relating the Peclet number (Pe) and the width of the channel will determine the distance required for full mixing of the particles which is based on the diffusion coefficient of the particle.

Using the equation for efficient mixing:

$$mixing = Pe\,.w = \frac{w^2 v}{D_s} \qquad\qquad Equation\ 10.3$$

Where v is the velocity of the fluid (m/s), w is the length scale (m) and D_s is the diffusion coefficient (m^2/s).

Complete mixing will occur after a distance of 26 metres under the controlled environment, which is very large compared to the dimensions of the microfluidic flow cell which has a length of 12 mm. Therefore it can assumed that the mixing or migration of CNTs from the streamline is negligible within the channel, which further confirms the advection transport kinetics of CNTs.

Further confirmation is found in Figure 8.9 which showed little to no diffusion present in the transport of SWCNTs in the absence of a salt gradient. Therefore, the diffusion-

like motion of the particles, which is called the effective diffusion coefficient in this thesis, will be compared to the calculated diffusion coefficient of SWCNTs. The effective diffusion coefficient D_{eff} is obtained from the data in Figure 8.11. This is done by dividing the area covered by the CNTs when diffusiophoretic migration stops, by the time taken to reach that equilibrium. These calculations will produce a ratio of D_{eff}/D_s for different salt concentrations injected in the microfluidic channel (Figure 10.11).
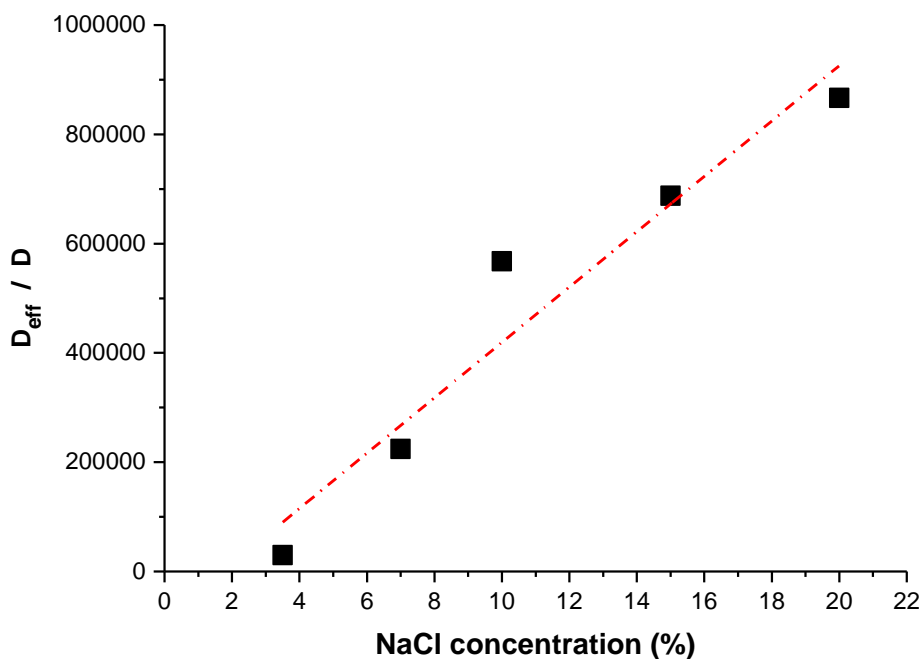
Figure 10.11: Relationship between the diffusion coefficient of SWCNTs in the controlled environment and at different concentration of NaCl salt injection.

From Figure 10.11 above, there is a clear linear trend of proportionality between an increase in effective diffusion and an increase in salt concentration. This shows that the salt gradient is the primary driving factor. It must be emphasized that the effective diffusion coefficient of the SWCNT is not the same as colloidal diffusion coefficient since it is dependent on the salt diffusion properties. The author uses the term diffusion coefficient to demonstrate the diffusion – like behaviour of SWCNTs that is induced by the diffusiophoretic mobility under the solute gradient.

Table 10.5 below shows calculations made to determine the distance at which the particles will be fully mixed if the effective diffusion coefficient D_{eff} was not dependent on the salt diffusion.

Table 10.7: Efficient mixing of different effective diffusion coefficient of SWCNTs which originated from different injected concentration of NACL solution

Concentration of NaCl injected	Effective diffusion coefficient (m^2/s)	Pe. w(mm)
3.5%	3.0E-08	3.55E-01
7%	2.2E-07	4.74E-02
10%	5.7E-07	1.87E-02
15%	6.9E-07	1.54E-02
20%	8.7E-07	1.23E-02

It can be seen that if the particle migration was independent of the salt diffusion then the particles will achieve full spread in less than a millimetre. Therefore, the results show that diffusiophoresis, which is due to presence of a salt gradient in the system, will perturb the transport of CNTs flowing in an aqueous solution.

This dependency is further confirmed due the simulation results from COMSOL showing the salt gradient is negligible after 6 mm from junction inlets of the channel (Figure 10.12). The maximum salt gradient at any section of the channel occurs at the centre. Figure 8.8 in Chapter 8 shows that all particle migration had stopped at this point for all experiments conducted. Which indicates that the electric field generated by the salt gradient is insufficient for diffusiophoresis to occur.
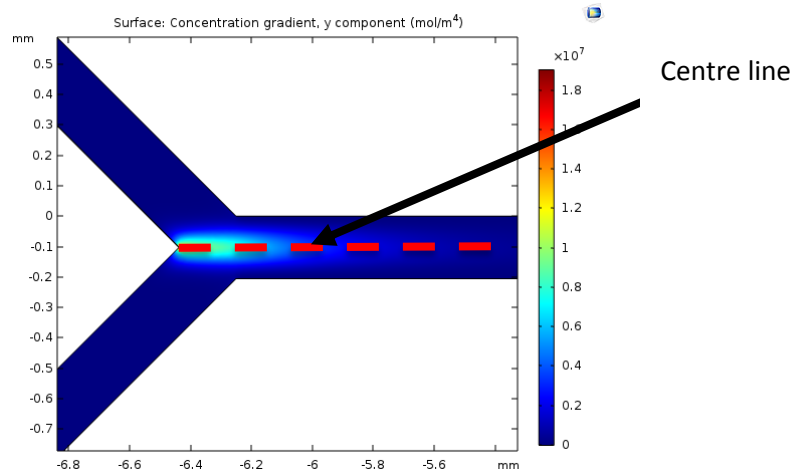
Figure 10.12: Y –Junction Channel diagram highlighting the centre line of the channel
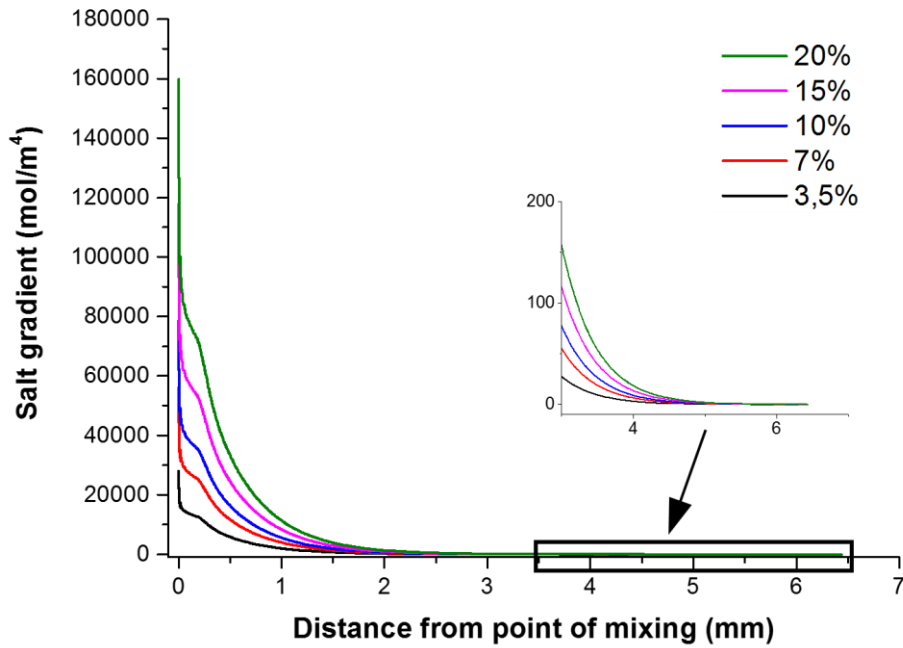
Figure 10.13: Salt gradients along the channel from the centre line of the channel

Diffusiophoresis occurs under two primary mechanisms; electrophoresis and chemiphoresis. For absolute values of zeta potentials below 42 mV, electrophoresis dominates in the system [115, 214, 215]. As the measured zeta potential of the SWCNT used in this thesis is -14 mV, the Smoluchowski equation shows the relationship between the electrophoretic velocity of the particles and the applied

electric field generated from the salt diffusion in the system at a given zeta potential [115, 215, 216].

$$v_{ep} = \frac{\varepsilon \zeta E}{\eta}$$
<div align="right">*Equation 9.4*</div>

Where ε is the dielectric permittivity (F/m) of the fluid and v_{ep} is the electrophoretic velocity (m/s)

This equation is a good approximation for any particle shape or for particles with non-uniform surface charge which using the average zeta potential of the particle surface [115].

It has already been established from literature that there is a relationship between the electric field and the salt concentration gradient. It shows that the electric field generated is directly proportional to the salt gradient. Therefore, it can ascertained from Figure 8.10 that the relationship between salt concentration gradient and diffusiophoretic velocity exist and is the main driving force of the particle migrations across the channel.

10.5.2 Effect of surfactant on diffusiophoretic migration of SWCNTs.

The key factors that affect diffusiophoretic velocity are concentration gradient, finite zeta potential and the ionic diffusivities of the salt in question. For SWCNTs suspended in aqueous solution in the presence of an ionic surfactant (in this case SDBS), the zeta potential rises to -44 mV, which indicates that chemiphoresis is the dominant mechanism due to the increase in ionic surfactant. However, no quantifiable analysis could be done at this point as there was an instant migration of particles at the converging junction, which is the point at which the salt water meets the particles suspended in aqueous solution. Furthermore, the migration did not follow a steady state trajectory like the tween 80 suspended particles. Studies have shown that SBDS and salt solution effect each other in different ways. Mohsin *et al* [217] showed that SDBS precipitates in the presences of salt solution. There may be other underlying factors that could explain the effect of SBDS on diffusiophoresis, however, that is beyond the scope of this thesis.

10.6 Relevance of results to the NAST methodology

From the developed Raman-microfluidic integrated system, adsorption experiments have produced results that have vital information that could improve the NAST methodology. Results have shown that there is a maximum CNT concentration needed to get the maximum adsorption capacity on salinized walls.

The efficiency of the adsorption diminishes as the CNT concentration increases past that optimum point. This concentration is affected by the type of surfactant and the amount of surfactant used to disperse the CNTs in aqueous solution. Furthermore, results show that reducing the pH level of the aqueous solution can improve the adsorption capacity of the APTES coated channel surfaces. Finally, it has been established that the driving mechanism for CNT adsorption on APTES coated surfaces is physisorption, which indicates that the attachment of the CNTs to the APTES coated wall surface is electrostatically bonded. This means that it is possible for some particles to detach from the surface under certain conditions such as high flow rates.

The Raman-microfluidic integrated set up also produced relevant transport kinetics studies of CNTs injected in the microfluidic channel. It established the well-known advection transport kinetic of particles such as CNTs under creeping flow condition thereby showcased the capabilities of the set up in performing transport kinetic studies of CNTs in microfluidic channels.

The effect of diffusiophoresis was shown to perturb the transport of CNTs from the streamlines of the fluid. As stated previously, diffusiophoresis occurs due to salt gradients in the channels or systems and this can have an impact on the placement of CNTs. Due to formation water in the reservoir which can contain a high amount of salt ions, a low salinity level of the injection water will cause a salt gradient to occur when the two waters meet, causing diffusiophoresis. Previous studies have shown that diffusiophoresis can aid in the placement of particles or polymers in dead end pore channel, spreading in channel networks and enhanced mixing of suspended particles [118, 121, 218]. Therefore, having an understanding of how salt gradients affects the migration of particle is vital in deciding the salinity level of water used in injecting the particles.

As stated earlier, the diffusiophoretic drift of the particles are coupled to the underlying salt diffusion process. Hence, a different transport dynamics of the particles will be obtained for different geometries and in more complex porous media. For example, if the salt gradient is sustained for a larger distance due to geometry or in the case of NAST an oil reservoir, then a uniform diffusiophoretic drift of the particle may occur. With this in mind, it is possible to use a salt gradient to enhance the transport of CNTs in porous media.

Lastly, results from transport experiments show that the type of surfactant used to disperse the particles will have an effect on the diffusiophoretic migration of particles which shows an understanding of these effects in vital in determining the best type of surfactant to use in dispersing the particles in environments were salt gradients are likely to occur.

10.7 Summary

This chapter has shown the capability of Raman microscopy to detect and quantify CNTs suspended in aqueous solution below CNT concentrations used for acute toxicity tests on aquatic organisms. This was achieved with minimal sample preparation which is necessary for the NAST methodology. As a result, Raman can be used as onsite monitoring system for the NAST methodology.

Also presented are some factors that might affect the adsorption of CNTs. As a result, a better understanding of the adsorption mechanisms of CNTs in microfluidic systems has been achieved. Also presented in this chapter are the factors that affected the transport kinetics of CNTs. Different environmental parameters such as pH and flow rates as well as CNT concentration were tested to investigate their affect the transport kinetics of the particles. During injection, the salinity of the water will determine the magnitude of the salt gradient created when the injected water meets the formation waters located in the reservoirs. From the experiments, salt gradients were found to affect the transport kinetics of the particles.

As a result of all the experiments conducted, the summary of the discoveries are as follows:

- It was found that CNT concentration can affect the adsorption capacity of APTES coated surfaces. Results show that there is a CNT concentration level that obtains the maximum adsorption capacity on APTES coated surfaces at a neutral pH level. Any higher concentration after this point will be detrimental to the adsorption capacity

- It was found that at low pH, the adsorption capacity of CNTs increases and reduces for high pH.

- Adsorption kinetics studies show that at the initial period of the adsorption process, the driving mechanism (first order) of the CNT adsorption on the APTES coated surface is physisorption. At a later period, chemisorption mechanism (Second order) appears to be driving the adsorption process.

- The one factor affecting the transport kinetics of CNTs under creeping flow regime is the salt gradient in the solution. The higher the salt gradient, the higher the perturbed particle migration.

- Ionic surfactants such as SDBS can affect the diffusiophoretic migration of CNTs.

- These experimental results showcased the capabilities of the Raman microfluidic setup in performing adsorption and transport kinetic experiments of SWCNTs flowing in microfluidic channels.

Chapter 11. Conclusions and future work

This thesis aimed to provide an insight to factors affecting the first part of the NAST methodology, NAST1. Furthermore, it aimed to investigate ways to monitor the amount of CNT particles leaving the reservoir during oil production. To achieve this, two analytical techniques were investigated to establish their suitability in detecting and quantifying CNTs in aqueous solution. One of these techniques was then integrated with a microfluidic setup to perform particle adsorption and transport experiments. This system is a platform for NAST experiments which are at the early stages, and can be improved and used for future experiments to optimize the NAST methodology.

11.1 Choice of analytical technique for monitoring CNT concentrations

Raman microscopy and ICP were used to determine the accuracy, precision and limit of detection of CNTs with minimum sample preparation. It was found that due to the resonance effect on Raman scatter, metallic or semi-conducting SWCNTs produced exceptional Raman signal which put the limit of detection to ppb levels. It also showed that MWCNTs can be detected and quantified, albeit to a limited level when compared to SWCNTs. This instrument can be used as an online CNT concentration monitoring system for needed for the NAST methodology.

Previous studies have shown that with proper sample preparation, ICP can detect CNTs in aqueous solution to the ppt level, however, even with a one-step procedure, ICP can detect CNTs to the ppb level. ICP can be used for off-site analysis if ppt level of detection is required. It can be done by adding a digestion step capable of fully digesting the particles and releasing all the metallic content within the particles.

11.2 Usefulness and novelty of Raman microfluidic set up

This thesis has demonstrated for the first time the use of integrating Raman microscopy and microfluidic flow cells to conduct carbon nanotube transport and adsorption experiments. For this thesis, SWCNTs were used as a proxy to understand the adsorption and transport kinetics of CNTs. The results obtained from this study provide information necessary for optimizing the concentration of CNT injected into oil reservoirs. Finally, it showed the effect of pH on the adsorption of CNTs on APTES

coated surfaces. Transport studies were conducted to study the effect of pH, particle concentration, flow rates and salt gradients on transport kinetics of CNTs in microfluidic channels.

These results show the capability for the integrated system to conduct adsorption and transport experiments as an alternative to optical microscopic systems. This study has shown the advantages of using of Raman microscopy in perform such experiments by:

- The ability to distinguish CNTs within the system using their signature peaks as a tracer.

- The ability to make quantifiable measurements of the amount of CNTs adsorbed in the channels using these peaks.

11.3 Summary and contribution of findings to the NAST methodology

Chapter 6 showed that there is an maximum CNT concentration needed to achieve a maximum adsorption capacity on APTES coated walls. This was explained using DLVO theory and steric interactions. The initial period of adsorption fits a first order kinetics which means there is a physical adsorption occurring. The effect of pH was also studied and it was found that at lower pH levels the adsorption capacity increased and displayed more of a physisorption mechanism and can be explained by the effect of pH on the surface charge of the silane.

Chapter 7 and 8 showed that salt gradient will have an effect on the transport kinetics of CNTs. The chapters also showed the effect of surfactants on the diffusiophoretic migration of CNTs.

These findings contribute to the NAST methodology in the following areas:

- Results highlighting the effect of CNT concentration on the adsorption capacity of APTES coated wall surfaces can be used to decide what concentration of CNT should be injected into the reservoir.

- The effect of pH on CNT adsorption on the walls shows that the pH level of the injected water must be considered and maybe adjusted to achieve different adsorption capacities in the reservoirs.

- Salt gradients plays a role in particle migration. The transport kinetic results show that the salinity of the injected water and the type of surfactant used will affect the CNT placement in the reservoir. Therefore, knowledge of the salinity of formation waters can be used to determine the salinity of the injected water.

11.4 Future work

Following on from the research conducted within this thesis, there are several area that can be put forward for further in-depth study.

11.4.1 Raman Microfluidic integrated system

- The map scan can be improved by increasing the spot scan in a given area as this will improve the resolution of the map scan. However, this might come at the expense of longer scan time.

- The current set up is limited to room temperature experiments as there is little room in the Raman instrument's chamber to integrate a heating instrument. It is possible to include an external heating system outside the chamber.

11.4.2 Adsorption tests

- Further research is required to understand the adsorption kinetics of CNTs in more realistic reservoir conditions such as high temperature, high pressure conditions. Performing experiments using complex microfluidic channel geometries will highlight the effect of pore geometry on the adsorption kinetics of CNTs. As the injected and reservoir waters will have a certain level of salinity, experiments investigating the effect of salinity on adsorption kinetics of CNTs will provide more realistic results needed for the NAST methodology.

- Desorption experiments will show factors that effects the strength of the bond between the CNTs and the APTES coated surface. This is critical for NAST 3, which is further down the NAST methodology.

11.4.3 Transport studies of CNTs in microfluidic channels

- As well as the need to perform transport kinetics experiments of CNTs in more realistic reservoir conditions, further research is required to understand to the effects of pH, temperature and particle charge on particle migration. Furthermore, more realistic complex brine solutions should be used in transport kinetic experiments to provide a better understanding of particle transport in realistic conditions.

- Different channel geometries will affect the way ions will diffuse, which will in turn affect the salt gradient produced. Therefore, experimental studies on diffusiophoresis of particles in more complex pore channels should be done to investigate the placement of CNTs in porous media.

- The COMSOL simulations can be developed to include the electric field generated by the salt gradient. From this point, the electric field simulated can be used to generate the force required to cause particle migration from the flow streamlines. This can open the door for the simulation of diffusiophoresis of particles under various conditions.

References

1.   Contractor D. EIA anticipates 48% rise in world energy consumption by 2040 2016, May 12. Available from: http://www.drillingcontractor.org/eia-anticipates-48-rise-world-energy-consumption-2040-39524.

2.   Kong X, Ohadi M. Applications of Micro and Nano Technologies in the Oil and Gas Industry - Overview of the Recent Progress. 2010/1/1/. SPE: Society of Petroleum Engineers.

3.   Adminstration USEI. INTERNATIONAL ENERGY OUTLOOK 2018. 2018, July 24.

4.   Chen T, Neville A, Yuan M. Calcium carbonate scale formation—assessing the initial stages of precipitation and deposition. Journal of Petroleum Science and Engineering. 2005;46(3):185-94.

5.   Torsaeter O, Li S, Hendraningrat L, editors. Enhancing Oil Recovery of Low-Permeability Berea Sandstone through Optimised Nanofluids Concentration. SPE Enhanced Oil Recovery Conference; 2013: Society of Petroleum Engineers.

6.   Mackay E, Sorbie K, editors. An evaluation of simulation techniques for modelling squeeze treatments. SPE Annual Technical Conference and Exhibition; 1999: Society of Petroleum Engineers.

7.   Hussein AK. Applications of nanotechnology in renewable energies—A comprehensive overview and understanding. Renewable and Sustainable Energy Reviews. 2015;42:460-76.

8.   El-Diasty AI, Ragab AMS. Applications of Nanotechnology in the Oil & Gas Industry: Latest Trends Worldwide & Future Challenges in Egypt. 2013/4/15/. SPE: Society of Petroleum Engineers.

9.   Serrano E, Rus G, García-Martínez J. Nanotechnology for sustainable energy. Renewable and Sustainable Energy Reviews. 2009;13(9):2373-84.

10.   Nouailhat A. The Uses of Nanotechnologies: They are Everywhere! An Introduction to Nanoscience and Nanotechnology: ISTE; 2010. p. 107-41.

11.   Ghorbani N, Wilson MCT, Kapur N, Fleming N, Neville A. Carbon Nanotubes: A New Methodology for Enhanced Squeeze Lifetime CNTs. SPE International Oilfield Scale Conference and Exhibition; 2014/5/14/; Aberdeen, Scotland. SPE: Society of Petroleum Engineers; 2014.

12.   Mattison NT, O'Carroll DM, Kerry Rowe R, Petersen EJ. Impact of porous media grain size on the transport of multi-walled carbon nanotubes. Environ Sci Technol. 2011;45(22):9765-75.

13.   Kadhum MJ, Swatske DP, Chen C, Resasco DE, Harwell JH, Shiau B, editors. Propagation of carbon nanotube hybrids through porous media for advancing oilfield technology. SPE International Symposium on Oilfield Chemistry; 2015: Society of Petroleum Engineers.

14.   Feng T, Hoagland DA, Russell TP. Assembly of Acid-Functionalized Single-Walled Carbon Nanotubes at Oil/Water Interfaces. Langmuir. 2014;30(4):1072-9.

15. Soleimani H, Yahya N, Baig MK, Khodapanah L, Sabet M, Burda M, Oechsner A, Awang M. Oil Gas Research. 2015;1(1):1-5.
16. Nazari Moghaddam R, Bahramian A, Fakhroueian Z, Karimi A, Arya S. Comparative study of using nanoparticles for enhanced oil recovery: wettability alteration of carbonate rocks. Energy & Fuels. 2015;29(4):2111-9.
17. Holesinger TG, DePaula R, Rowley J, Sperling K, Pappas J, editors. Carbon nanotube composite cables for ultra-deepwater oil and gas fields. Offshore Technology Conference; 2014: Offshore Technology Conference.
18. Manohara HM, Mojarradi M, Toda R, Lin RH, editors. Carbon nanotube-based high temperature vacuum microelectronics for E&P applications. SPE International Oilfield Nanotechnology Conference and Exhibition; 2012: Society of Petroleum Engineers.
19. Rahimirad M, Dehghani Baghbadorani J, editors. Properties of oil well cement reinforced by carbon nanotubes. SPE International Oilfield Nanotechnology Conference and Exhibition; 2012: Society of Petroleum Engineers.
20. Fazelabdolabadi B, Khodadadi AA, Sedaghatzadeh M. Thermal and rheological properties improvement of drilling fluids using functionalized carbon nanotubes. Applied Nanoscience. 2015;5(6):651-9.
21. Khalil M, Jan BM, Tong CW, Berawi MA. Advanced nanomaterials in oil and gas industry: Design, application and challenges. Applied Energy. 2017;191:287-310.
22. Ghorbani N, Wilson MCT, Kapur N, Fleming N, Tjomsland T, Neville A. Adsorption of polyphosphinocarboxylic acid (PPCA) scale inhibitor on carbon nanotubes (CNTs): A prospective method for enhanced oilfield scale prevention. Journal of Petroleum Science and Engineering. 2017;150:305-11.
23. Liu Y, Zhao Y, Sun B, Chen C. Understanding the Toxicity of Carbon Nanotubes. Accounts of Chemical Research. 2013;46(3):702-13.
24. Qi W, Tian L, An W, Wu Q, Liu J, Jiang C, Yang J, Tang B, Zhang Y, Xie K, Wang X, Li Z, Wu W. Curing the Toxicity of Multi-Walled Carbon Nanotubes through Native Small-molecule Drugs. Scientific Reports. 2017;7(1):2815.
25. Kim KT, Klaine SJ, Lin SJ, Ke PC, Kim SD. Acute toxicity of a mixture of copper and single-walled carbon nanotubes to Daphnia magna. Environ Toxicol Chem. 2010;29(1):122.
26. Mouchet F, Landois P, Puech P, Pinelli E, Flahaut E, Gauthier L. Carbon nanotube ecotoxicity in amphibians: Assessment of multiwalled carbon nanotubes and comparison with double-walled carbon nanotubes. Nanomedicine. 2010;5(6):963.
27. Schlagenhauf L, Buerki-Thurnherr T, Kuo YY, Wichser A, Nuesch F, Wick P, Wang J. Carbon Nanotubes Released from an Epoxy-Based Nanocomposite: Quantification and Particle Toxicity. Environ Sci Technol. 2015;49(17):10616-23.
28. Fraser TWK, Reinardy HC, Shaw BJ, Henry TB, Handy RD. Dietary toxicity of single walled carbon nanotubes and fullerenes (C60) in rainbow trout (Oncorhynchus mykiss). Nanotoxicol. 2011;5(1):98.

29. Galloway T, Lewis C, Dolciotti I, Johnston BD, Moger J, Regoli F. Sublethal toxicity of nano-titanium dioxide and carbon nanotubes in a sediment dwelling marine polychaete. Environ Pollut. 2010;158(5):1748.

30. Luongo LA, Zhang XQ. Toxicity of carbon nanotubes to the activated sludge process. J Hazard Mater. 2010;178(1–3):356.

31. Wan J, Tokunaga TK, Tsang C-F, Bodvarsson GS. Improved Glass Micromodel Methods for Studies of Flow and Transport in Fractured Porous Media. Water Resources Research. 1996;32(7):1955-64.

32. Dawe RA, Grattoni CA. The visualization of the pore-scale physics of hydrocarbon recovery from reservoirs. first break. 1998;16(11):371-86.

33. Marchington RF. Applications of microfluidic chips in optical manipulation & photoporation: University of St Andrews; 2010.

34. Tabeling P. Introduction to microfluidics: Oxford University Press; 2010.

35. Choi JH, Nam YW, Hong JS. Microfluidic study on CNT dispersion during breakup of aqueous alginic acid drop in continuous PDMS phase. Korea-Australia Rheology Journal. 2013;25(1):1-8.

36. Wang Q, Lee J-H, Jeong S-W, Jang A, Lee S, Choi H. Mobilization and deposition of iron nano and sub-micrometer particles in porous media: A glass micromodel study. Journal of hazardous materials. 2011;192(3):1466-75.

37. Chrimes A. Nanotechnology enabled microfluidics/Raman spectroscopy systems for bio applications. 2013.

38. Gupta R, Bastani B, Goddard N, Grieve B. Absorption spectroscopy in microfluidic flow cells using a metal clad leaky waveguide device with a porous gel waveguide layer. Analyst. 2013;138(1):307-14.

39. Sabuncu AC, Zhuang J, Kolb JF, Beskok A. Microfluidic impedance spectroscopy as a tool for quantitative biology and biotechnology. Biomicrofluidics. 2012;6(3):034103.

40. Jahn I, Žukovskaja O, Zheng X-S, Weber K, Bocklitz T, Cialla-May D, Popp J. Surface-enhanced Raman spectroscopy and microfluidic platforms: challenges, solutions and potential applications. Analyst. 2017;142(7):1022-47.

41. Subhono B. Deploying nanotechnology for oil and gas flow assurance: Understanding the transport and penetration of nano-particles in porous media: University of Leeds; 2014.

42. Fletcher A, Davis J. How EOR Can be Transformed by Nanotechnology. 2010/1/1/. SPE: Society of Petroleum Engineers.

43. Lake LW. Enhanced oil recovery. 1989.

44. Mackay E, Sorbie K, Kavle V, Sørhaug E, Melvin K, Sjursæther K, Jordan M, editors. Impact of in-situ sulphate stripping on scale management in the Gyda Field, paper SPE 100516. SPE 8th International Symposium on Oilfield Scale; 2006.

45. Ghorbani N. Nanotechnology enhanced squeeze treatments for efficient oilfield scale management. Leeds U6 - ctx_ver=Z39.88-2004&ctx_enc=info%3Aofi%2Fenc%3AUTF-8&rfr_id=info:sid/summon.serialssolutions.com&rft_val_fmt=info:ofi/fmt:kev:mtx:dissertation&rft.genre=dissertation&rft.title=Nanotechnology+enhanced+squeeze+treatments+for+efficient+oilfield+scale+manage

ment&rft.DBID=%7E%7EZ&rft.au=Ghorbani%2C+Nasser&rft.date=20
12-01-01&rft.externalDocID=b34231201&paramdict=en-US U7 -
Dissertation2012.

46.   Eroini V. Kinetic study of calcium carbonate formation and inhibition by using an in-situ flow cell: University of Leeds; 2011.

47.   Haghtalab A, Kamali MJ, Shahrabadi A. Prediction mineral scale formation in oil reservoirs during water injection. Fluid Phase Equilibria. 2014;373:43-54.

48.   Crabtree M, Eslinger D, Fletcher P, Miller M, Johnson A, King G. Fighting Scale—Removal and Prevention.

49.   Sanders L. An integrated study of corrosion and scale interactions in the absence and presence of combined chemicals: University of Leeds; 2014.

50.   Sandengen K. Prediction of mineral scale formation in wet gas condensate pipelines and in MEG (mono ethylene glycol) regeneration plants: Norwegian University of Science and Technology; 2006.

51.   Duggirala PY. Formation of Calcium Carbonate Scale and Control Strategies in Continuous Digesters.

52.   Sanni OS. Calcium carbonate surface/bulk scaling mechanisms and kinetics in a once-through in-situ flow visualization rig: University of Leeds; 2016.

53.   Waly T. Minimizing the use of chemicals to control scaling in SWRO. Taylor & Francis, London; 2011.

54.   Pytkowicz RM. Rates of inorganic calcium carbonate nucleation. The Journal of Geology. 1965;73(1):196-9.

55.   Chen T, Neville A, Yuan M. Assessing the effect of Mg^{2+} on $CaCO_3$ scale formation–bulk precipitation and surface deposition. Journal of Crystal Growth. 2005;275(1-2):e1341-e7.

56.   Alamdari A, Alamdari A, Mowla D. Kinetics of calcium carbonate precipitation through CO_2 absorption from flue gas into distiller waste of soda ash plant. Journal of Industrial and Engineering Chemistry. 2014;20(5):3480-6.

57.   Söhnel O, Mullin J. A method for the determination of precipitation induction periods. Journal of Crystal Growth. 1978;44(4):377-82.

58.   Mullin JW. Crystallization: Elsevier; 2001.

59.   Stamatakis E, Stubos A, Palyvos J, Chatzichristos C, Muller J. An improved predictive correlation for the induction time of $CaCO_3$ scale formation during flow in porous media. Journal of colloid and interface science. 2005;286(1):7-13.

60.   Garside J. Industrial crystallization from solution. Chemical Engineering Science. 1985;40(1):3-26.

61.   Mullin JW. 5 - Nucleation. In: Mullin JW, editor. Crystallization (Fourth Edition). Oxford: Butterworth-Heinemann; 2001. p. 181-215.

62.   Erdemir D, Lee AY, Myerson AS. Nucleation of crystals from solution: classical and two-step models. Accounts of chemical research. 2009;42(5):621-9.

63.   Yu J, Lei M, Cheng B, Zhao X. Facile preparation of calcium carbonate particles with unusual morphologies by precipitation reaction. Journal of crystal growth. 2004;261(4):566-70.

64. Nancollas G, Purdie N. The kinetics of crystal growth. Quarterly Reviews, Chemical Society. 1964;18(1):1-20.

65. Xiang L, Xiang Y, Wang ZG, Jin Y. Influence of chemical additives on the formation of super-fine calcium carbonate. Powder Technology. 2002;126(2):129-33.

66. Berner RA. The role of magnesium in the crystal growth of calcite and aragonite from sea water. Geochimica et Cosmochimica Acta. 1975;39(4):489-504.

67. Li G, Li Z, Ma H. Synthesis of aragonite by carbonization from dolomite without any additives. International Journal of Mineral Processing. 2013;123:25-31.

68. Parkin SJ, Vogel R, Persson M, Funk M, Loke VL, Nieminen TA, Heckenberg NR, Rubinsztein-Dunlop H. Highly birefringent vaterite microspheres: production, characterization and applications for optical micromanipulation. Optics Express. 2009;17(24):21944-55.

69. Han YS, Hadiko G, Fuji M, Takahashi M. Factors affecting the phase and morphology of $CaCO_3$ prepared by a bubbling method. Journal of the European Ceramic Society. 2006;26(4–5):843-7.

70. Feng B, Yong AK, An H. Effect of various factors on the particle size of calcium carbonate formed in a precipitation process. Materials Science and Engineering: A. 2007;445–446:170-9.

71. Dyer SJ, Graham GM. The effect of temperature and pressure on oilfield scale formation. Journal of Petroleum Science and Engineering. 2002;35(1–2):95-107.

72. Gal J-Y, Fovet Y, Gache N. Mechanisms of scale formation and carbon dioxide partial pressure influence. Part II. Application in the study of mineral waters of reference. Water Research. 2002;36(3):764-73.

73. Shutemov D. Modeling and Management of Scale Potential in an Oil Field Production Network. 2013.

74. Sigfusson B, Gunnarsson I, Energy R, editors. Scaling prevention experiments in the hellisheiði power plant, Iceland.

75. Pardue JE. A New Inhibitor for Scale Squeeze Applications. 1991/1/1/. SPE: Society of Petroleum Engineers.

76. Fink JK. Chapter 7 - Scale Inhibitors. In: Fink JK, editor. Petroleum Engineer's Guide to Oil Field Chemicals and Fluids. Boston: Gulf Professional Publishing; 2012. p. 253-74.

77. Brown MRW, Kornberg A. Inorganic polyphosphate in the origin and survival of species. Proceedings of the National Academy of Sciences of the United States of America. 2004;101(46):16085-7.

78. Bache Ø, Nilsson S. Ester Cross-Linking of Polycarboxylic Acid Scale Inhibitors as a Possible Means to Increase Inhibitor Squeeze Lifetime. 2000/1/1/. SPE: Society of Petroleum Engineers.

79. Yang S-T, Huang H, Tay A, Qin W, De Guzman L, Nicolas ECS. Chapter 16 - Extractive Fermentation for the Production of Carboxylic Acids. In: Yang S-T, editor. Bioprocessing for Value-Added Products from Renewable Resources. Amsterdam: Elsevier; 2007. p. 421-46.

80. Ketrane R, Saidani B, Gil O, Leleyter L, Baraud F. Efficiency of five scale inhibitors on calcium carbonate precipitation from hard water: Effect of temperature and concentration. Desalination. 2009;249(3):1397-404.

81. Zhang H, Mackay EJ, Chen P, Sorbie KS. Non-Equilibrium Adsorption and Precipitation of Scale Inhibitors: Corefloods and Mathematical Modelling. 2000/1/1/. SPE: Society of Petroleum Engineers.

82. Tantayakom V, Fogler H, Charoensirithavorn P, Chavadej S. Kinetic study of scale inhibitor precipitation in squeeze treatment. Crystal growth & design. 2005;5(1):329-35.

83. Graham GM. A mechanistic examination of the factors influencng downhole BaSO4 oilfield scale inhibitors and the design of new species: Heriot-Watt University; 1994.

84. Vazquez O, Herrero P, Mackay E, Jordan M. Non-aqueous vs aqueous overflush scale inhibitor squeeze treatment in an oilfield offshore Norway. Journal of Petroleum Science and Engineering. 2016;138:1-10.

85. Chen T, Chen P, Montgomerie H, Hagen T, Heath S, editors. Scale Squeeze Treatments in Short Perforation and High Water Production ESP Wells-Application of Oilfield Scale Management Toolbox. IPTC 2013: International Petroleum Technology Conference; 2013.

86. Ghosh B, Li X. Effect of surfactant composition on reservoir wettability and scale inhibitor squeeze lifetime in oil wet carbonate reservoir. Journal of Petroleum Science and Engineering. 2013;108:250-8.

87. Sorbie K, Wat R, Todd A. Interpretation and theoretical modeling of scale-inhibitor/tracer corefloods. SPE production engineering. 1992;7(03):307-12.

88. Heath SM, Juliussen B, Chen P, Chen T, Benvie R. Novel Scale Squeeze Technology and Treatment Designs for Improving Scale Inhibitor Retention and Treatment Lifetimes - Use of Ionic Polymers in the Overflush. 2012/1/1/. SPE: Society of Petroleum Engineers.

89. Schimmel T. Nanotechnology. An Introduction. By Jeremy J. Ramsden. Angewandte Chemie International Edition. 2012;51(39):9733-.

90. Ayatollahi S, Zerafat MM. Nanotechnology-Assisted EOR Techniques: New Solutions to Old Challenges. 2012/1/1/. SPE: Society of Petroleum Engineers.

91. Zhang T, Espinosa D, Yoon KY, Rahmani AR, Yu H, Caldelas FM, Ryoo S, Roberts M, Prodanovic M, Johnston KP, Milner TE, Bryant SL, Huh C. Engineered Nanoparticles as Harsh-Condition Emulsion and Foam Stabilizers and as Novel Sensors. 2011/1/1/. OTC: Offshore Technology Conference.

92. Turkenburg D, Chin PTK, Fischer H. Use of Modified Nanoparticles in Oil and Gas Reservoir Management. 2012/1/1/. SPE: Society of Petroleum Engineers.

93. Zhang X, Gu H, Fujii M. Experimental Study on the Effective Thermal Conductivity and Thermal Diffusivity of Nanofluids. International Journal of Thermophysics. 2006;27(2):569-80.

94. Torsater O, Engeset B, Hendraningrat L, Suwarno S. Improved Oil Recovery by Nanofluids Flooding: An Experimental Study. 2012/1/1/. SPE: Society of Petroleum Engineers.

95. Iijima S. Helical microtubules of graphitic carbon. nature. 1991;354(6348):56.

96.   Mubarak NM, Abdullah EC, Jayakumar NS, Sahu JN. An overview on methods for the production of carbon nanotubes. Journal of Industrial and Engineering Chemistry. 2014;20(4):1186-97.

97.   Yawei L, Aneziris CG, Shengli J, Shaobai S, Xilai C. Application of Multi-Walled Carbon Nanotubes for Innovation in Advanced Refractories. 2011.

98.   Martins-Júnior P, Alcântara C, Resende R, Ferreira A. Carbon nanotubes directions and perspectives in oral regenerative medicine. Journal of dental research. 2013:0022034513490957.

99.   Vazquez O, Thanasutives P, Eliasson C, Fleming N, Mackay E. Modeling the Application of Scale-Inhibitor-Squeeze Retention-Enhancing Additives. SPE-141384-PA. 2011;26(03):270-7.

100.   Koch M, Evans A, Brunnschweiler A, Evans A, Brunnschweiler A. Microfluidic technology and applications: Research Studies Press Philadelphia, PA, USA:; 2000.

101.   Rendall HA. Applications of microfluidics and optical manipulation for photoporation and imaging: University of St Andrews; 2015.

102.   Ismagilov RF, Rosmarin D, Kenis PJ, Chiu DT, Zhang W, Stone HA, Whitesides GM. Pressure-driven laminar flow in tangential microchannels: an elastomeric microfluidic switch. Analytical chemistry. 2001;73(19):4682-7.

103.   Squires TM, Quake SR. Microfluidics: Fluid physics at the nanoliter scale. Reviews of modern physics. 2005;77(3):977.

104.   Kirby BJ. Micro-and nanoscale fluid mechanics: transport in microfluidic devices: Cambridge university press; 2010.

105.   Kamholz AE, Weigl BH, Finlayson BA, Yager P. Quantitative analysis of molecular interaction in a microfluidic channel: the T-sensor. Analytical chemistry. 1999;71(23):5340-7.

106.   Elimelech M, Gregory J, Jia X. Particle deposition and aggregation: measurement, modelling and simulation: Butterworth-Heinemann; 2013.

107.   Lu GW, Gao P. CHAPTER 3 - Emulsions and Microemulsions for Topical and Transdermal Drug Delivery. In: Kulkarni VS, editor. Handbook of Non-Invasive Drug Delivery Systems. Boston: William Andrew Publishing; 2010. p. 59-94.

108.   Pan H, Marsh JN, Christenson ET, Soman NR, Ivashyna O, Lanza GM, Schlesinger PH, Wickline SA. Chapter two - Postformulation Peptide Drug Loading of Nanostructures. In: Düzgüneş N, editor. Methods in Enzymology. 508: Academic Press; 2012. p. 17-39.

109.   Gumustas M, Sengel-Turk CT, Gumustas A, Ozkan SA, Uslu B. Chapter 5 - Effect of Polymer-Based Nanoparticles on the Assay of Antimicrobial Drug Delivery Systems. In: Grumezescu AM, editor. Multifunctional Systems for Combined Delivery, Biosensing and Diagnostics: Elsevier; 2017. p. 67-108.

110.   Sharma S, Shukla P, Misra A, Mishra PR. Chapter 8 - Interfacial and colloidal properties of emulsified systems: Pharmaceutical and biological perspective. In: Ohshima H, Makino K, editors. Colloid and Interface Science in Pharmaceutical Research and Development. Amsterdam: Elsevier; 2014. p. 149-72.

111. Laboratory of Colloid and Surface Chemistry L. Overview of DLVO theory 2017, November 16. Available from: http://www.colloid.ch/index.php?name=dlvo.

112. Bahiraei M. Particle migration in nanofluids: a critical review. International Journal of Thermal Sciences. 2016;109:90-113.

113. Yu W, Xie H. A review on nanofluids: preparation, stability mechanisms, and applications. Journal of nanomaterials. 2012;2012:1.

114. Yang L, Du K, Niu X, Li Y, Zhang Y. An experimental and theoretical study of the influence of surfactant on the preparation and stability of ammonia-water nanofluids. International Journal of Refrigeration. 2011;34(8):1741-8.

115. Velegol D, Garg A, Guha R, Kar A, Kumar M. Origins of concentration gradients for diffusiophoresis. Soft Matter. 2016;12(21):4686-703.

116. Prieve DC. Particle transport: Salt and migrate. Nature materials. 2008;7(10):769.

117. Khair AS. Diffusiophoresis of colloidal particles in neutral solute gradients at finite Péclet number. Journal of Fluid Mechanics. 2013;731:64-94.

118. Mauger C, Volk R, Machicoane N, Bourgoin M, Cottin-Bizonne C, Ybert C, Raynal F. Diffusiophoresis at the macroscale. Physical Review Fluids. 2016;1(3):034001.

119. Abécassis B, Cottin-Bizonne C, Ybert C, Ajdari A, Bocquet L. Boosting migration of large particles by solute contrasts. Nature materials. 2008;7(10):785.

120. Chiang T-Y, Velegol D. Multi-ion diffusiophoresis. Journal of colloid and interface science. 2014;424:120-3.

121. Shin S, Um E, Sabass B, Ault JT, Rahimi M, Warren PB, Stone HA. Size-dependent control of colloid transport via solute gradients in dead-end channels. Proceedings of the National Academy of Sciences. 2016;113(2):257-61.

122. Kar A, Chiang T-Y, Ortiz Rivera I, Sen A, Velegol D. Enhanced transport into and out of dead-end pores. ACS nano. 2015;9(1):746-53.

123. Rivet S, Lake LW, Pope GA, editors. A coreflood investigation of low-salinity enhanced oil recovery. SPE Annual Technical Conference and Exhibition; 2010: Society of Petroleum Engineers.

124. Masel RI. Principles of adsorption and reaction on solid surfaces: John Wiley & Sons; 1996.

125. Syafiuddin A, Salmiati S, Jonbi J, Fulazzaky MA. Application of the kinetic and isotherm models for better understanding of the behaviors of silver nanoparticles adsorption onto different adsorbents. Journal of environmental management. 2018;218:59-70.

126. Ho YS, McKay G. Sorption of dye from aqueous solution by peat. Chemical Engineering Journal. 1998;70(2):115-24.

127. Ho Y-S, McKay G. Pseudo-second order model for sorption processes. Process biochemistry. 1999;34(5):451-65.

128. Petersen EJ, Flores-Cervantes DX, Bucheli TD, Elliott LC, Fagan JA, Gogos A, Hanna S, Kagi R, Mansfield E, Bustos AR, Plata DL, Reipa V, Westerhoff P, Winchester MR. Quantification of Carbon Nanotubes

in Environmental Matrices: Current Capabilities, Case Studies, and Future Prospects. Environ Sci Technol. 2016;50(9):4587-605.

129. Plata DL, Ferguson PL, Westerhoff P. Express it in numbers: efforts to quantify engineered nanoparticles in environmental matrices advance. ACS Publications; 2012.

130. Selck H, Handy RD, Fernandes TF, Klaine SJ, Petersen EJ. Nanomaterials in the aquatic environment: A European Union–United States perspective on the status of ecotoxicity testing, research priorities, and challenges ahead. Environmental toxicology and chemistry. 2016;35(5):1055-67.

131. Mansfield E, Kar A, Hooker SA. Applications of TGA in quality control of SWCNTs. Anal Bioanal Chem. 2010;396(3):1071-7.

132. von der Kammer F, Ferguson PL, Holden PA, Masion A, Rogers KR, Klaine SJ, Koelmans AA, Horne N, Unrine JM. Analysis of engineered nanomaterials in complex matrices (environment and biota): General considerations and conceptual case studies. Environmental Toxicology and Chemistry. 2012;31(1):32-49.

133. Amer MS. Raman spectroscopy, fullerenes and nanotechnology: Royal Society of Chemistry; 2010.

134. Athalin H, Lefrant S. A correlated method for quantifying mixed and dispersed carbon nanotubes: analysis of the Raman band intensities and evidence of wavenumber shift. Journal of Raman Spectroscopy. 2005;36(5):400-8.

135. Bokobza L, Bruneel J-L, Couzi M. Raman spectroscopy as a tool for the analysis of carbon-based materials (highly oriented pyrolitic graphite, multilayer graphene and multiwall carbon nanotubes) and of some of their elastomeric composites. Vibrational Spectroscopy. 2014;74:57-63.

136. Lopez-Lorente AI, Simonet BM, Valcarcel M. Determination of carboxylic SWCNTs in river water by microextraction in ionic liquid and determination by Raman spectroscopy. Talanta. 2013;105:75-9.

137. Herrero-Latorre C, Álvarez-Méndez J, Barciela-García J, García-Martín S, Peña-Crecente RM. Characterization of carbon nanotubes and analytical methods for their determination in environmental and biological samples: A review. Analytica Chimica Acta. 2015;853:77-94.

138. Bouchard D, Zhang W, Powell T, Rattanaudompol US. Aggregation kinetics and transport of single-walled carbon nanotubes at low surfactant concentrations. Environ Sci Technol. 2012;46(8):4458-65.

139. Saleh NB, Pfefferle LD, Elimelech M. Aggregation kinetics of multiwalled carbon nanotubes in aquatic systems: measurements and environmental implications. Environmental science & technology. 2008;42(21):7963-9.

140. Ge C, Lao F, Li W, Li Y, Chen C, Qiu Y, Mao X, Li B, Chai Z, Zhao Y. Quantitative analysis of metal impurities in carbon nanotubes: efficacy of different pretreatment protocols for ICPMS spectroscopy. Analytical chemistry. 2008;80(24):9426-34.

141. Reed RB, Goodwin DG, Marsh KL, Capracotta SS, Higgins CP, Fairbrother DH, Ranville JF. Detection of single walled carbon nanotubes by monitoring embedded metals. Environ Sci: Processes Impacts. 2013;15(1):204-13.

142. Liang Q, Jing H, Gregoire DC. Determination of trace elements in granites by inductively coupled plasma mass spectrometry. Talanta. 2000;51(3):507-13.
143. Kamal M, Huang B, Hamid S, Amin M, Maadhah A. Handbook of Polymer Degradation1992. 127 p.
144. Braun EI, Pantano P. The importance of an extensive elemental analysis of single-walled carbon nanotube soot. Carbon. 2014;77:912-9.
145. Kleinstreuer C. Microfluidics and Nanofluidics: Theory and Selected Applications: John Wiley & Sons; 2013.
146. Henrik B. Theoretical microfluidics. MIC-Department of micro and Nanotechnology, Technical University of Denmark. 2005;2.
147. Kumar CS. Microfluidic devices in nanotechnology: applications: John Wiley & Sons; 2010.
148. Al-Kharusi ASZ. Pore-scale characterization of carbonate rocks2007.
149. Hendraningrat L, Shidong L, editors. A glass micromodel experimental study of hydrophilic nanoparticles retention for EOR project. SPE Russian Oil and Gas Exploration and Production Technical Conference and Exhibition; 2012: Society of Petroleum Engineers.
150. Chrimes AF, Khoshmanesh K, Stoddart PR, Mitchell A, Kalantar-zadeh K. Microfluidics and Raman microscopy: current applications and future challenges. Chemical Society Reviews. 2013;42(13):5880-906.
151. Dent G, Smith G. Modern Raman spectroscopy: a practical approach: Wiley; 2005.
152. Larkin P. Chapter 2-Basic Principles. Infrared and Raman Spectroscopy. 2011:7-25.
153. Rai Y. In-situ Interface Chemical Characterisation of a Boundary Lubricated Contact: University of Leeds; 2015.
154. Smith E, Dent G. Modern Raman spectroscopy: a practical approach: John Wiley & Sons; 2013.
155. Ferraro JR. Introductory raman spectroscopy: Elsevier; 2003.
156. Khaemba DN. Raman spectroscopic studies of friction modifier Molybdenum DialkyldiThioCarbamate (MoDTC): University of Leeds; 2016.
157. Vandenabeele P. Practical Raman spectroscopy: an introduction: John Wiley & Sons; 2013.
158. McCreery RL. Raman spectroscopy for chemical analysis: John Wiley & Sons; 2005.
159. König K, Liang H, Berns M, Tromberg B. Cell damage in near-infrared multimode optical traps as a result of multiphoton absorption. Optics letters. 1996;21(14):1090-2.
160. Ramser K, Enger J, Goksör M, Hanstorp D, Logg K, Käll M. A microfluidic system enabling Raman measurements of the oxygenation cycle in single optically trapped red blood cells. Lab on a Chip. 2005;5(4):431-6.
161. Strehle KR, Cialla D, Rösch P, Henkel T, Köhler M, Popp J. A reproducible surface-enhanced Raman spectroscopy approach. Online SERS measurements in a segmented microfluidic system. Analytical chemistry. 2007;79(4):1542-7.

162. Ackermann KR, Henkel T, Popp J. Quantitative online detection of low-concentrated drugs via a SERS microfluidic system. ChemPhysChem. 2007;8(18):2665-70.
163. März A, Ackermann KR, Malsch D, Bocklitz T, Henkel T, Popp J. Towards a quantitative SERS approach–online monitoring of analytes in a microfluidic system with isotope-edited internal standards. Journal of biophotonics. 2009;2(4):232-42.
164. Gras SL, Mahmud T, Rosengarten G, Mitchell A, Kalantar-zadeh K. Intelligent control of surface hydrophobicity. ChemPhysChem. 2007;8(14):2036-50.
165. Rong H, Kuo Y-H, Xu S, Liu A, Jones R, Paniccia M, Cohen O, Raday O. Monolithic integrated Raman silicon laser. Optics Express. 2006;14(15):6705-12.
166. Rong H, Xu S, Kuo Y-H, Sih V, Cohen O, Raday O, Paniccia M. Low-threshold continuous-wave Raman silicon laser. Nature Photonics. 2007;1(4):232.
167. Graham D, Faulds K. Quantitative SERRS for DNA sequence analysis. Chemical Society Reviews. 2008;37(5):1042-51.
168. Ashok PC, Singh GP, Rendall HA, Krauss TF, Dholakia K. Waveguide confined Raman spectroscopy for microfluidic interrogation. Lab on a Chip. 2011;11(7):1262-70.
169. Dochow S, Krafft C, Neugebauer U, Bocklitz T, Henkel T, Mayer G, Albert J, Popp J. Tumour cell identification by means of Raman spectroscopy in combination with optical traps and microfluidic environments. Lab on a Chip. 2011;11(8):1484-90.
170. Stoddart P, White D. Optical fibre SERS sensors. Analytical and bioanalytical chemistry. 2009;394(7):1761-74.
171. Hunt HC, Wilkinson JS. Kinoform microlenses for focusing into microfluidic channels. Optics Express. 2012;20(9):9442-57.
172. Grosse RL. Handbook of Raman Spectroscopy: From the Research Laboratory to the Process Line Edited by Ian R. Lewis (Kaiser Optical Systems) and Howell G. M. Edwards (University of Bradford). Dekker: New York, Basel. 2001. xiv + 1054 pp. $225. ISBN 0-8247-0557-2. Journal of the American Chemical Society. 2002;124(19):5601-2.
173. Wachs IE, Roberts CA. Monitoring surface metal oxide catalytic active sites with Raman spectroscopy. Chemical Society Reviews. 2010;39(12):5002-17.
174. Dieterle M, Mestl G. Raman spectroscopy of molybdenum oxides Part II. Resonance Raman spectroscopic characterization of the molybdenum oxides Mo4O11 and MoO2. Physical Chemistry Chemical Physics. 2002;4(5):822-6.
175. Ni Z, Wang Y, Yu T, Shen Z. Raman spectroscopy and imaging of graphene. Nano Research. 2008;1(4):273-91.
176. Loeffen P, Maskall G, Bonthron S, Bloomfield M, Tombling C, Matousek P. Spatially Offset Raman Spectroscopy (SORS) for Liquid Screening2011.
177. Egashira K, Nishi N. Low-Frequency Raman Spectroscopy of Ethanol−Water Binary Solution: Evidence for Self-Association of Solute and Solvent Molecules. The Journal of Physical Chemistry B. 1998;102(21):4054-7.

178. Cheng M, Zeng G, Huang D, Yang C, Lai C, Zhang C, Liu Y. Advantages and challenges of Tween 80 surfactant-enhanced technologies for the remediation of soils contaminated with hydrophobic organic compounds. Chemical Engineering Journal. 2017;314:98-113.

179. Database OC. Tween 80 2018, 22 September Available from: https://pubchem.ncbi.nlm.nih.gov/compound/443315#section=Top.

180. Database OC. 3-(Triethoxysilyl)propylamine. 2018, 22 September.

181. Sartor M. Dynamic light scattering. University of California, San Diego. 2003:2-21.

182. Goldburg WI. Dynamic light scattering. American Journal of Physics. 1999;67(12):1152-60.

183. Beckingham LE, Peters CA, Um W, Jones KW, Lindquist WB. 2D and 3D imaging resolution trade-offs in quantifying pore throats for prediction of permeability. Advances in Water Resources. 2013;62:1-12.

184. Lehman JH, Terrones M, Mansfield E, Hurst KE, Meunier V. Evaluating the characteristics of multiwall carbon nanotubes. Carbon. 2011;49(8):2581-602.

185. Lopez-Lorente A, Simonet B, Valcárcel M. Qualitative detection and quantitative determination of single-walled carbon nanotubes in mixtures of carbon nanotubes with a portable Raman spectrometer. Analyst. 2013;138(8):2378-85.

186. Irurzun VM, Ruiz MP, Resasco DE. Raman intensity measurements of single-walled carbon nanotube suspensions as a quantitative technique to assess purity. Carbon. 2010;48(10):2873-81.

187. López-Lorente A, Simonet B, Valcárcel M. Raman spectroscopic characterization of single walled carbon nanotubes: influence of the sample aggregation state. Analyst. 2014;139(1):290-8.

188. Ngo CL, Le QT, Ngo TT, Nguyen DN, Vu MT. Surface modification and functionalization of carbon nanotube with some organic compounds. Advances in Natural Sciences: Nanoscience and Nanotechnology. 2013;4(3):035017.

189. Lopez-Lorente AI, Simonet BM, Valcarcel M. Qualitative detection and quantitative determination of single-walled carbon nanotubes in mixtures of carbon nanotubes with a portable Raman spectrometer. Analyst. 2013;138(8):2378-85.

190. Sattler KD. Handbook of nanophysics: nanotubes and nanowires: CRC press; 2010.

191. Zhao J, Lui H, McLean DI, Zeng H. Automated autofluorescence background subtraction algorithm for biomedical Raman spectroscopy. Applied spectroscopy. 2007;61(11):1225-32.

192. Tian YA, Gao B, Ziegler KJ. High mobility of SDBS-dispersed single-walled carbon nanotubes in saturated and unsaturated porous media. J Hazard Mater. 2011;186(2–3):1766.

193. Bjørlykke K, Gran K. Salinity variations in North Sea formation waters: implications for large-scale fluid movements. Marine and Petroleum Geology. 1994;11(1):5-9.

194. Kwak HT, Zhang G, Chen S, editors. The effects of salt type and salinity on formation water viscosity and NMR responses.

proceedings of the international symposium of the Society of Core Analysts, Toronto, Canada; 2005.

195. Ward K, Fan ZH. Mixing in microfluidic devices and enhancement methods. Journal of Micromechanics and Microengineering. 2015;25(9):094001.

196. Njobuenwu D, Fairweather M. Effect of shape on inertial particle dynamics in a channel flow. Flow, turbulence and combustion. 2014;92(1-2):83-101.

197. Gnanavelu AB. A geometry independent integrated method to predict erosion wear rates in a slurry environment: The University of Leeds; 2010.

198. Pinder GF, Gray WG. Essentials of multiphase flow in porous media: John Wiley & Sons; 2008.

199. Purcell EM. Life at low Reynolds number. Am J Phys. 1977;45(1):3-11.

200. Jorio A, Pimenta M, Souza Filho A, Saito R, Dresselhaus G, Dresselhaus M. Characterizing carbon nanotube samples with resonance Raman scattering. New Journal of Physics. 2003;5(1):139.

201. Rastogi R, Kaushal R, Tripathi SK, Sharma AL, Kaur I, Bharadwaj LM. Comparative study of carbon nanotube dispersion using surfactants. Journal of Colloid and Interface Science. 2008;328(2):421-8.

202. Pakarinen K, Petersen EJ, Leppanen MT, Akkanen J, Kukkonen JVK. Adverse effects of fullerenes (nC60) spiked to sediments on Lumbriculus variegatus (Oligochaeta). Environ Pollut. 2011;159:3750.

203. Metwalli E, Haines D, Becker O, Conzone S, Pantano C. Surface characterizations of mono-, di-, and tri-aminosilane treated glass substrates. Journal of colloid and interface science. 2006;298(2):825-31.

204. Savaji KV, Niitsoo O, Couzis A. Influence of particle/solid surface zeta potential on particle adsorption kinetics. Journal of Colloid and Interface Science. 2014;431:165-75.

205. Polowczyk I, Koźlecki T, Bastrzyk A. Adsorption of silver nanoparticles on glass beads surface. Adsorption Science & Technology. 2015;33(6-8):731-7.

206. Ho Y, Ng J, McKay G. Kinetics of pollutant sorption by biosorbents. Separation and purification methods. 2000;29(2):189-232.

207. Rahman MM, Younes H, Subramanian N, Al Ghaferi A. Optimizing the Dispersion Conditions of SWCNTs in Aqueous Solution of Surfactants and Organic Solvents. Journal of Nanomaterials. 2014;2014:1-11.

208. Elimelech M. Effect of Particle Size on the Kinetics of Particle Deposition under Attractive Double Layer Interactions. Journal of Colloid and Interface Science. 1994;164(1):190-9.

209. van der Maaden K, Tomar J, Jiskoot W, Bouwstra J. Chemical Modifications of Silicon Surfaces for the Generation of a Tunable Surface Isoelectric Point. Langmuir. 2014;30(7):1812-9.

210. Burgin TP, Lewenstein JC, Werho D. Investigations into the Mechanism of Adsorption of Carbon Nanotubes onto Aminopropylsiloxane Functionalized Surfaces. Langmuir. 2005;21(14):6596-602.

211. Anderson JL, Prieve DC. Diffusiophoresis: Migration of Colloidal Particles in Gradients of Solute Concentration. Separation and Purification Methods. 1984;13(1):67-103.
212. Shin S, Ault JT, Warren PB, Stone HA. Accumulation of Colloidal Particles in Flow Junctions Induced by Fluid Flow and Diffusiophoresis. Physical Review X. 2017;7(4):041038.
213. Ault JT, Warren PB, Shin S, Stone HA. Diffusiophoresis in one-dimensional solute gradients. Soft Matter. 2017;13(47):9015-23.
214. Hunter RJ. Chapter 7 - Influence of Simple Inorganic Ions on Zeta Potential. In: Hunter RJ, editor. Zeta Potential in Colloid Science: Academic Press; 1981. p. 258-304.
215. Anderson JL. Effect of nonuniform zeta potential on particle movement in electric fields. Journal of colloid and interface science. 1985;105(1):45-54.
216. Morrison Jr F. Electrophoresis of a particle of arbitrary shape. Journal of Colloid and Interface Science. 1970;34(2):210-4.
217. Qazi MJ, Liefferink RW, Schlegel SJ, Backus EH, Bonn D, Shahidzadeh N. Influence of Surfactants on Sodium Chloride Crystallization in Confinement. Langmuir. 2017;33(17):4260-8.
218. Deseigne J, Cottin-Bizonne C, Stroock AD, Bocquet L, Ybert C. How a "pinch of salt" can tune chaotic mixing of colloidal suspensions. Soft matter. 2014;10(27):4795-9.

Appendix A

Calculations for thesis

Calculating the volume of the map scan area.

The shape of the microfluidic channel used in this thesis is geometrically represented as half a cylinder (Figure A1). The volume of half a cylinder is

$$Volume = \frac{\pi r^2}{2} \; x \; L \hspace{5cm} Equation \; A1$$

Where L is the length of the channel (m) and r is the radius of the cylinder (m).
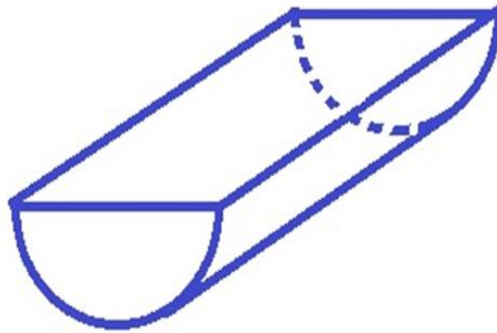
Figure A1: Schematic diagram of half a cylinder

The dimension of the map scan can be represented by the diameter of the channel and the length along the channel as shown in Figure A2. Therefore, the volume can be calculated by multiplying the cross – sectional area x the length along the channel.
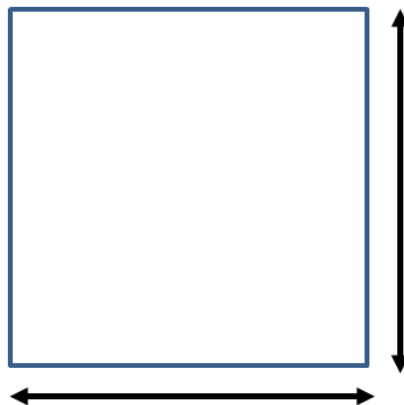
Figure A2: Geometrical representation of map scan

Calculations for changing volume of map scan area

The area of a semi-circle can be represented as follows:

$$\frac{\pi r^2}{2} = \int_{-x}^{x} \sqrt{r^2 - x^2}$$
<div align="right">*Equation A1*</div>

Where x ranges from 0 to 102.5 µm and r is radius of the channel which is a constant 102.5 µm.

Therefore, for the full scan the x value will represent the radius.

$$\int_{-102.5x10^{-6}}^{102.5x10^{-6}} \sqrt{(102.5x10^{-6})^2 - x^2}\ dx$$
<div align="right">*Equation A2*</div>

This can further be simplified to:

$$\int_{-102.5x10^{-6}}^{102.5x10^{-6}} \sqrt{\frac{1681}{160000000000} - x^2}\ dx$$
<div align="right">*Equation A3*</div>

Apply linearity:

$$\frac{1}{400000} \int_{-102.5x10^{-6}}^{102.5x10^{-6}} \sqrt{1681 - 160000000000x^2}\ dx$$
<div align="right">*Equation A4*</div>

Now solving:

$$\int_{-102.5x10^{-6}}^{102.5x10^{-6}} \sqrt{1681 - 160000000000x^2}\ dx$$
<div align="right">*Equation A5*</div>

Perform trigonometric substitution:

$$Subsituting\ x = \frac{41 \sin u}{400000} \xrightarrow{yields} u = \arcsin \frac{400000x}{41},$$
<div align="right">*Equation A6*</div>

$$dx = \frac{41 \cos(u)}{400000}\ du$$
<div align="right">*Equation A7*</div>

$$\int_{-102.5x10^{-6}}^{102.5x10^{-6}} \frac{41 \cos(u) \sqrt{1681 - 1681\ sin^2(u)}}{400000}\ du$$
<div align="right">*Equation A8*</div>

Simplify using $1681 - 1681 \sin^2 (u) = 1681 \cos^2 (u) = 1681 \cos^2 (u)$:

$$\frac{1681}{400000} \int cos^2(u) \, du \qquad \qquad \text{Equation A9}$$

Now solving:

$$\int cos^2(u) \, du \qquad \qquad \text{Equation A10}$$

Apply reduction formula:

$$\int cos^n(u) du = \frac{n-1}{n} \int cos^{n-2}(u) du + \frac{cos^{n-1}(u) sin(u)}{n} \qquad \qquad \text{Equation A11}$$

With n = 2

$$= \frac{cos(u) sin(u)}{2} + \frac{1}{2} \int 1 \, du \qquad \qquad \text{Equation A12}$$

Now solving:

$$\int 1 \, du \qquad \qquad \text{Equation A13}$$

Apply constant rule:

$$= u$$

Plug in solved integrals:

$$\frac{cos(u) sin(u)}{2} + \frac{1}{2} \int 1 \, du \qquad \qquad \text{Equation A14}$$

$$\frac{cos(u) sin(u)}{2} + \frac{u}{2} \qquad \qquad \text{Equation A15}$$

Plug in solved integrals:

$$\frac{1681}{400000} \int cos^2(u) du \qquad \qquad \text{Equation A16}$$

$$\frac{1681 \, cos(u) \, sin(u)}{800000} + \frac{1681u}{800000} \qquad \qquad \text{Equation A17}$$

Undo substitution $u = \arcsin\left(\frac{400000x}{41}\right)$, *Equation A18*

Use:

$$\sin\left(\arcsin\left(\frac{400000x}{41}\right)\right) = \frac{400000x}{41}$$ *Equation A19*

$$\cos\left(\arcsin\left(\frac{400000x}{41}\right)\right) = \sqrt{1 - \frac{160000000000\, x^2}{1681}}$$ *Equation A20*

$$\frac{1681 \arcsin\left(\frac{400000x}{41}\right)}{800000} + \frac{41x \sqrt{1 - \frac{160000000000\, x^2}{1681}}}{2}$$ *Equation A21*

Plug in solved integrals:

$$\frac{1}{400000} \int \sqrt{1681 - 160000000000\, x^2}\; dx$$ *Equation A22*

$$\frac{1681 \arcsin\left(\frac{400000x}{41}\right)}{320000000000} + \frac{41x \sqrt{1 - \frac{160000000000\, x^2}{1681}}}{800000}$$ *Equation A23*

The problem is solved:

$$\int \sqrt{\frac{1681}{160000000000} - x^2}\; dx$$ *Equation A24*

$$\frac{1681 \arcsin\left(\frac{400000x}{41}\right)}{320000000000} + \frac{41x \sqrt{1 - \frac{160000000000\, x^2}{1681}}}{800000} + C$$ *Equation A25*

$$\frac{1681 \arcsin\left(\frac{400000x}{41}\right) + 400000x\sqrt{1 - 160000000000\, x^2}}{320000000000} + C \quad \text{Equation A26}$$

$$using \int f(x)\, dx = F(x) =$$

$$\frac{1681 \arcsin\left(\frac{400000x}{41}\right)}{320000000000} + \frac{x\sqrt{\frac{1681}{160000000000} - x^2}}{2} + C \qquad \text{Equation A27}$$

Using definite integral:

$$\int_{-102.5x10^{-6}}^{102.5x10^{-6}} f(x)\, dx \qquad\qquad\qquad \text{Equation A28}$$

$$\frac{1681\pi}{320000000000} \qquad\qquad\qquad \text{Equation A30}$$

At full map scan, the cross-sectional area of the semi $-$ circle is $1.65\ x\ 10^{-8}\ m^2$

From here, the volume of the map scan area can be calculated by multiplying the cross $-$ sectional area by the length along the channel.

Table A1: Data for the different map scan sizes

	Area (m²)	Length (m)	Volume (m³)
Full scan	1.65E-08	2.00E-04	3.30E-12
100um	9.82E-09	2.00E-04	1.96E-12
40um	4.07E-09	2.00E-04	8.14E-13
side	2.26E-09	2.00E-04	4.52E-13

From here, volume in cubic meters is converted to litres by dividing the value by 1000. This value in liters is then multiplied with the injecting concentration to CNT in mg/L to provide the mass in mg flowing through the scan area.

Stoke – Einstein equation

$$D_s = \frac{k_B T}{6 \pi \eta r} \qquad\qquad Equation\ A31$$

Where k_B is Boltzmann's constant, T is temperature, η is the dynamic viscosity, r is the radius of particle.

Appendix B

MATLAB data processing codes

```
function varargout = map_fit_tool(varargin)
% MAP_FIT_TOOL MATLAB code for map_fit_tool.fig
%      MAP_FIT_TOOL, by itself, creates a new MAP_FIT_TOOL or
raises the existing
%      singleton*.
%
%      H = MAP_FIT_TOOL returns the handle to a new MAP_FIT_TOOL or
the handle to
%      the existing singleton*.
%
%      MAP_FIT_TOOL('CALLBACK',hObject,eventData,handles,...) calls
the local
%      function named CALLBACK in MAP_FIT_TOOL.M with the given
input arguments.
%
%      MAP_FIT_TOOL('Property','Value',...) creates a new
MAP_FIT_TOOL or raises the
%      existing singleton*.  Starting from the left, property value
pairs are
%      applied to the GUI before map_fit_tool_OpeningFcn gets
called.  An
%      unrecognized property name or invalid value makes property
application
%      stop.  All inputs are passed to map_fit_tool_OpeningFcn via
varargin.
%
```

```
%       *See GUI Options on GUIDE's Tools menu.  Choose "GUI allows
only one
%       instance to run (singleton)".
%
% See also: GUIDE, GUIDATA, GUIHANDLES

% Edit the above text to modify the response to help map_fit_tool

% Last Modified by GUIDE v2.5 26-Jun-2015 18:44:08

% Begin initialization code - DO NOT EDIT
gui_Singleton = 1;
gui_State = struct('gui_Name',       mfilename, ...
                   'gui_Singleton',  gui_Singleton, ...
                   'gui_OpeningFcn', @map_fit_tool_OpeningFcn, ...
                   'gui_OutputFcn',  @map_fit_tool_OutputFcn, ...
                   'gui_LayoutFcn',  [] , ...
                   'gui_Callback',   []);
if nargin && ischar(varargin{1})
    gui_State.gui_Callback = str2func(varargin{1});
end

if nargout
    [varargout{1:nargout}] = gui_mainfcn(gui_State, varargin{:});
else
    gui_mainfcn(gui_State, varargin{:});
end
% End initialization code - DO NOT EDIT


% --- Executes just before map_fit_tool is made visible.
function map_fit_tool_OpeningFcn(hObject, ~, handles, varargin)
% This function has no output args, see OutputFcn.
% hObject    handle to figure
% eventdata  reserved - to be defined in a future version of MATLAB
% handles    structure with handles and user data (see GUIDATA)
% varargin   command line arguments to map_fit_tool (see VARARGIN)

% Choose default command line output for map_fit_tool
handles.output = hObject;

% Update handles structure
```

```matlab
guidata(hObject, handles);

fs_init;
fs_new('');
global ui_formulaIndex;
ui_formulaIndex=1;
sd_init;
ui_sd_init;

% UIWAIT makes map_fit_tool wait for user response (see UIRESUME)
% uiwait(handles.ui_map_fit_tool);


% --- Outputs from this function are returned to the command line.
function varargout = map_fit_tool_OutputFcn(~, ~, handles)
% varargout  cell array for returning output args (see VARARGOUT);
% hObject    handle to figure
% eventdata  reserved - to be defined in a future version of MATLAB
% handles    structure with handles and user data (see GUIDATA)

% Get default command line output from handles structure
varargout{1} = handles.output;



% --- Executes during object creation, after setting all
properties.
function ui_map_fit_tool_CreateFcn(hObject, ~, ~)
global ui_map_fit_tool;
ui_map_fit_tool=hObject;



function ui_formulas_CreateFcn(hObject, ~, ~)
set(hObject,'data',{'Input your formulas here'});
set(hObject,'columnname',{'formulas'});
set(hObject,'columneditable',true);
set(hObject,'columnformat',{'char'});

global ui_formulas;
ui_formulas=hObject;
```

```matlab
function ui_parameters_CreateFcn(hObject, ~, ~)
set(hObject,'data',{});
set(hObject,'columnname',{'argument','val','...'});
set(hObject,'columneditable',[false,true,true]);
set(hObject,'columnformat',{'char','numeric','numeric'});

global ui_parameters;
ui_parameters=hObject;



% ---------- Formula Object Methods ----------
function fo=fo_new(formula)
fo.formula=formula;
arglist=symvar(fo.formula);
arglist(find(strcmp(arglist,'w')))=[]; %delete w from the formula
variable list
fo.args=[];
fo.I0Pos=0;
fo.w0Pos=0;
for i=1:length(arglist)                %find the position of
variables in the list
    name=arglist{i};
    if(strcmp(name,'I0'))
        fo.I0Pos=i;
    end
    if(strcmp(name,'w0'))
        fo.w0Pos=i;
    end
    fo.args(i).name=name;
    fo.args(i).val=0;
end

function nfo=fo_change(fo,formula)
old=symvar(fo.formula);
new=symvar(formula);
old(find(strcmp(old,'w')))=[];
new(find(strcmp(new,'w')))=[];
fo.formula=formula;
fo.args(find(~ismember(old,new)))=[];
toadd=setdiff(new,old);
j=length(fo.args)+1;
for i=1:length(toadd)
```

```matlab
        name=toadd{i};
        if(strcmp(name,'I0'))
            fo.I0Pos=j;
        end
        if(strcmp(name,'w0'))
            fo.w0Pos=j;
        end
        fo.args(j).name=name;
        fo.args(j).val=0;
        j=j+1;
    end
nfo=fo;


function fo=fo_set(fo,argName,argVal)
for i=1:length(fo.args)
    if(strcmp(fo.args(i).name,argName))
        fo.args(i).val=argVal;
        break;
    end
end


function val=fo_get(fo,argName)
val=0;
for i=1:length(fo.args)
    if(strcmp(fo.args(i).name,argName))
        val=fo.args(i).val;
        break;
    end
end


% ---------- End of formula Object Methods ----------

% ---------- formula Set Methods ----------
%initialise fs (set of formulas)
function fs_init
global fs;
fs=[];
fs_updateToUi;

%set up fs and get and index for a new formula object
function index=fs_new(string)
global fs;
```

```
fo=fo_new(string);
fs=[fs,fo];
fs_updateToUi;
index=length(fs);

%delete fs
function fs_delete(index)
if(index<1)
    return
end
global fs;
fs(index)=[];
fs_updateToUi;

function index=fs_change(index,string)
if(index<1)
    return
end
global fs;
fo=fo_change(fs(index),string);
%display(fo);
fs(index)=fo;
fs_updateToUi;

function fs_toUi(index)
global ui_parameters;
if(index<1)
    set(ui_parameters,'data',{});
    return
end
global fs;
fo=fs(index);
data={};
for i=1:length(fo.args)
    data{i,1}=fo.args(i).name;
    data{i,2}=fo.args(i).val;
end
%display(data);
set(ui_parameters,'data',data);

function fs_fromUi(index)
if(index<1)
```

```matlab
        return
    end
    global fs;
    fo=fs(index);
    global ui_parameters;
    data=get(ui_parameters,'data');
    for i=1:length(fo.args)
        fo.args(i).val=data{i,2};
    end
    fs(index)=fo;


function fs_updateToUi
    global fs;
    global ui_formulas;
    data={};
    for i=1:length(fs)
        data{i,1}=fs(i).formula;
    end
    set(ui_formulas,'data',data);


% ---------- End of formula Set Methods ----------



% ---------- UI for Set Methods ----------

function ui_new_formula_Callback(hObject, eventdata, handles)
    fs_new('');
    global fs;
    global ui_formulaIndex;
    ui_formulaIndex=length(fs);
    fs_toUi(ui_formulaIndex);
    ui_refresh


function ui_delete_formula_Callback(hObject, eventdata, handles)
    global ui_formulaIndex;
    %display(ui_formulaIndex);
    if(~isempty(ui_formulaIndex) && ui_formulaIndex~=0)
        fs_delete(ui_formulaIndex);
    end
    global fs;
    if(ui_formulaIndex>length(fs))
```

```matlab
        ui_formulaIndex=length(fs);
end
fs_toUi(ui_formulaIndex);
%display(ui_formulaIndex);
ui_refresh


function ui_add_formula_CreateFcn(hObject, eventdata, handles)
if ispc && isequal(get(hObject,'BackgroundColor'),
get(0,'defaultUicontrolBackgroundColor'))
    set(hObject,'BackgroundColor','white');
end
set(hObject,'string',{'Select an
formula','Gaussian','Lorentzian','BWF'});

% executes when adding a formula to the table
function ui_add_formula_Callback(hObject, eventdata, handles)
contents=cellstr(get(hObject,'String'));
sel=contents{get(hObject,'value')};
string='';
switch(sel)
    case 'Gaussian'
        string='I0*exp(-((w-w0)/Gamma).^2)';
    case 'Lorentzian'
        string='I0/(1+((w-w0)/Gamma).^2)';
    case 'BWF'
        string='I0*(1+2*(w-w0)/(Q*Gamma))^2/(1+(2*(w-
w0)/Gamma)^2)';
end
global ui_formulaIndex;
global fs;
index=0;
ui_formulaIndex
fs(ui_formulaIndex).formula
if(~isempty(string))
    if(ui_formulaIndex~=0 && isempty(fs(ui_formulaIndex).formula))
        index=fs_change(ui_formulaIndex,string);
    else
        index=fs_new(string);
        ui_formulaIndex=length(fs);
    end
    fs_toUi(ui_formulaIndex);
end
```

```matlab
if(index~=0)
    switch(sel)
        case 'Gaussian'
            width=100;
            fs(index)=fo_set(fs(index),'Gamma',100);
        case 'Lorentzian'
            width=100;
            fs(index)=fo_set(fs(index),'Gamma',100);
        case 'BWF'
            width=100;
            fs(index)=fo_set(fs(index),'Gamma',100);
            fs(index)=fo_set(fs(index),'Q',10);

    end
    fs_toUi(ui_formulaIndex);
end
ui_refresh


function ui_formulas_CellSelectionCallback(hObject, eventdata,
handles)
global ui_formulaIndex;
global fs;
if(~isempty(eventdata.Indices))
    if(ui_formulaIndex~=0)
        fs_fromUi(ui_formulaIndex);
    end
    if(eventdata.Indices(1)~=0 || length(fs)==0)
        ui_formulaIndex=eventdata.Indices(1);
        fs_toUi(ui_formulaIndex);
    end
end
ui_refresh


function ui_formulas_CellEditCallback(hObject, eventdata, handles)
global ui_formulaIndex;
if(~isempty(eventdata.Indices))
    ui_formulaIndex=eventdata.Indices(1);
    fs_change(ui_formulaIndex,eventdata.NewData);
    %display(eventdata.NewData);
    fs_toUi(ui_formulaIndex);
```

```matlab
    else
        ui_formulaIndex=0;
    end
    ui_refresh


function ui_parameters_CellEditCallback(hObject, eventdata, handles)
global ui_formulaIndex;
if(ui_formulaIndex~=0)
    fs_fromUi(ui_formulaIndex);
end
ui_refresh


function ui_spectrum_ButtonDownFcn(hObject, eventdata, handles)
global ui_formulaIndex;
global fs;
p=get(gca,'CurrentPoint') ;%????
if(ui_formulaIndex~=0)
    fo=fs(ui_formulaIndex);

    fo=fo_set(fo,'I0',p(3));
    fo=fo_set(fo,'w0',p(2));
    fs(ui_formulaIndex)=fo;
    fs_toUi(ui_formulaIndex);
    ui_refresh;
end

% ---------- End of UI for Set Methods ----------



% ---------- Spectrum Data Object ----------

function sd_init
global sd;
sd={};

function sd_load(filename)
sd_init;
global sd;

% Import data
data=importdata(filename);
```

```matlab
dataX=data(:,1);
dataY=data(:,2);
dataShift=data(:,3);
dataIntensity=data(:,4);
clear data;

% Detect interval between points
intXcount=1;
if dataX(length(dataX))-dataX(1)~=0
while (dataX(intXcount+1)-dataX(intXcount))==0,
    intXcount=intXcount+1;
end
intervalX=dataX(intXcount+1)-dataX(intXcount);
else
    intervalX=1;
end

intYcount=1;
if dataY(length(dataY))-dataY(1)~=0
while (dataY(intYcount+1)-dataY(intYcount))==0,
    intYcount=intYcount+1;
end
intervalY=dataY(intYcount+1)-dataY(intYcount);
else
    intervalY=1;
end

% Set indices for every point X,Y
X=round((dataX-min(dataX))/intervalX+1);
Y=round((dataY-min(dataY))/intervalY+1);
sd.rangeX=[min(X),max(X)];
sd.rangeY=[min(Y),max(Y)];
sd.rangeShift=[min(dataShift),max(dataShift)];
sd.rangeIntensity=[min(dataIntensity),max(dataIntensity)];

% sd.samples storages every sample with shift, intensity, x, y
% sd.union storages all the spectra in a row
sd.samples=[];
sd.union.shift=[];
sd.union.intensity=[];

bg=1;ox=X(bg);oy=Y(bg);
```

```
for ed=1:length(X)
    if X(ed)~=ox || Y(ed)~=oy
        if ed>bg
            shift=dataShift(bg:ed-1);
            intensity=dataIntensity(bg:ed-1);
            if(shift(1)>shift(length(shift)))
                shift=flipud(shift);
                intensity=flipud(intensity);
            end
            sd.samples(ox,oy).shift=shift;
            sd.samples(ox,oy).intensity=intensity;
            sd.samples(ox,oy).x=dataX(bg);
            sd.samples(ox,oy).y=dataY(bg);
            sd.union.shift=[sd.union.shift;shift;0/0];
            sd.union.intensity=[sd.union.intensity;intensity;0/0];
        end
        bg=ed;ox=X(bg);oy=Y(bg);
    end
end
ed=length(X)+1;
if ed>bg
    shift=dataShift(bg:ed-1);
    intensity=dataIntensity(bg:ed-1);
    if(shift(1)>shift(length(shift)))
        shift=flipud(shift);
        intensity=flipud(intensity);
    end
    sd.samples(ox,oy).shift=shift;
    sd.samples(ox,oy).intensity=intensity;
    sd.samples(ox,oy).x=dataX(bg);
    sd.samples(ox,oy).y=dataY(bg);
    sd.union.shift=[sd.union.shift;shift];
    sd.union.intensity=[sd.union.intensity;intensity];
end

for x=sd.rangeX(1):sd.rangeX(2)
    for y=sd.rangeY(1):sd.rangeY(2)
        sd.samples(x,y).background=[];
        sd.samples(x,y).fitResult=[];
    end
end
```

```
sd.map=[];
for x=sd.rangeX(1):sd.rangeX(2)
    for y=sd.rangeY(1):sd.rangeY(2)

sd.map(x,y)=abs(trapz(sd.samples(x,y).shift,sd.samples(x,y).intensi
ty));
    end
end

sd.region=sd.rangeShift;
tmpw=(sd.rangeShift(2)-sd.rangeShift(1))/10;
sd.region(1)=sd.region(1)+tmpw;
sd.region(2)=sd.region(2)-tmpw;
sd.windowSize=tmpw;

function sd_save_spectra
global sd
Aacc=[];
for x=sd.rangeX(1):sd.rangeX(2)
    for y=sd.rangeY(1):sd.rangeY(2)

Aspec=[sd.samples(x,y).x*ones(length(sd.samples(x,y).shift),1),sd.s
amples(x,y).y*ones(length(sd.samples(x,y).shift),1),...
            sd.samples(x,y).shift,sd.samples(x,y).intensity];
        A=[Aacc;Aspec];
        Aacc=A;
    end
end
sd.savespectra=A;

function sd_save_map
global sd
Aacc=[];
for x=sd.rangeX(1):sd.rangeX(2)
    for y=sd.rangeY(1):sd.rangeY(2)
        Aspec=[sd.samples(x,y).x, sd.samples(x,y).y, sd.map(x,y)];
        A=[Aacc;Aspec];
        Aacc=A;
    end
end
sd.savemap=A;
```

```matlab
% ---------- End of Spectrum Data Object ----------


% ---------- Spectrum Data UI ----------

function ui_sd_init
global ui_sd;
ui_sd=[];


% --- Executes on button press in ui_load.
function ui_load_Callback(hObject, eventdata, handles)
[filename,pathname]=uigetfile('*.txt','Open Raman Data');
%filename='1.txt';
if(filename==0)
    beep;return;
end
sd_load(filename);
global ui_sd;
ui_sd.curX=1;
ui_sd.curY=1;
ui_sd.showAll=true;
ui_refresh;

% --- Executes on button press in ui_save.
function ui_save_Callback(hObject, eventdata, handles)
global sd;
sd_save_spectra;
[filename,pathname]=uiputfile('*.txt','Save Raman Data');
dlmwrite([pathname,filename],sd.savespectra,'delimiter','\t');
%filename='1.txt';

% hObject    handle to ui_save (see GCBO)
% eventdata  reserved - to be defined in a future version of MATLAB
% handles    structure with handles and user data (see GUIDATA)

% --- Executes on button press in ui_save_map.
function ui_save_map_Callback(hObject, eventdata, handles)
global sd;
sd_save_map;
[filename,pathname]=uiputfile('*.txt','Save Raman Data');
dlmwrite([pathname,filename],sd.savemap,'delimiter','\t');
```

```matlab
% hObject    handle to ui_save_map (see GCBO)
% eventdata  reserved - to be defined in a future version of MATLAB
% handles    structure with handles and user data (see GUIDATA)


function ui_map_CreateFcn(hObject, ~, ~)
global ui_map;
ui_map=hObject;

function ui_spectrum_CreateFcn(hObject, ~, ~)
global ui_spectrum;
ui_spectrum=hObject;

function ui_map_ButtonDownFcn(~, ~, ~)
p=get(gca,'CurrentPoint');
global ui_sd;
%ui_sd.curX=round(p(1,1));ui_sd.curY=round(p(1,2));ui_sd.showAll=false;
ui_sd.curY=round(p(1,1));ui_sd.curX=round(p(1,2));ui_sd.showAll=false;
ui_refresh;

% --- Executes on button press in ui_show_all.
function ui_show_all_Callback(~, ~, ~)
global ui_sd;
ui_sd.showAll=true;
ui_refresh;

function ui_set_region_Callback(hObject, eventdata, handles)
global sd;
if(isempty(sd))
    beep;
    return;
end
[x,~,success]=ginput(1);
if(~success)
    return
end
stem(x,sd.rangeIntensity(2),'marker','none');
tmp(1)=x;
[x,y,success]=ginput(1);
if(~success)
```

```
        return
    end
tmp(2)=x;
tmp=sort(tmp);
sd.region=tmp;
ui_refresh;

% ---------- End of Spectrum Data U ----------

% ---------- Algorithms ----------

% Background removal
function do_background(x,y)
global sd;
sample=sd.samples(x,y);
sd.samples(x,y).intensity=vra_bg(sample.shift,sample.intensity);

function do_background_all()
global sd;
if(isempty(sd))
    beep;
    return;
end
%global ui_nIter;
%nIter=str2num(get(ui_nIter,'string'));
total=sd.rangeX(2)*sd.rangeY(2);
count=0;
h_Wait=waitbar(0,'background fitting...');
for x=sd.rangeX(1):sd.rangeX(2)
    for y=sd.rangeY(1):sd.rangeY(2)
        waitbar(count/total,h_Wait,['background
fitting...',num2str(count),' of ',num2str(total)]);
        do_background(x,y);
        count=count+1;
    end
end
close(h_Wait);
% end of background removal

%fitting
function do_fit(x,y)
[ft,fo]=getFit();
```

```matlab
if(isempty(ft))
    beep;
    return
end
%display(ft);display(fo);keyboard;
global sd;
if(isempty(sd.samples(1).background))
    do_background_all;
end
sample=sd.samples(x,y);
shift=sample.shift;
intensity=sample.intensity-sample.background;
beginIndex=find(shift>sd.region(1),1,'first');
endIndex=find(shift<sd.region(2),1,'last');
shift=shift(beginIndex:endIndex);
intensity=intensity(beginIndex:endIndex);
sd.samples(x,y).fitResult=fit(shift,intensity,ft,fo);
beep;

function do_fit_all()
[ft,fo]=getFit();
if(isempty(ft))
    beep;
    return
end
%display(ft);display(fo);keyboard;
global sd;
total=sd.rangeX(2)*sd.rangeY(2);
count=0;
if(isempty(sd.samples(1).background))
    do_background_all;
end
h_Wait=waitbar(0,'curve fitting...');
for x=sd.rangeX(1):sd.rangeX(2)
    for y=sd.rangeY(1):sd.rangeY(2)
        waitbar(count/total,h_Wait,['curve
fitting...',num2str(count),' of ',num2str(total)]);
        sample=sd.samples(x,y);
        shift=sample.shift;
        intensity=sample.intensity-sample.background;
        beginIndex=find(shift>sd.region(1),1,'first');
        endIndex=find(shift<sd.region(2),1,'last');
```

```matlab
            shift=shift(beginIndex:endIndex);
            intensity=intensity(beginIndex:endIndex);
            sd.samples(x,y).fitResult=fit(shift,intensity,ft,fo);
            count=count+1;
        end
    end
end
close(h_Wait);
beep;


function exp=addToken(expression,token)
exp=expression;
exp=strrep(exp,'.*','*');
exp=strrep(exp,'.^','^');
s=sym(exp);
args=symvar(s);
for i=1:length(args)
    if(~isequaln(char(args(i)),'w'))
        s=subs(s,args(i),sym([token,char(args(i))]));
    end
end
exp=char(s);
exp=strrep(exp,'*','.*');
exp=strrep(exp,'/','./');
exp=strrep(exp,'^','.^');


function [ft,fo]=getFit()
exp='0';
global fs;
for r=1:length(fs);
    fo=fs(r);
    if(~isempty(fo.formula))
        token=['arg',num2str(r),'_'];
        formula=addToken(fo.formula,token);
        exp=[exp,'+(',formula,')'];
    end
end
if(strcmp(exp,'0'))
    ft=[];fo=[];return;
end
%display(exp);%keyboard;
ft=fittype(exp,'independent','w');
```

```matlab
args=coeffnames(ft);
sp=[];
for i=1:length(args)
    arg=args{i};
    m=regexp(arg,'arg[0-9]+_','match');
    m=m{1};
    m=m(4:length(m)-1);
    r=str2num(m);
    arg=regexprep(arg,'arg[0-9]+_','',1);
    sp(i)=fo_get(fs(r),arg);
end
%display(args);display(sp);
fo=fitoptions(fitoptions(ft),'StartPoint',sp);
%display(fo);


% ---------- End of Algorithms ----------



% ---------- UI of Algorithms ----------
function ui_nIter_CreateFcn(hObject, eventdata, handles)
global ui_nIter;
ui_nIter=hObject;
if ispc && isequal(get(hObject,'BackgroundColor'),
get(0,'defaultUicontrolBackgroundColor'))
    set(hObject,'BackgroundColor','white');
end



% Executes background fit to all spectra on pressing button
function ui_background_fit_Callback(hObject, eventdata, handles)
global sd;
global ui_sd;
if(isempty(ui_sd))
    beep;return;
end
do_background_all;
sd.union.shift=[];
sd.union.intensity=[];
for x=1:sd.rangeX(2);
    for y=1:sd.rangeY(2);
        shift=sd.samples(x,y).shift;
        intensity=sd.samples(x,y).intensity;
```

```matlab
            sd.union.shift=[sd.union.shift;shift];
            sd.union.intensity=[sd.union.intensity;intensity];
        end
    end
ui_refresh;



function ui_fit_this_Callback(hObject, eventdata, handles)
global ui_sd;
if(~isempty(ui_sd))
    do_fit(ui_sd.curX,ui_sd.curY);
    ui_refresh;
else
    beep;
end

function ui_fit_all_Callback(hObject, eventdata, handles)
global ui_sd;
if(isempty(ui_sd))
    beep;return;
end
do_fit_all();
ui_refresh;




function ui_nIter_Callback(~, ~, ~)

% ---------- End of UI of Algorithms ----------



% Refresh of plots in GUI.
function ui_refresh
global sd;
global ui_sd;
if(isempty(ui_sd))
    return
end

%show map
```

```matlab
global ui_map;
axes(ui_map);
hold off;
pic=imshow(mat2gray(sd.map));
set(pic,'ButtonDownFcn',{@ui_map_ButtonDownFcn});
hold all;

%show spectrum data
global ui_spectrum;
axes(ui_spectrum);
hold off;
if(ui_sd.showAll)
    hp=plot(sd.union.shift,sd.union.intensity);
    set(hp,'hittest','off');
    hold all;
else
    sample=sd.samples(ui_sd.curX,ui_sd.curY);
    hp=plot(sample.shift,sample.intensity);
    set(hp,'hittest','off');
    hold all;
    if(~isempty(sample.background))
        hp=plot(sample.shift,sample.background);
        set(hp,'hittest','off');
        hold all;
    end
    if(~isempty(sample.fitResult))

hp=plot(sample.shift,sample.fitResult(sample.shift)+sample.backgrou
nd);
        set(hp,'hittest','off');
        hold all;
    end
end
%show region
if(~isempty(sd.region))
    stem(sd.region(1),sd.rangeIntensity(2),'marker','none');
    stem(sd.region(2),sd.rangeIntensity(2),'marker','none');
end
%show formula set
global fs;
for i=1:length(fs)
    fo=fs(i);
```

```matlab
    if(~isempty(fo.formula))
        formula=addToken(fo.formula,'token_');
        args=fo.args;
        for j=1:length(args)
            name=args(j).name;
            val=args(j).val;
            if(~strcmp(name,'w'))
                name=['token_',name];
            end
            %try
                eval([name,'=',num2str(val),';']);
            %end
        end
        w=linspace(sd.rangeShift(1),sd.rangeShift(2));
        %try
            %keyboard;
            I=eval([formula,';']);
            hp=plot(w,I);
            set(hp,'HitTest','off');
            hold all;
        %end
    end
end




set(gca,'xlim',sd.rangeShift);
set(gca,'ylim',[0,max(sd.union.intensity)]);
set(gca,'ButtonDownFcn',{@ui_spectrum_ButtonDownFcn});




function ui_debug_Callback(~, ~, ~)
getFit();




% --- Executes on button press in Intensity_at_x.
function Intensity_at_x_Callback(hObject, eventdata, handles)
% hObject    handle to Intensity_at_x (see GCBO)
% eventdata  reserved - to be defined in a future version of MATLAB
% handles    structure with handles and user data (see GUIDATA)

global sd
```

```matlab
sd.map=[];
for x=sd.rangeX(1):sd.rangeX(2)
    for y=sd.rangeY(1):sd.rangeY(2)
        %
sd.map(x,y)=abs(trapz(sd.samples(x,y).shift,sd.samples(x,y).intensi
ty));
        sample=sd.samples(x,y);
        shift=sample.shift;
        intensity=sample.intensity;
        beginIndex=find(shift>sd.region(1),1,'first');
        endIndex=find(shift<sd.region(2),1,'last');
        shift=shift(beginIndex:endIndex);
        intensity=intensity(beginIndex:endIndex);
        sd.map(x,y)=max(intensity);
    end
end
ui_refresh

% --- Executes on button press in WavenumberatmaxIntensityatregx.
function WavenumberatmaxIntensityatregx_Callback(hObject,
eventdata, handles)
% hObject    handle to WavenumberatmaxIntensityatregx (see GCBO)
% eventdata  reserved - to be defined in a future version of MATLAB
% handles    structure with handles and user data (see GUIDATA)
global sd
sd.map=[];
for x=sd.rangeX(1):sd.rangeX(2)
    for y=sd.rangeY(1):sd.rangeY(2)
        %
sd.map(x,y)=abs(trapz(sd.samples(x,y).shift,sd.samples(x,y).intensi
ty));
        sample=sd.samples(x,y);
        shift=sample.shift;
        intensity=sample.intensity;
        beginIndex=find(shift>sd.region(1),1,'first');
        endIndex=find(shift<sd.region(2),1,'last');
        shift=shift(beginIndex:endIndex);
        intensity=intensity(beginIndex:endIndex);
        [maxYValue, indexAtMaxY] = max(intensity);
        xValueAtMaxYValue = shift(indexAtMaxY(1));
        sd.map(x,y)=xValueAtMaxYValue;
    end
```

```
end
ui_refresh


%[maxYValue, indexAtMaxY] = max(y);
%xValueAtMaxYValue = x(indexAtMaxY(1));
```

Appendix C

Adsorption kinetics

The section shows the rest of the adsorption kinetics models plotted in graph form for all CNT concentrations used for both set of times.
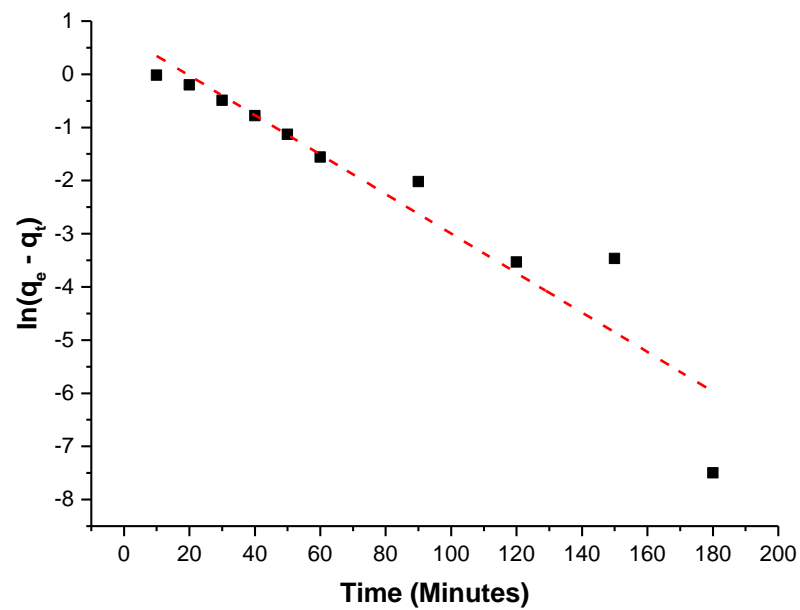
Figure C1 : First order kinetic model for 5 mg/L CNT concentration for the entire duration of experiment.
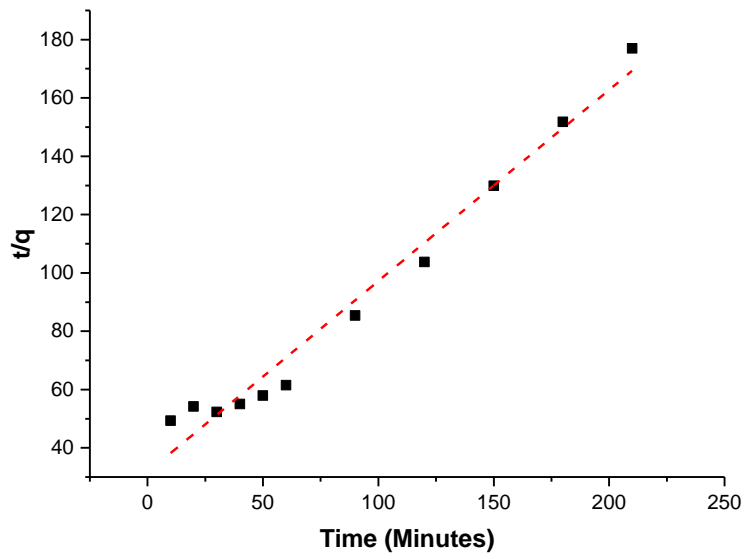
Figure C2: Second order kinetic model for 5 mg/L CNT concentration for the entire duration of experiment.
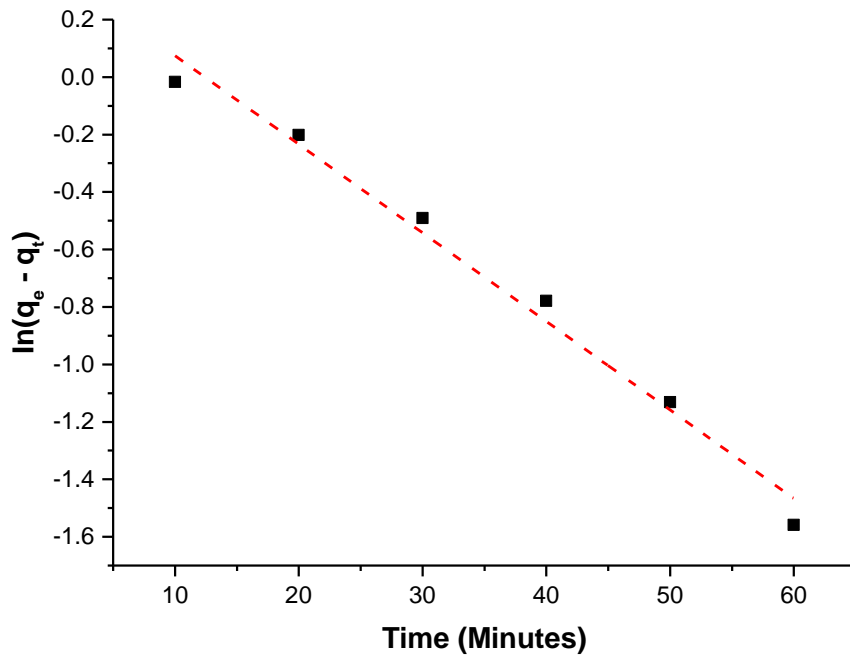
Figure C3 : First order kinetic model for 5 mg/L CNT concentration for the first 60 minutes of the experiment.
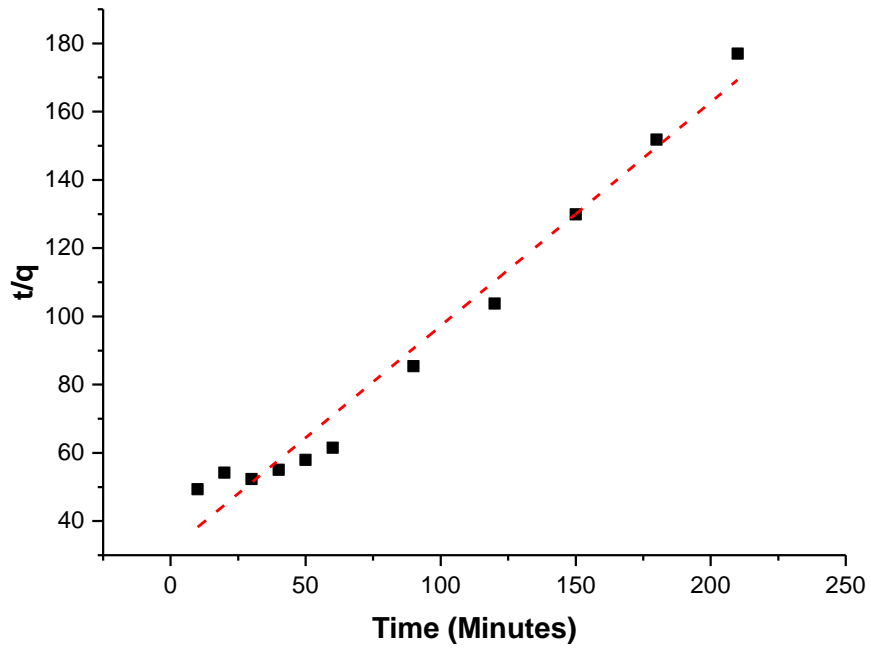
Figure C4 : Second order kinetic model for 5 mg/L CNT concentration for the first 60 minutes of the experiment.
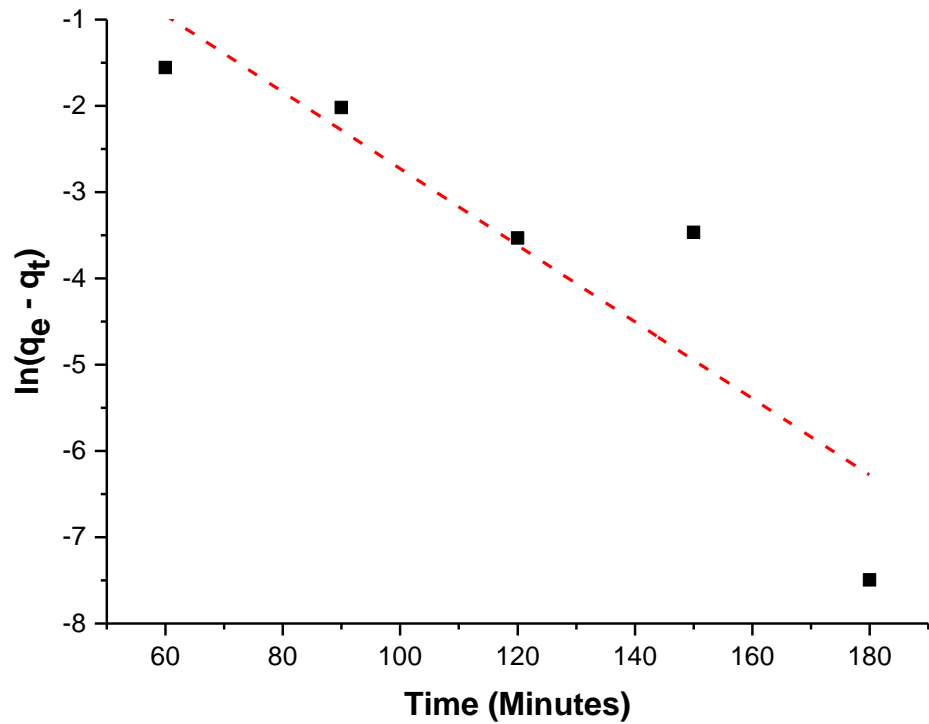
Figure C3 : First order kinetic model for 5 mg/L CNT concentration for the Second period of the experiment.
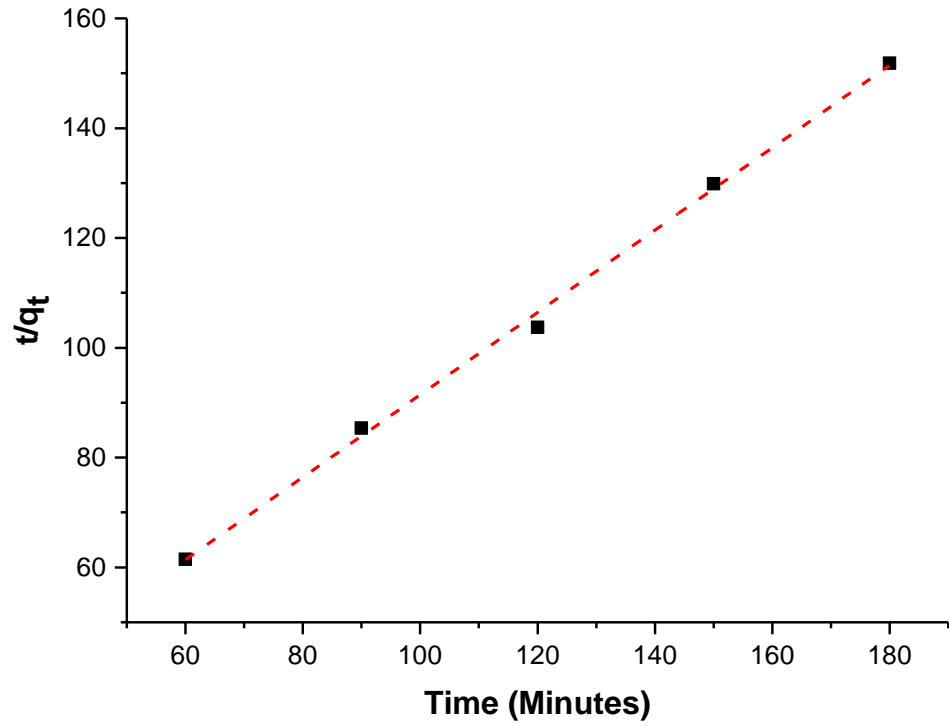
Figure C3 : Second order kinetic model for 5 mg/L CNT concentration for the second period of the experiment.
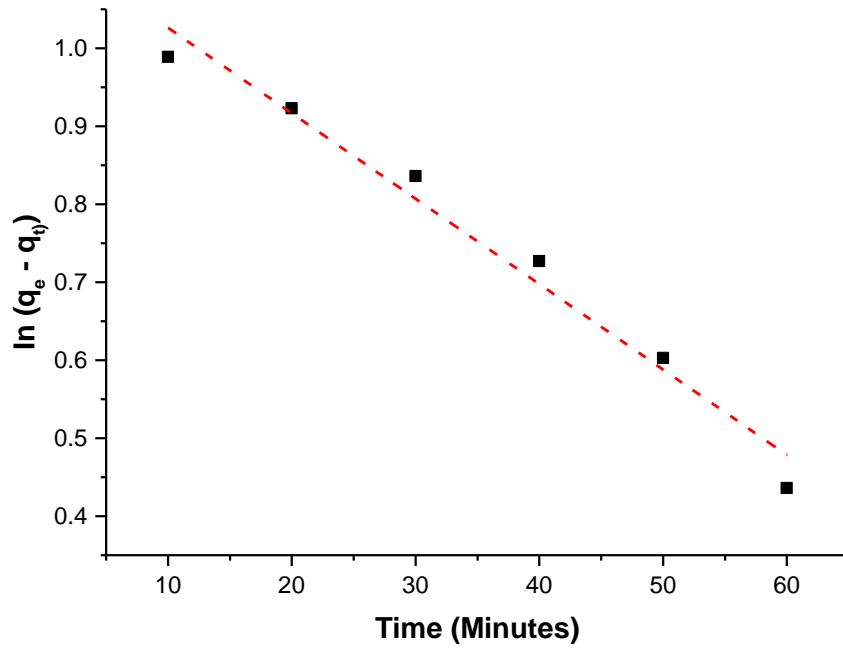
Figure C5: First order kinetic model for 10 mg/L CNT concentration for the first 60 minutes of the experiment.
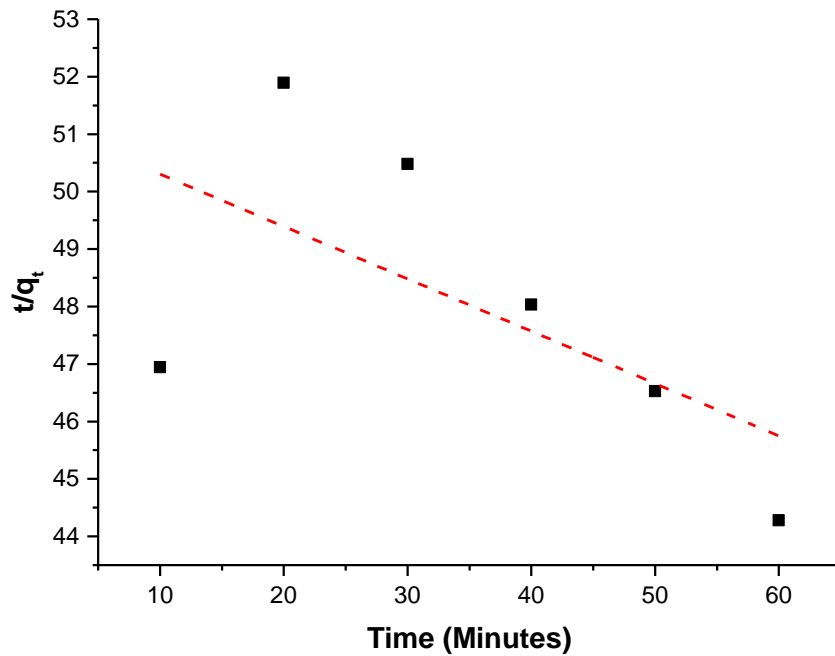
Figure C6: Second order kinetic model for 10 mg/L CNT concentration for the first 60 minutes of the experiment.
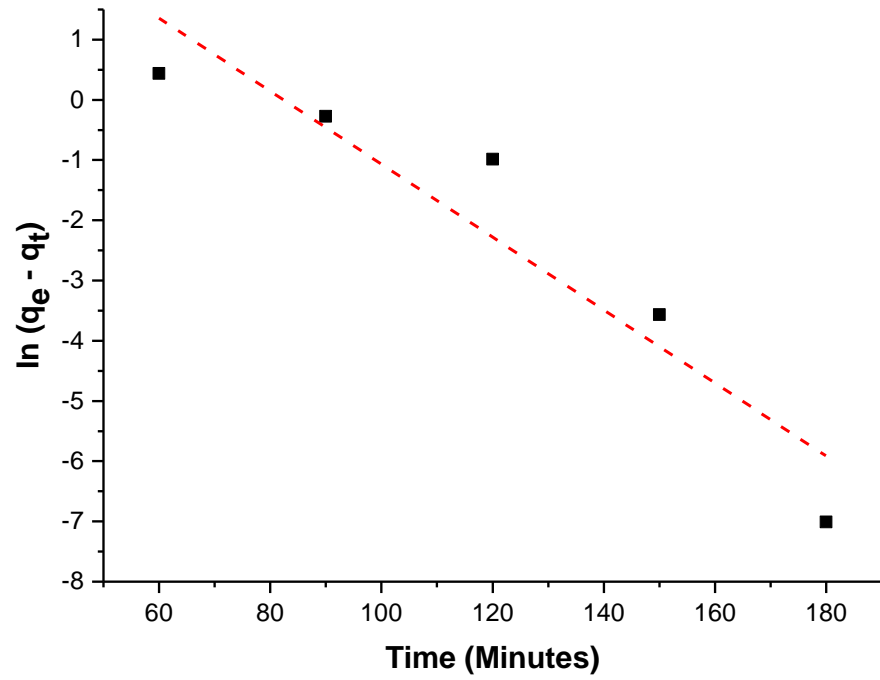
Figure C3 : First order kinetic model for 10 mg/L CNT concentration for the Second period of the experiment.
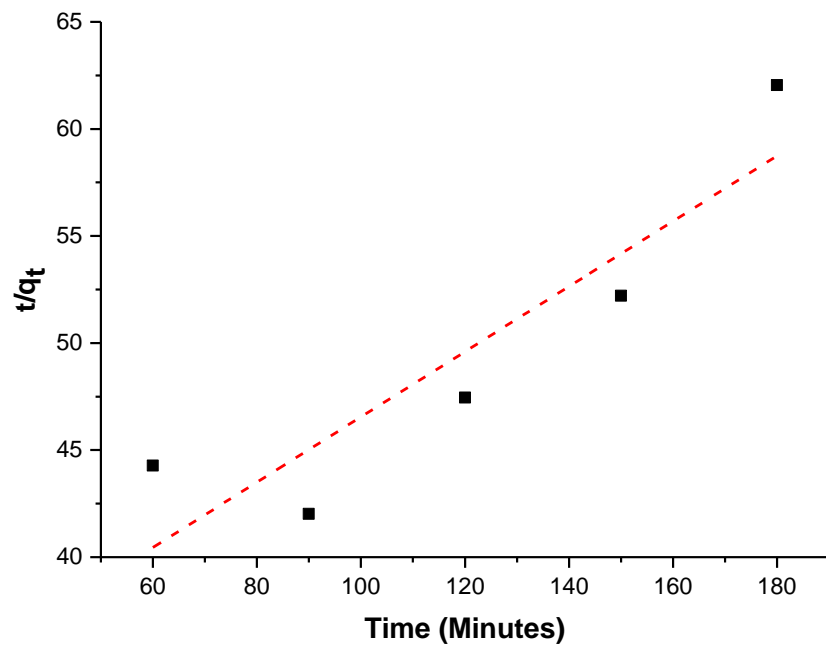
Figure C3: Second order kinetic model for 10 mg/L CNT concentration for the second period of the experiment.
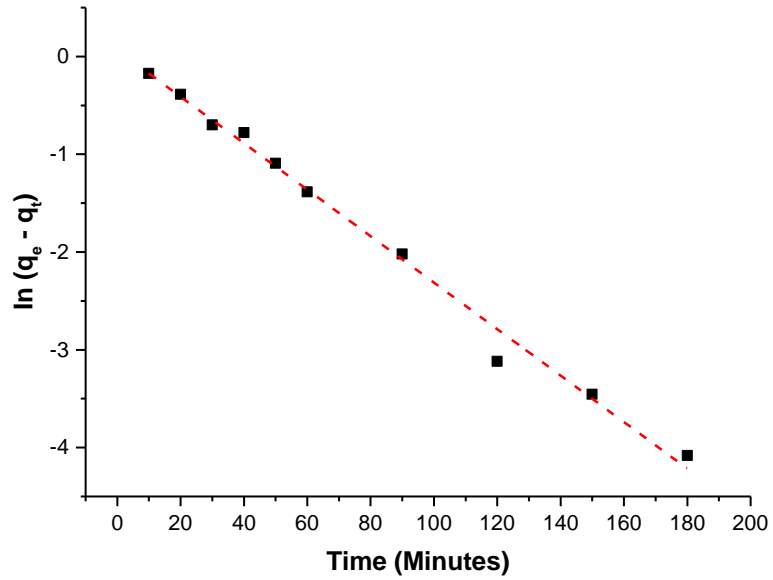
Figure C7: First order kinetic model for 15 mg/L CNT concentration for the entire duration of experiment
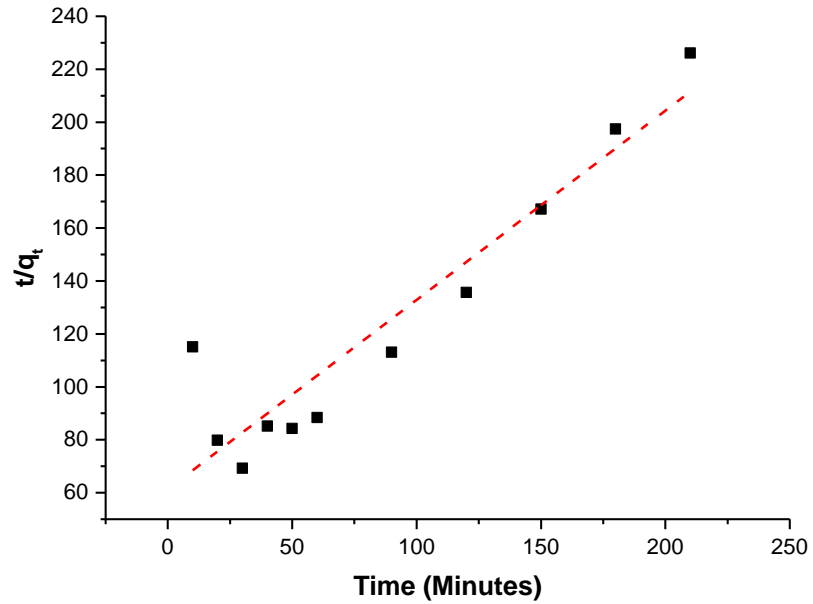
Figure C8: Second order kinetic model for 15 mg/L CNT concentration for the entire duration of experiment
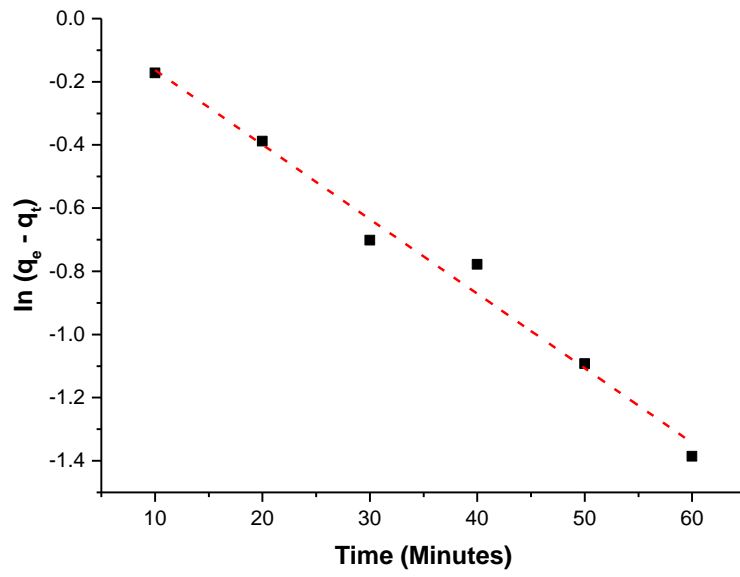
Figure C9: First order kinetic model for 15 mg/L CNT concentration for the first 60 minutes of the experiment.
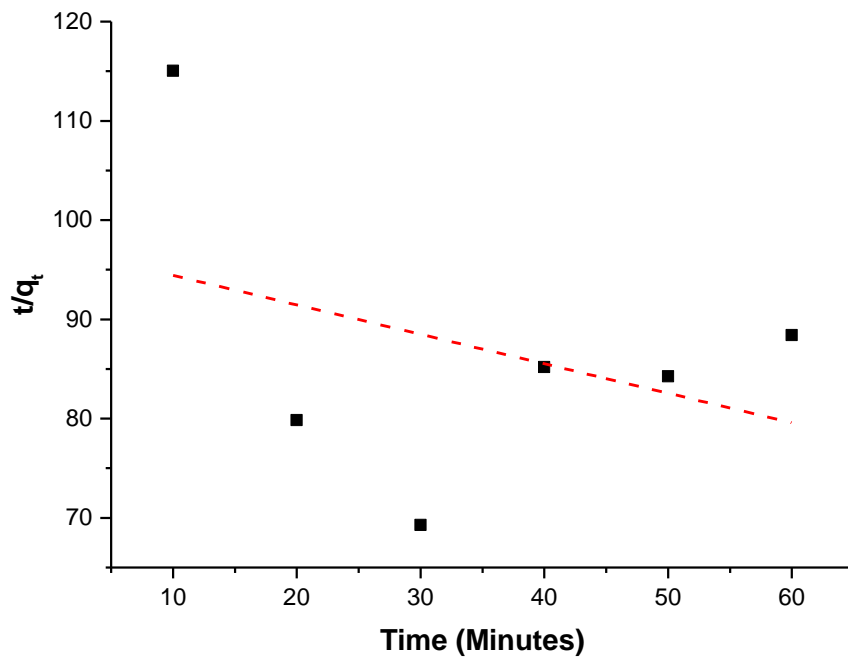
Figure C10: Second order kinetic model for 15 mg/L CNT concentration for the first 60 minutes of the experiment.
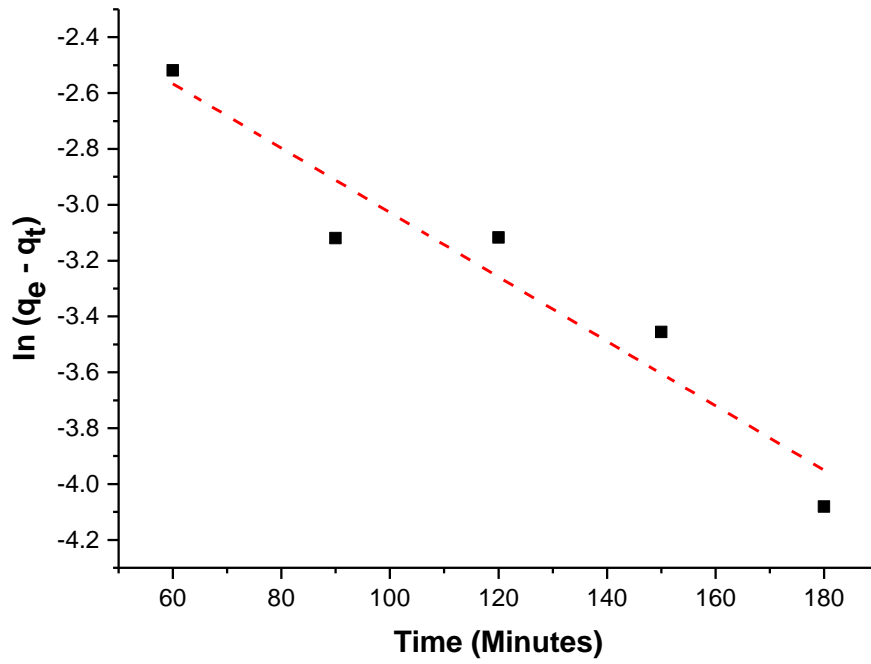
Figure C11: First order kinetic model for 15 mg/L CNT concentration for the second period of the experiment.
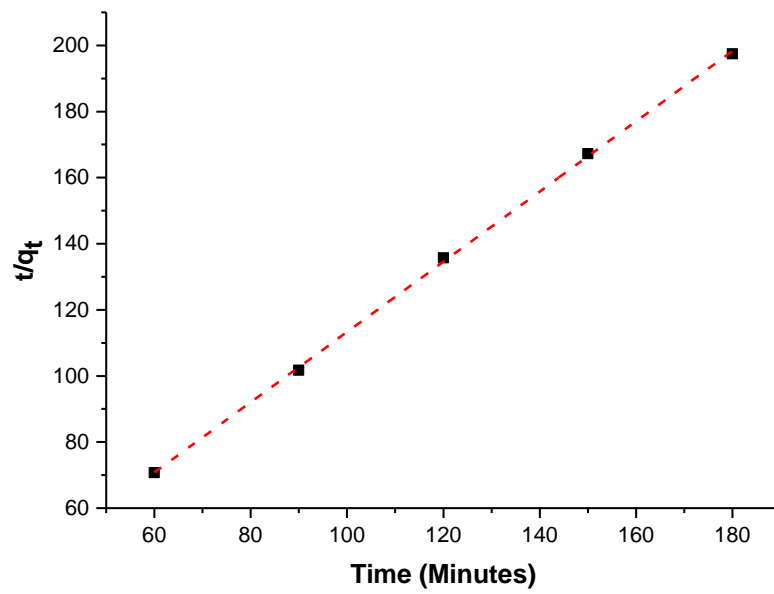
Figure C12: Second order kinetic model for 15 mg/L CNT concentration for second period of the experiment.
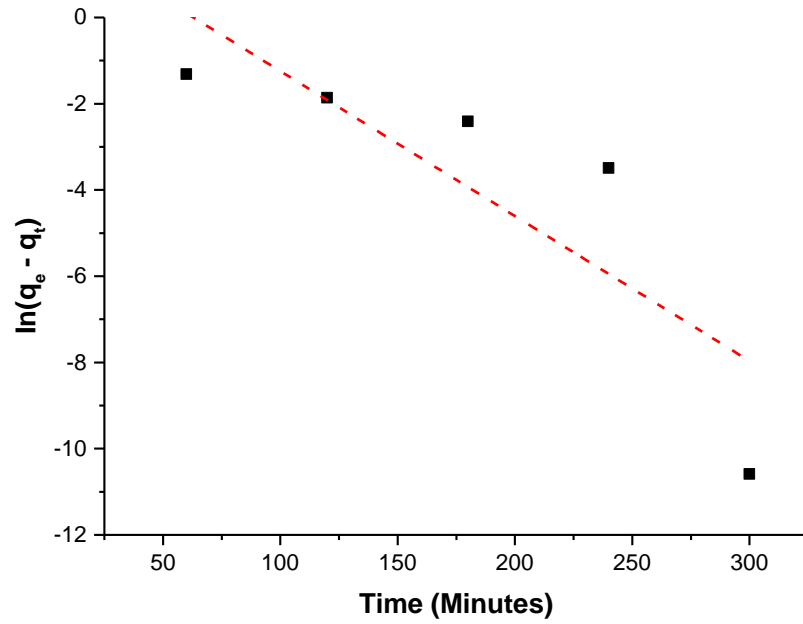
Figure C13: First order kinetic model for 20 mg/L CNT concentration for the entire duration of experiment.
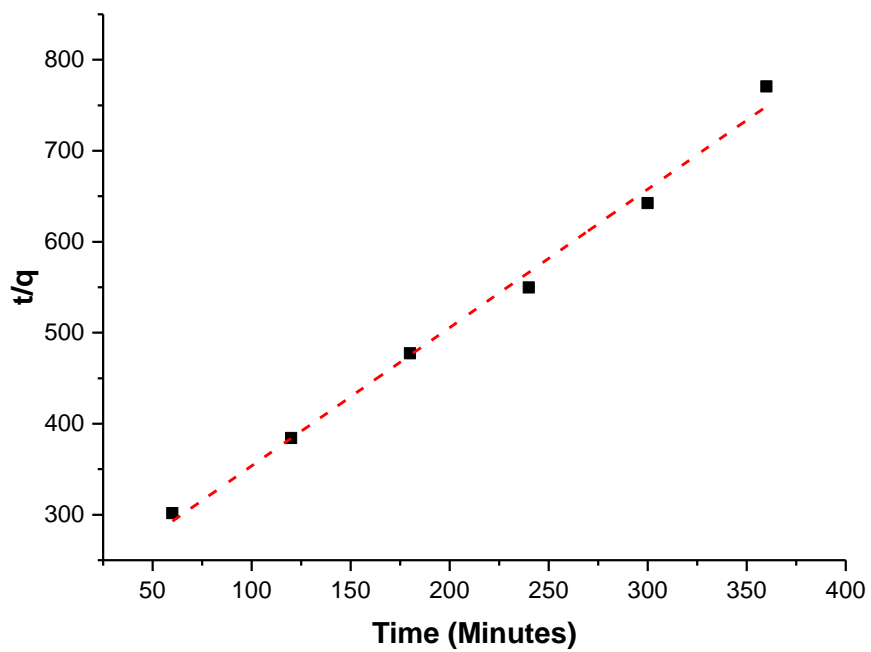
Figure C14: Second order kinetic model for 20 mg/L CNT concentration for the entire duration of experiment
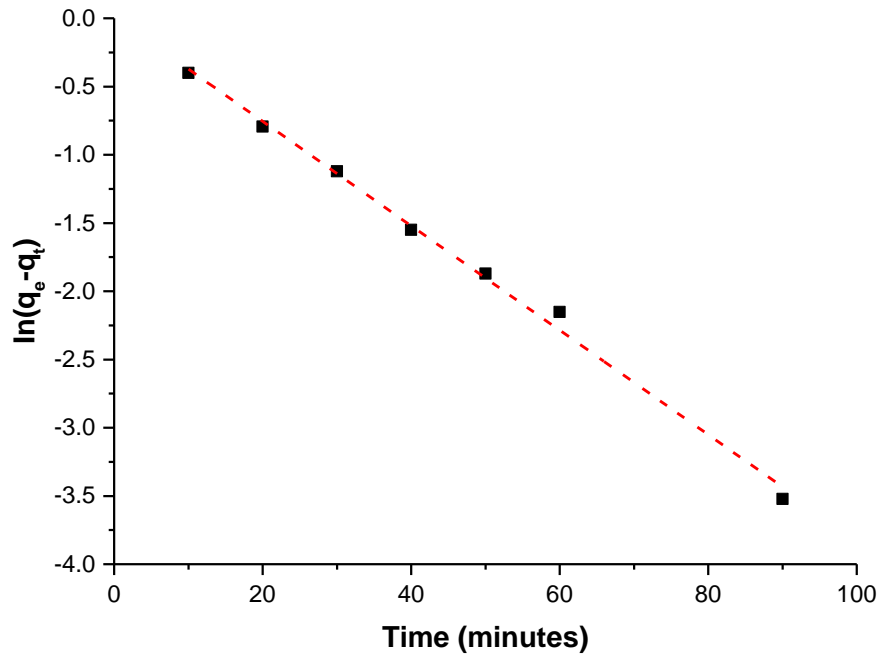
Figure C15: First order kinetic model for 20 mg/L CNT concentration for the entire duration of experiment at pH 4.
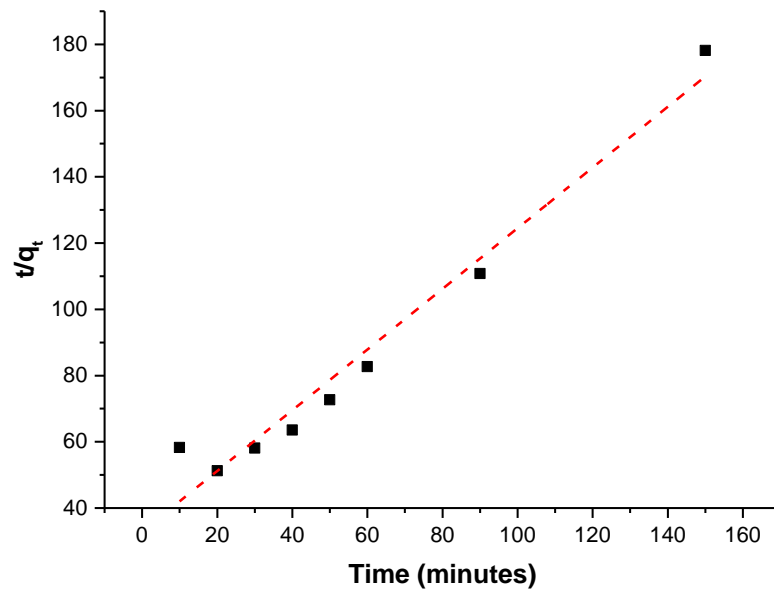
Figure C16: First order kinetic model for 20 mg/L CNT concentration for the entire duration of experiment at pH 4